"NANOTHERANOSTICS" FOR TUMOR IMAGING AND TARGETED DRUG DELIVERY

by

Peng Zou

A dissertation submitted in partial fulfillment
of the requirements for the degree of
Doctor of Philosophy
(Pharmaceutical Sciences)
in The University of Michigan
2011

Doctoral Committee:

        Associate Professor Duxin Sun, Chair
        Professor David E. Smith
        Professor Steven P. Schwendeman
        Professor Shaomeng Wang

To my family

ACKNOWLEDGEMENT

The work presented in this dissertation would not have been possible without the support of many people. I would like to thank my advisor and dissertation committee chairman, Dr. Duxin Sun, for his guidance and mentorship throughout my Ph.D. study. He has created a great environment in which graduate students can work on projects that are interesting, challenging, and relevant to the scientific community. During the past five years, he taught me many things about research, presentation, and being professional. I greatly appreciate his support and encouragement for both my research and life.

I would also like to thank my dissertation committee members, Dr. David E. Smith, Dr. Steven P. Schwendeman and Dr. Shaomemg Wang, for their insight and valuable suggestions. They help me turn my thesis dream into a reality. In particular, I would like to thank Dr Wang, who involved me into the development of MDM2 inhibitors for the treatment of human cancer. Under Dr Sun and Dr Wang's instruction, I gained a lot of experience in preclinical DMPK studies.

I would like to thank Dr Andrew Wang from Ocean Nanotech Inc. for sharing the nanomaterials and his expertise in nanocrystal fabrication. I also gratefully acknowledge the technical assistance of Dr Sam Straight from Center for Living Cell imaging, for helping me analyze FRET confocal images.

I must acknowledge all of the professors whom I have taken classes from, both at University of Michigan and the Ohio State University: Professors Rose Feng, Victor Chi-

TABLE OF CONTENTS

LIST OF TABLES

LIST OF FIGURES

ABSTRACT

"Nanotheranostics" for Tumor Imaging and Targeted Drug Delivery

The magnetic resonance imaging (MRI) technique is a promising tool that improves cancer detection, facilitates diagnosis and monitors therapeutic effects. Superparamagnetic iron oxide nanoparticles (SPIOs) have emerged as MRI contrast agents for tumor imaging and as potential vectors for targeted anti-cancer drug delivery; nevertheless, the application of SPIOs has been hampered due to a lack of specificity to tumor tissues and premature drug release. This project aims at developing multifunctional SPIOs for both cancer imaging and targeted drug delivery via conjugation of tumor specific antibodies with SPIOs. The application of anti-TAG-72 antibodies as tumor targeting modalities was evaluated in cultured colorectal cancer cells and in xenograft models by using fluorescent imaging and positron emission tomography (PET) imaging. It was demonstrated that antibody-labeled SPIOs were superior imaging agents and drug carriers for increased tumor specificity. The regulation and kinetics of intracellular drug release from SPIOs were explored by means of fluorescence imaging. *In vitro* and *in vivo* fluorescence resonance energy transfer (FRET) imaging was employed to investigate the mechanisms of premature drug release from nanocarriers. The large volume and high hydrophobicity of cell membranes were found to play an important role in premature drug release. The encapsulation of SPIOs into nanocarriers decreased drug release in a dose-dependent mode. This study provided future opportunities to improve the efficiency of nanocarriers by exploring the mechanism of drug release and disassembly of SPIO-loaded polymeric nanoparticles.

CHAPTER I

Background and Introduction

1.1 Current challenges in nanoscale drug delivery platforms

Chemotherapy is designed to kill cancer cells. Unfortunately, anticancer drugs often kill healthy cells and cause serious side effects. It is desirable to specifically deliver anticancer drugs to targeted cancer cells. Nanoparticles might act as carriers for anticancer drugs since the nanocarriers can accumulate in the tumors by the enhanced permeability and retention (EPR) effect and/or by the specific binding between targeting ligands and tumors tissues[1]. However, several challenges were encountered in the development of nanocarriers for targeted anticancer drug delivery.

One of the top challenges of the nanocarriers is the lack of targeting efficacy. The passive accumulation of nanocarriers is driven only by the size of particles and EPR effect[1]. Although the conjugation with ligands, aptamers, and small peptides that bind to surface markers expressed in the tumor cells or tumor microenvironment can improve tumor targeting, the expression of makers and receptors in some normal tissues and nonspecific binding to normal tissues usually attenuate the cancer-specificity of target moieties and nanocarriers. Another strategy of targeted drug delivery is to trigger site-specific drug release from nanocarriers by light, heat, pH and redox and amperometric reactions[2]. However, this strategy depends on the successful delivery of nanocarriers to tumor tissues.

The second challenge is the existence of various biological barriers which the nanocarriers need to bypass in the body, including biophysical barriers and functional barriers. Among these biophysical barriers are the endothelial and epithelial barriers in blood vessel walls, the placenta, brains and intestines, abnormal flow of blood, osmotic pressure gradients at target sites, hemodynamical aspects of particle margination [1, 3]. Furthermore, cell membrane and intracellular organelles are also obstacles to be bypass. For example, nanoparticles can be trapped in endosomes. The functional barriers include enzymatic degradation, uptake by scavenging phagocytic cells, and molecular and ionic efflux pumps that expel drugs from target cells [3]. Such barriers significantly prevent the successful delivery of nanocarriers and targeting moieties to tumor tissues. For example, only a small fraction of systemically administrated targeting moieties such as an antibody or peptide reaches tumors[1].

The third issue is the development of imaging modalities for visualizing the biodistribution of nanocarriers and drugs in real-time. Currently, the only technique that can quantitative detect nanocarriers *in vivo* is through radionuclide labeling [3]. Usually, radionuclides are labeled to nanocarriers through chemical conjugation and chelation. The radionuclide chelation may be unstable in the body, leading to unreliable results. Furthermore, current imaging techniques could not distinguish the released drug and unreleased drug, resulting in their inability to visualize the *in vivo* drug release.

Premature drug release is another challenge for lipid and polymer-based nanocarrier such as micelles and liposomes[4]. Although the encapsulation of drug in the liposomal aqueous phase could decrease drug leakage[5], the burst drug release is still a limitation

of micelle nanocarriers. Additionally, the reasons for rapid premature drug release are still not clear.

The fifth challenge is to develop new mathematical and computer models to predict the risk and benefit parameters of nanoparticles for targeted delivery[3]. The relationships between the biodistribution and the properties of nanoparticles such as size, shape, charges, composition, surface chemistry and level of aggregation should be established.

Finally, to ensure the safety, more efforts should be made to address the biocompatibility and toxicity issues of nanocarriers. Because of quantum size effects and large surface area to volume ratio, nanoparticles have unique properties. A fundamental understanding of the relationship between the properties (size, shape, charges, composition, surface chemistry and level of aggregation) of nanoparticles and their toxicity (for example, immunotoxicity) will facilitate the design and optimization of safe nanoscale drug delivery systems[6].

1.2 Application of MRI in tumor imaging

The application of cancer imaging modalities such as magnetic resonance imaging (MRI) has advanced cancer detection, diagnosis and treatment options. When a magnetic field is applied to a human body, the protons of water align with the direction of the field. When this field is turned off, the protons release this energy at a resonance radio frequency which can be detected by a MRI scanner and manipulated by additional magnetic fields to build up enough information to construct an image of the body[7]. Different tissues can be distinguished because the protons in different tissues return to their equilibrium state at different rates. Although the tumors may be visualized in T_1-and T_2-weighted MRI images, the differences in T_1 and T_2 relaxation times with regard to

3

benign and malignant changes are not significant, and therefore, false positives would arise. Paramagnetic gadolinium chelates which generate extremely bright T_1-weighted images, have been used clinically as MRI contrast agents to image tumors because of tumor-mediated angiogenesis[8]. However, gadolinium chelates are not tumor-specific and the conjugation of adequate amounts of gadolinium to tumor-specific monoclonal antibodies is difficult to achieve [8, 9]. Furthermore, certain gadolinium based contrast agents are likely to cause nephrogenic systematic fibrosis (NSF)[10]. A new MRI contrast agent is needed to be developed.

1.3 Anti-TAG-72 monoclonal antibodies

To improve the cancer-specific targeting of contrast agents for MRI and drug delivery, a cancer-specific targeting ligand is required. TAG-72 (Tumor Associated Glycoprotein-72) is a human mucin-like glycoprotein complex that is over-expressed in many epithelial-derived cancers including colorectal, pancreatic, breast, ovarian, non-small cell lung, and gastric cancers [11-13]. ^{125}I-labeled anti-TAG72 antibodies (murine CC49 and humanized HuCC49ΔCH2) combined with a handheld gamma detection probe have been used for intraoperative tumor detection. In xenograft models (with TAG-72 expressing colon cancer cells LS174T) [11, 14-21], ^{125}I-labeled anti-TAG-72 antibodies (B72.3 and CC49) localized 18-fold higher in tumors than in normal tissues [21-23]. In more than 300 colorectal cancer patients, anti-TAG-72 antibodies (CC49 and HuCC49ΔCH2) localized 77% to 89% of primary colorectal tumors [24-26] and 78% to 97% of metastatic lesions [27-29]. More importantly, anti-TAG-72 antibodies not only detect visible gross tumors but also clinically occult disease within lymph nodes in more than 70% of the cases [27-29], which are normally undetectable by traditional surgical

4

exploration and pathological examination. The detection of occult tumor and subsequent resection are critical for improving patient survival. In 97 patients with primary colorectal cancer with a 2.5 to 5 years follow up, survival rate is 87.5% for patients with no anti-TAG-72- bound tissue remaining after surgery, while the survival rate is only 12.5 to 30% for patients with antibody-bound tissue remaining at the completion of surgery [30-33]. In 131 patients with recurrent colorectal cancer in a 2.5 year follow up, the survival is 55% for patients with no antibody bound tissue remaining, and 0% for patients with antibody bound tissue remaining[34]. Since the anti-TAG-72 antibodies can detect both early-stage and late-satge colorectal tumors, we intend to utilize the antibodies as a targeting ligand to deliver MRI contrast agent and drug to tumors.

1.4 Superparamagnetic iron oxide nanoparticles as an MRI contrast agent

Recently, superparamagnetic iron oxide nanoparticles (SPIOs) have a surge of interest because of their potentials in MRI. Compared with paramagnetic ions, superparamagnetic iron oxide nanoparticles (SPIOs) can produce enhanced relaxation rates at significantly lower doses (μmol/kg) due to their larger magnetic moment, leading to a higher sensitivity of MRI. SPIOs decrease T_2 relaxation time and appear dark on T_2*-weighted images[35]. SPIOs have been used to improve the diagnostic quality of MRI investigations of liver, bone marrow, splenic lymphomas, lymph nodes and tumors[36, 37].

The magnetism properties and cell internalization of SPIO are strongly size-dependent[38]. SPIOs less than 30 nm in size are superparamagnetic while larger SPIOs are ferromagnetic[39]. The magnetization value changes from 25 to 43, 80, and 102 emu/(g Fe) as the size of SPIOs increases from 4 to 6, 9, and 12 nm, respectively [40].

Size, charge and surface chemistry of the SPIOs also strongly influence their biodistribution[41, 42]. Due to the reticuloendothelial system (RES) clearance, SPIOs are eliminated very effectively from blood and distribute in the liver, spleen, bone marrow and lymphnodes[43]. SPIOs with a rational size, charge and surface coating are expected to localize in tumors due to the enhanced permeability and retention (EPR) effect [44]. Following systematic administration, SPIO larger than 200 nm are usually sequestered by the spleen as a result of mechanical filtration and are eventually removed by RES. SPIOs larger than 50 nm are considered to be liver-specific. Small SPIOs less than 50 nm are designed for extrahepatic targets, such as lymph nodes and tumors. On the other hand, smaller particles less than 10 nm are rapidly removed through extravasation and renal clearance[42, 45]. Charged SPIOs are uptaked by RES faster than low charged and uncharged SPIOs, positively charged ones faster than the negatively charged[42]. Increasing the surface hydrophilicity of SPIOs reduces the liver uptake[42]. Furthermore, surface coating with hydrophilic polymer polyethyleneglycol (PEG) significantly reduces the non-specific RES uptake by 86% and prolongs the circulation time [41, 46]. Hence, SPIOs with a diameter less than 50 nm and hydrophilic surface coating are expected to exhibit a longer circulation in the blood and accumulate in extrahepatic tissues.

1.5 Preparation and surface coating of SPIOs

A conventional chemical method coprecipitation was utilized to synthesize SPIOs, by adding a base to the Fe^{2+} and Fe^{3+} aqueous salt solutions [47]. Different pH, ionic strength, temperature, Fe^{2+} and Fe^{3+} ratio resulted in SPIOs with different size, shape and composition [47-49]. Although the coprecipitation technique was simple and low-cost, the size distribution and morphology of SPIOs were hard to control. Since the magnetic

properties and biodistribution of SPIOs are highly dependent on their size and shape, it is important to produce monodisperse SPIOs (size variation < 5%) [50]. Some other methods such as microemulsion, ultrasound irradiation, sol-gel syntheses, electrospray syntheses, hydrothermal synthesis and thermal decomposition have been developed to produce monodisperse SPIOs [49, 51-53]. Currently, thermal decomposition method is widely used for large-scale synthesis of SPIOs [50]. Basically, iron–oleate complex was produced from metal chlorides and sodium oleate. The iron–oleate complex was an excellent growth source for nanocrystals. In the presence of oleic acid, the iron–oleate complex in organic solvent such as 1-octadecene was slowly heated to 320 °C, and was aged at that temperature for 30 min, generating SPIO nanocrystals. The SPIO nanocrystals could easily be re-dispersed in organic solvents including toluene and chloroform. The particle size of SPIOs was controlled by the boiling point of the organic solvent (For example, 1-octadecene 317 °C and 1-hexadecene 274 °C), the concentration of oleic acid, reaction time and reaction temperature. As the boiling point of the solvent increased or the concentration of oleic acid increased, the diameter of the iron oxide nanocrystals increased.

SPIOs synthesized by thermal decomposition are covered with a lipophilic oleic acid layer, resulting in aqueous insolubility. To improve the aqueous solubility and stability, reduce nonspecific binding and uptake, and incorporate functional groups to SPIOs, various materials have been applied to coat SPIOs and convert organic phase SPIOs to water-soluble SPIOs, such as silica [54], carbon [55], small surfactants[56], lipids[57] and amphiphilic polymers[58, 59]. For example, the lipophilic block of amphiphilic polymers interdigitates into the oleic acid surface of SPIOs through hydrophobic

interactions. The hydrophilic block faces outward, which makes SPIO surface hydrophilic, soluble, and stable in aqueous solution. Furthermore, surface coating has introduced functional groups such as carboxyls, amines and thiols to the surface of SPIOs, which make the conjugation with tumor targeting molecules possible. To improve the tumor targeting of SPIOs, various tumor targeting molecules have been attached to SPIOs, including antibody[41, 60, 61] and antibody fragments[62], peptides[63, 64], oligonucleotides[65], and receptor ligands, such as epithelial growth factor (EGF)[66], folic acid[67, 68], somatostatin analogues[69] and transferrin[70].

1.6 SPIO as a drug carrier for image-guided target delivery

Most MRI contrast agents only provide diagnostic advantage without offering therapeutic efficacy. In contrast, SPIOs or targeting ligand labeled SPIOs have been used for targeted delivery of anticancer drugs. Drug molecules are either entrapped in the SPIO surface layer through physical interactions (electrostatic interaction or hydrophobic interaction) or covalently conjugated to the functional groups (carboxyl, primary amine or thiol) on the SPIO surface and released in target tissues through pH or temperature dependent release or enzymatic cleavage. For example, phosphodiester[71], azido or alkyiie groups[72], and enzymatic cleavable peptides[73] may be used a cross-linker to conjugate drug molecules to SPIO. In addition, SPIO is also formulated into thermal sensitive magnetoliposomes as a drug carrier [74-76]. The thermal sensitive phospholipids outshell is ruptured to release the encapsulated drugs when encapsulated SPIOs are exposed to an exogenous magnetic field.

SPIOs coated with oleic acid show excellent colloidal stability and solubility in organic solvents. Different procedures such as coating with amphiphilic polymers are

employed to convert the hydrophobic oleic acid coated SPIOs into hydrophilic SPIOs. The hydrophobic moiety of the amphiphilic polymer anchors on the oleic acid layer and form a hydrophobic layer, while the hydrophilic moiety of the polymer towards outside. The hydrophobic layer is utilized as a reservoir for the loading and pH-dependant release of anticancer drug doxorubicin (DOX) and paclitaxel[63, 77-81]. The hydrophobic DOX (log$P$1.85) and paclitaxel (log$P$ 4)[77] will partition into the hydrophobic layer when pH>7.4. The aqueous solubility of DOX is dramatically increased at pH<6 due to the protonation of DOX (The pKa of the doxorubicin amino group is 7.6 at 37°C, ionic strength 0.15[82]). The encapsulated drug is released from SPIOs. Furthermore, the release of DOX and paclitaxel from SPIOs was observed to extend over three weeks [77], which is likely due to the slow dissociation of coating polymers from SPIOs. Hence, the drug encapsulated into SPIOs will exhibit prolonged circulation time, which is especially important for drugs with a short half-life.

To be delivered to tumor tissues, the drug-loaded SPIOs should be biocompatible and stable in the circulation. However, the uncoated SPIOs tend to aggregate in blood stream through van der Waals attractions, leading to the rapid elimination by reticulo-endothelial system (RES)[83]. Although coating with some hydrophilic polymers such as dextran or starch have improved the colloidal stability, reduced RES uptake and prolonged the circulation of SPIOs, the coated SPIOs have limited drug loading capacity and the drug rapidly dissociates in the circulation after i.v. administration [84]. To increase drug loading capacity and prevent the drug "leaking" from SPIOs in circulation, more rigid SPIO coating or drug loading methods should be employed.

1.7 Self-assemble block copolymer micelles for drug delivery

During the past decade, block copolymers (BCP), especially pH sensitive amphiphilic (hydrophobic-polar) BCP have been used to form self-assembled micelles or vesicles for drug, gene and protein delivery [85-90]. Compared with lipid vesicles and micelles, BCP vesicles and micelles are more stable and robust while their morphologies are easier to be controlled[85]. BCP micelles possess a core-shell structure. When the organic solution (both blocks have good solubility in this common solvent) of BCP is diluted by water, the hydrophobic blocks of BCPs will be held together to form the micelle core, while the outside hydrophilic blocks of BCPs will suspend in aqueous media to form the corona. The morphology of the BCP micelles is maintained by a force balance between three factors: the degree of stretching of the core-forming blocks, the interfacial tension between the micelle core and the solvent outside the core, and the repulsive interactions among corona forming chains[91]. The particle size, shape, rigidity and loading capacity are controlled by molecular weight of polymer, hydrophobic to hydrophilic relative block length, lipophilicity of core-forming blocks, the width of the molecular weight distribution, polymer concentration, solvent nature and water content as well as the presence of additives such as surfactants and ions [92-94]. For example, to obtain spherical micelles with hydrophobic cores, the molecular weight of the corona-forming block should not exceed that of the core-forming block[95].

Polymeric micelles as carriers of hydrophobic drugs have drawn increasing research interests, due to their advantages in drug delivery [96]. First, polymeric micelles are very stable in aqueous solution because of their low critical micelle concentration (CMC), which is expected to prevent micelles from disruption upon dilution in the blood stream

after intravenous injection. Furthermore, the PEG surface and nanoscale size of micelles protect them from non-specific reticuloendothelial uptake and renal clearance and extend their blood circulation halflife. Also, the nanoscale polymeric micelles can escape from blood circulation due to enhanced permeability and retention (EPR) effect and accumulate in the tumors. In addition, the aqueous solubility for hydrophobic drugs can be dramatically increased when they are encapsulated into the core of micelles.

Hydrophobic drugs can be incorporated into the micelle core by either chemical conjugation or hydrophobic interaction[97]. For examples, paclitaxel was encapsulated into micelles consisting of poly(ethylene glycol)-distearoyl phosphoethanolamine conjugates (PEG-PE), solid triglycerides, and cationic lipids by hydrophobic interactions[98]. In this design, cationic lipids could help the micelles escape from endosomes and enter the cytoplasm. In contrast, Nakanishi and coworkers synthesized doxorubicin-conjugated poly(ethylene glycol)–poly (aspartic acid) block copolymer (PEG–PAsp-DOX) to form micelles and physically entrapped free doxorubicin into the PAsp-DOX core[99]. They found that the polymeric micelle with chemically conjugated DOX and physically entrapped DOX expressed high antitumor activity which was mainly caused by the physically entrapped DOX, while the chemically conjugated DOX showed negligible antitumor activity due to inability to escape endosomes/lysosomes[100]. To facilitate the escape from endosomes/lysosomes, DOX was conjugated to the micelle cores through acid-cleavable linkage, such as a hydrazone bond [101, 102]. The hydrazone linkage was cleaved in the endosomes/lysosomes to release free DOX molecules.

1.8 Stability of polymeric and lipid-based micelles

For drug molecules physically entrapped and chemically conjugated in the core of polymeric and lipid-based micelles, their delivery efficacy depends on the integrity of nanoparticles in blood circulation and specific release in target tissues[103]. An intractable problem for micelle delivery system is the rapid, premature release of drugs before the micelles reach their targets[95]. For example, the clinical trial of poly(aspartic acid)–b–poly(ethylene glycol) micelles physically entrapped with DOX showed that the micellar formulation only slightly improved the pharmacokinetic parameters of doxorubicin compared with free DOX (2-fold increase in area under plasma concentration-time curve (AUC) and 1.5-fold decrease in volume of distribution (V_d))[104]. In contrast, liposomal formation of DOX resulted in a 556-fold increase in AUC and 300-fold decrease in V_d[105]. Furthermore, Pluronic$^{®}$ block copolymer micelles non-covalently incorporated DOX showed similar AUC to free doxorubicin in patients [106]. All the pharmacokinetic data suggested the premature release of DOX. Similarly, premature drug release from lipid-based liposomes[107] and micelles[108, 109] is also reported.

Thermodynamically, micelles are disassembled into unimers at a concentration lower than the critical micelle concentration (CMC). It's generally believed that the premature release in blood stream is caused by dilution [103]. Micelle disassembly takes place in blood stream upon dilution even above the CMC with a decrease in the number of micelles, irrespective of the final concentration[110]. Hence, micelle modification such as stereocomplexation[111], cross-linking of the core/shell [112-115] and electrostatic interaction[110, 116] has been reported to prevent micelle disassembly and control the

kinetics of drug release. The core/shell cross-linked micelle which is constructed by linking the polymers with disulfides or other covalent bonds, behaves as a unimolecular micelle to exhibit stability independent of the concentration[110]. However, most of the modified micelles remain under *in vitro* investigation. *In vivo* study showed that modified polymeric micelles only slightly increased AUC of paclitaxel (two fold) compared with unmodified micelle formulation [116].

1.9 Assessment of cargo release from polymeric nanoparticles

Although the comparable pharmacokinetic profiles of micelle-loaded drugs and free drug observed in clinical trials [104, 106] indicated possible premature cargo release from polymeric micelles, it is still a challenge to directly examine the *in vitro* and *in vivo* integrity of nanoparticles and visualize the premature drug release [95, 103]. Currently, there are few practical experimental methods available to differentiate intact drug-loaded nanoparticles, drug-released empty nanoparticles and disrupted nanoparticles (unimers) in the blood stream.

Radiolabeling is the most efficient way so far of determining the *in vivo* fate of polymeric nanopaticles[117-120]. Usually, block copolymers are labeled with a radioactive agent and the biodistribution of nanoparticles is determined by the radioactivity of each tissue. The pharmacokinetic profiles of radiolabeled polymeric micelles in blood showed a fast distribution phase (1–2 h) followed by a slow elimination phase (2-90 h). Biliary and renal excretions are found to be major elimination routes of block copolymers. To detect the cargo release, cargo and the nanoparticle can be labeled with different radioactive tracers. For example, ^{14}C and ^{3}H were utilized to label the cargo ceramide and the liposome lipids[107]. The volume distribution of ceramide in

Sprague-Dawley rats was found to be 20-fold greater than that of liposome lipids. The hydrophobic ceramide was proposed to be released from liposomes to cell plasma membrane through a bilayer exchange mechanism [107]. Although the radiolabeling method detected different pharmacokinetics and biodistribution between cargos and nanoparticles, it failed to monitor the disassembly of nanoparticles by differentiating intact nanoparticles and their unimers. Furthermore, the cargo release process cannot be visualized in real-time.

Fluorescence labeling of polymers have been utilized to investigate cell internalization and intracellular distribution of polymeric nanoparticles[95]. A red fluorescent dye tetramethylrhodamine-5-carbonyl azide (TMRCA) was used to label the end of hydrophobic block of poly(ethylene glycol)-*b*-poly(caprolactone) (PEO-*b*-PCL) polymer and a green dye 5-dodecanoylaminofluorescein (DAF) was loaded to the core of TMRCA-labeled micelles [121]. Fluorescent microscope revealed the distribution of micelles in cytoplasm and different subcellular distribution between micelle-loaded DAF and free DAF. However, the conjugation with TMRCA, a cationic dye, might change the stability and subcellular distribution of PEO-*b*-PCL nanoparticles[122]. For example, the nonionic PEO-*b*-PCL micelles and unimers are unlikely to escape endosomes/lysosomes. In contrast, TMRCA-labeled PEO-*b*-PCL is a cationic polymer in lysosomes, which may disrupt lysosomes and facilitate the escape of TMRCA labeled micelles. Hence, to minimize the influence on the stability and distribution of nanoparticles, a neutral fluorescent is recommended for polymer labeling.

Quantitative fluorescence microscope techniques such as fluorescence resonance energy transfer (FRET) have been proposed to investigate the cargo release from

polymeric nanoparticles and nanoparticle-cell membrane interaction [95, 123-128]. The reason FRET can monitor drug release because it relies on the close physical interaction of two fluorophores. One fluorophore is called the donor and the other one is called the acceptor. The donor fluorophore is excited first and transfers energy to the acceptor fluorophore (in proximity, typically less than 10 nm and more than 2 nm) through nonradiative dipole–dipole coupling[129]. FRET does not occur if the distance between these fluorophores exceeds 10 nm. Meanwhile, to achieve FRET effect, the emission spectrum of the donor must overlap the excitation spectrum of the acceptor and the donor and acceptor must be appropriately orientated to allow energy transfer. Fluorescent proteins, fluorescent dyes and quantum dots have been successfully used as FRET donors and acceptors. FRET ratio is defined as $I_A/(I_A + I_D)$, where I_A and I_D are the fluorescence intensities of the acceptor and donor, respectively. When the distance between donor and acceptor increases, FRET ratio will decrease.

To monitor the cargo release, the hydrophobic donor dye and acceptor dye were entrapped into polymeric nanoparticles[125, 128]. When the donor and acceptor dyes were released from nanoparticles, FRET ratio was observed to decrease or disappear. Recent *in vitro* and *in vivo* studies have shown rapid release of hydrophobic dyes $DiOC_{18}$ (donor) and $DiIC_{18}$ (acceptor) from PEG-*b*-PCL and poly(ethylene glycol)-block-poly(D,L-lactic acid) (PEG-b-PDLLA) micelles in cell culture and blood circulation[128]. Alpha- and beta- globulins were found to cause the rapid cargo release in blood [126]. In another study[125], FRET analysis was used to compare the stability of micelles composed of PEG-block-poly(N-hexyl stearate L-aspartamide) (PEG-*b*-PHSA) and 1,2-distearoyl-sn-glycero-3-phosphoethanolamine-N-[amino(polyethylene glycol)] (PEG-

DSPE). PEG-*b*-PHSA micelles were found to be more stable than PEG-DSPE micelles in the presence of serum proteins, suggesting that the rapid cargo release can be reduced by increasing the hydrophobicity of the micelle core.

Recently, a FRET based screening approach was reported to monitor the cargo exchange between two micelles individually loaded with $DiOC_{18}$ and $DiIC_{18}$ in test tubes[127]. FRET will not be detected if there is no exchange of $DiOC_{18}$ and $DiIC_{18}$ entrapped in separate nanoparticles. FRET ratio will increase when the two kinds of nanoparticls are mixed if there are cargo release and cargo exchange. Based on this design, the authors found that cross-linked polymer nanogels exhibited higher encapsulation stability than pluronic block copolymer micelles and the leakage dynamics can be tuned by varying the cross-linking density. Similarly, in another study[124], a green dye 5-dodecanoylaminofluorescein (DAF) was used to stain cell membrane and a red dye nile red was encapsulated to PEG-b-PDLLA nanoparticles. FRET effect between DAF and nile red was detected on the cell membrane when the DAF stained cells were incubated with nile red-loaded nanoparticles, indicating the release of nile red to cell membrane. Compared with donor/acceptor co-loaded FRET nanoparticles, the individually loaded nanoparticles provide a more specific and sensitive method to monitor in vitro and in vivo cargo release.

Metal nanoparticle quenching is another strategy to probe the kinetics of cargo release from nanocarriers[130]. In this design, both pyrene and gold nanoparticles (AuNPs) were encapsulated into polystyrene-block-poly(acrylic acid) (PS-*b*-PAA) micelle. Due to the strong absorbance of AuNPs at 200–600 nm, fluorescence of pyrene was quenched by AuNPs at close proximity. In the presence of nanoacceptors, pyrene

was released to nanoacceptors and exhibited fluorescence. The results showed that pyrene was quickly transfer from PS-*b*-PAA) micelles to nanoacceptors. The authors found that this nanoacceptor-induced fast release followed the Fickian spherical diffusion model and could be explained by the short-distance diffusion of pyrene through water[130].

1.10 Assessment of polymeric nanoparticle disassembly

In polymeric nanoassemblies, polymer unimers always exist in a dynamic equilibrium with the nanoparticles at concentrations above the CMC. It's generally believed that the premature release in blood circulation is mainly caused by blood dilution and subsequent nanoparticle disassembly after i.v. administration [103, 131]. However, rapid cargo release was detected even when the blood concentration of polymer was much higher than their aqueous CMC[126], suggesting the rapid release was not caused simply by dilution. Meanwhile, in the same study, alpha- and beta-globulins were found to accelerate the cargo release. Although those two serum proteins were believed to be responsible for rapid cargo release and nanoparticle disassembly, no direct evidence was provided to support the nanoparticle disassembly. Furthermore, it was reported that Rhodamine was rapidly released from lipid-coated perfluorocarbon nanoparticles to cell plasma membranes without the need for entire nanoparticle internalization and nanoparticle disassembly[109]. Similarly, pyrene was observed to be rapidly released from gold nanoparticle-loaded PS-*b*-PAA nanoparticles to bovine serum albumin (BSA), L-alpha-phosphatidylcholine micelles, sodium dodecyl sulfate (SDS) micelles and PS-b-PAA micelles in aqueous solution, which was not caused by disassembly or fusion splitting of the polymer micelles[130].

To prevent the premature release, it's important to determine if the rapid release is caused by premature disassembly or leakage. It is generally believed that contacts with biological fluids, macromolecules, proteins, lipids and cells might cause the disassembly of polymeric nanoparticles. Although the disassembly of polymeric nanoparticles in simple aqueous solutions has been studied using classical microscopy-, spectroscopy-, and chromatography-based methods, the intracellular and *in vivo* disassembly is still hard to be monitored and direct evidence to support rapid *in vivo* disassembly is very limited[95, 132]. The only reported effort to monitor the intracellular and *in vivo* disassembly of polymeric nanoparticles is the development of a fluorogenic-based approach [132]. In this design, a fluorogenic dye fluorescein-5-carbonyl azide diacetate (F-5-CADA) was covalently conjugated to the hydrophobic block end of PEO-*b*-PCL. The fluorescence was not detectable until the PEO-*b*-PCL micelle was disrupted and the ester group of the dye was cleaved. Fluorescence corresponding to the spontaneous disruption of micelles was recorded at the end of incubation with media and cells. The maximal detectable fluorescence was determined by adding dimethylformamide (DMF) to disrupt the remaining intact micelles and sodium hydroxide to cleave the ester of F-5-CADA. The percent of micelle disruption was calculated from the ratio of the fluorescence at the end of incubation and the maximum detectable fluorescence. The *in vivo* micelle disruption after intramuscular and subcutaneous injections was determined as the ratio of the detected fluorescence and that of the background. The results showed 37% of disruption of PEO-*b*-PCL micelles after incubation in fetal bovine serum for 1hr. Only 20% of cell internalized micelles were disrupted after incubation with HTB-4 cancer cells for 20 hr. *In vivo* results revealed that more disassembly of micelles after

subcutaneous administration than intracmuscular administration. However, the limitation of this fluorogenic-based approach is obvious since it requires an additional F-5-CADA activation step (ester cleavage). The accurate estimation of disassembly is based on two assumptions: F-5-CADA in the core of intact micelles cannot be activated and F-5-CADA is rapidly and totally activated upon the micelle disassembly, which might not be true. Furthermore, fluorescein exhibits different fluorescence intensities in plasma, cell lysates and DMF as well as under different pH. The ratio of the fluorescence measured in the samples and DMF/NaOH solutions does not necessarily equal the percent of micelle disruption.

FRET provides additional opportunities to monitor the disruption of polymeric nanoparticles. Quantum dots (QDs), due to their broad excitation spectra, narrow, symmetric and tunable emission spectra, high quantum yields of photoluminescence and high resistance to photobleaching, have been excellent donors in FRET-based studies for biological analyses and applications[133]. Recently, QD and Cy5.5, a fluorescent dye, were used as FRET pair to monitor lipid exchange between lipoprotein-based nanoparticles and macrophage plasma membrane[134]. Cy5.5 was conjugated to phospholipids and QDs was then coated with Cy5.5 labeled and unlabeled phospholipids. The QD-loaded phospholipid nanoparticle exhibited FRET. During the incubation with macrophages, the lipid exchange between nanoparticles and cells resulted in a decrease of FRET and detection of Cy5.5 fluorescence in the cell membrane. Furthermore, the disassembly of nanoparticles was observed once taken up by the cells. Similarly, in another study[135], FRET was utilized to investigate the intracellular disassembly kinetics of chitosan, polyethylenimine, and polyphosphoramide by labeling plasmid

DNA and polymers with Cy5 dye and QDs, respectively. The QD-Cy5 FRET provides an effective tool to determine the stability and dissociation kinetics of polyplexes.

Metal nanoparticle quenching can also be used to detect the disassembly of polymeric nanoparticles. Due to their strong absorbance, AuNPs and SPIOs are able to quench the fluorescence of dyes [130, 136] and quantum dots[137, 138] in close proximity by attenuating both the excitation beam and the fluorescence signal (inner filter effect). In current study, SPIOs are encapsulated into the core of polymeric nanoparticle. The SPIOs in the core quench the dyes conjugated to the hydrophobic block end of polymer. The quenched fluorescence will recover upon the disassembly of polymeric nanoparticles. This design is superior to the fluorogenic-based approach discussed above since it does not require an additional ester cleavage step. Although similar SPIO-loaded micelles were reported, the complete fluorescence quenching has not been achieved. For example, fluorescence of tetramethylrhodamine (TMR)[139] and sulforhodamine 101[140] labeled to the hydrophobic block end of block copolymers could not be quenched by SPIOs since their positive charge prevent the close interaction with SPIOs. To acquire a potent fluorescence quenching by the core-loaded SPIOs, neutral and hydrophobic dyes are required.

1.11 SPIO-loaded polymeric nanoparticles for tumor imaging and drug delivery

SPIOs and therapeutic drugs have been encapsulated into various block copolymer nanoparticles as a platform for simultaneous MRI and drug delivery [58, 141-143]. Due the existence of PEO shell, SPIO-drug complex entrapped into the BCP micelles may escape the (reticuloendothelial system) RES uptake, resulting in longer blood circulation

and higher accumulation in tumors. Furthermore, the core-shell structure of the polymeric nanoparticle can increase the drug loading capacity[143].

To minimize the toxicity of polymeric nanoparticles, SPIOs were encapsulated into biodegradable polymers such as poly(D,L-lactic-co-glycolic acid) (PLGA) [143, 144], poly(L,L-lactide-*b*-ethylene glycol) (PLLA-*b*-PEG) [139, 145, 146], poly(ethylene glycol)-*b*-poly(e-caprolactone) (PEO-*b*-PCL)[147], poly(lactic acid)-D-α-tocopherol polyethylene glycol (PLA-TPGS)[148] and poly(2-hydroxyethyl aspartamide) (PHEA)[149]. The biocompatible polymers are expected to be biodegraded by proteolytic enzyme *in vivo* and show low toxicity.

SPIOs and small-molecule drugs were reported to be encapsulated into pH sensitive polymeric nanoparticles[60, 140, 150]. Under acidic condition, the amphiphilic polymer was hydrolyzed which triggered the release of SPIOs and drug, resulting in aggregation of hydrophobic SPIOs. The aggregation increased the sensitivity and rapid detectability by MRI since the SPIOs in aggregated state efficiently change the spin–spin relaxation time of adjacent water protons.

Temperature-sensitive polymer was utilized for SPIOs encapsulation[151-154]. For example, nanocomposites were synthesized by incorporation of SPIOs and drug in the thermally sensitive poly (N-isopropylacrylamide) hydrogels[154]. The application of a high frequency alternating magnetic field resulted in the heating of the nanocomposites, which triggered the collapse of polymer coating and rapid drug release.

One trend in nanomedicine research is the development of nanoparticles for multi-modality imaging and drug delivery. One advantage of polymeric nanoaprticles is their capacity to encapsulate multiple components. Both SPIOs and QDs were encapsulated

into polymeric nanoparticles for simultaneous MRI, fluorescence microscopy imaging and drug delivery[145]. Similarly, a fluorescent and magnetic bioprobe was developed by encapsulating SPIOs and QDs into PS-*b*-PAA copolymer nanoparticles[59]. Recently, SPIOs were encapsulated into TMR and cRGD labeled PEG-b-PDLLA micelles for targeted dual-modality imaging [139]. All these nanoaprticles offer opportunities for multi-modality detection of solid tumors and chemotherapy or photothermal therapy.

1.12 Intengrity of SPIO-loaded polymeric nanoparticles

The successful delivery of SPIO-loaded polymeric nanoparticles and encapsulated drugs highly depends on the nanoparticle integrity during blood circulation. Although numerous SPIO-loaded polymeric nanopaticles have been developed and examined *in vitro* and *in vivo*, the knowledge of their *in vivo* integrity and drug release from SPIOs is still limited. Hydrophobic drugs can partitions into the oleic acid coating of SPIOs[78]. Sustained release of the incorporated drug from SPIOs to aqueous buffer was observed over 2 weeks. The encapsulation of hydrophobic SPIOs is expected to stabilize the polymeric nanoparticles[142] and decrease the drug release rate. However, recent studies showed that the drug release from nanocarriers in cellular environment was different from that in bulk solutions[130]. Rapid cargo release from polymeric nanoparticles to cell plasma membrane was observed[128]. It is important to examine if the hydrophobic SPIOs can decrease or prevent the drug release from polymeric nanoparticles.

MRI has shown that polymeric nanoparticle successfully delivered SPIOs to xenograft tumors[139, 141, 155]. However, for SPIO-loaded polymeric nanoparticles, one concern is the *in vivo* stability because they are formed by dynamic selfassembly. The polymer concentration, temperature, pressure and interaction with blood proteins,

lipids and cells may affect their *in vivo* integrity [146]. Currently, it is still a challenge to monitor the *in vivo* integrity of SPIO-loaded polymeric nanoparticles. A noninvasive imaging approach is required to detect the disassembly of SPIO-loaded polymeric nanoparticles.

1.13 Specific Aims

The overall goal of this project is to develop cancer-specific multifunctional SPIOs for colorectal tumor imaging and targeted drug delivery. To realize our goal, we should focus on two critical issues: cancer-specific targeting and integrity of nanocarriers. We hypothesize that anti-TAG72 antibody will facilitate the cancer-specific delivery of SPIOs and anticancer drugs and SPIOs will decrease the premature drug release from nanocarriers.

Aim 1: to develop anti-TAG72 antibody labeled SPIOs for colon cancer imaging and targeted anticancer drug delivery.

Aim 2: to elucidate the mechanisms of premature drug release from SPIO-loaded polymeric nanoparticles.

Aim 3: to monitor the *in vitro* and *in vivo* disassembly of SPIO-loaded polymeric nanoparticles in real-time.

1.14 References

1.   Riehemann, K., et al., *Nanomedicine--challenge and perspectives.* Angew Chem Int Ed Engl, 2009. **48**(5): p. 872-97.
2.   LaVan, D.A., T. McGuire, and R. Langer, *Small-scale systems for in vivo drug delivery.* Nat Biotechnol, 2003. **21**(10): p. 1184-91.
3.   Sanhai, W.R., et al., *Seven challenges for nanomedicine.* Nat Nanotechnol, 2008. **3**(5): p. 242-4.
4.   Peer, D., et al., *Nanocarriers as an emerging platform for cancer therapy.* Nat Nanotechnol, 2007. **2**(12): p. 751-60.

5.   Gabizon, A.A., H. Shmeeda, and S. Zalipsky, *Pros and cons of the liposome platform in cancer drug targeting.* J Liposome Res, 2006. **16**(3): p. 175-83.

6.   Holsapple, M.P., et al., *Research strategies for safety evaluation of nanomaterials, part II: toxicological and safety evaluation of nanomaterials, current challenges and data needs.* Toxicol Sci, 2005. **88**(1): p. 12-7.

7.   Lauterbu.Pc, *Image Formation by Induced Local Interactions - Examples Employing Nuclear Magnetic-Resonance.* Nature, 1973. **242**(5394): p. 190-191.

8.   Laniado, M., et al., *1st Use of Gddtpa Dimeglumine in Man.* Physiological Chemistry and Physics and Medical Nmr, 1984. **16**(2): p. 157-165.

9.   Remsen, L.G., et al., *MR of carcinoma-specific monoclonal antibody conjugated to monocrystalline iron oxide nanoparticles: the potential for noninvasive diagnosis.* AJNR Am J Neuroradiol, 1996. **17**(3): p. 411-8.

10.   Perazella, M.A., *Current status of gadolinium toxicity in patients with kidney disease.* Clin J Am Soc Nephrol, 2009. **4**(2): p. 461-9.

11.   Fang, L., et al., *Enzyme Specific Activation of Benzoquinone Ansamycin Prodrugs Using HuCC49DeltaCH2-beta-Galactosidase Conjugates.* J Med Chem, 2006. **49**(21): p. 6290-6297.

12.   Colcher, D., et al., *Characterization and biodistribution of recombinant and recombinant/chimeric constructs of monoclonal antibody B72.3.* Cancer Res, 1989. **49**(7): p. 1738-45.

13.   Johnson, V.G., et al., *Analysis of a human tumor-associated glycoprotein (TAG-72) identified by monoclonal antibody B72.3.* Cancer Res, 1986. **46**(2): p. 850-7.

14.   Roberson, P.L., et al., *Three-dimensional dose model for the comparison of 177Lu-HuCC49DeltaCH2 and 177Lu-HuCC49 radioimunotherapy in mice bearing intraperitoneal xenografts.* Cancer Biother Radiopharm, 2003. **18**(2): p. 239-47.

15.   Graves, S.S., et al., *Combination therapy with Pretarget CC49 radioimmunotherapy and gemcitabine prolongs tumor doubling time in a murine xenograft model of colon cancer more effectively than either monotherapy.* Clin Cancer Res, 2003. **9**(10 Pt 1): p. 3712-21.

16.   Domingo, R.J. and R.M. Reilly, *Pre-targeted radioimmunotherapy of human colon cancer xenografts in athymic mice using streptavidin-CC49 monoclonal antibody and 90Y-DOTA-biotin.* Nucl Med Commun, 2000. **21**(1): p. 89-96.

17.   Nieroda, C.A., et al., *Improved tumor radioimmunodetection using a single-chain Fv and gamma-interferon: potential clinical applications for radioimmunoguided surgery and gamma scanning.* Cancer Res, 1995. **55**(13): p. 2858-65.

18.   Greiner, J.W., et al., *Improved radioimmunotherapeutic efficacy of an anticarcinoma monoclonal antibody (131I-CC49) when given in combination with gamma-interferon.* Cancer Res, 1993. **53**(3): p. 600-8.

19.   Greiner, J.W., et al., *Improved experimental radioimmunotherapy of colon xenografts by combining 131I-CC49 and interferon-gamma.* Dis Colon Rectum, 1994. **37**(2 Suppl): p. S100-5.

20.   Pancino, G., et al., *Purification and characterisation of a breast-cancer-associated glycoprotein not expressed in normal breast and identified by monoclonal antibody 83D4.* Br J Cancer, 1991. **63**(3): p. 390-8.

21. Horan Hand, P., et al., *Influence of spatial configuration of carcinoma cell populations on the expression of a tumor-associated glycoprotein.* Cancer Res, 1985. **45**(2): p. 833-40.

22. Colcher, D., et al., *Prolonged binding of a radiolabeled monoclonal antibody (B72.3) used for the in situ radioimmunodetection of human colon carcinoma xenografts.* Cancer Res, 1984. **44**(12 Pt 1): p. 5744-51.

23. Colcher, D., et al., *Radioimmunolocalization of human carcinoma xenografts with B72.3 second generation monoclonal antibodies.* Cancer Res, 1988. **48**(16): p. 4597-603.

24. Nieroda, C.A., et al., *Radioimmunoguided surgery in primary colon cancer.* Cancer Detect Prev, 1990. **14**(6): p. 651-6.

25. Sickle-Santanello, B.J., et al., *Radioimmunoguided surgery using the monoclonal antibody B72.3 in colorectal tumors.* Dis Colon Rectum, 1987. **30**(10): p. 761-4.

26. Cohen, A.M., et al., *Radioimmunoguided surgery using iodine 125 B72.3 in patients with colorectal cancer.* Arch Surg, 1991. **126**(3): p. 349-52.

27. Fang, L., et al., *Population Pharmacokinetics of Humanized Monoclonal Antibody HuCC49{triangleup}CH2 and Murine Antibody CC49 in Colorectal Cancer Patients.* J Clin Pharmacol, 2007. **47**(2): p. 227-37.

28. Xiao, J., et al., *Pharmacokinetics and clinical evaluation of 125I-radiolabeled humanized CC49 monoclonal antibody (HuCC49DCH2) in recurrent and metastatic colorectal cancer patients.* Cancer Biotherapy & Radiopharmaceuticals, 2005. **20**(1): p. 16-26.

29. Sun, D., et al., *Radioimmunoguided surgery (RIGS), PET/CT image-guided surgery, and fluorescence image-guided surgery: Past, present, and future.* Journal of Surgical Oncology, 2007. **96**(4): p. 297-308.

30. Arnold, M.W., et al., *Staging of colorectal cancer: biology vs. morphology.* Dis Colon Rectum, 1998. **41**(12): p. 1482-7.

31. Bertsch, D.J., et al., *Radioimmunoguided surgery for colorectal cancer.* Ann Surg Oncol, 1996. **3**(3): p. 310-6.

32. Gardner, B., *Five-year survival after extended resection of colon cancer.* J Surg Oncol, 1987. **34**(4): p. 258-61.

33. Arnold, M.W., et al., *Radioimmunoguided surgery in primary colorectal carcinoma: an intraoperative prognostic tool and adjuvant to traditional staging.* Am J Surg, 1995. **170**(4): p. 315-8.

34. Bertsch, D.J., et al., *Radioimmunoguided Surgery system improves survival for patients with recurrent colorectal cancer.* Surgery, 1995. **118**(4): p. 634-8; discussion 638-9.

35. Weissleder, R., et al., *Ultrasmall Superparamagnetic Iron-Oxide - Characterization of a New Class of Contrast Agents for Mr Imaging.* Radiology, 1990. **175**(2): p. 489-493.

36. Chertok, B., et al., *Iron oxide nanoparticles as a drug delivery vehicle for MRI monitored magnetic targeting of brain tumors.* Biomaterials, 2008. **29**(4): p. 487-496.

37. Tiefenauer, L.X., G. Kuhne, and R.Y. Andres, *Antibody Magnetite Nanoparticles - in-Vitro Characterization of a Potential Tumor-Specific Contrast Agent for Magnetic-Resonance-Imaging.* Bioconjugate Chemistry, 1993. **4**(5): p. 347-352.

38.   Chouly, C., et al., *Development of superparamagnetic nanoparticles for MRI: Effect of particle size, charge and surface nature on biodistribution.* Journal of Microencapsulation, 1996. **13**(3): p. 245-255.

39.   Widder, D.J., et al., *Magnetite Albumin Microspheres - a New Mr Contrast Material.* American Journal of Roentgenology, 1987. **148**(2): p. 399-404.

40.   Jun, Y.W., et al., *Nanoscale size effect of magnetic nanocrystals and their utilization for cancer diagnosis via magnetic resonance imaging.* Journal of the American Chemical Society, 2005. **127**(16): p. 5732-5733.

41.   Tiefenauer, L.X., et al., *In vivo evaluation of magnetite nanoparticles for use as a tumor contrast agent in MRI.* Magnetic Resonance Imaging, 1996. **14**(4): p. 391-402.

42.   Lind, K., et al., *A novel formulation for superparamagnetic iron oxide (SPIO) particles enhancing MR lymphography: Comparison of physicochemical properties and the in vivo behaviour.* Journal of Drug Targeting, 2002. **10**(3): p. 221-230.

43.   Neuberger, T., et al., *Superparamagnetic nanoparticles for biomedical applications: Possibilities and limitations of a new drug delivery system.* Journal of Magnetism and Magnetic Materials, 2005. **293**(1): p. 483-496.

44.   Lee, H., et al., *Thermally cross-linked superparamagnetic iron oxide nanoparticles: synthesis and application as a dual imaging probe for cancer in vivo.* J Am Chem Soc, 2007. **129**(42): p. 12739-45.

45.   Gupta, A.K. and S. Wells, *Surface-modified superparamagnetic nanoparticles for drug delivery: Preparation, characterization, and cytotoxicity studies.* Ieee Transactions on Nanobioscience, 2004. **3**(1): p. 66-73.

46.   Meincke, M., et al., *Iron oxide - loaded liposomes for MR imaging.* Frontiers in Bioscience, 2008. **13**: p. 4002-4008.

47.   Gupta, A.K. and M. Gupta, *Synthesis and surface engineering of iron oxide nanoparticles for biomedical applications.* Biomaterials, 2005. **26**(18): p. 3995-4021.

48.   Sjogren, C.E., et al., *Magnetic characterization of iron oxides for magnetic resonance imaging.* Magn Reson Med, 1994. **31**(3): p. 268-72.

49.   Laurent, S., et al., *Magnetic iron oxide nanoparticles: synthesis, stabilization, vectorization, physicochemical characterizations, and biological applications.* Chem Rev, 2008. **108**(6): p. 2064-110.

50.   Park, J., et al., *Ultra-large-scale syntheses of monodisperse nanocrystals.* Nat Mater, 2004. **3**(12): p. 891-5.

51.   Thorek, D.L., et al., *Superparamagnetic iron oxide nanoparticle probes for molecular imaging.* Ann Biomed Eng, 2006. **34**(1): p. 23-38.

52.   Lu, A.H., E.L. Salabas, and F. Schuth, *Magnetic nanoparticles: synthesis, protection, functionalization, and application.* Angew Chem Int Ed Engl, 2007. **46**(8): p. 1222-44.

53.   Hyeon, T., et al., *Synthesis of highly crystalline and monodisperse maghemite nanocrystallites without a size-selection process.* J Am Chem Soc, 2001. **123**(51): p. 12798-801.

54. Zhang, C., et al., *Silica- and alkoxysilane-coated ultrasmall superparamagnetic iron oxide particles: a promising tool to label cells for magnetic resonance imaging.* Langmuir, 2007. **23**(3): p. 1427-34.

55. Ma, Y., et al., *Plasma synthesis of carbon magnetic nanoparticles and immobilization of doxorubicin for targeted drug delivery.* J Biomater Sci Polym Ed, 2004. **15**(8): p. 1033-49.

56. Kim, J., Y. Piao, and T. Hyeon, *Multifunctional nanostructured materials for multimodal imaging, and simultaneous imaging and therapy.* Chem Soc Rev, 2009. **38**(2): p. 372-90.

57. Martina, M.S., et al., *Generation of superparamagnetic liposomes revealed as highly efficient MRI contrast agents for in vivo imaging.* J Am Chem Soc, 2005. **127**(30): p. 10676-85.

58. Hickey, R.J., et al., *Controlling the self-assembly structure of magnetic nanoparticles and amphiphilic block-copolymers: from micelles to vesicles.* J Am Chem Soc. **133**(5): p. 1517-25.

59. Hu, J., et al., *A multicomponent recognition and separation system established via fluorescent, magnetic, dualencoded multifunctional bioprobes.* Biomaterials. **32**(4): p. 1177-84.

60. Chen, T.J., et al., *Targeted Herceptin-dextran iron oxide nanoparticles for noninvasive imaging of HER2/neu receptors using MRI.* J Biol Inorg Chem, 2009. **14**(2): p. 253-60.

61. Serda, R.E., et al., *Targeting and cellular trafficking of magnetic nanoparticles for prostate cancer imaging.* Mol Imaging, 2007. **6**(4): p. 277-88.

62. Yang, L., et al., *Single chain epidermal growth factor receptor antibody conjugated nanoparticles for in vivo tumor targeting and imaging.* Small, 2009. **5**(2): p. 235-43.

63. Yang, Y., et al., *Preparation and properties of a novel drug delivery system with both magnetic and biomolecular targeting.* J Mater Sci Mater Med, 2009. **20**(1): p. 301-7.

64. Zhang, C., et al., *Specific targeting of tumor angiogenesis by RGD-conjugated ultrasmall superparamagnetic iron oxide particles using a clinical 1.5-T magnetic resonance scanner.* Cancer Res, 2007. **67**(4): p. 1555-62.

65. Wang, A.Z., et al., *Superparamagnetic iron oxide nanoparticle-aptamer bioconjugates for combined prostate cancer imaging and therapy.* ChemMedChem, 2008. **3**(9): p. 1311-5.

66. Aaron, J.S., et al., *Increased optical contrast in imaging of epidermal growth factor receptor using magnetically actuated hybrid gold/iron oxide nanoparticles.* Opt Express, 2006. **14**(26): p. 12930-43.

67. Landmark, K.J., et al., *Synthesis, characterization, and in vitro testing of superparamagnetic iron oxide nanoparticles targeted using folic Acid-conjugated dendrimers.* ACS Nano, 2008. **2**(4): p. 773-83.

68. Stella, B., et al., *Design of folic acid-conjugated nanoparticles for drug targeting.* J Pharm Sci, 2000. **89**(11): p. 1452-64.

69. Li, X., et al., *Specific targeting of breast tumor by octreotide-conjugated ultrasmall superparamagnetic iron oxide particles using a clinical 3.0-Tesla magnetic resonance scanner.* Acta Radiol, 2009. **50**(6): p. 583-94.

70. Kresse, M., et al., *Targeting of ultrasmall superparamagnetic iron oxide (USPIO) particles to tumor cells in vivo by using transferrin receptor pathways.* Magn Reson Med, 1998. **40**(2): p. 236-42.

71. Hwu, J.R., et al., *Targeted Paclitaxel by conjugation to iron oxide and gold nanoparticles.* J Am Chem Soc, 2009. **131**(1): p. 66-8.

72. Sun, E.Y., L. Josephson, and R. Weissleder, *"Clickable" nanoparticles for targeted imaging.* Mol Imaging, 2006. **5**(2): p. 122-8.

73. Kohler, N., et al., *Methotrexate-modified superparamagnetic nanoparticles and their intracellular uptake into human cancer cells.* Langmuir, 2005. **21**(19): p. 8858-64.

74. Sun, J.B., et al., *Preparation and anti-tumor efficiency evaluation of doxorubicin-loaded bacterial magnetosomes: magnetic nanoparticles as drug carriers isolated from Magnetospirillum gryphiswaldense.* Biotechnol Bioeng, 2008. **101**(6): p. 1313-20.

75. Liu, T.Y., et al., *Instantaneous drug delivery of magnetic/thermally sensitive nanospheres by a high-frequency magnetic field.* Langmuir, 2008. **24**(23): p. 13306-11.

76. Babincova, M., et al., *AC-magnetic field controlled drug release from magnetoliposomes: design of a method for site-specific chemotherapy.* Bioelectrochemistry, 2002. **55**(1-2): p. 17-9.

77. Jain, T.K., et al., *Magnetic nanoparticles with dual functional properties: drug delivery and magnetic resonance imaging.* Biomaterials, 2008. **29**(29): p. 4012-21.

78. Jain, T.K., et al., *Iron oxide nanoparticles for sustained delivery of anticancer agents.* Mol Pharm, 2005. **2**(3): p. 194-205.

79. Yang, L.L., et al., *Development of Receptor Targeted Magnetic Iron Oxide Nanoparticles for Efficient Drug Delivery and Tumor Imaging.* Journal of Biomedical Nanotechnology, 2008. **4**(4): p. 439-449.

80. Munnier, E., et al., *Novel method of doxorubicin-SPION reversible association for magnetic drug targeting.* Int J Pharm, 2008. **363**(1-2): p. 170-6.

81. Yu, M.K., et al., *Drug-loaded superparamagnetic iron oxide nanoparticles for combined cancer imaging and therapy in vivo.* Angew Chem Int Ed Engl, 2008. **47**(29): p. 5362-5.

82. Dalmark, M., *Characteristics of doxorubicin transport in human red blood cells.* Scand J Clin Lab Invest, 1981. **41**(7): p. 633-9.

83. Talelli, M., et al., *Superparamagnetic iron oxide nanoparticles encapsulated in biodegradable thermosensitive polymeric micelles: toward a targeted nanomedicine suitable for image-guided drug delivery.* Langmuir, 2009. **25**(4): p. 2060-7.

84. Alexiou, C., et al., *Locoregional cancer treatment with magnetic drug targeting.* Cancer Res, 2000. **60**(23): p. 6641-8.

85. Discher, D.E. and A. Eisenberg, *Polymer vesicles.* Science (New York, N Y), 2002. **297**(5583): p. 967-73.

86. Choucair, A., P.L. Soo, and A. Eisenberg, *Active loading and tunable release of doxorubicin from block copolymer vesicles.* Langmuir : the ACS journal of surfaces and colloids, 2005. **21**(20): p. 9308-13.

87. Chen, Q., H. Schonherr, and G.J. Vancso, *Block-copolymer vesicles as nanoreactors for enzymatic reactions.* Small (Weinheim an der Bergstrasse, Germany), 2009. **5**(12): p. 1436-45.

88. Liu, S.-Q., et al., *Bio-functional micelles self-assembled from a folate-conjugated block copolymer for targeted intracellular delivery of anticancer drugs.* Biomaterials, 2007. **28**(7): p. 1423-33.

89. Kyriakides, T.R., et al., *pH-sensitive polymers that enhance intracellular drug delivery in vivo.* Journal of Controlled Release, 2002. **78**(1-3): p. 295-303.

90. Lee, E.S., et al., *Super pH-sensitive multifunctional polymeric micelle for tumor pH(e) specific TAT exposure and multidrug resistance.* Journal of Controlled Release, 2008. **129**(3): p. 228-236.

91. Zhang, L.F. and A. Eisenberg, *Formation of crew-cut aggregates of various morphologies from amphiphilic block copolymers in solution.* Polymers for Advanced Technologies, 1998. **9**(10-11): p. 677-699.

92. Zhang, L., K. Yu, and A. Eisenberg, *Ion-Induced Morphological Changes in "Crew-Cut" Aggregates of Amphiphilic Block Copolymers.* Science, 1996. **272**(5269): p. 1777-9.

93. Choucair, A., C. Lavigueur, and A. Eisenberg, *Polystyrene-b-poly(acrylic acid) vesicle size control using solution properties and hydrophilic block length.* Langmuir, 2004. **20**(10): p. 3894-900.

94. Zhang, L. and A. Eisenberg, *Multiple Morphologies of "Crew-Cut" Aggregates of Polystyrene-b-poly(acrylic acid) Block Copolymers.* Science, 1995. **268**(5218): p. 1728-31.

95. Savic, R., A. Eisenberg, and D. Maysinger, *Block copolymer micelles as delivery vehicles of hydrophobic drugs: micelle-cell interactions.* J Drug Target, 2006. **14**(6): p. 343-55.

96. Shuai, X., et al., *Micellar carriers based on block copolymers of poly(epsilon-caprolactone) and poly(ethylene glycol) for doxorubicin delivery.* J Control Release, 2004. **98**(3): p. 415-26.

97. Kataoka, K., A. Harada, and Y. Nagasaki, *Block copolymer micelles for drug delivery: design, characterization and biological significance.* Adv Drug Deliv Rev, 2001. **47**(1): p. 113-31.

98. Wang, J., D. Mongayt, and V.P. Torchilin, *Polymeric micelles for delivery of poorly soluble drugs: preparation and anticancer activity in vitro of paclitaxel incorporated into mixed micelles based on poly(ethylene glycol)-lipid conjugate and positively charged lipids.* J Drug Target, 2005. **13**(1): p. 73-80.

99. Nakanishi, T., et al., *Development of the polymer micelle carrier system for doxorubicin.* J Control Release, 2001. **74**(1-3): p. 295-302.

100. Yokoyama, M., et al., *Characterization of physical entrapment and chemical conjugation of adriamycin in polymeric micelles and their design for in vivo delivery to a solid tumor.* J Control Release, 1998. **50**(1-3): p. 79-92.

101. Yoo, H.S., E.A. Lee, and T.G. Park, *Doxorubicin-conjugated biodegradable polymeric micelles having acid-cleavable linkages.* J Control Release, 2002. **82**(1): p. 17-27.

102. Yoo, H.S. and T.G. Park, *Biodegradable polymeric micelles composed of doxorubicin conjugated PLGA-PEG block copolymer.* J Control Release, 2001. **70**(1-2): p. 63-70.

103. Bae, Y.H. and H. Yin, *Stability issues of polymeric micelles.* J Control Release, 2008. **131**(1): p. 2-4.

104. Matsumura, Y., et al., *Phase I clinical trial and pharmacokinetic evaluation of NK911, a micelle-encapsulated doxorubicin.* Br J Cancer, 2004. **91**(10): p. 1775-81.

105. Gabizon, A., et al., *Prolonged circulation time and enhanced accumulation in malignant exudates of doxorubicin encapsulated in polyethylene-glycol coated liposomes.* Cancer Res, 1994. **54**(4): p. 987-92.

106. Danson, S., et al., *Phase I dose escalation and pharmacokinetic study of pluronic polymer-bound doxorubicin (SP1049C) in patients with advanced cancer.* Br J Cancer, 2004. **90**(11): p. 2085-91.

107. Zolnik, B.S., et al., *Rapid distribution of liposomal short-chain ceramide in vitro and in vivo.* Drug Metab Dispos, 2008. **36**(8): p. 1709-15.

108. Lanza, G.M., et al., *Targeted antiproliferative drug delivery to vascular smooth muscle cells with a magnetic resonance imaging nanoparticle contrast agent: implications for rational therapy of restenosis.* Circulation, 2002. **106**(22): p. 2842-7.

109. Partlow, K.C., G.M. Lanza, and S.A. Wickline, *Exploiting lipid raft transport with membrane targeted nanoparticles: a strategy for cytosolic drug delivery.* Biomaterials, 2008. **29**(23): p. 3367-75.

110. Cha, E.J., J.E. Kim, and C.H. Ahn, *Stabilized polymeric micelles by electrostatic interactions for drug delivery system.* Eur J Pharm Sci, 2009. **38**(4): p. 341-6.

111. Kang, Y. and T.A. Taton, *Core/Shell gold nanoparticles by self-assembly and crosslinking of micellar, block-copolymer shells.* Angew Chem Int Ed Engl, 2005. **44**(3): p. 409-12.

112. Xu, P., et al., *Enhanced stability of core-surface cross-linked micelles fabricated from amphiphilic brush copolymers.* Biomacromolecules, 2004. **5**(5): p. 1736-44.

113. Chan, Y., et al., *Acid-labile core cross-linked micelles for pH-triggered release of antitumor drugs.* Biomacromolecules, 2008. **9**(7): p. 1826-36.

114. Sun, J., et al., *Formation of reversible shell cross-linked micelles from the biodegradable amphiphilic diblock copolymer poly(L-cysteine)-block-poly(L-lactide).* Langmuir, 2008. **24**(18): p. 10099-106.

115. Duong, H.T., et al., *Core-cross-linked micelles synthesized by clicking bifunctional Pt(IV) anticancer drugs to isocyanates.* Biomacromolecules. **11**(9): p. 2290-9.

116. Lee, S.W., et al., *Ionically fixed polymeric nanoparticles as a novel drug carrier.* Pharm Res, 2007. **24**(8): p. 1508-16.

117. Batrakova, E.V., et al., *Distribution kinetics of a micelle-forming block copolymer Pluronic P85.* J Control Release, 2004. **100**(3): p. 389-97.

118. Liu, J., F. Zeng, and C. Allen, *In vivo fate of unimers and micelles of a poly(ethylene glycol)-block-poly(caprolactone) copolymer in mice following intravenous administration.* Eur J Pharm Biopharm, 2007. **65**(3): p. 309-19.

119. Novakova, K., et al., *Pharmacokinetics and distribution of 125I-PLA-b-PEO block copolymers in rats.* Pharm Dev Technol, 2003. **8**(2): p. 153-61.

120. Yamamoto, Y., et al., *Long-circulating poly(ethylene glycol)-poly(D,L-lactide) block copolymer micelles with modulated surface charge.* J Control Release, 2001. **77**(1-2): p. 27-38.

121. Savic, R., et al., *Micellar nanocontainers distribute to defined cytoplasmic organelles.* Science, 2003. **300**(5619): p. 615-8.

122. Moghimi, S.M., et al., *Cellular distribution of nonionic micelles.* Science, 2004. **303**(5658): p. 626-8; author reply 626-8.

123. Barauskas, J., et al., *Interactions of lipid-based liquid crystalline nanoparticles with model and cell membranes.* Int J Pharm. **391**(1-2): p. 284-91.

124. Xiao, L., et al., *Role of cellular uptake in the reversal of multidrug resistance by PEG-b-PLA polymeric micelles.* Biomaterials. **32**(22): p. 5148-57.

125. Diezi, T.A., Y. Bae, and G.S. Kwon, *Enhanced stability of PEG-block-poly(N-hexyl stearate l-aspartamide) micelles in the presence of serum proteins.* Mol Pharm. **7**(4): p. 1355-60.

126. Chen, H., et al., *Fast release of lipophilic agents from circulating PEG-PDLLA micelles revealed by in vivo forster resonance energy transfer imaging.* Langmuir, 2008. **24**(10): p. 5213-7.

127. Jiwpanich, S., et al., *Noncovalent encapsulation stabilities in supramolecular nanoassemblies.* J Am Chem Soc. **132**(31): p. 10683-5.

128. Chen, H., et al., *Release of hydrophobic molecules from polymer micelles into cell membranes revealed by Forster resonance energy transfer imaging.* Proc Natl Acad Sci U S A, 2008. **105**(18): p. 6596-601.

129. Gordon, G.W., et al., *Quantitative fluorescence resonance energy transfer measurements using fluorescence microscopy.* Biophys J, 1998. **74**(5): p. 2702-13.

130. Wang, H., et al., *Probing the kinetics of short-distance drug release from nanocarriers to nanoacceptors.* Angew Chem Int Ed Engl. **49**(45): p. 8426-30.

131. Moghimi, S.M., A.C. Hunter, and J.C. Murray, *Long-circulating and target-specific nanoparticles: theory to practice.* Pharmacol Rev, 2001. **53**(2): p. 283-318.

132. Savic, R., et al., *Assessment of the integrity of poly(caprolactone)-b-poly(ethylene oxide) micelles under biological conditions: a fluorogenic-based approach.* Langmuir, 2006. **22**(8): p. 3570-8.

133. Fu, R.H., et al., *Spatial control of cells, peptide delivery and dynamic monitoring of cellular physiology with chitosan-assisted dual color quantum dot FRET peptides.* Acta Biomater. **6**(9): p. 3621-9.

134. Skajaa, T., et al., *Quantum Dot and Cy5.5 Labeled Nanoparticles to Investigate Lipoprotein Biointeractions via Forster Resonance Energy Transfer.* Nano Lett.

135. Chen, H.H., et al., *Quantitative comparison of intracellular unpacking kinetics of polyplexes by a model constructed from quantum dot-FRET.* Mol Ther, 2008. **16**(2): p. 324-32.

136. Manciulea, A., A. Baker, and J.R. Lead, *A fluorescence quenching study of the interaction of Suwannee River fulvic acid with iron oxide nanoparticles.* Chemosphere, 2009. **76**(8): p. 1023-7.

137. Mandal, S.K., et al., *Encapsulation of magnetic and fluorescent nanoparticles in emulsion droplets.* Langmuir, 2005. **21**(9): p. 4175-9.

138. Quarta, A., et al., *Fluorescent-magnetic hybrid nanostructures: preparation, properties, and applications in biology.* IEEE Trans Nanobioscience, 2007. **6**(4): p. 298-308.

139. Kessinger, C.W. et al., *In vivo angiogenesis imaging of solid tumors by alpha(v)beta(3)-targeted, dual-modality micellar nanoprobes.* Exp Biol Med (Maywood). **235**(8): p. 957-65.

140. GuangHui Gao, JungHee Lee and DooSung Lee, *An acidic pH-triggered polymeric micelle for dual-modality MR and optical imaging.* Journal of Materials Chemistry, 2010. **20**: p. 5454-5461.

141. Kumagai, M., et al., *Enhanced magnetic resonance imaging of experimental pancreatic tumor in vivo by block copolymer-coated magnetite nanoparticles with TGF-beta inhibitor.* J Control Release, 2009. **140**(3): p. 306-11.

142. Kamps, A.C., et al., *Nanoparticle-directed self-assembly of amphiphilic block copolymers.* Langmuir. **26**(17): p. 14345-50.

143. Lee, P.W., et al., *The characteristics, biodistribution, magnetic resonance imaging and biodegradability of superparamagnetic core-shell nanoparticles.* Biomaterials. **31**(6): p. 1316-24.

144. Butoescu, N., et al., *Magnetically retainable microparticles for drug delivery to the joint: efficacy studies in an antigen-induced arthritis model in mice.* Arthritis Res Ther, 2009. **11**(3): p. R72.

145. Andrea Fornara, A.R., Jian Qin, Abhilash Sugunan, Fei Ye, Sophie Laurent, Robert N. Muller, Jing Zou, Abo-Ramadan Usama, Muhammet S. Toprak and Mamoun Muhammed *Polymeric/inorganic multifunctional nanoparticles for simultaneous drug delivery and visualization.* Mater. Res. Soc. Symp. Proc., 2010. **1257**: p. O04-03.

146. Yang, X., et al., *Multifunctional SPIO/DOX-loaded wormlike polymer vesicles for cancer therapy and MR imaging.* Biomaterials. **31**(34): p. 9065-73.

147. H. Ai, C.F., B. Weinberg, X.-T. Shuai, M. D. Pagel, D. Farrell, J. Duerk, J. Gao, *Magnetite-Loaded Polymeric Micelles as Ultrasensitive Magnetic-Resonance Probes.* Advanced Materials, 2005. **17**(16): p. 1949-1952.

148. Prashant, C., et al., *Superparamagnetic iron oxide--loaded poly(lactic acid)-D-alpha-tocopherol polyethylene glycol 1000 succinate copolymer nanoparticles as MRI contrast agent.* Biomaterials. **31**(21): p. 5588-97.

149. Yang, H.M., et al., *HER2/neu Antibody Conjugated Poly(amino acid)-Coated Iron Oxide Nanoparticles for Breast Cancer MR Imaging.* Biomacromolecules.

150. Yang, X., et al., *Multifunctional stable and pH-responsive polymer vesicles formed by heterofunctional triblock copolymer for targeted anticancer drug delivery and ultrasensitive MR imaging.* ACS Nano. **4**(11): p. 6805-17.

151. Rahimi, M., et al., *In vitro evaluation of novel polymer-coated magnetic nanoparticles for controlled drug delivery.* Nanomedicine. **6**(5): p. 672-80.

152. Nash, M.A., et al., *Mixed stimuli-responsive magnetic and gold nanoparticle system for rapid purification, enrichment, and detection of biomarkers.* Bioconjug Chem. **21**(12): p. 2197-204.

153. Strong, L.E. and J.L. West, *Thermally responsive polymer-nanoparticle composites for biomedical applications.* Wiley Interdiscip Rev Nanomed Nanobiotechnol. **3**(3): p. 307-17.

154. Satarkar, N.S. and J.Z. Hilt, *Magnetic hydrogel nanocomposites for remote controlled pulsatile drug release.* J Control Release, 2008. **130**(3): p. 246-51.

155. Kievit, F.M., et al., *Chlorotoxin labeled magnetic nanovectors for targeted gene delivery to glioma.* ACS Nano. **4**(8): p. 4587-94.

CHAPTER II

Near-Infrared Fluorescence Labeled Anti-TAG-72 Monoclonal Antibodies for Tumor Imaging in Colorectal Cancer Xenograft Mice

2.1 Abstract

Anti-TAG-72 monoclonal antibodies target the tumor-associated glycoprotein (TAG)-72 in various solid tumors. This study evaluated the use of anti-TAG-72 monoclonal antibodies, both murine CC49 and humanized CC49 (HuCC49ΔC$_H$2), for near-infrared fluorescent (NIR) tumor imaging in colorectal cancer xenograft models. The murine CC49 and HuCC49ΔC$_H$2 were conjugated with Cy7 monofunctional N-hydroxysuccinimide ester (Cy7-NHS). Both *in vitro and in vivo* anti-TAG-72 antibody binding studies were performed. The *in vitro* study utilized the human colon adenocarcinoma cell line LS174T that was incubated with Cy7, antibody-Cy7 conjugates, or excessive murine CC49 followed by the antibody-Cy7 conjugates and was imaged by fluorescence microscopy. The *in vivo* study utilized xenograft mice, bearing LS174T subcutaneous tumor implants, that received tail vein injections of Cy7, murine CC49-Cy7, HuCC49ΔC$_H$2-Cy7, or non-specific IgG-Cy7 and were imaged by the Xenogen IVIS 100 system from 15 minutes to 288 hours. The biodistribution of the fluorescence labeled antibodies was determined by imaging the dissected tissues. The *in vitro* study revealed that the antibody-Cy7 conjugates bound to LS174T cells and were blocked by excessive murine CC49. The *in vivo* study demonstrated that murine CC49 achieved a tumor/blood ratio of 15 at 96 hours post- injection. In comparison, HuCC49ΔC$_H$2-Cy7 cleared

much faster than murine CC49-Cy7 from the xenograft mice, and HuCC49ΔC$_H$2-Cy7 achieved a tumor/blood ratio of 12 at 18 hours postinjection. In contrast, Cy7 and Cy7 labeled non-specific IgG resulted in no demonstrable tumor accumulation. When mice were injected with excessive unlabeled murine CC49 at 6 hours before the injection of murine CC49-Cy7 or HuCC49ΔC$_H$2-Cy7, both the intensity and retention time of the fluorescence from the tumor was reduced. In summary, the Cy7 labeled murine CC49 and HuCC49ΔC$_H$2 demonstrate tumor-targeting capabilities in living colorectal cancer xenograft mice and provide an alternative modality for tumor imaging.

2.2 Introduction

Tumor associated glycoprotein 72 (TAG-72) is a human mucin (MUC1)-like glycoprotein complex, which is over-expressed in many epithelial-derived cancers, including colorectal, breast, ovarian, non-small cell lung, gastric, and pancreatic cancers [1]. Anti-TAG-72 antibodies have been studied in preclinical animal model and clinical patients for cancer detection based on their high specificity against cancer antigens in various solid cancers [2]. As previously reported, we have utilized monoclonal antibodies against TAG-72 for tumor detection in radioimmunoguided surgery (RIGS) [3-7]. RIGS combines radioactive-labeled (i.e., I^{125}) monoclonal antibodies and a handheld gamma probe, to identify tumor tissues for resection intraoperatively in colorectal and pancreatic cancer patients [5]. The successful detection of additional occult disease within regional lymph nodes and the subsequent complete resection of the antibody-bound tissues significantly improved survival rates [8-11]. Three generations of anti-TAG-72 antibodies, i.e., murine B72.3, murine CC49, and humanized HuCC49ΔC$_H$2, were

evaluated for RIGS in colorectal cancer patients for tumor detection to guide surgical procedure in a real-time [4]. B72.3 is a murine monoclonal antibody generated against TAG-72 using membrane-enriched extracts of human metastatic mammary carcinoma lesions, while CC49 is a second-generation murine monoclonal antibody generated against purified TAG-72 from colon cancer [12, 13]. To circumvent the shortcomings of B72.3 and CC49, including host antimouse antibodies (HAMA) response and slow plasma clearance, a humanized CH2 domain-deleted MAb (HuCC49$\Delta C_H 2$) has been developed for RIGS [3, 4].

RIGS with anti-TAG-72 antibodies have been shown to detect 77% to 89% of primary colorectal cancers [13-15] and 78% to 97% of metastatic lesions in more than 300 patients [3, 5, 8, 11, 14, 16-23]. Furthermore, RIGS detects both visible gross tumors and clinically occult disease within lymph nodes in more than 70% of the cases [11, 15, 16, 19, 22-28], which are normally undetectable by traditional surgical exploration and pathological examination. This occult disease (i.e., RIGS-positive tissue) within "normal" appearing lymph nodes is itself responsible for the development of subsequent clinical-evident metastatic relapse, and thus complete resection of this occult disease can translate into improved patient survival after surgical intervention [29].

Despite the success of ^{125}I-directed RIGS in multiple previously published clinical trials, the intraoperative and postoperative handling as well as disposal of I[125] (which has a relatively long half-life of 60 days), are the major limitations to the widespread acceptance and implementation of this technology [29]. In addition, the use of ^{125}I in RIGS does not allow for the generation of high-quality preoperative imaging, which is due to the extremely low gamma photon emission energy (i.e., 35 keV) of ^{125}I, and results

in weak tissue penetration, and high soft tissue attenuation, and resultant poor image quality[30].

The near-infrared fluorescence Cy dyes (NIR, 650-900 nm) have been used as imaging agents for living animals due to their strong tissue penetration ability [31-34]. Properties such as small size, good aqueous solubility, pH insensitivity between pH 3–10, and low non-specific binding, make Cy dyes good fluorescent agents for tumor imaging. Cy7 is especially suitable for the use in living animals secondary to its long excitation wavelength at 747 nm and emission wavelength at 776 nm, where autofluorescence of tissues is greatly reduced [35]. Although Cy7 is not approved for clinical use, a very similar compound (indocyanine green) has been used for human clinical applications without reported toxicity. Several intraoperative fluorescence imaging techniques have recently been described, such as endoscopic evaluation of gastrointestinal cancer [36, 37] and stereomicroscopic imaging of head and neck cancer and cervical metastases, which demonstrated the potential of fluorescent immunoguided surgery[38-41].

In this paper, we intend to study the feasibility of using Cy7 labeled CC49 and HuCC49ΔC_H2 for fluorescent tumor imaging in colorectal cancer xenograft mice. We describe noninvasive fluorescent imaging of living mice and quantification of fluorescence intensities on xenograft tumors and livers. Tumor specificity and tumor accumulation of both fluorescence labeled CC49 and HuCC49ΔC_H2 were observed. The images of the dissected organs showed the biodistribution and tumor-to-blood ratios of fluorescent antibodies. In addition, the emission spectra of Cy7, CC49-Cy7, and HuCC49ΔC_H2-Cy7 were characterized by a non-invasive optical probe in tumors and various normal tissues/organs.

2.3 Materials and Methods

2.3.1 Materials

Cy7-NHS was purchased from Amersham Biosciences (Piscataway, NJ). The murine CC49 antibody was produced and purified by Rockland Immunochemicals, Inc. (Gilbertsville, PA). The HuCC49ΔC$_H$2 antibody was supplied by National Cancer Institute (Bethesda, MD). Phosphate buffered saline (PBS, 0.01 mol/L; pH 7.4) was purchased from Invitrogen (Carlsbad, CA). The non-specific IgG antibodies from human and mouse serum as well as all other reagents were purchased from Sigma-Aldrich Chemical Co. (St. Louis, MO).

2.3.2 Synthesis of Cy7 antibody conjugates

The pH of 1.5 mL PBS solution containing CC49 antibody (20.5 nmol/mL) was adjusted to 8.3 by adding Na$_2$CO$_3$/NaHCO$_3$ buffer (pH=10). A total of 1 mg of Cy7-NHS ester was dissolved in 400 μL of DMSO. 100.8 μL of Cy7-NHS ester DMSO solution (307.5 nmol) was gradually added to the CC49 solution while stirring. The solution was diluted to 2.5 mL using PBS and was stirred for 2 more hours at room temperature in the dark. The solution was loaded on a PD-10 desalting column (Amersham Biosciences, Piscataway, NJ) and washed with PBS. The CC49-Cy7 fraction (3.5 mL) was collected in a 10 kD cutoff Amicon Ultra-15 centrifugal filter (Millipore Corp, Billerica, MA) and was washed with 10 mL of PBS three times (each time 5000$g\times$ 20 min). 70 nmol of HuCC49ΔC$_H$2, 20 nmol of murine non-specific IgG as well as 20 nmol of human non-specific IgG were labeled with Cy7 and purified following a similar procedure. A Du640 spectrophotometer from Beckman Coulter, Inc (Fullerton, CA) was used to determine the molar extinction coefficient of unlabeled antibodies at 280 nm (E^{280nm}) and the

absorbance of the antibody-Cy7 at 280 nm (A_{280}) and 747 nm (A_{747}). The molar extinction coefficient at 747 nm and 280 nm of Cy7 was 200000 and 22000, respectively [42]. The ratio of the Cy7 and the antibodies of the final conjugates can be calculated with the following formula.

$$\frac{Cy7}{antibody} = \frac{\left[E^{280nm}A_{747}\right]}{\left[200000A_{280} - 22000A_{747}\right]}$$

2.3.3 Cell culture and reagents

Human colon adenocarcinoma cells (LS174T) were obtained from the American Type Culture Collection (Manassas, VA) and cultured in Dulbecco's modified Eagle high glucose medium (DMEM) supplemented with 10% fetal bovine serum (FBS) and 1% penicillin-streptomycin (Invitrogen Life Technologies, Carlsbad, CA). The cells were maintained in a humidified atmosphere of 5% CO_2 at 37 ºC, with the medium changed every other day. A confluent monolayer was detached with 0.25% trypsin-EDTA (Invitrogen Life Technologies, Carlsbad, CA) and dissociated into a single-cell suspension for further cell culture.

2.3.4 *In vitro* binding studies

Cells were cultured on 4-well chamber slides (Thermo Fisher Scientific, Rochester, NY) and incubated in a humidified atmosphere of 5% CO2 at 37 ºC overnight. After washing twice with PBS, the cells were incubated in 3.7% paraformaldehyde for 15 minutes and then washed again with PBS. Cy7 (0.5 nmol), murine CC49-Cy7 (0.49 nmol equivalent Cy7) or HuCC49ΔC_H2–Cy7 conjugate (0.49 nmol equivalent Cy7) was added into each well and diluted to 0.3 mL with PBS. For the blocking study, murine CC49 antibody (4 nmol) was added 1 hour before the addition of murine CC49-Cy7 or HuCC49ΔC_H2 –Cy7 conjugate. After an incubation period of 2 hours at room temperature, cells were washed with PBS (5 mins × 4). The coverslips were mounted

with a drop of fluoromount G (Southern Biotech, Birmingham, AL). Microscopic examination was conducted on a Zeiss-Axiophot microscope (Carl Zeiss, Inc., Jena, German). The microscope is equipped with a RT KE slider digital camera (Diagnostic Instruments Inc. Sterling Heights, MI), a HBO 103 W/2 mercury lamp (Carl Zeiss, Inc., Jena, German), a Cy7 filter set with an excitation wavelength of 680-740 nm and an emission wavelength of 775-850 nm (Chroma Technology Corp., Rochingham VT), and a Metavue software (Molecular Devices, Downingtown, PA) for image acquisition, processing, and analysis. The image magnification is 100X. The exposure time is 4000 ms for the fluoresence images and 300 ms for the transparent images. The space resolution for all images is 1600×1200 pixels and image bit depth is 24 bit. The pseudocolor of Cy7 is red.

2.3.5 Tumor xenografts

The animal procedures were performed according to a protocol approved by the University Committee for the Use and Care of Animals (UCUCA) at The Ohio State University. Female athymic nude mice (nu/nu), obtained from National Cancer Institute (Bethesda, MD) at 4 to 6 weeks of age, were subcutaneously inoculated in the back with 5×10^6 LS174T cells suspended in a mixture of 50 µL of PBS and 50 µL of matrixgel basement membrane (BD Biosciences, San Jose, CA). When the tumor implants reached 0.4 to 0.6 cm in diameter (approximately 14 days after implantation), the tumor-bearing mice were subjected to the *in vivo* studies.

2.3.6 *In vivo* optical tumor imaging

In vivo fluorescence imaging was performed with an IVIS 100 small animal imaging system (Xenogen, Alameda, CA). An ICG filter (excitation wavelength 710-760 nm and

emission wavelength 810-875 nm) was used for acquiring Cy7, murine CC49-Cy7, HuCC49ΔC$_H$2-Cy7, and non-specific IgG-Cy7 fluorescence imaging *in vivo*. Identical illumination settings, such as exposure time (1s), binning factor (8), f/stop (1), and field of views (25 × 25 cm), were used for acquiring all images, and fluorescence emission was normalized to photons per second per centimeter squared per steradian (p s^{-1} cm^{-2} sr^{-1}). The imaging was acquired and overlaid. The pseudocolor image represents the spatial distribution of photon counts within the animal. Background fluorescence was measured and subtracted by setting up a background measurement. Images were acquired and analyzed using Living Image 2.5 software (Xenogen, Alameda, CA).

Mice bearing LS174T tumor were injected via the tail vein with 1 nmol of Cy7-NHS, 0.33 nmol of murine CC49-Cy7 (1nmol equivalent Cy7/mouse), 0.73 nmol of HuCC49ΔC$_H$2-Cy7 (1 nmol equivalent Cy7/mouse), 0.38 nmol of non-specific murine IgG-Cy7, or 0.50 nmol of non-specific human IgG-Cy7 (1 nmol equivalent Cy7/mouse). For the blocking study, 3.3 nmol of unlabeled murine CC49 was injected (i.v.) 6 hours before injection of the conjugates. One mouse bearing the LS174T tumor was not injected and was used as a blank control. Mice were anesthetized with isoflurane (Abbott Laboratories, Chicago, IL) and images were obtained every 15 minutes for up to 3 hours after injection of each fluorescent antibody. Each mouse was imaged again 4, 5, 6, 7, 18, 24, 48, 72, 96, and 288 hours after injection of each fluorescent antibody. Both the dorsal and ventral sides of each mouse were imaged. The tumor area and the liver area were designated as the two regions of interest (ROI). The relative mean fluorescent intensity of each ROI was obtained by subtracting the mean fluorescence intensity of the

corresponding ROI on the blank mouse from the measured mean fluorescent intensity and was plotted as a function of time.

2.3.7 Optical imaging of fresh tissues

As described above in *in vivo* tumor imaging, two additional groups of LS174T tumor xenograft mice were given Cy7-NHS, murine CC49-Cy7, murine CC49/murine CC49-Cy7, or non-specific murine IgG-Cy7. One group of mice was sacrificed at 2 hours and the other group of mice was sacrificed at 96 hours after intravenous injection of fluorescent marker tagged antibodies. Following the same procedure, two additional groups of LS174T tumor xenograft mice were given Cy7-NHS, HuCC49ΔC_H2-Cy7, murine CC49/HuCC49ΔC_H2-Cy7 or non-specific human IgG-Cy7 and sacrificed at 2 hours and 18 hours post injection, respectively. The dissected tissues (tumor, spleen, kidneys, lung, heart, liver, stomach, and intestine) were imaged immediately. The mean fluorescent intensity of each tissue sample was obtained by subtracting the mean fluorescent intensity of corresponding tissue from the blank mouse. The fluorescent intensities in the heart were used to reflect the fluorescent intensities in the blood. The tissue to heart ratio for fluorescence was calculated.

2.3.8 Non-invasive measurement of fluorescent emission spectra

All the fluorescent emission spectra were measured using a USB4000-FL fluorescence spectrometer (Ocean Optics Inc., Dunedin, FL). A HL6738MG diode laser (Thorlabs, Newton, NJ) was used to excite the samples at the wavelength of 690 nm. To measure the emission spectra of contrast agents in cuvettes, the excitation laser beam was incident from one side of the cuvette. The detector and a 715 nm long pass filter (Thorlabs, Newton, NJ) were placed in a direction perpendicular to the excitation laser

beam. For the measurement of emission spectra from organs in living animals, the excitation laser source was oriented perpendicular to the animal skin above the specific organs. The detector and the 715 nm long pass filter were aligned at 45 degree to the laser beam. The measurement was carried out 24 hrs post injection of murine CC49-Cy7. The raw data was processed by the Matlab curve fitting toolbox (The Mathworks Inc, Natick, MA). Local regression with weighted linear least squares and a 1st degree polynomial model were used for curve fitting the spectrum.

2.4 Results

2.4.1 Synthesis of murine CC49-Cy7 and HuCC49ΔC_H2-Cy7

The antibody was labeled with Cy7-NHS ester by acylating the primary amines of the antibody. The 280 nm emission line, E^{280nm} of murine CC49 and HuCC49ΔC_H2 were measured to be 157000 $M^{-1}cm^{-1}$ and 182400 $M^{-1}cm^{-1}$ respectively. The Cy7/murine CC49 ratio, Cy7/HuCC49ΔC_H2 ratio, Cy7/murine IgG ratio, and Cy7/human IgG ratio were determined to be 3.02, 1.36, 2.60, and 2.01, respectively.

2.4.2 *In vitro* binding studies

Figure 2.1 shows the fluorescent microscopic images of LS174T cells incubated with PBS, Cy7, murine CC49-Cy7 conjugate, murine CC49 plus murine CC49-Cy7 conjugate, HuCC49ΔC_H2-Cy7 conjugate, and murine CC49 plus HuCC49ΔC_H2-Cy7 conjugate. No autofluorescence was detected from the cells incubated with PBS and negligible signals were detected from cells incubated with Cy7. In contrast, fluorescent signals were observed from cells incubated with murine CC49-Cy7 or HuCC49ΔC_H2-Cy7 conjugate, suggesting that both conjugates bound to the cells. Furthermore, binding of murine

43

CC49-Cy7 or HuCC49ΔC$_H$2-Cy7 to the cells was completely blocked when the cells were pretreated with excessive murine CC49 antibody.

2.4.3 *In vivo* **optical tumor imaging**

As previously reported, the LS174T tumor has a high level of TAG-72 expression [43]. Whole-body imaging of subcutaneous LS174T tumor xenograft mice was accomplished by using an IVIS 100 system to monitor *in vivo* biodistribution of murine CC49-Cy7 and HuCC49ΔC$_H$2-Cy7. Figure 2.1A shows typical NIR images of mice bearing LS174T tumors 15 minutes and 96 hours after i.v. injection of Cy7 or murine CC49-Cy7. No autofluorescence was detected from the blank mouse. The fluorescent signal was detected from the whole body of a mouse 15 minutes after injection of Cy7, suggesting the rapid distribution of Cy7 in the mouse body. Subsequently, Cy7 is rapidly eliminated from the kidney and no fluorescence was detected on this mouse 96 hours post-injection. In contrast, a fluorescent signal was detected from the abdominal area of the mice injected with the murine CC49-Cy7 or murine IgG-Cy7, suggesting the distribution of the antibody-Cy7 in the liver or spleen immediately post-injection. 96 hours post injection, fluorescence of murine CC49-Cy7 was clearly visualized in the tumors of two mice while the fluorescence of non-specific murine IgG-Cy7 was hard to be detected. The previously observed fluorescence from the abdominal area did not present. When the mice were injected with the unlabeled murine CC49 before administration of the murine CC49-Cy7 (i.e., blocked), the fluorescent intensity from the tumor was found to be significantly lower than that from the tumor of the murine CC49-Cy7 mouse. This suggests that the TAG-72 was blocked by excessive murine CC49 antibody.

Similar results were obtained when HuCC49ΔC$_H$2-Cy7 was used as the imaging agent (Figure 2.1B). The tumor could clearly be visualized from the surrounding background tissues 18 hours post injection of HuCC49ΔC$_H$2-Cy7 while no fluorescence signal was detected from the tumor of the mouse blocked with excessive murine CC49 antibody and the mouse injected with non-specific human IgG-Cy7. Intense fluorescence signal was still detected from the abdominal areas of the mouse injected with HuCC49ΔC$_H$2-Cy7 and the blocked mouse 18 hours after injection of HuCC49ΔC$_H$2-Cy7. This data suggests that both HuCC49ΔC$_H$2-Cy7 and murine CC49-Cy7 are able to target tumors for non-invasive fluorescent tumor imaging. Nevertheless, HuCC49ΔC$_H$2-Cy7 may have faster clearance than murine CC49-Cy7 in xenograft models.

2.4.4 Non-invasive characterization of emission spectra

The emission spectra from Cy7 and murine CC49-Cy7 solutions as well as from the tissues in the living mice were recorded with a USB4000-FL fluorescence spectrometer. As shown in Figure 2.3, the maximum emission wavelengths of Cy7 and murine CC49-Cy7 solution were determined to be 770.3 nm and 777.1 nm, respectively. A shift in the maximum emission of 6.9 nm to longer wavelengths was detected when Cy7 was attached to the murine CC49 antibody. The maximum emission wavelengths of fluorescent signals from the liver, tumor and bladder of the mouse injected with murine CC49-Cy7 were determined to be 778.5 nm, 778.9 nm and 776.1 nm, respectively.

2.4.5 Dynamic fluorescence intensities in tumors and livers

The fluorescent intensities from the tumors and livers were measured non-invasively during a period of 0 to 288 hours after the injection of Cy7, murine CC49-Cy7, or HuCC49ΔC$_H$2-Cy7. The measured intensities were then reduced to relative values by

subtracting the mean fluorescence intensity from the tumor or liver of the blank mouse. Figure 2.4 shows the relative fluorescence intensity as a function of time for the regions of interest corresponding to tumors and livers. Both the maximum intensities (Cmax) and retention times (Tmax) of fluorescence from the tumor are different among Cy7, blocked, and murine CC49-Cy7 mice (Figure 2.4A). The concentration of Cy7 in the tumor decreased rapidly and Cy7 was completely eliminated from the tumor 4 hours post-injection. The tumor fluorescence in the mouse injected with the murine CC49-Cy7, reached the highest intensity at 48 hours post-injection and remained so between 72 to 120 hours. Tumor fluorescence was detected as far as 288 hours post-injection. In contrast, the peak fluorescent intensity from the tumor of the mouse with excessive unlabeled murine CC49 was detected at 24 hours post-injection after which the intensity decreased rapidly. The fluorescent intensity from the tumor of the mouse with excessive unlabeled murine CC49 was significantly lower than that from the tumor of the murine CC49-Cy7 mouse. Figure 2.4C shows the dynamic biodistribution of HuCC49ΔC$_H$2-Cy7 in the tumors. The mouse with HuCC49ΔC$_H$2-Cy7 as well as the mouse with excessive unlabeled murine CC49 and HuCC49ΔC$_H$2-Cy7 showed the highest fluorescent intensities from the tumors 5 hrs after injection of HuCC49ΔC$_H$2-Cy7. The elimination of HuCC49ΔC$_H$2-Cy7 from the tumors was much faster than the removal of murine CC49-Cy7. When the mouse was pretreated with excessive murine CC49, the fluorescent intensities from the tumor was significantly lower than that in the tumor of the unblocked HuCC49ΔC$_H$2-Cy7 mouse. The murine CC49 blockage also decreased the retention time of HuCC49ΔC$_H$2-Cy7 in the tumor from 96 hours to 48 hours. This data suggests that the HuCC49ΔC$_H$2-Cy7 and murine CC49-Cy7 target LS174T tumors antigen-specifically.

In contrast, murine CC49-Cy7 and HuCC49ΔC$_H$2-Cy7 exhibit maximum concentrations in the liver at 6 hours post-injection for both murine CC49-Cy7 and HuCC49ΔC$_H$2-Cy7 mice, as well as the mice pretreated with excessive murine CC49 (Figure 2.4B, 2.4D). No obvious difference in fluorescent intensity from the liver was found between the two groups of mice. Fluorescence from the livers of both mice disappeared 96 hours after the injection of murine CC47-Cy7 and HuCC49ΔC$_H$2-Cy7. This data suggests that the accumulation of murine CC47-Cy7 and HuCC49 ΔC$_H$2-Cy7 in the liver is nonspecific.

2.4.6 Analysis of fluorescence from fresh tissues

Fluorescent signals from different freshly dissected tissues were quantified by optical imaging. Figure 2.5A shows the images of dissected tissues of blank, Cy7, murine CC49 pretreated, murine CC49-Cy7, and non-specific murine IgG-Cy7 mice that were sacrificed at 2 hours or 96 hours post-injection of fluorescent agents. Figure 2.6A shows the images of dissected tissues of blank, Cy7, murine CC49 pretreated, HuCC49ΔC$_H$2-Cy7, and non-specific human IgG-Cy7 mice that were sacrificed at 2 or 18 hours post-injection of fluorescent agents. The relative fluorescent intensity from each tissue, obtained by subtracting the mean fluorescent intensity from the corresponding tissue of the blank mouse, is labeled in Figures 2.5A and 2.6A. The tissue imaging data revealed that the fluorescent signals from the abdomen and pelvis of the mice were mainly due to the distribution of antibody-Cy7 in the liver, gastrointestinal tract, spleen, and kidneys. A low level of autofluorescence was detected from the stomach and intestines even though no fluorescent agent was injected to the blank mouse. As shown in Figures 2.5A and 2.6A, Cy7 was mainly distributed in kidneys, tumor, and stomach 2 hours post-injection.

A small amount of fluorescence was detected from the spleen and liver. Cy7 was completely eliminated from all tissues at 18 hours post-injection. In the murine CC49-Cy7 mice, murine CC49-Cy7 was mainly distributed in the liver, lung, kidneys, spleen, heart and tumor at 2 hrs post-injection (Figure 2.5A). Most fluorescence from the spleen, kidneys, lung, and heart appeared to be cleared at 96 hrs post-injection. The fluorescence intensities from the tumors doubled while the fluorescence intensities from the livers decreased. The fluorescence intensity from the tumor of the murine CC49-Cy7 mouse was higher than that from the tumor of the mouse pretreated with excessive murine CC49. The non-specific murine IgG-Cy7 mainly localized in liver and kidneys 2 hours post injection and was cleared from the body 96 hours post injection. The fluorescent intensity from the heart was used to reflect the fluorescent intensity from the blood. Figures 2.5A and 2.5c show the tissue to heart ratios for the fluorescence at 2 hours and 96 hours after injection of Cy7, murine CC49-Cy7, or non-specific murine IgG-Cy7. From 2 hours to 96 hours post-injection, the tumor to heart ratio for the murine CC49-Cy7 mouse increased from 1.3 to 15.5 and the tumor to heart ratio for the mouse pretreated with excessive murine CC49 increased from 0.7 to 9.9. In contrast, the tumor to heart ratio for the Cy7 mouse decreased from 2.9 to 1.3 while the tumor to heart ratio for the non-specific murine IgG-Cy7 mouse slightly increased from 0.65 to 1.62. In the murine CC49-Cy7 mouse as well as the mouse pretreated with excessive murine CC49, the spleen to heart, kidneys to heart, and lung to heart ratios decreased or remained unchanged while the liver to heart ratios increased.

Much like murine CC49-Cy7, HuCC49$\Delta C_H 2$-Cy7 was mainly distributed in the tumor, liver, spleen, kidneys, lung, and heart. The fluorescent signal detected from the

stomach and intestine of the mice may be due to autofluorescence. Figures 2.6B and 2.6C show the tissue to heart ratios for the fluorescence at 2 hours and 18 hours after injection of Cy7, HuCC49ΔC$_H$2-Cy7 or non-specific human IgG-Cy7. From 2 hrs to 18 hours post-injection, only the tumor and the liver had a dramatic increase of fluorescent intensity. The tumor to heart ratio for the HuCC49ΔC$_H$2-Cy7 mouse increased from 2.1 to 12.0 and the tumor to heart ratio for the mouse pretreated with excessive murine CC49 increased from 0.9 to 9.8. In contrast, the tumor to heart ratio for the Cy7 mouse decreased from 3.4 to 0.2 and the tumor to heart ratio for the non-specific human IgG-Cy7 mouse decreased from 1.94 to 1.47. For the murine CC49-Cy7 mice, the spleen to heart, kidneys to heart and lung to heart ratios decreased or showed no change while the liver to heart ratios increased.

2.5 Discussion

NIR fluorescence imaging is emerging as a powerful tool for noninvasive imaging for use in both preclinical and clinical investigations. In this regard, it has great potential for use in the arena of clinical cancer diagnosis and monitoring of cancer therapeutics [43]. Our previous studies [11-19] have shown that human cancer cell lines LS174T and human colorectal cancer tissues express high levels of TAG-72. Radioisotope-labeled CC49 and HuCC49ΔC$_H$2 antibodies localize and target more than 80% of colorectal cancer in both preclinical testing and clinical investigations. Encouraged by these results, we hypothesize that conjugation of the CC49 antibody with Cy7 will not change the cancer targeting ability of the antibody and that the conjugates can be used for tumor

imaging in living subjects. Therefore, the CC49-Cy7 and HuCC49ΔC$_H$2-Cy7 conjugates were synthesized and evaluated in a colorectal cancer xenograft mice model.

When labeling antibodies with NHS esters, it is necessary to optimize the ratio of NHS ester to antibody and pH in order to give the final Cy dye to protein (D/P) ratio that yields maximum fluorescence. A previous study on Cy5 found that the brightest antibodies had a D/P ratio of 2-3 [44]. However, no fluorescence was observed for a D/P ratio of 6 secondary to the self-quenching characteristics of the fluorescent dye. Another study conducted by GE Healthcare showed that Cy NHS ester to antibody ratios of 1:1, 5:1, 10:1, and 20:1 gave final D/P ratios of 0.28:1, 1.16:1, 2.3:1, and 4.6:1, respectively (29). Considering all the above factors, we selected a ratio of Cy7 NHS ester to antibody of 10:1 in the synthesis reaction. In addition, the pH is also known to affect the D/P ratio. D/P ratios of 5–6 were obtained after ten minutes using a pH 8.5–9.4 [45]. To obtain D/P of 2-3, we used a pH of 8.3. The final Cy7/CC49 ratio was 3.02 and the final Cy7/ HuCC49ΔC$_H$2 ratio was only 1.36. The low labeling efficiency of HuCC49ΔC$_H$2 can be explained due to the fact that the HuCC49ΔC$_H$2 was chelated by DOTA, which consumed some primary amino groups on the antibody.

Cy5.5 is a widely used cyanine dye for NIR fluorescence imaging of living animals [31]. However, Cy5.5 may have low tissue penetration and autofluorescence from imaging larger tissue volumes [35]. Ke et al. [31] reported that the contents in the gastrointestinal tract from the mouse's diet might cause intense autofluorescence and reduce the imaging efficacy of Cy5.5 labeled target protein. In our whole-body imaging with antibody-Cy7, no autofluorescence was detected from the abdominal and pelvic areas of the blank mice (Figure 2.2). Only limited autofluorescence was found in the

images of the dissected stomach and intestines of the blank mouse (Figure 2.5 and 2.6), which might have resulted from the mouse diet. Compared with Cy5.5, the longer excitation and emission wavelengths of Cy7 provide increased tissue penetration with minimal tissue autofluorescence [35].

The *in vitro* binding studies (Figure 2.1) showed the specific binding between the antibody-Cy7 conjugate and the LS174T cells. The possibility of nonspecific binding between free Cy7 and LS174T cells was excluded by the finding that negligible fluorescence was detected from the cells incubated with free Cy7. Furthermore, excessive CC49 antibody successfully blocked the binding of CC49-Cy7 or HuCC49ΔC_H2-Cy7 to the LS174T cells, indicating that the binding was mediated through TAG-72.

The dynamic imaging data revealed different pharmacokinetics and distribution of Cy7, CC49-Cy7 and HuCC49ΔC_H2-Cy7. The rapid distribution and elimination of Cy7 in the whole mouse body can be explained by its very small molecular weight (818 Dalton). In contrast, only a limited amount of fluorescence was detected 15 mins after injection of the antibody-Cy7 conjugate, suggesting that its larger molecular size of may be responsible in slowing down its diffusion and distribution. The dynamic imaging data also illustrated that the HuCC49ΔC_H2-Cy7 conjugate was cleared from the body of the mouse much faster than the CC49-Cy7 conjugate, which is consistent with the previously reported data. Previous studies with [125]I- or ^{177}Lu-labeled CC49 in non-tumor-bearing athymic mice gave $t_{1/2\alpha}$ values ranging from 1.8 to 5.6 hrs and $t_{1/2\beta}$ values in the range of 77.2–179.4 hrs [46]. Studies with ^{177}Lu-labeled HuCC49ΔC_H2 administered intravenously to LS174T tumor-bearing athymic mice yielded a $t_{1/2\alpha}$ of 13.3 minutes and a $t_{1/2\beta}$ of 5.3 hrs [47]. Another study showed a shorter plasma clearance $t_{1/2}$ of [177]Lu-

51

labeled HuCC49ΔC$_H$2 at 2.7 hrs [48]. The faster clearance of HuCC49ΔC$_H$2 is due to the C$_H$2 domain deletion, which prevents the binding between HuCC49ΔC$_H$2 and FcRn receptors. The unbound HuCC49ΔC$_H$2 undergoes lysosomal degradation and cannot recycle into serum [46].

CC49-Cy7 conjugate demonstrated a longer retention time in the tumor (288 hrs) compared to the HuCC49ΔC$_H$2-Cy7 conjugate (96 hrs), likely due to the long plasma clearance half-life of the CC49-Cy7 conjugate. The slow plasma clearance increased tumor accumulation of CC49-Cy7. It has been reported previously that HuCC49ΔC$_H$2 has a modest decrease in tumor localization, as compared to the intact CC49 [48]. Interestingly, CC49-Cy7, HuCC49ΔC$_H$2-Cy7 and non-specific IgG-Cy7 demonstrated a high level of distribution and long retention times in livers, which may be due to the chemical conjugation of the antibodies to the Cy7. The accumulation of CC49-Cy7 and HuCC49ΔC$_H$2-Cy7 conjugates in livers was also similar to that reported in previous studies. For instance, the accumulation in the liver was also observed for chelated and radioisotope-labeled CC49 [49] and single-chain Fv of CC49 [50]. Mohsin *et al*. [49] suggested that the high accumulation in the liver was likely due to the metabolism of the chelated antibody in the liver. Clearance and metabolism of IgG antibody occur predominantly through the reticuloendothelial system (RES), primarily in the liver and spleen which contain the Kupffer cells. Furthermore, antibodies are bound and internalized by asialoglycoprotein receptors in the liver cells, increasing the retention of CC49 in the liver [49]. A long retention time for the antibodies in the liver and spleen were therefore expected.

Our dynamic imaging data also shows that pretreatment with excessive CC49 antibody could reduce the accumulation and retention times of CC49-Cy7 and HuCC49ΔC_H2-Cy7 conjugates in tumors (Figure 2.4). The results were confirmed by quantification of fluorescent signals in dissected tumor tissues (Figure 2.5A and 2.6A). In contrast, the accumulation of CC49-Cy7 and HuCC49ΔC_H2-Cy7 conjugates in the liver did not show significant change when the mice were pretreated with excessive CC49. This data suggests that CC49-Cy7 and HuCC49ΔC_H2-Cy7 specifically target the TAG-72 antigen in xenograft tumor tissues with nonspecific accumulation in the liver. Consistent with our finding, fluorescence intensities in the tumors were also observed to decrease when the xenograft nude mice were pretreated with overdose trastuzumab or C225 antibody to block HER2 [51] or EGFr [52]1. However, it was also reported that antibody blockage with cetuximab did not decrease fluorescence intensity in xenograft tumors on SCID mice [38, 39]. The inconsistency may be caused by the different antibodies, tumor cells, animal models and dosages of unlabeled antibody.

To optimize the efficacy of tumor detection, it is important to determine the point in time at which the maximum tumor to normal tissue ratio for the antibody is obtained. Mohsin *et al.* reported that the maximum tumor to blood ratios for [149]Pm-, [166]Ho-, and ^{177}Lu-MeO-DOTA-CC49 conjugates were obtained between 96-168 hrs post-injection [49]. Our dynamic imaging data (Figures 2.4A and 2.4B) also show that fluorescent intensity in the tumor reaches a high level at 120 hrs after injection of the CC49-Cy7, while the fluorescence intensity in the liver decreases to a low level at 96 hrs post-injection. Two additional groups of mice injected with the CC49-Cy7 conjugate were sacrificed at 2 hrs and 96 hrs post-injection for fresh tissue imaging. The concentration of

the CC49-Cy7 in the heart is regarded to be equal to the concentration of CC49-Cy7 in the blood. The tumor to heart ratio for CC49-Cy7 at 96 hrs post-injection was 15.5, which is comparable to previously reported data (34, 40). Chinn *et al.* [53] reported the tumor to blood ratio for ^{111}In-CC49 at 24 hrs post-injection to be 3.7 and Slavin-Chiorini *et al.* [46] reported the tumor to blood ratios for the iodine-CC49 at 24, 48, and 72 hrs post-injection to be 2.4, 3.0, and 7.4, respectively. The high tumor to heart ratio for the CC49-Cy7 obtained at 96 hrs post-injection suggests that 4 day after injection of the CC49-Cy7 is the optimal time for tumor detection and imaging using fluorescence.

Dynamic imaging showed that the concentration of the HuCC49ΔC_H2-Cy7 conjugate in the tumor decreased rapidly (Figure 2.4C). Therefore, we performed tumor imaging within 24 hrs post-injection of the HuCC49ΔC_H2-Cy7. The plasma clearance $t_{1/2}$ of the HuCC49ΔC_H2 in the LS-174T tumor-bearing athymic mice has been reported previously to range from 2.7-5.3 hrs [47, 48], suggesting that more than 90% of the HuCC49ΔC_H2 has been cleared from blood circulation at 18 hrs post-injection. Two additional groups of HuCC49ΔC_H2-Cy7 mice were sacrificed at 2 hrs and 18 hrs post-injection for fresh tissue imaging. The tumor to heart ratio for the HuCC49ΔC_H2-Cy7 conjugate was determined to be 12.0. Our data are also consistent with previous findings which reported that ^{177}Lu-HuCC49ΔC_H2 and ^{111}In-HuCC49ΔC_H2 demonstrated tumor-to-blood ratios of 12.3 and 16.0 in LS174T xenograft mice at 24 hrs post-injection, respectively [47, 53, 54].

Both CC49-Cy7 and HuCC49ΔC_H2-Cy7 conjugates accumulated to some extent in the spleen, kidneys, and lungs. However, the clearance of the antibodies from these tissues was faster compared to clearance from the tumor, suggesting that localization of CC49-Cy7 and HuCC49ΔC_H2-Cy7 conjugates in the spleen, kidneys, and lungs was not

likely due to specific antigen-antibody interaction, as reported in a previous study [50]. The fluorescence observed from the kidneys was probably due to accumulation of metabolites of the antibody-Cy7 conjugates and non-specific binding between the metabolites and brush border of the renal proximal tubule [49].

In summary, the CC49 monoclonal antibody targets the tumor-associated glycoprotein (TAG)-72 overexpressed on a wide spectrum of carcinomas, including colon, ovarian, pancreatic, breast, and prostate cancers. The CC49 antibody conjugated with a non-radioactive fluorescent marker may have many applications for tumor imaging and target drug delivery. Therefore we conjugated the murine CC49 monoclonal antibody (CC49 MAb) and humanized C_H2 domain-deleted CC49 monoclonal antibody (HuCC49ΔC_H2 MAb) with a near-infrared (NIR) fluorophore Cy7 and tested the feasibility of the CC49-Cy7 and HuCC49ΔC_H2-Cy7 conjugates for NIR fluorescence imaging of tumors in a preclinical xenograft animal model. Tumor targeting and retention of the Cy7-NHS, CC49-Cy7, HuCC49ΔC_H2-Cy7 and non-specific IgG-Cy7 in a subcutaneous LS174T tumor model have been evaluated and quantified using a Xenogen IVIS 100 optical cooled charged-coupled device system. The results showed that antibody-Cy7 was indeed localized in tumor tissues. CC49 antibody achieved a tumor/blood ratio of 15 at 96 hrs postinjection. In comparison, HuCC49ΔC_H2 was cleared much faster than murine CC49 in xenograft mouse, and HuCC49ΔC_H2 antibody achieved a tumor/blood ratio of 12 at 18 hrs postinjection. In contrast, Cy7 and non-specific IgG-Cy7 had short retention times in the tumors. Additionally, for the mice pretreated with excessive CC49, the retention time of the CC49-Cy7 in the tumor was reduced from 288 hrs to 240 hrs and the retention time of the HuCC49ΔC_H2-Cy7 was

reduced from 96 hrs to 48 hrs. These data suggest that both CC49-Cy7 and HuCC49ΔC$_H$2-Cy7 conjugates targeted TAG-72, and the excessive CC49 blocked the TAG-72 on the tumor. In conclusion, the Cy7 labeled CC49 and HuCC49ΔC$_H$2 demonstrate tumor-targeting capabilities in colorectal cancer xenograft mice and provide an alternative modality for tumor imaging.

2.6 Acknowledgement

2.7 References

1. Johnson, V.G., et al., *Analysis of a human tumor-associated glycoprotein (TAG-72) identified by monoclonal antibody B72.3.* Cancer Res, 1986. **46**(2): p. 850-7.
2. Colcher, D., et al., *Characterization and biodistribution of recombinant and recombinant/chimeric constructs of monoclonal antibody B72.3.* Cancer Res, 1989. **49**(7): p. 1738-45.
3. Xiao, J., et al., *Pharmacokinetics and clinical evaluation of 125I-radiolabeled humanized CC49 monoclonal antibody (HuCC49deltaC(H)2) in recurrent and metastatic colorectal cancer patients.* Cancer Biother Radiopharm, 2005. **20**(1): p. 16-26.
4. Lanyan Fang, N.H.G.H., George Hinkle, Xianhua Cao, Mark Bloomston, Jim J Xiao, Seth Gibbs, Osama Habib Al Saif, James T. Dalton, Kenneth K. Chan, Jeffrey Schlom, Edward T. Martin Jr, and Duxin Sun, *, *Population Pharmacokinetics of Humanized Monoclonal Antibody HuCC49?CH2 and Murine Antibody CC49 in Colorectal Cancer Patients.* J Clin Pharmacol, 2007. **47 (2)**: p. 227-237
5. Nieroda, C.A., et al., *Radioimmunoguided surgery (RIGS) in recurrent colorectal cancer.* Cancer Detect Prev, 1991. **15**(3): p. 225-9.
6. Nieroda, C.A., et al., *The impact of radioimmunoguided surgery (RIGS) on surgical decision-making in colorectal cancer.* Dis Colon Rectum, 1989. **32**(11): p. 927-32.
7. Sardi, A., et al., *Intra-abdominal recurrence of colorectal cancer detected by radioimmunoguided surgery (RIGS system).* Arch Surg, 1989. **124**(1): p. 55-9.

8.   Bertsch, D.J., et al., *Radioimmunoguided Surgery system improves survival for patients with recurrent colorectal cancer.* Surgery, 1995. **118**(4): p. 634-8; discussion 638-9.

9.   Bertsch, D.J., et al., *Radioimmunoguided surgery for colorectal cancer.* Ann Surg Oncol, 1996. **3**(3): p. 310-6.

10.   Gardner, B., *Five-year survival after extended resection of colon cancer.* J Surg Oncol, 1987. **34**(4): p. 258-61.

11.   Arnold, M.W., et al., *Radioimmunoguided surgery in primary colorectal carcinoma: an intraoperative prognostic tool and adjuvant to traditional staging.* Am J Surg, 1995. **170**(4): p. 315-8.

12.   Molinolo, A., et al., *Enhanced tumor binding using immunohistochemical analyses by second generation anti-tumor-associated glycoprotein 72 monoclonal antibodies versus monoclonal antibody B72.3 in human tissue.* Cancer Res, 1990. **50**(4): p. 1291-8.

13.   Sickle-Santanello, B.J., et al., *Radioimmunoguided surgery using the monoclonal antibody B72.3 in colorectal tumors.* Dis Colon Rectum, 1987. **30**(10): p. 761-4.

14.   Nieroda, C.A., et al., *Radioimmunoguided surgery in primary colon cancer.* Cancer Detect Prev, 1990. **14**(6): p. 651-6.

15.   Cohen, A.M., et al., *Radioimmunoguided surgery using iodine 125 B72.3 in patients with colorectal cancer.* Arch Surg, 1991. **126**(3): p. 349-52.

16.   Martin, E.W., Jr. and M.O. Thurston, *Intraoperative radioimmunodetection.* Semin Surg Oncol, 1998. **15**(4): p. 205-8.

17.   Agnese, D.M., et al., *Pilot study using a humanized CC49 monoclonal antibody (HuCC49DeltaCH2) to localize recurrent colorectal carcinoma.* Ann Surg Oncol, 2004. **11**(2): p. 197-202.

18.   Martinez, D.A., et al., *Radioimmunoguided Surgery for Gastrointestinal Malignancies: An Analysis of 14 Years of Clinical Experience.* Cancer Control, 1997. **4**(6): p. 505-516.

19.   LaValle, G.J., et al., *Assessment of disseminated pancreatic cancer: a comparison of traditional exploratory laparotomy and radioimmunoguided surgery.* Surgery, 1997. **122**(5): p. 867-71; discussion 871-3.

20.   Arnold, M.W., et al., *Staging of colorectal cancer: biology vs. morphology.* Dis Colon Rectum, 1998. **41**(12): p. 1482-7.

21.   Arnold, M.W., et al., *Intraoperative detection of colorectal cancer with radioimmunoguided surgery and CC49, a second-generation monoclonal antibody.* Ann Surg, 1992. **216**(6): p. 627-32.

22.   Arnold, M.W., et al., *Intra-abdominal patterns of disease dissemination in colorectal cancer identified using radioimmunoguided surgery.* Dis Colon Rectum, 1996. **39**(5): p. 509-13.

23.   Arnold, M.W., S. Schneebaum, and E.W. Martin, Jr., *Radioimmunoguided Surgery in the Treatment and Evaluation of Rectal Cancer Patients.* Cancer Control, 1996. **3**(1): p. 42-45.

24.   Cote, R.J., et al., *Intraoperative detection of occult colon cancer micrometastases using 125 I-radiolabled monoclonal antibody CC49.* Cancer, 1996. **77**(4): p. 613-20.

25.   Sardi, A., et al., *Radioimmunoguided surgery in recurrent colorectal cancer: the role of carcinoembryonic antigen, computerized tomography, and physical examination.* South Med J, 1989. **82**(10): p. 1235-44.

26.   Kim, J.A., P.L. Triozzi, and E.W. Martin, Jr., *Radioimmunoguided surgery for colorectal cancer.* Oncology (Williston Park), 1993. **7**(2): p. 55-60; discussion 60, 63-4.

27.   Arnold, M.W., et al., *Radioimmunoguided surgery challenges traditional decision making in patients with primary colorectal cancer.* Surgery, 1992. **112**(4): p. 624-9; discussion 629-30.

28.   Schneebaum, S., et al., *The significance of intraoperative periportal lymph node metastasis identification in patients with colorectal carcinoma.* Cancer, 1995. **75**(12): p. 2809-17.

29.   Sun, D., et al., *Radioimmunoguided surgery (RIGS), PET/CT image-guided surgery, and fluorescence image-guided surgery: Past, present, and future.* Journal of Surgical Oncology, 2007. **96**(4): p. 297-308.

30.   King, M.A., et al., *Introduction to the physics of molecular imaging with radioactive tracers in small animals.* Journal of Cellular Biochemistry, 2002(Suppl. 39): p. 221-230.

31.   Ke, S., et al., *Near-infrared optical imaging of epidermal growth factor receptor in breast cancer xenografts.* Cancer Res, 2003. **63**(22): p. 7870-5.

32.   Cheng, Z., et al., *Near-infrared fluorescent deoxyglucose analogue for tumor optical imaging in cell culture and living mice.* Bioconjug Chem, 2006. **17**(3): p. 662-9.

33.   Cheng, Z., et al., *Near-infrared fluorescent RGD peptides for optical imaging of integrin alphavbeta3 expression in living mice.* Bioconjug Chem, 2005. **16**(6): p. 1433-41.

34.   Tanisaka, H., et al., *Near-infrared fluorescent labeled peptosome for application to cancer imaging.* Bioconjug Chem, 2008. **19**(1): p. 109-17.

35.   Hawrysz, D.J. and E.M. Sevick-Muraca, *Developments toward diagnostic breast cancer imaging using near-infrared optical measurements and fluorescent contrast agents.* Neoplasia, 2000. **2**(5): p. 388-417.

36.   Nimura, H., et al., *Infrared ray electronic endoscopy combined with indocyanine green injection for detection of sentinel nodes of patients with gastric cancer.* British Journal of Surgery, 2004. **91**(5): p. 575-579.

37.   Soltesz, E.G., et al., *Sentinel lymph node mapping of the gastrointestinal tract by using invisible light.* Annals of Surgical Oncology, 2006. **13**(3): p. 386-396.

38.   Gleysteen, J.P., et al., *Fluorescent labeled anti-EGFR antibody for identification of regional and distant metastasis in a preclinical xenograft model.* Head and Neck-Journal for the Sciences and Specialties of the Head and Neck, 2008. **30**(6): p. 782-789.

39.   Rosenthal, E.L., et al., *Use of fluorescent labeled anti-epidermal growth factor receptor antibody to image head and neck squamous cell carcinoma xenografts.* Molecular Cancer Therapeutics, 2007. **6**(4): p. 1230-1238.

40.   Kulbersh, B.D., et al., *Sensitivity and specificity of fluorescent immunoguided neoplasm detection in head and neck cancer xenografts.* Archives of Otolaryngology-Head & Neck Surgery, 2007. **133**(5): p. 511-515.

41. Rosenthal, E.L., et al., *In vivo detection of head and neck cancer orthotopic xenografts by immunofluorescence.* Laryngoscope, 2006. **116**(9): p. 1636-1641.

42. Healthcare, G., *Protocol for Amersham CyDye monoreactive NHS Esters.* 2006.

43. Xu, R.X. and S.P. Povoski, *Diffuse optical imaging and spectroscopy for cancer.* Expert Review of Medical Devices, 2007. **4**(1): p. 83-95.

44. Gruber, H.J., et al., *Anomalous fluorescence enhancement of Cy3 and Cy3.5 versus anomalous fluorescence loss of Cy5 and Cy7 upon covalent linking to IgG and noncovalent binding to avidin.* Bioconjugate Chemistry, 2000. **11**(5): p. 696-704.

45. Mujumdar, R.B., et al., *Cyanine dye labeling reagents: sulfoindocyanine succinimidyl esters.* Bioconjug Chem, 1993. **4**(2): p. 105-11.

46. Slavin-Chiorini, D.C., et al., *Biological properties of chimeric domain-deleted anticarcinoma immunoglobulins.* Cancer Res, 1995. **55**(23 Suppl): p. 5957s-5967s.

47. Milenic, D.E., et al., *In vivo comparison of macrocyclic and acyclic ligands for radiolabeling of monoclonal antibodies with Lu-177 for radioimmunotherapeutic applications.* Nuclear Medicine and Biology, 2002. **29**(4): p. 431-442.

48. Rogers, B.E., et al., *Intraperitoneal radioimmunotherapy with a humanized anti-TAG-72 (CC49) antibody with a deleted CH2 region.* Cancer Biother Radiopharm, 2005. **20**(5): p. 502-13.

49. Mohsin, H., et al., *Radiolanthanide-labeled monoclonal antibody CC49 for radioimmunotherapy of cancer: Biological comparison of DOTA conjugates and Pm-149, Ho-166, and Lu-177.* Bioconjugate Chemistry, 2006. **17**(2): p. 485-492.

50. Yokota, T., et al., *Microautoradiographic analysis of the normal organ distribution of radioiodinated single-chain Fv and other immunoglobulin forms.* Cancer Res, 1993. **53**(16): p. 3776-83.

51. Sampath, L., et al., *Dual-labeled trastuzumab-based imaging agent for the detection of human epidermal growth factor receptor 2 overexpression in breast cancer.* Journal of Nuclear Medicine, 2007. **48**(9): p. 1501-1510.

52. Ke, S., et al., *Near-infrared optical imaging of epidermal growth factor receptor in breast cancer xenografts.* Cancer Research, 2003. **63**(22): p. 7870-7875.

53. Chinn, P.C., et al., *Pharmacokinetics and ibmor localization of In-111-labeled HuCC49 Delta C(H)2 in BALB/c mice and athymic murine colon carcinoma xenograft.* Cancer Biotherapy and Radiopharmaceuticals, 2006. **21**(2): p. 106-116.

54. Milenic, D.E., et al., *In vivo comparison of macrocyclic and acyclic ligands for radiolabeling of monoclonal antibodies with 177Lu for radioimmunotherapeutic applications.* Nucl Med Biol, 2002. **29**(4): p. 431-42.

Figure 2.1 Fluorescence microscopic images of LS174T cells. The cells were fixed with 3.7% paraformaldehyde and incubated for 1 hour at room temperature with PBS, Cy7, murine CC49-Cy7, murine CC49 followed by murine CC49-Cy7, HuCC49ΔC$_H$2-Cy7, and murine CC49 followed by HuCC49ΔC$_H$2-Cy7.
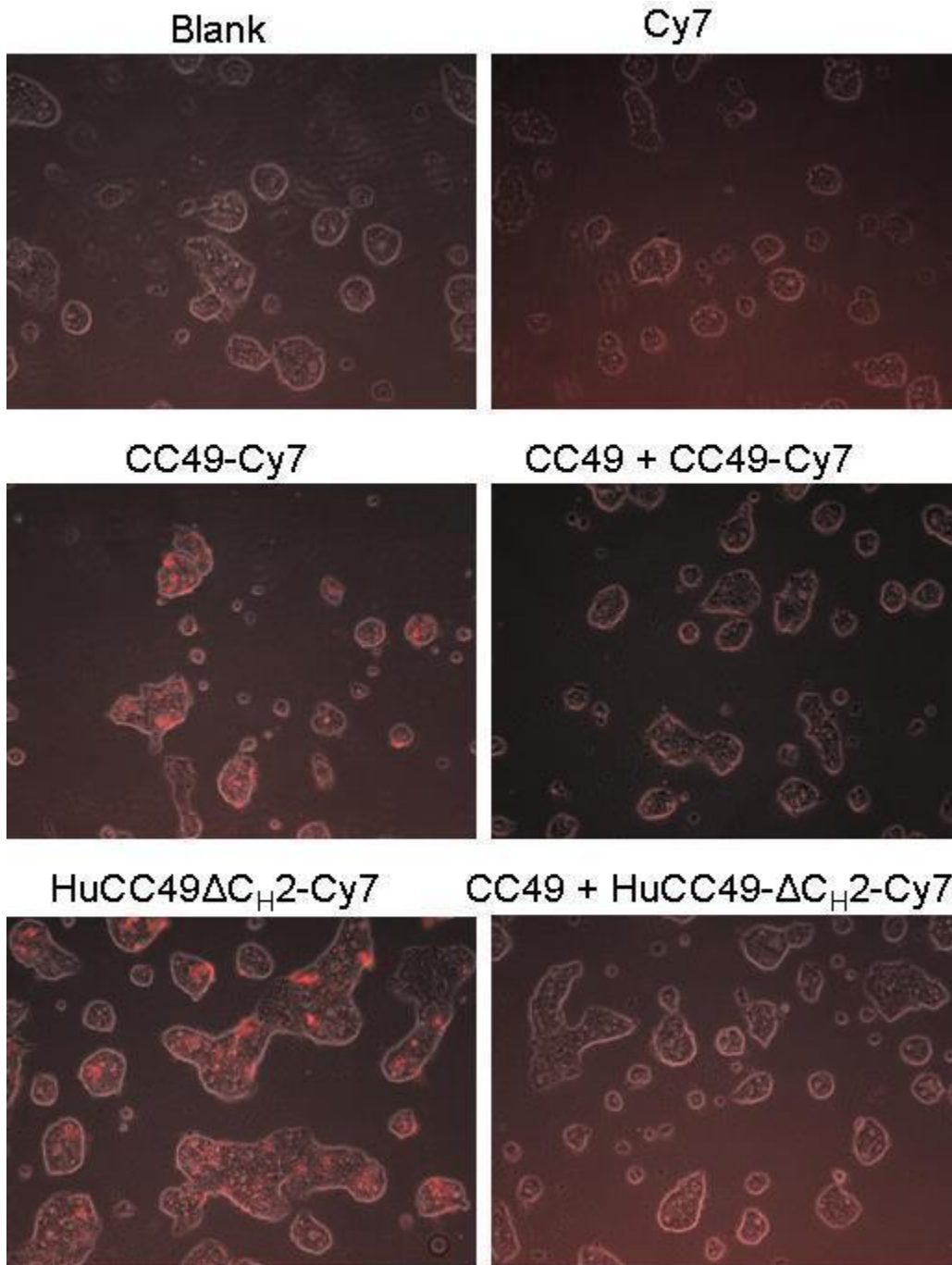
Figure 2.2 Typical *in vivo* fluorescence images of nude mice bearing LS174T xenografts after intravenous injection of Cy7-labeled antibodies. (A) 1 nmol of Cy7, excessive murine CC49 followed by 0.33 nmol of murine CC49-Cy7, 0.33 nmol of murine CC49-Cy7, or 0.38 nmol non-specific murine IgG-Cy7; (B) 1 nmol of Cy7, excessive murine CC49 followed by 0.73 nmol HuCC49ΔC_H2-Cy7, 0.73 nmol HuCC49ΔC_H2-Cy7, or 0.50 nmol non-specific human IgG-Cy7. The location of the tumors was indicated by the circles.
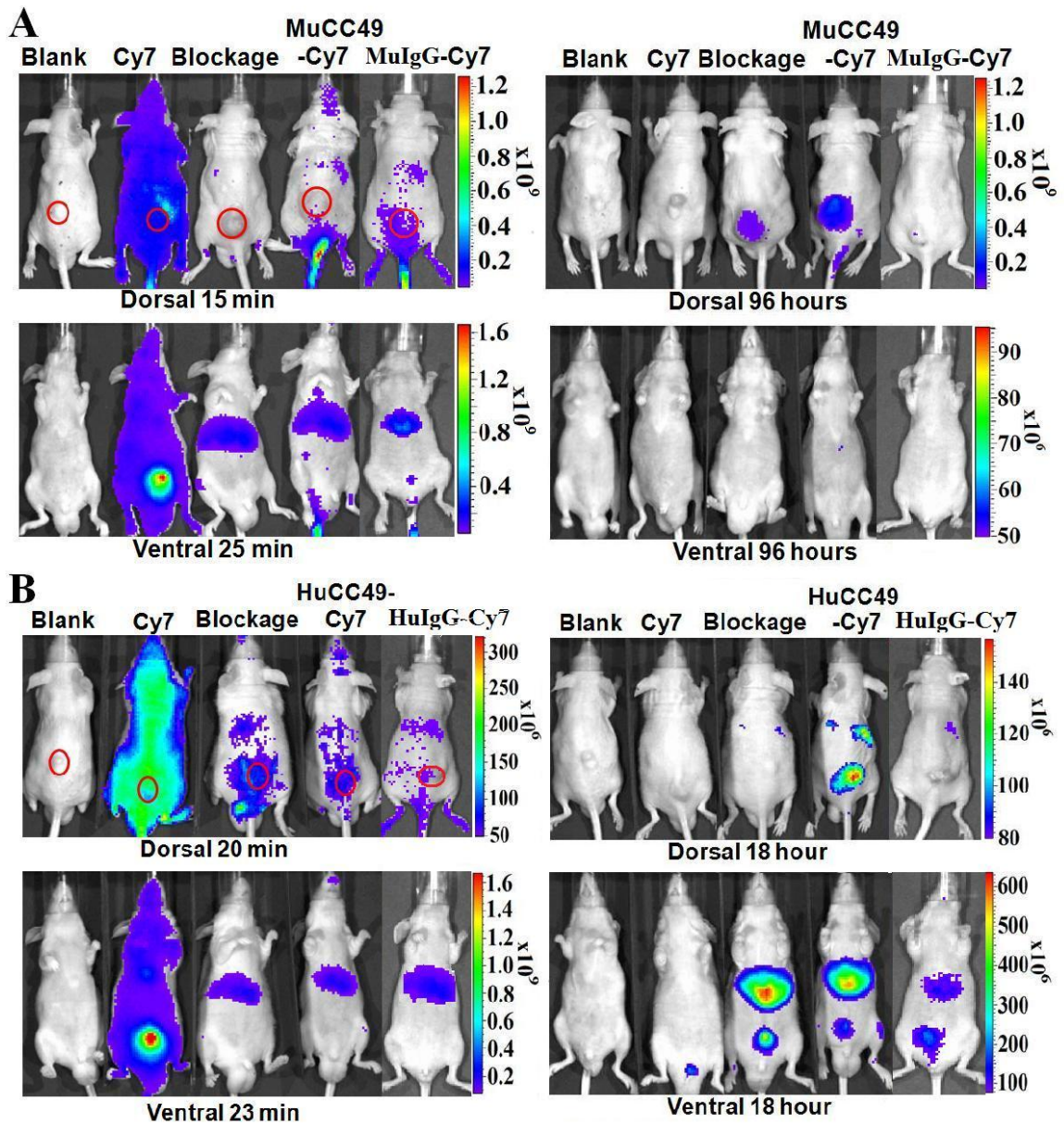
Figure 2.3 Emission spectra of (A) Cy7 and murine CC49-Cy7 and (B) fluorescence signals from the bladder, liver and tumor of an athymic nude mouse bearing LS174T xenograft tumor 24 hours after i.v. injection of murine CC49-Cy7.
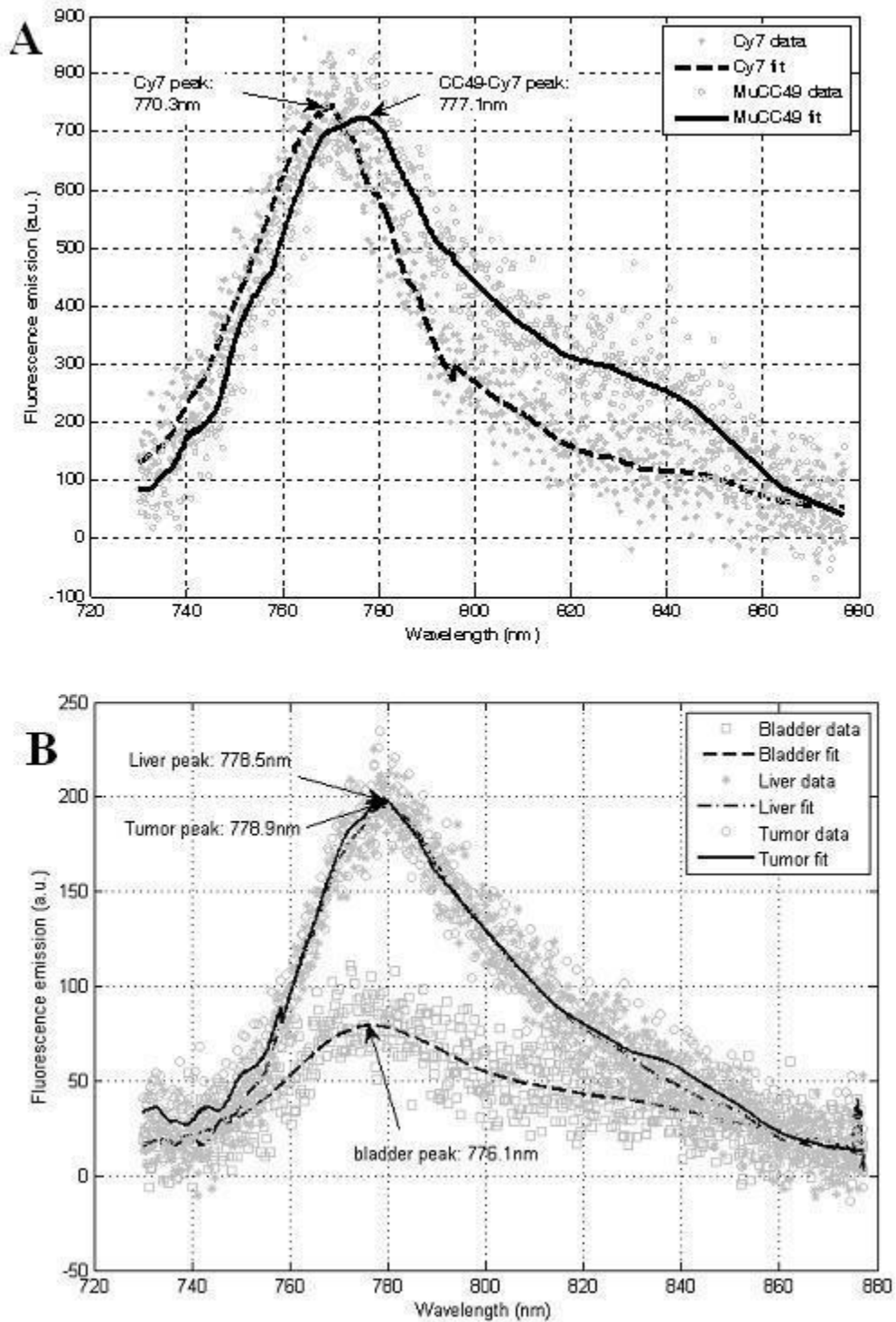
Figure 2.4 The relative mean fluorescence intensity in the tumor and liver regions of interest (ROIs) as a function of time after injection of (A, B) Cy7, excessive murine CC49 plus murine CC49-Cy7, or murine CC49-Cy7 and (C, D) Cy7, excessive murine CC49 plus HuCC49ΔC$_H$2-Cy7, or HuCC49ΔC$_H$2-Cy7.
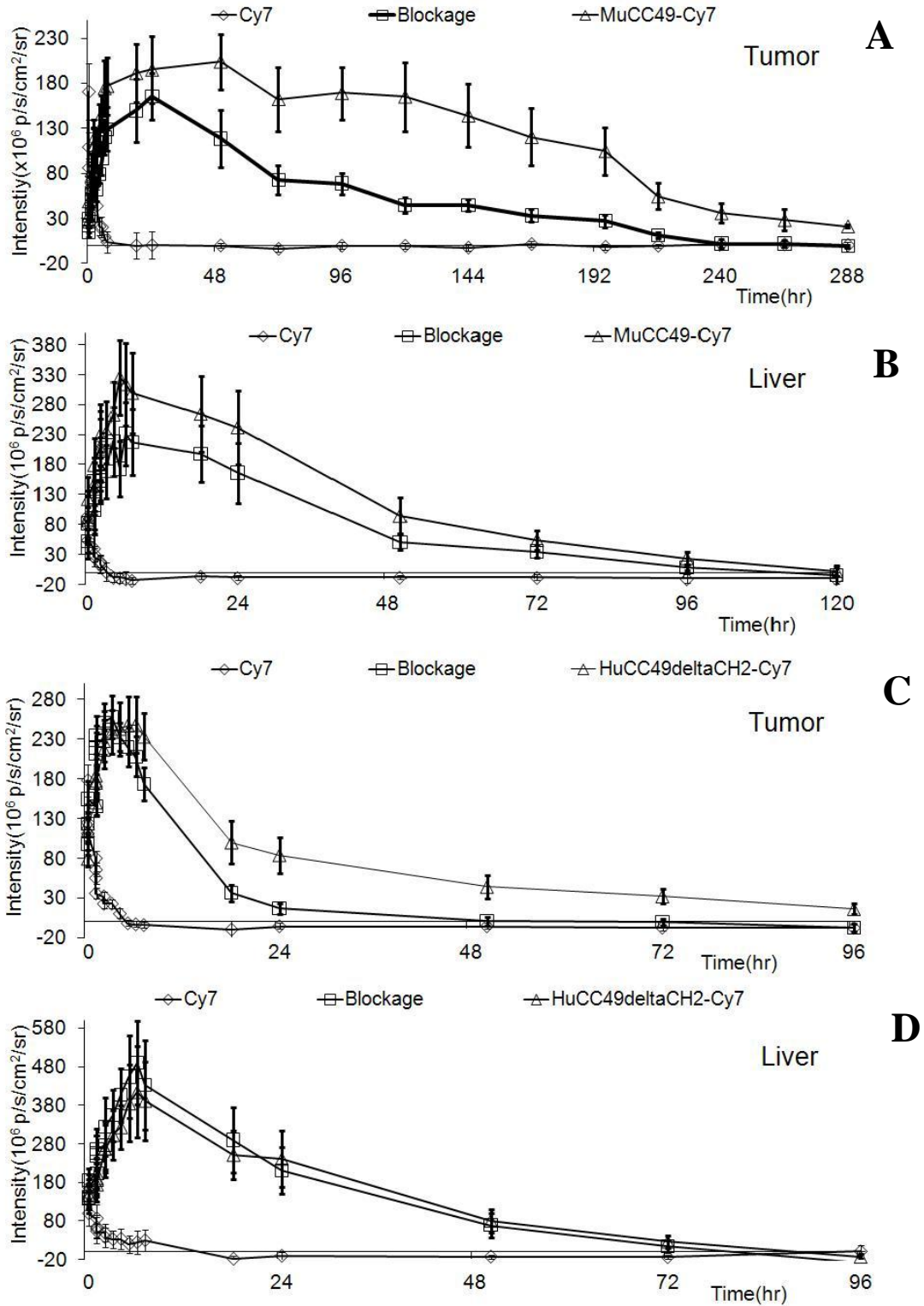
Figure 2.5 (A) Representative images of dissected organs of athymic nude mice bearing LS174T xenograft tumor sacrificed 2 hours or 96 hours after intravenous injection of 1 nmol of Cy7, excessive murine CC49 followed by 0.33 nmol of murine CC49-Cy7, 0.33 nmol of murine CC49-Cy7, or 0.38 nmol non-specific murine IgG-Cy7. The relative fluorescence intensity of each tissue was labeled near the corresponding tissue. Tissue-to-heart ratios for (B) the mice sacrificed 2 hours after injection and (C) the mice sacrificed 96 hours after injection.
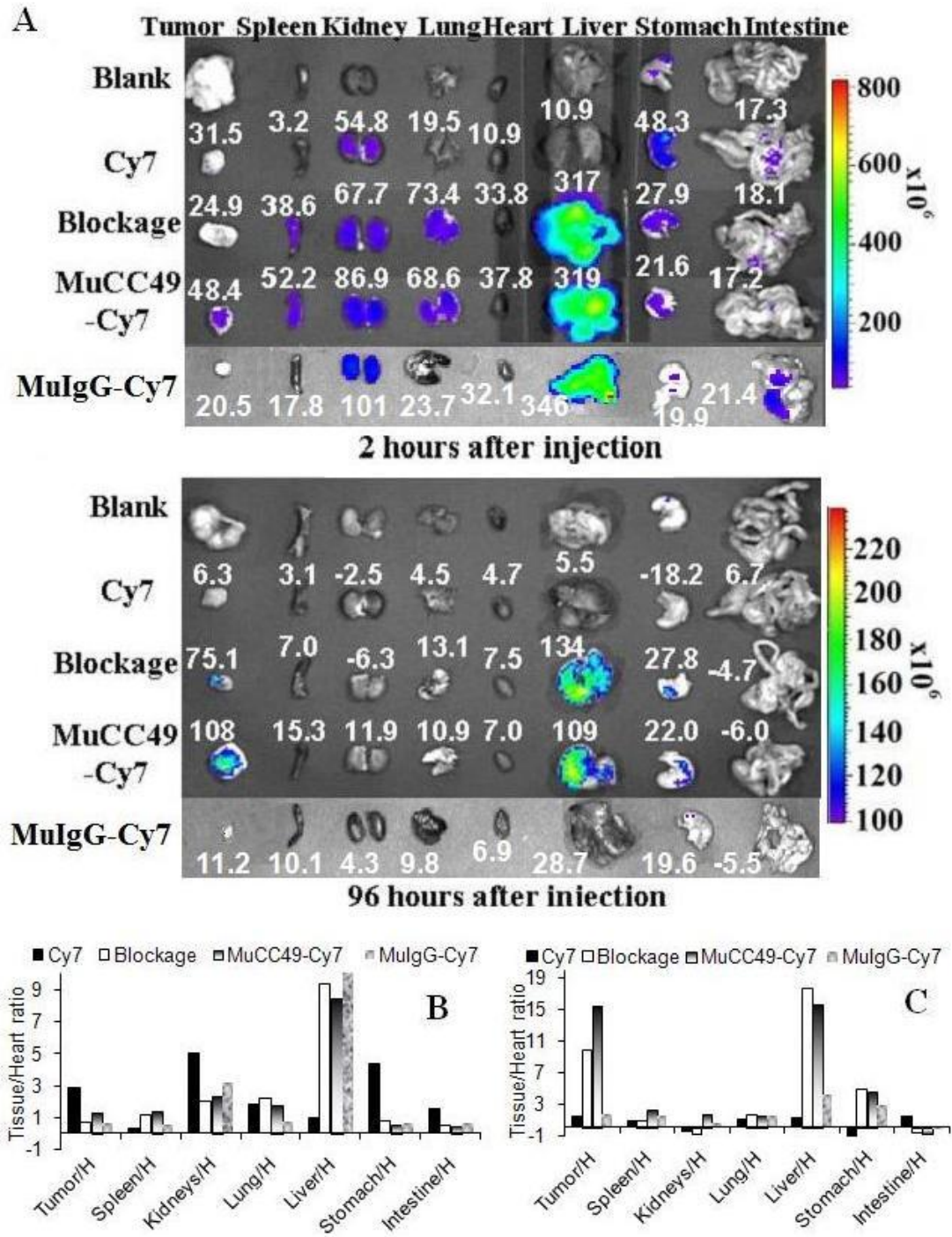
Figure 2.6 (A) Representative images of dissected organs of athymic nude mice bearing LS174T xenograft tumor sacrificed 2 hours or 96 hours after intravenous injection of 1 nmol of Cy7, excessive murine CC49 followed by 0.73 nmol HuCC49ΔC_H2-Cy7, 0.73 nmol HuCC49ΔC_H2-Cy7, or 0.50 nmol non-specific human IgG-Cy7. The relative fluorescence intensity of each tissue was labeled near the corresponding tissue. Tissue-to-heart ratios for (B) the mice sacrificed 2 hours after injection and (C) the mice sacrificed 18 hours after injection.
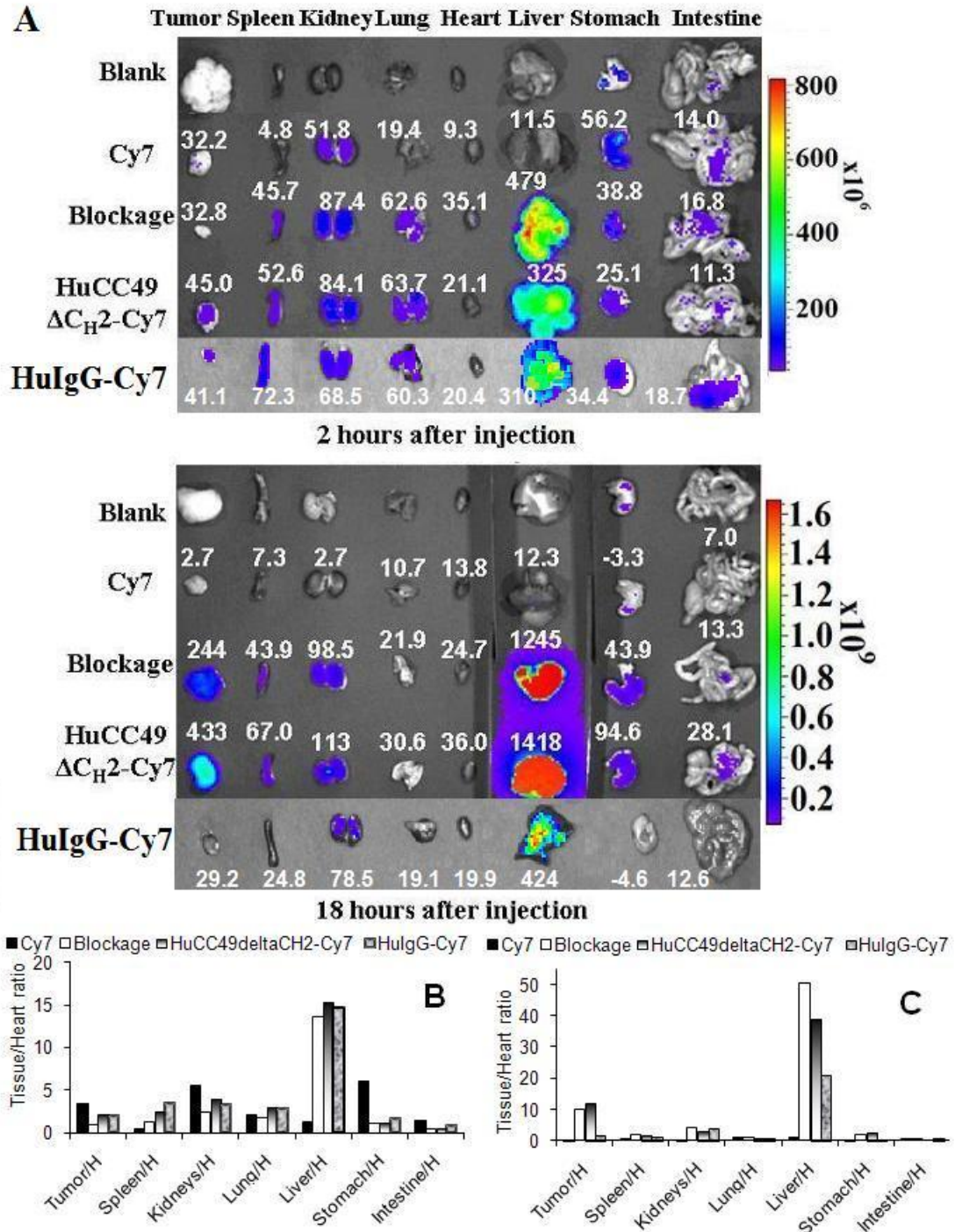
CHAPTER III

^{124}I-HuCC49ΔC$_H$2 for TAG-72 Antigen-Directed Positron Emission Tomography (PET) Imaging of LS174T Colon Tumor Implants in Xenograft Mice

3.1 Abstract

^{18}F-fluorodeoxyglucose positron emission tomography (^{18}F-FDG-PET) is widely used in diagnostic cancer imaging. However, the use of ^{18}F-FDG in PET-based imaging is limited by a variety of specificity and sensitivity issues. In contrast, anti-TAG (tumor associated antigen)-72 monoclonal antibodies are highly specific for binding to a variety of adenocarcinomas, including colorectal cancer. The aim of our current study was to evaluate a complimentary determining region (CDR)-grafted humanized domain-deleted anti-TAG-72 monoclonal antibody (HuCC49ΔC$_H$2), radiolabeled with iodine-124 (^{124}I), as an antigen-directed and cancer-specific targeting agent for PET-based imaging. HuCC49ΔC$_H$2 was radiolabeled with ^{124}I. Subcutaneous tumor implants of LS174T colon adenocarcinoma cells, that express the TAG-72 antigen, were grown on athymic Nu/Nu nude mice as the xenograft mouse model. Intravascular (i.v.) and intraperitoneal (i.p.) administration of ^{124}I-HuCC49ΔC$_H$2 was then evaluated in this xenograft mouse model at various time points from approximately 1 hour to 24 hours after injection using microPET imaging. This was compared to i.v. injection of ^{18}F-FDG in this same xenograft mouse model using microPET imaging at 50 minutes post injection. At approximately 1 hour after i.v. injection, ^{124}I-HuCC49ΔC$_H$2 was distributed within the systemic circulation, while at approximately 1 hour after i.p. injection, ^{124}I-HuCC49ΔC$_H$2

66

was distributed within the peritoneal cavity. At time points from 18 hours to 24 hours after i.v. and i.p. injection, ^{124}I-HuCC49ΔC$_H$2 demonstrated a significantly increased level of specific localization to LS174T tumor implants (p=0.001) when compared to 1 hour images. In contrast, approximately 50 minutes after injection, ^{18}F-FDG failed to demonstrate any increased level of specific localization to a LS174T tumor implant, but showed the propensity toward more nonspecific uptake within the heart, Harderian glands of the eye orbits, neck muscles, kidneys, and bladder. In summary, ^{124}I-HuCC49ΔC$_H$2 demonstrates an increased level of specific localization to tumor implants of LS174T colon adenocarcinoma cells in the xenograft mouse model on delayed imaging, while ^{18}F-FDG failed to demonstrate this. The antigen-directed and cancer-specific ^{124}I-radiolabled anti-TAG-72 monoclonal antibody conjugate, ^{124}I-HuCC49ΔC$_H$2, has great potential for use in human clinical trials for preoperative, intraoperative, and postoperative PET-based imaging strategies, including fused-modality PET-based imaging platforms.

3.2 Introduction

The origin of positron imaging dates back to the early 1950's [1], culminating in the development of positron emission tomography (PET) and its subsequent evolution over the last 40 years [1-4]. The clinical application of PET-based imaging strategies to the field of oncology has had a significant impact upon the care of cancer patients [5-11]. Therefore, the development and selection of the most appropriate and specific radiotracer for PET-based imaging is critical to its success in oncology [12-15].

^{18}F-fluorodeoxyglucose (^{18}F-FDG), by far, is currently the most widely used radiotracer for PET-based imaging strategies [16]. In this regard, ^{18}F-FDG-PET-based

imaging is currently considered state-of-the-art for the diagnostic imaging, staging, and follow-up of a wide variety of malignancies, including colorectal cancer [10,11]. However, there are several intrinsic limitations related to the use of ^{18}F-FDG-PET imaging that remain a challenges and a concern to those involved in the care of cancer patients [6-9,16-24]. First, false positive results can occur with ^{18}F-FDG-PET imaging in the presence of any pathologic conditions in which there is a high rate of glucose metabolism, such as inflammatory or infections processes. Second, false negative results can occur with ^{18}F-FDG-PET imaging secondary to poor avidity of ^{18}F-FDG to certain tumor types and secondary to impaired uptake of ^{18}F-FDG in patients with elevated blood glucose levels. Third, due to system resolution limitations, ^{18}F-FDG-PET imaging is generally limited in its ability to detect small-volume, early-stage primary disease or to detect microscopic disease within the lymph nodes. Fourth, ^{18}F-FDG-PET imaging can produce either false positive or false negative results secondary to the normal physiologic accumulation of ^{18}F-FDG within certain tissues with an elevated level of glucose metabolism (most striking in the brain and heart, and to a lesser degree in the mucosa and smooth muscle of the stomach, small intestine and colon, as well as in liver, spleen, skeletal muscle, thyroid, and brown fat) and secondary to the excretion and accumulation of ^{18}F-FDG within the urinary tract (kidneys, ureters, and bladder). Overall, these factors have a negative impact on optimizing the specificity and sensitivity of ^{18}F-FDG-PET for accurate diagnostic cancer imaging [6-9,16-24].

A PET-based imaging approach that specifically targets the cancer cell environment would clearly have a significant potential advantage for improving the accuracy of diagnostic cancer imaging over that of the more nonspecific nature of ^{18}F-FDG. In that

regard, tumor-associated glycoprotein-72 (TAG-72) is a mucin-like glycoprotein complex that is overexpressed by many adenocarcinomas, including colorectal, pancreatic, gastric, esophageal, ovarian, endometrial, breast, prostate, and lung [22,24-27]. In xenograft mice bearing subcutaneous tumor implants of the TAG-72-expressing human colon adenocarcinoma cell line, LS174T [27-29], anti-TAG-72 monoclonal antibodies have been shown to localized up to 18-fold higher in LS174T tumor implants than in normal tissues [25,30,31]. Over the last 25 years, our group at The Ohio State University, as well as others, have evaluated a variety of radioiodine labeled anti-TAG72 monoclonal antibodies for tumor-specific antigen targeting at the time of surgery for known primary, recurrent, and metastatic disease, as well as for targeting occult disease and affected lymph nodes in colorectal cancer patients [22,24,32-59]. Most recently, we have evaluated the complimentary determining region (CDR)-grafted humanized domain-deleted anti-TAG-72 monoclonal antibody, HuCC49ΔC_H2 [60-63], radiolabeled with iodine-125 (^{125}I), for intraoperative tumor detection of colorectal cancer in both a preclinical xenograft mouse model and in a human clinical trial [22,24,57-59]. Collectively, our experience with radiolabeled anti-TAG-72 monoclonal antibodies in combination with a handheld gamma detection probe has clearly shown that this technology provides the surgeon with real-time intraoperative information for more precise tumor localization and resection and has demonstrated improved long-term patient survival after surgery [22,24].

Because of the drawbacks of using ^{125}I as the radioiodine label for anti-TAG-72 monoclonal antibodies, including the extremely long physical half-life of ^{125}I of approximately 60 days (which generates handling, storage, and disposal issues within the

69

operating room environment and in the surgical pathology department) and the inability

of ^{125}I to allow for diagnostic imaging capabilities, other radionuclides have been sought

for use with anti-TAG-72 monoclonal antibodies. One such alternative is iodine-124 (^{124}I)

[64]. In this regard, ^{124}I is a positron emitting radionuclide that has a physical half-life of

approximately 4.2 days, for which its positron emitting properties makes it well-suited for

PET-based imaging and for which its shorter physical half-life simplifies the handling,

storage, and disposal issues. Therefore, the aim of our current preliminary study was to

evaluate ^{124}I-HuCC49ΔC_H2 as a cancer-specific targeting agent for PET-based imaging.

3.3 Materials and Methods

3.3.1 Cell culture and reagents

Cell culture medium (DMEM), fetal bovine serum (FBS), trypsin, and other tissue

culture materials were purchased from Invitrogen (Carlsbad, California). The human

colon adenocarcinoma cells (LS174T) [27-29] were purchased from American Type

Culture Collection (ATCC) (Manassas, VA). LS174T cells were cultured in DMEM (10%

FBS, 1% penicillin/streptomycin) at 37˚C under 5% CO2 for 24 hours. LS174T cells

were split every week. LS174T cells were trypsinized, collected, and washed with PBS,

and then resuspended in DMEM (10% FBS) for subculture. LS174T cells were stored in

DMEM (20% FBS, 10% DMSO) in liquid N_2. DOTA chelated HuCC49ΔC_H2 antibody

was supplied by Dr. Jeffrey Schlom (Laboratory of Tumor Immunology and Biology,

National Cancer Institute, National Institutes of Health, Bethesda, MD). Phosphate

buffered ^{18}F-FDG (200 MBq/ml) was supplied by IBA Molecular (Dulles, VA).

3.3.2 Iodination (^{124}I) of HuCC49ΔC$_H$2

Iodogen-coated Vials: Iodogen (1,3,4,6-tetrachloro-3α-6α-diphenylglycouril) (Pierce, Rockford, IL) was dissolved in methylene chloride (1.0 mg/ml), and was pipetted into (1 ml) a sterile/pyrogen free 10 ml vial. The vial was rotated and dried under nitrogen to evaporate methylene chloride.

Anion Exchange Resin Filters: 100 to 200-mesh AG1X8 anion exchange resin (Bio-Rad Labs, Richmond, CA) was washed using sterile, pyrogen free water. The anion exchange resin was aseptically loaded onto a 0.22 μm filter disc (1.1 to 1.5 gram wet resin/filter unit) (Millipore Corp, Milford, MA). The resin was washed using following solutions in a sequence: 10 ml sterile, pyrogen-free water; 10 ml sterile 0.1 N NaOH; 10 ml pyrogen free water; 10 ml 0.1 N sodium phosphate buffer (pH 7.4); and finally by 3.3 ml 0.1 N sodium phosphate buffer with 1% HSA.

Labeling process [65,66]: 0.50 ml of HuCC49ΔC$_H$2 antibody (1.5 mg/ml) was added to a 10 ml vial coated with 1 mg of iodogen. Then, 0.8 ml of phosphate buffered Na^{124}I (150 MBq/ml) (IBA Molecular, Dulles, VA) was added to the vial. The reagents were allowed to react for 15 minutes. Free ^{124}I was removed using an exchange resin filter disc. Then, 1 ml of 5% sucrose with 0.05% Tween 20 in saline was used to elute the labeled antibody. The purified ^{124}I-HuCC49ΔC$_H$2 was passed through a 0.22 mm Millipore filter (Millipore Corp, Milford, MA) for *in vivo* applications. Radiolabeling efficiency was monitored using radio thin layer chromatography (TLC), which was performed on silica-gel-impregnated glass fiber sheets (Pall Corp., East Hills, NY, USA). 0.02 M citrate buffer (pH 5.0) was used as the mobile phase.

3.3.3 Xenograft mouse model

The human colon adenocarcinoma cells, LS174T, were trypsinized for 2 minutes, collected, and washed with PBS under 1000 rpm x 2 minutes. The washed cells (5×10^6 cells) were resuspended in a mixture of 50 μl of PBS and 50 μl of matrigel medium (Invitrogen, Carlsbad, California), and then injected subcutaneously into the dorsal surface (back) of female Athymic Nu/Nu nude mice (National Cancer Institute at Frederick, Frederick, MD) that were 4 to 6 weeks of age. The resultant tumor implants on the xenograft mice were allowed to grow for approximately two weeks, reaching a tumor implant volume of up to 300 mm^3. The xenograft mice used in this preliminary study were not pretreated with an oral saturated solution of potassium iodide (SSKI).

3.3.4 ^{124}I-HuCC49ΔCH2 and ^{18}F-FDG administration

Two xenograft mice were successfully injected intravenously (i.v.), by way of tail vein injection, with ^{124}I -HuCC49ΔC$_H$2, at a dose of 0.6 MBq and 0.75 MBq, respectively. Two additional xenograft mice were successfully injected intraperitoneally (i.p.) with ^{124}I-HuCC49ΔC$_H$2, at a dose of 1.4 MBq and 2.5 MBq, respectively. As a control, one xenograft mouse was successfully injected i.v., by way of tail vein injection, with 7.4 MBq of ^{18}F-FDG.

3.3.5 MicroPET tumor imaging

Selection of imaging time points was based on historical data as well as the physical half-lives of ^{18}F (110 minutes) and ^{124}I (4.2 days). For ^{18}F-FDG, the standard accepted injection to scan time for humans and small animals is approximately 60±10 minutes [67-69]. For ^{124}I-HuCC49ΔC$_H$2 injected xenograft mice, we used an initial 1 hour time point for baseline microPET imaging as well as a time range of delayed microPET imaging

from 18 hours to 24 hours after administration of ^{124}I-HuCC49ΔC$_H$2 to allow for distribution, uptake, and clearance. At selected time points (ranging from approximately 1 hour to 24 hours after injection of ^{124}I-HuCC49ΔC$_H$2), the xenograft mice were anesthetized with i.p. Ketamine (100 mg/kg)/Xylazine (10 mg/kg) and then scanned on an Inveon microPET scanner (Siemens Medical Solutions, Knoxville, TN). Image acquisition and analysis were performed by using Inveon Acquisition Workplace (Siemens Medical Solutions, Knoxville, TN). Xenograft mice initially underwent a transmission scan with a cobalt-57 source for 402 seconds for attenuation correction and quantification. Xenograft mice then underwent a PET emission scan at approximately 1 hour, 18 hours, and 20 hours after injection of ^{124}I-HuCC49ΔC$_H$2 with an acquisition time of 400 seconds and again at approximately 23 hours or 24 hours after injection of ^{124}I-HuCC49ΔC$_H$2 with an acquisition time of 800 seconds. For the ^{18}F-FDG injected xenograft mouse, a PET emission scan was obtained at approximately 50 minutes after injectionof ^{18}F-FDG with an acquisition time of 400 seconds. The energy window of all PET emission scans was set to 350 keV to 650 keV, with a time resolution of 3.4 ns. Each emission acquisition data set was attenuation corrected with the attenuation transmission scan taken of each individual mouse at each designated time point and arranged into sinograms. The resultant sinograms were iteratively reconstructed into three dimensional volumes using an ordered-subset expectation maximization (OSEM) reconstruction algorithm. The transmission acquisition yielded an approximation of body volume and anatomic localization, such that regions of interest (ROI) could be created to represent portions of the mouse anatomy, specifically, whole body, the LS174T tumor implant, and a designated background area (i.e., left lower quadrant of the abdomen).

The ROI, for determination of tumor implant volume, was drawn manually by qualitative assessment to cover the entire tumor implant volume by summation of voxels using the Inveon software (Siemens Medical Solutions, Knoxville, TN) in a manner similar to that previously published by Jensen et al [69]. In the study by Jensen et al, they compared the accuracy of xenograft measurement by *in vivo* caliper measurement versus microCT-based and microPET-based measurement and found microCT to be the most accurate measurement method [69]. We used a similar method in conjunction with the transmission image to generate the tumor implant volume. PET activity within the volumetric ROI then yielded the resultant average intensity counts for the tumor implant and for the designated background area. Finally, to generate a quantification measurement value for the activity of ^{124}I-HuCC49ΔC$_H$2 within the tumor implant and a measurement value for the activity of ^{18}F-FDG within the tumor implant, we utilized the unitless value of the relative ratio of the average intensity counts, as determined by dividing the average intensity counts from the tumor implant volume by the average intensity counts of the designated background area.

Fused microPET/CT imaging was obtained on one of the five xenograft mice. We imaged this xenograft mouse on the combined microPET/CT system in order to correlate anatomy with the transmission images and assist in accurate determination of tumor implant volume from the transmission scan.

3.3.6 Statistical analysis

The software program IBM SPSS® 18 for Windows® (SPSS, Inc., Chicago, Illinois) was used for the data analysis. One-way analysis of variance (ANOVA) was utilized for the comparison of the relative ratio of intensity counts of the LS174T tumor implants.

3.4 Results

After chromatographic purification, 98% of ^{124}I was bound to the chelated HuCC49ΔC$_H$2 antibody, as determined by thin layer chromatography. The radioactivity of ^{124}I-HuCC49ΔC$_H$2 obtained was 15 MBq/ml.

Figure 3.1a and 3.1b show the xenograft mice injected i.v. with ^{124}I-HuCC49ΔC$_H$2 at a dose of 0.6 MBq and 0.75 MBq, respectively. At approximately 1 hour after i.v. injection, ^{124}I-HuCC49ΔC$_H$2 was distributed within the systemic circulation, and demonstrated no significant localization within the LS174T tumor implants. At the time points of 18 hours and 23 hours after i.v. injection, ^{124}I-HuCC49ΔC$_H$2 was found to have specific localization within the LS174T tumor implants. The thyroid showed expected uptake of ^{124}I, secondary to the lack of pre-treatment with SSKI. The bladder exhibited accumulation of ^{124}I, indicating the degradation of ^{124}I-HuCC49ΔC$_H$2 and the excretion of free ^{124}I into the urine.

Figure 3.2a and 3.2b show the xenograft mice injected i.p. with ^{124}I-HuCC49ΔC$_H$2 at a dose of 1.4 MBq and 2.5 MBq, respectively. At approximately 1 hour after i.p. injection, ^{124}I-HuCC49ΔC$_H$2 was distributed only within the peritoneal cavity, and demonstrated no significant localization within the LS174T tumor implants. At the time points of 20 hours and 24 hours after i.p. injection, ^{124}I-HuCC49ΔC$_H$2 was found to have specific localization within the LS174T tumor implants. The thyroid showed expected uptake of ^{124}I, secondary to the lack of pre-treatment with SSKI. The bladder exhibited accumulation of ^{124}I, indicating the degradation of ^{124}I-HuCC49ΔC$_H$2 and the excretion of free ^{124}I into the urine. ^{124}I-HuCC49ΔC$_H$2 was also observed to accumulate within the liver on the microPET images and was most pronounced at the time points of 20 hours

and 24 hours after i.p. injection of ^{124}I-HuCC49ΔC$_H$2 at a dose of 2.5 MBq. This was presumed to be secondary to use of the chelated form of the HuCC49ΔC$_H$2 antibody.

Figure 3.3 shows the xenograft mouse injected i.v. with 7.4 MBq of ^{18}F-FDG and imaged by the microPET at approximately 50 minutes after injection. Multiple sites of tumor-nonspecific ^{18}F-FDG accumulation were noted in the xenograft mouse. ^{18}F-FDG was noted to avidly accumulate in the heart and the Harderian glands of the eye orbits, secondary to the high rate glucose metabolism within these tissues. ^{18}F-FDG was noted to accumulate in the neck muscles, secondary to procedural handling of the neck region of the mouse. ^{18}F-FDG was noted to be rapidly eliminated from kidneys and bladder within 50 minutes after the i.v. injection. Only very minimal localization of ^{18}F-FDG to the LS174T tumor implant was noted in the xenograft mouse model.

To generate a quantification measurement value for the localization of ^{124}I-HuCC49ΔC$_H$2 within the LS174T tumor implant and a quantification measurement value for the localization of ^{18}F-FDG within the LS174T tumor implant, we utilized the unitless value of the relative ratio of the average intensity counts, as determined by dividing the average intensity counts of the LS174T tumor implant by the average intensity counts of the designated background area. For comparing the localization of ^{124}I-HuCC49ΔC$_H$2 within the LS174T tumor implants at approximately 1 hour after injection versus at 18 hours to 24 hours after injection, the mean relative ratio of the average intensity counts was determined to be 0.34 (SD ±0.29, range 0.06 to 0.64, n=4) at approximately 1 hour after injection, as compared to 2.58 (SD ±0.99, range 1.57 to 4.57, n=8) at 18, 20, 23, and 24 hours after injection (p=0.001). For comparing the localization of ^{124}I-HuCC49ΔC$_H$2 within the LS174T tumor implants for the i.v. injection route versus the i.p. injection

route, the mean relative ratio of the average intensity counts was determined to be 2.31 (SD ±0.71, range 1.83 to 3.356, n=4) for the i.v. injection route at 18 and 23 hours after injection, as compared to 2.85 (SD ±1.26, range 1.57 to 4.57, n=4) for the i.p. injection route at 20 hours and 24 hours after injection (p=0.481). For comparing the localization of ^{124}I-HuCC49ΔC_H2 within the LS174T tumor implants at differing dosages of ^{124}I-HuCC49ΔC_H2, the mean relative ratio of the average intensity counts was determined to be 2.03 (SD ±0.14, range 1.93 to 2.13, n=2) at the lowest dose administered (i.e., 0.6 MBq), as compared to 3.70 (SD ±1.23, range 2.84 to 4.57, n=2) at the highest dose administered (i.e., 2.5 MBq) (p=0.195). It is probable that both the comparison of the localization of ^{124}I-HuCC49ΔC_H2 within the LS174T tumor implants by the injection route (i.e., i.v. versus i.p.) and by the injection dose (i.e., 0.6 MBq versus 2.5 MBq) did not reach statistical significance secondary to the statistic restraints of the small sample size in our current preliminary study in which we used only four ^{124}I-HuCC49ΔC_H2 injected xenograft mice and one ^{18}F-FDG injected xenograft mouse. Finally, for comparing the localization of ^{124}I-HuCC49ΔC_H2 versus ^{18}F-FDG within the LS174T tumor implants, the mean relative ratio of the average intensity counts was 2.58 (SD ±0.99, range 1.57 to 4.57, n=8) for ^{124}I-HuCC49ΔC_H2 at 18, 20, 23, and 24 hours after injection, as compared to 1.05 (n=1) for ^{18}F-FDG at approximately 50 minutes after injection (p=0.188). Although this demonstrates that there was 2.46 times greater localization of ^{124}I-HuCC49ΔC_H2 within LS174T tumor implants as compared to ^{18}F-FDG, this particular p-value similarly did not reach statistical significance, and this is likely attributable to the statistic restraints of comparing only one time point for a single

^{18}F-FDG injected xenograft mouse to that of 8 time points for 4 xenograft mice injected with ^{124}I-HuCC49ΔC$_H$2.

3.5 Discussion

In current study, ^{124}I-HuCC49ΔC$_H$2 demonstrated a significantly increased level of specific localization to LS174T tumor implants as compared to background tissues (p=0.001) in the xenograft mouse model at 18 hours to 24 hours after injection as compared to at approximately 1 hour after injection. In contrast, in the same xenograft mouse model, ^{18}F-FDG failed to demonstrate any increased level of specific localization to a LS174T tumor implant as compared to background tissues at approximately 50 minutes after injection. This re-enforces the limitations of an ^{18}F-FDG-based PET imaging strategy as compared to an antigen-directed and cancer-specific ^{124}I-HuCC49ΔC$_H$2-based PET imaging strategy.

In the current preliminary report, both i.v. and i.p. administration of ^{124}I-HuCC49ΔC$_H$2 resulted in specific localization on microPET imaging to the LS174T tumor implants in the xenograft mouse model at 18 and 23 hours and at 20 and 24 hours after injection, respectively, validating the use of both injection routes for use in preclinical animal studies evaluating ^{124}I-HuCC49ΔC$_H$2. Therefore, the end result of the transport of ^{124}I-HuCC49ΔC$_H$2 from the peritoneal cavity to the LS174T tumor implants after i.p. administration was similar to the transport of ^{124}I-HuCC49ΔC$_H$2 from the systemic circulation to LS174T tumor implants after i.v. administration. These results with ^{124}I-HuCC49ΔC$_H$2 are consistent with previous studies which have demonstrated the efficacy of i.p. administered anti-TAG-72 monoclonal antibodies in patients with

78

colorectal cancer [81,98]. Although not statistically significant secondary to the small sample size in our current preliminary study, it appeared that localization of ^{124}I-HuCC49ΔC$_H$2 within the LS174T tumor implants was augmented by the i.p. injection route and by a higher dose of ^{124}I-HuCC49ΔC$_H$2. Yet, these factors are somewhat difficult to sort out since the i.p. doses administered in our current preliminary study were higher than the i.v. doses administered.

Overall, these preliminary results in the LS174T colon adenocarcinoma xenograft mouse model are very encouraging and lay the ground work for further investigations into the use of this antigen-directed and cancer-specific ^{124}I-radiolabeled anti-TAG-72 monoclonal antibody conjugate in human clinical trials related to preoperative, intraoperative, and postoperative PET-based imaging strategies [72]. Such an approach that utilizes PET-based imaging in conjunction with ^{124}I-HuCC49ΔC$_H$2 is clinically feasible and could potentially have a significant impact upon the current management of colorectal cancer, as well as upon other TAG-72 antigen-expressing adenocarcinomas.

Despite the promising results of our current preliminary report that clearly show that the ^{124}I-radiolabled anti-TAG-72 monoclonal antibody conjugate, ^{124}I-HuCC49ΔC$_H$2, shows high degree of specific localization to TAG-72 antigen expressing tumor implants in the xenograft mouse model, there are several shortcomings of our current experimental study design which led to non-optimization of our reported results and that will need to be further addressed in future experiments. These shortcomings are the lack of thyroid block by oral administration of SSKI, the use of the chelated form of the HuCC49ΔC$_H$2 antibody, and the limited availability of the microCT scanner at the time of these

preliminary experiments for obtaining fused microPET/CT imaging of all the xenograft mice studied.

First, as is shown in Figures 3.1a, 3.1b, 3.2a, and 3.2b, significant thyroid uptake was seen on microPET imaging at the time points of 18 hours and 23 hours after i.v. injection and at the time points of 20 hours and 24 hours after i.p. injection of ^{124}I-HuCC49ΔC$_H$2. It has long been well-known in the nuclear medicine literature that if the thyroid is not blocked by the oral administration of SSKI, then resultant thyroid uptake of circulating radioactive iodine will freely occur [73-75]. This has been previously experimentally evaluated with radioiodine labeled anti-TAG-72 monoclonal antibodies [76]. As such, in the current animal experiments, the lack of thyroid blockade resulted in significant thyroid uptake of free ^{124}I as the unbound ^{124}I-HuCC49ΔC$_H$2 was metabolized in the body and before the free circulating ^{124}I was excreted into the urine. Therefore, pre-treatment of the xenograft mice with oral administration of SSKI to minimize thyroid uptake of free ^{124}I would have resulted in more optimal microPET imaging, thus better illustrating our take-home message of specific localization of ^{124}I-HuCC49ΔC$_H$2 to LS174T tumor implants by minimizing the degree of thyroid localization of free ^{124}I. This shortcoming was an oversight on our part and will be subsequently re-addressed in future xenograft mouse model experiments in which the xenograft mice are pretreated with oral SSKI.

Second, nonspecific liver uptake of ^{124}I-HuCC49ΔC$_H$2 was seen on microPET imaging. As best illustrated in Figure 3.2b, significant nonspecific liver uptake was most pronounced at the time points of 20 hours and 24 hours after i.p. administration of the higher dose (2.5 MBq) of ^{124}I-HuCC49ΔC$_H$2. This nonspecific liver uptake was less

80

intense on microPET imaging at the time points of 20 hours and 24 hours after i.p. administration of a lower dose (1.4 MBq) of ^{124}I-HuCC49ΔC$_H$2 (Figure 3.2a) and was minimally present on microPET imaging at the time points of 18 hours and 23 hours after i.v. administration of either dose (0.6 MBq or 0.75 MBq) of ^{124}I-HuCC49ΔC$_H$2 (Figure 3.1a and Figure 3.1b). A similar pattern of accumulation within the liver has been previously reported for various chelated radiolabeled CC49 monoclonal antibodies [77], as well as for a single-chain Fv version of the radiolabeled CC49 monoclonal antibody [78]. It has been suggested that the high accumulation of these radiolabeled monoclonal antibody in the liver is likely due to the metabolism of the chelated form of the antibody within the liver [77]. Clearance and metabolism of IgG antibodies occurs predominantly through the reticuloendothelial system (RES), primarily in the liver and spleen, which both contain Kupffer cells [77,78]. Furthermore, IgG antibodies are bound and internalized by asialoglycoprotein receptors in the liver cells, increasing the retention of IgG antibodies within the liver. Therefore, it is our contention that the nonspecific liver uptake of ^{124}I-HuCC49ΔC$_H$2 seen on microPET imaging is explainable by our use of chelated form of the HuCC49ΔC$_H$2 antibody. It should be noted that our inadvertent use of the chelated form of the HuCC49ΔC$_H$2 antibody was not recognized until after analysis of the microPET imaging, as is best exemplified at the time points of 20 hours and 24 hours after i.p. administration of 2.5 MBq of ^{124}I-HuCC49ΔC$_H$2. Therefore, use of the non-chelated form of the HuCC49ΔC$_H$2 antibody would have potentially eliminated the nonspecific liver uptake of ^{124}I-HuCC49ΔC$_H$2, thus better illustrating our take-home message of specific localization of ^{124}I-HuCC49ΔC$_H$2 to LS174T tumor implants. This shortcoming was an oversight on our part and will be subsequently re-

addressed in future xenograft mouse model experiments in which the non-chelated form of the HuCC49ΔC$_H$2 antibody is utilized.

Third, at the time of this preliminary experiment, there was limited availability of the microCT scanner for obtaining fused microPET/CT imaging of all the xenograft mice. Therefore, while all five xenograft mice were imaged by the dedicated microPET scanner, only one xenograft mouse (i.v. injection of [124]I-HuCC49ΔC$_H$2 at a dose of 0.75 MBq) was also imaged with the microCT scanner, thus allowing for reconstruction of fused microPET/CT images. An example of a preliminary image that was generated using a fused microPET/CT imaging platform is shown in Figure 3.4. It is evident within the molecular imaging literature that fused-modality PET-based imaging is superior to PET alone-based imaging, both within the PET/CT platform and the PET/ MRI platform [72,79-82]. These fused imaging platforms can provide both molecular/functional information and structural information that can more accurately and more precise localize various disease processes. It is our intention to subsequently re-address this shortcoming in future xenograft mouse model experiments by utilizing a fused microPET/CT imaging platform.

3.6 Conclusions

On microPET imaging, [124]I-HuCC49ΔC$_H$2 demonstrates an increased level of specific localization to tumor implants of LS174T colon adenocarcinoma cells as compared to background tissues in the xenograft mouse model, while [18]F-FDG failed to demonstrate this same finding. Clearly, a PET-based imaging approach that utilizes [124]I-HuCC49ΔC$_H$2 is feasible and could potentially have a significant impact upon the current

management of colorectal cancer and other TAG-72 antigen-expressing adenocarcinomas. This antigen-directed and cancer-specific [124]I-radiolabled anti-TAG-72 monoclonal antibody conjugate has great potential for use in human clinical trials for preoperative, intraoperative, and postoperative PET-based imaging strategies, including fused-modality PET-based imaging platforms.

3.7 References

1. Brownell G.L., *A history of positron imaging*. 1999 [http://www.mit.edu/~glb/].
2. Chesler D.A., *Three-dimensional activity distribution from multiple positron scintigraphs*. J Nucl Med 1971, **12**:347-348.
3. Ter-Pogossian M.M., Phelps M.E., Hoffman E.J., Mullani N.A., *A positron-emission transaxial tomograph for nuclear imaging (PETT)*. Radiology 1975, **114**:89-98.
4. Hoffmann E.J., Phelps M.E., Mullani N.A., Higgins C.S., Ter-Pogossian M.M., *Design and performance characteristics of a whole-body positron transaxial tomograph*. J Nucl Med 1976, **17**:493-502.
5. Hoh C.K., Schiepers C., Seltzer M.A., Gambhir S.S., Silverman D.H., Czernin J., Maddahi J., Phelps M.E., *PET in oncology: will it replace the other modalities?* Semin Nucl Med 1997, **27**:94-106.
6. Otsuka H., Graham M., Kubo A., Nishitani H., *Clinical utility of FDG PET*. J Med Invest 2004, **51**:14-19.
7. Endo K., Oriuchi N., Higuchi T., Iida Y., Hanaoka H., Miyakubo M., Ishikita T., Koyama K., *PET and PET/CT using 18F-FDG in the diagnosis and management of cancer patients*. Int J Clin Oncol 2006, **11**:286-296.
8. Maldonado A., González-Alenda F.J., Alonso M., Sierra J.M., *PET-CT in clinical oncology*. Clin Transl Oncol 2007, **9**:494-505.
9. Otsuka H., Morita N., Yamashita K., Nishitani H., *FDG-PET/CT for cancer management*. J Med Invest 2007, **54**:195-199.
10. Poeppel T.D., Krause B.J., Heusner T.A., Boy C., Bockisch A., Antoch G., *PET/CT for the staging and follow-up of patients with malignancies*. Eur J Radiol 2009, **70**:382-92.
11. Vriens D., de Geus-Oei L.F., van der Graaf W.T., Oyen W.J., *Tailoring therapy in colorectal cancer by PET-CT*. Q J Nucl Med Mol Imaging 2009, **53**:224-244.
12. Kumar R., Dhanpathi H., Basu S., Rubello D., Fanti S., Alavi A., *Oncologic PET tracers beyond [(18)F]FDG and the novel quantitative approaches in PET imaging*. Q J Nucl Med Mol Imaging 2008, **52:**50-65.
13. Dunphy M.P., Lewis J.S., *Radiopharmaceuticals in preclinical and clinical development for monitoring of therapy with PET*. J Nucl Med 2009, **50**(Suppl 1):106S-121S.

14. Murphy PS, Bergström M: Radiopharmaceuticals for oncology drug development: a pharmaceutical industry perspective. Curr Pharm Des 2009, 15:957-965.
15. Larson S.M., Schoder H., *New PET tracers for evaluation of solid tumor response to therapy*. Q J Nucl Med Mol Imaging 2009, **53**:158-166.
16. Vallabhajosula S., *(18)F-labeled positron emission tomographic radiopharmaceuticals in oncology: an overview of radiochemistry and mechanisms of tumor localization*. Semin Nucl Med 2007, **37**:400-419.
17. Pauwels E.K., Ribeiro M.J., Stoot J.H., McCready V.R., Bourguignon M., Mazière B., *FDG accumulation and tumor biology*. Nucl Med Biol 1998, **25**:317-322.
18. Shields A.F., Grierson J.R., Dohmen B.M., Machulla H.J., Stayanoff J.C., *Lawhorn-Crews JM, Obradovich JE, Muzik O, Mangner TJ: Imaging proliferation in vivo with [F-18]FLT and positron emission tomography*. Nat Med 1998, **4**:1334-1336.
19. Lind P., Igerc I., Beyer T., Reinprecht P., Hausegger K., *Advantages and limitations of FDG PET in the follow-up of breast cancer.* Eur J Nucl Med Mol Imaging 2004, **31** (Suppl 1):S125-S134.
20. Lim H.S., Yoon W., Chung T.W., Kim J.K., Park J.G., Kang H.K., Bom H.S., Yoon J.H., *FDG PET/CT for the detection and evaluation of breast diseases: usefulness and limitations.* Radiographics 2007, **27**(Suppl 1):S197-S213.
21. Metser U., Even-Sapir E., *Increased (18)F-fluorodeoxyglucose uptake in benign, nonphysiologic lesions found on whole-body positron emission tomography/computed tomography (PET/CT): accumulated data from four years of experience with PET/CT.* Semin Nucl Med 2007, **37**:206-222.
22. Sun D., Bloomston M., Hinkle G., Al-Saif O.H., Hall N.C., Povoski S.P., Arnold M.W., Martin E.W., *Radioimmunoguided surgery (RIGS), PET/CT image-guided surgery, and fluorescence image-guided surgery: past, present, and future.* J Surg Oncol 2007, **96**:297-308.
23. Schöder H., Moskowitz C., *PET imaging for response assessment in lymphoma: potential and limitations*. Radiol Clin North Am 2008, **46**:225-241.
24. Povoski S.P., Neff R.L., Mojzisik C.M., O'Malley D.M., Hinkle G.H., Hall N.C., Murrey D.A. Jr, Knopp M.V., Martin E.W. Jr: *A comprehensive overview of radioguided surgery using gamma detection probe technology.* World J Surg Oncol 2009, **7**:11.
25. Horan Hand P., Colcher D., Salomon D., Ridge J., Noguchi P., Schlom J., *Influence of spatial configuration of carcinoma cell populations on the expression of a tumor-associated glycoprotein*. Cancer Res 1985, **45**:833-840.
26. Johnson V.G., Schlom J., Paterson A.J., Bennett J., Magnani J.L., Colcher D., *Analysis of a human tumor-associated glycoprotein (TAG-72) identified by monoclonal antibody B72.3.* Cancer Res 1986, **46**:850-857.
27. Sheer D.G., Schlom J., Cooper H.L., *Purification and composition of the human tumor-associated glycoprotein (TAG-72) defined by monoclonal antibodies CC49 and B72.3.* Cancer Res 1988, **48**:6811-6818.
28. Tom B.H., Rutzky L.P., Jakstys M.M., Oyasu R., Kaye C.I., Kahan B.D., *Human colonic adenocarcinoma cells. I. Establishment and description of a new line*. In Vitro 1976, **12**:180-191.

29. Tom B.H., Rutzky L.P., Oyasu R., Tomita J.T., Goldenberg D.M., Kahan B.D., *Human colon adenocarcinoma cells. II. Tumorigenic and organoid expression in vivo and in vitro.* J Natl Cancer Inst 1977, **58**:1507-1512.

30. Colcher D., Keenan A.M., Larson S.M., Schlom J., *Prolonged binding of a radiolabeled monoclonal antibody (B72.3) used for the in situ radioimmunodetection of human colon carcinoma xenografts*. Cancer. Res. 1984, **44**:5744-5749.

31. Colcher D., Minelli M.F., Roselli M., Muraro R., Simpson-Milenic D., Schlom J., *Radioimmunolocalization of human carcinoma xenografts with B72.3 second generation monoclonal antibodies*. Cancer Res 1988, **48**:4597-4603.

32. Sickle-Santanello B.J., O'Dwyer P.J., Mojzisik C., Tuttle S.E., Hinkle G.H., Rousseau M., Schlom J., Colcher D., Thurston M.O., Nieroda C., Sardi A., Farrar W.B., Minton J.P., Martin E.W. Jr, *Radioimmunoguided surgery using the monoclonal antibody B72.3 in colorectal tumors.* Dis Colon Rectum 1987, **30**:761-764.

33. Tuttle S.E., Jewell S.D., Mojzisik C.M., Hinkle G.H., Colcher D., Schlom J., Martin E.W. Jr, *Intraoperative radioimmunolocalization of colorectal carcinoma with a hand-held gamma probe and MAb B72.3: comparison of in vivo gamma probe counts with in vitro MAb radiolocalization.* Int J Cancer 1988, **42**:352-358.

34. Martin E.W. Jr, Mojzisik C.M., Hinkle G.H., Sampsel J., Siddiqi M., Tuttle S.E., Sickle-Santanello B., Colcher D., Thurston M.O., Bell J., Farrar W.B., Schlom J., *Radioimmunoguided surgery using monoclonal antibody*. Am J Surg 1988, **156**:386-392.

35. Nieroda C.A., Mojzisik C., Sardi A., Farrar W.B., Hinkle G., Siddiqi M.A., Ferrara P.J., James A., Schlom J., Thurston M.O., Martin E.W., *Staging of carcinoma of the breast using a hand-held gamma detecting probe and monoclonal antibody B72.3.* Surg Gynecol Obstet 1989, **169**:35-40.

36. Sardi A., Siddiqi M.A., Hinkle G.H., Rousseau M., Gersman M., Hill T., Olsen J., Tuttle S.E., Young D., Houchens D., Thurston M., Martin E.W. Jr, *Localization by hand-held gamma probe of tumor labeled with antibody "cocktail"*. J Surg Res 1989, **47**:227-234.

37. Nieroda C.A., Mojzisik C., Sardi A., Ferrara P., Hinkle G., Thurston M.O., Martin E.W. Jr, *Radioimmunoguided surgery in primary colon cancer.* Cancer Detect Prev 1990, **14:** 651-656.

38. Nieroda C.A., Mojzisik C., Hinkle G., Thurston M.O., Martin E.W. Jr, *Radioimmunoguided surgery (RIGS) in recurrent colorectal cancer.* Cancer Detect Prev 1991, **15**:225-229.

39. Cohen A.M., Martin E.W. Jr, Lavery I., Daly J., Sardi A., Aitken D., Bland K., Mojzisik C., Hinkle G., *Radioimmunoguided surgery using iodine 125 B72.3 in patients with colorectal cancer*. Arch Surg 1991, **126:**349-352.

40. Martin E.W. Jr, Carey L.C., *Second-look surgery for colorectal cancer. The second time around*. Ann Surg 1991, **214**:321-325.

41. Arnold M.W., Schneebaum S., Berens A., Petty L., Mojzisik C., Hinkle G., Martin E.W. Jr, *Intraoperative detection of colorectal cancer with radioimmunoguided surgery and CC49, a second-generation monoclonal antibody.* Ann Surg 1992, **216**:627-632.

42. Arnold M.W., Schneebaum S., Berens A., Mojzisik C., Hinkle G., Martin E.W. Jr, *Radioimmunoguided surgery challenges traditional decision making in patients with primary colorectal cancer.* Surgery 1992, **112:**624-629.

43. Schneebaum S., Arnold M.W., Houchens D.P., Greenson J.K., Cote R.J., Hitchcock C.L., Young D.C., Mojzisik C.M., Martin E.W. Jr, *The significance of intraoperative periportal lymph node metastasis identification in patients with colorectal carcinoma.* Cancer 1995, **75**:2809-2817.

44. Bertsch D.J., Burak W.E., Young D.C., Arnold M.W., Martin E.W. Jr, *Radioimmunoguided surgery improves survival for patients recurrent colorectal cancer.* Surgery 1995, **118**:634-638.

45. Arnold M.W., Young D.C., Hitchcock C.L., Schneebaum S., Martin E.W. Jr, *Radioimmunoguided surgery in primary colorectal carcinoma: an intraoperative prognostic tool and adjuvant to traditional staging.* Am J Surg 1995, **170**:315-318.

46. Cote R.J., Houchens D.P., Hitchcock C.L., Saad A.D., Nines R.G., Greenson J.K., Schneebaum S., Arnold M.W., Martin E.W. Jr, *Intraoperative detection of occult colon cancer micrometastases using 125 I-radiolabled monoclonal antibody CC49.* Cancer 1996, **77**:613-620.

47. Arnold M.W., Hitchcock C.L., Young D.C., Burak W.E. Jr, Bertsch D.J., Martin E.W. Jr, *Intra-abdominal patterns of disease dissemination in colorectal cancer identified using radioimmunoguided surgery.* Dis Colon Rectum 1996, **39**:509-513.

48. Bertsch D.J., Burak W.E. Jr, Young D.C., Arnold M.W., Martin E.W. Jr, *Radioimmunoguided surgery for colorectal cancer.* Ann Surg Oncol 1996, **3:**310-316.

49. Martinez D.A., Barbera-Guillem E., LaValle G.J., Martin E.W. Jr, *Radioimmunoguided surgery for gastrointestinal malignancies: an analysis of 14 years of clinical experience*. Cancer Control 1997, **4**:505-516.

50. Martin E.W. Jr, Thurston M.O., *Intraoperative radioimmunodetection.* Semin Surg Oncol 1998, **15**:205-208.

51. Bakalakos E.A., Young D.C., Martin E.W. Jr, *Radioimmunoguided surgery for patients with liver metastases secondary to colorectal cancer*. Ann Surg Oncol 1998, **5**:590-594.

52. Arnold M.W., Young D.M., Hitchcock C.L., Barberá-Guillem E., Nieroda C., Martin E.W. Jr, *Staging of colorectal cancer: biology vs. morphology.* Dis Colon Rectum 1998, **41**:1482-1487

53. Schneebaum S., Troitsa A., Avital S., Haddad R., Kashtan H., Gitstein G., Baratz M., Brazovsky E., Papo J., Skornick Y., *Identification of lymph node metastases in recurrent colorectal cancer.* Recent Results Cancer Res 2000, **157**:281-292.

54. Avital S., Haddad R., Troitsa A., Kashtan H., Brazovsky E., Gitstein G., Skornick Y., Schneebaum S., *Radioimmunoguided surgery for recurrent colorectal cancer manifested by isolated CEA elevation*. Cancer 2000, **89**:1692-1698.

55. Schneebaum S., Troitsa A., Haddad R., Avital S., Kashtan H., Baratz M., Brazovsky E., Papo J., Skornick Y., *Immunoguided lymph node dissection in colorectal cancer: a new challenge?* World J Surg 2001, **25**:1495-1498.

56. Haddad R., Avital S., Troitsa A., Chen J., Baratz M., Brazovsky E., Gitstein G., Kashtan H., Skornick Y., Schneebaum S., Benefits *of radioimmunoguided surgery for pelvic recurrence. Eur J Surg Oncol 2001, **27**:298-301.*

57. Agnese D.M., Abdessalam S.F., Burak W.E., Arnold M.W., Soble D., Hinkle G.H., Young D., Kazaeli M.B., Martin E.W. Jr, *Pilot study using a humanized CC49 monoclonal antibody (HuCC49ΔC$_H$2) to localize recurrent colorectal carcinoma.* Ann Surg Oncol 2004, **11:**197-202.

58. Xiao J., Horst S., Hinkle G., Cao X., Kocak E., Fang J., Young D., Khazaeli M., Agnese D., Sun D., Martin E.W. Jr, *Pharmacokinetics and clinical evaluation of 125I-radiolabeled humanized CC49 monoclonal antibody (HuCC49ΔC(H)2) in recurrent and metastatic colorectal cancer patients.* Cancer Biother Radiopharm 2005, **20**:16-26.

59. Fang L., Holford N.H., Hinkle G., Cao X., Xiao J.J., Bloomston M., Gibbs S., Saif O.H., Dalton J.T., Chan K.K., Schlom J., Martin E.W. Jr, Sun D., *Population pharmacokinetics of humanized monoclonal antibody HuCC49ΔCH2 and murine antibody CC49 in colorectal cancer patients.* J Clin Pharmacol 2007, **47**:227-237.

60. Calvo B., Kashmiri S.V., Hutzell P., Hand P.H., Slavin-Chiorini D.C., Schlom J., Zaremba S., *Construction and purification of domain-deleted immunoglobulin variants of the recombinant/chimeric B72.3 (y1) monoclonal antibody.* Cancer Biother 1993, **8:**95-109.

61. Slavin-Chiorini D.C., Horan Hand P.H., Kashmiri S.V., Calvo B., Zaremba S., Schlom J., *Biologic properties of a CH2 domain-deleted recombinant immunoglobulin.* Int J Cancer 1993, **53**:97-103.

62. Slavin-Chiorini D.C., Kashmiri S.V., Schlom J., Calvo B., Shu L.M., Schott M.E., Milenic D.E., Snoy P., Carrasquillo J., Anderson K., Horan Hand P., *Biological properties of chimeric domain-deleted anticarcinoma immunoglobulins.* Cancer Res 1995, **55(23 Suppl)**:5957s-5967s.

63. Slavin-Chiorini D.C., Kashmiri S.V., Lee H.S., Milenic D.E., Poole D.J., Bernon E., Schlom J., Hand P.H., *A CDR-grafted (humanized) domain-deleted antitumor antibody.* Cancer Biother Radiopharm 1997, **12**:305-316.

64. Pentlow K.S., Graham M.C., Lambrecht R.M., Daghighian F., Bacharach S.L., Bendriem B., Finn R.D., Jordan K., Kalaigian H., Karp J.S., Robeson W.R., Larson S.M., *Quantitative imaging of iodine-124 with PET.* J Nucl Med 1996, **37:**1557-1562.

65. Hinkle G.H., Nabi H.A., Miller E.A., Schlanger L.E., Houchens D.P., Thurston M.O., Aitken D.R., Mojzisik C.M., Olsen J.O., Tuttle S.E., Hansen H.J., Haagensen D.E. Jr, Martin E.W. Jr, *Radioimmunodetection of implanted tumors with gamma probe.* NCI Monogr 1987, **3**:83-87.

66. Unak T., Akgün Z., Yildirim Y., Duman Y., Erenel G., *Self-radioiodination of iodogen.* Appl Radiat Isot 2001, **54**:749-752.

67. Shankar L.K., Hoffman J.M., Bacharach S., Graham M.M., Karp J., Lammertsma A.A., Larson S., Mankoff D.A., Siegel B.A., Van den Abbeele A., Yap J., Sullivan D., *Consensus recommendations for the use of 18F-FDG PET as an indicator of therapeutic response in patients in National Cancer Institute Trials.* J Nucl Med 2006,**47**:1059-1066.

68. Dandekar M., Tseng J.R., Gambhir S.S., *Reproducibility of 18F-FDG microPET studies in mouse tumor xenografts.* J Nucl Med 2007, **48**:602-607.

69. Jensen M.M., Jørgensen J.T., Binderup T., Kjaer A., *Tumor volume in subcutaneous mouse xenografts measured by microCT is more accurate and reproducible than*

determined by 18F-FDG-microPET or external caliper. BMC Med Imaging 2008, **8**:16.

70. Colcher D., Esteban J., Carrasquillo J.A., Sugarbaker P., Reynolds J.C., Bryant G., Larson S.M., Schlom J., *Complementation of intracavitary and intravenous administration of a monoclonal antibody (B72.3) in patients with carcinoma*. Cancer Res 1987, **47**:4218-4224.

71. Schlom J., Siler K., Colcher D., Carrasquillo J.A., Reynolds J.C., Sugarbaker P., Larson S.M., *Binding of radiolabeled MAb B72.3 administered intravenously and intraperitoneally in colorectal cancer patients. An overview*. Acta Radiol Suppl 1990, **374**:123-128.

72. Hall N.C., Zhang J., Povoski S.P., Martin E.W., Knopp M.V., *New developments in imaging and functional biomarker technology for the assessment and management of cancer patients*. Expert Rev Med Devices 2009, **6**:347-351.

73. Pochin E.E., Barnaby C.F., *The effect of pharmacological doses of non-radioactive iodide on the course of radio-iodine uptake by the thyroid*. Health Phys 1962, **7**:125-126.

74. Blum M., Eisenbud M., *Reduction of thyroid irradiation from 131-I by potassium iodide*. JAMA 1967, **200**:1036-1040.

75. Meck R.A., Chen M.S., Kenny P.J., *Criteria for the administration of KI for thyroid blocking of radioiodine*. Health Phys 1985, **48**:141-157.

76. Abdel-Nabi H., Waldman W.J., Hinkle G.H., Miller E.A., Trembath L., Olsen J.O., Martin E.W. Jr., *Comparison of L-thyroxine and a saturated solution of potassium iodide in preventing damage to the thyroid following iodine-131-labeled antibody injection*. NCI Monogr 1987, **3**:63-66.

77. Mohsin H., Jia F., Sivaguru G., Hudson M.J., Shelton T.D., Hoffman T.J., Cutler C.S., Ketring A.R., Athey P.S., Simón J., Frank R.K., Jurisson S.S., Lewis M.R., *Radiolanthanide-labeled monoclonal antibody CC49 for radioimmunotherapy of cancer: biological comparison of DOTA conjugates and 149Pm, 166Ho, and 177Lu*. Bioconjug Chem 2006, **17**:485-492.

78. Yokota T., Milenic D.E., Whitlow M., Wood J.F., Hubert S.L., Schlom J., *Microautoradiographic analysis of the normal organ distribution of radioiodinated single-chain Fv and other immunoglobulin forms*. Cancer Res 1993, **53**:3776-3783.

79. Townsend D.W., *Dual-modality imaging: combining anatomy and function*. J Nucl Med 2008, **49**:938-955.

80. Townsend D.W.: *Multimodality imaging of structure and function*. Phys Med Biol 2008, **53**:R1-R39.

81. Pichler B.J., Judenhofer M.S., Pfannenberg C., *Multimodal imaging approaches: PET/CT and PET/MRI*. Handb Exp Pharmacol 2008, **185(Pt 1):**109-32.

82. Cherry S.R., *Multimodality imaging: beyond PET/CT and SPECT/CT*. Semin Nucl Med 2009, **39:**348-353.

Figure 3.1 Intravenous (i.v.) administration of ^{124}I-HuCC49ΔC$_H$2 for microPET imaging of the LS174T xenograft mouse model. ^{124}I- HuCC49ΔC$_H$2 at a dose of 0.6 MBq (Figure 3.1a) and 0.75 MBq Figure 3.1b) was injected i.v. through the tail vein, and micoPET imaging is shown at approximately 1 hour and at 23 hours after injection in coronal, sagittal, and transaxial views.

Figure 3.1a ^{124}I-HuCC49deltaC$_H$2-PET (i.v. 0.6 MBq)
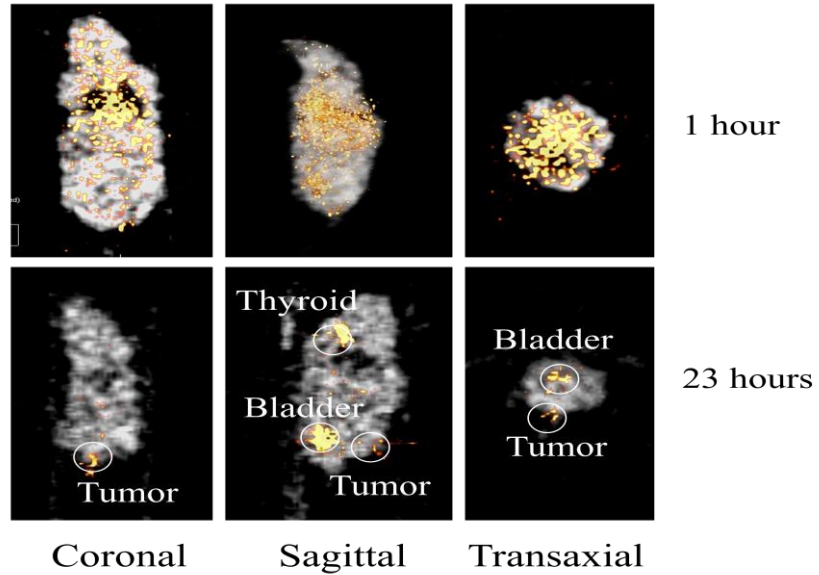
Figure 3.1b ^{124}I-HuCC49deltaC$_H$2-PET (i.v. 0.75 MBq)
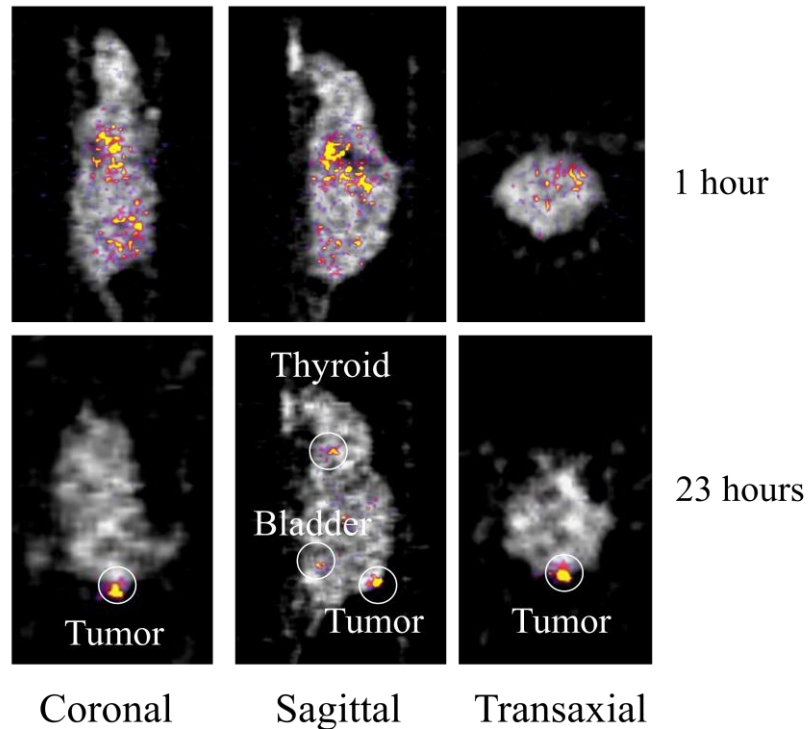
Figure 3.2 Intraperitoneal (i.p.) administration of ^{124}I-HuCC49ΔC$_H$2 for microPET imaging of the LS174T xenograft mouse model. ^{124}I-HuCC49ΔC$_H$2 at a dose of 1.4 MBq (Figure 3.2a) and 2.5 MBq (Figure 3.2b) was injected i.p., and micoPET imaging is shown at approximately 1 hour and at 24 hours after injection in coronal, sagittal, and transaxial views.

Figure 3.2a ^{124}I-HuCC49deltaC$_H$2-PET (i.p. 1.4 MBq)
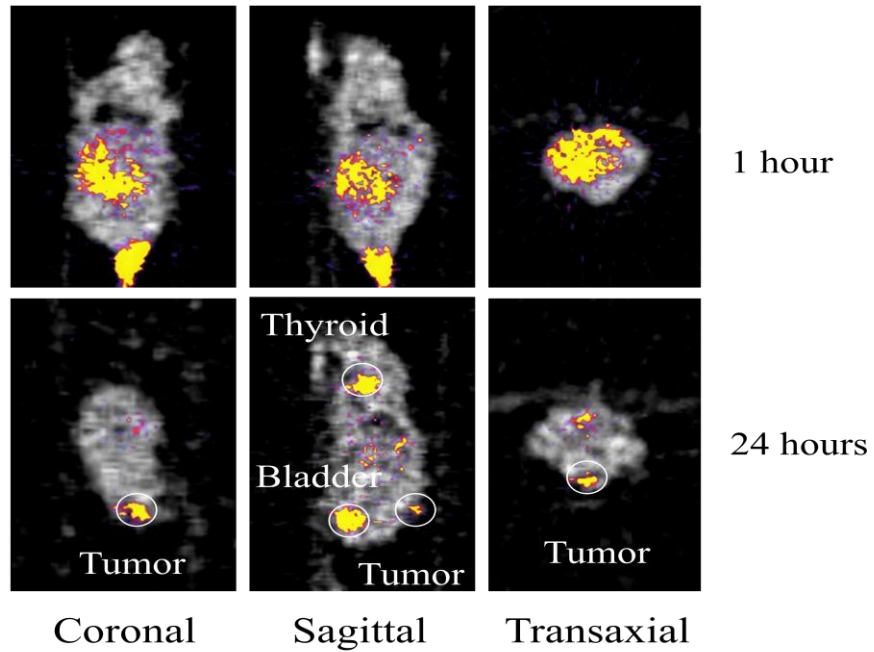
Figure 3.2b ^{124}I-HuCC49deltaC$_H$2-PET (i.p. 2.5 MBq)
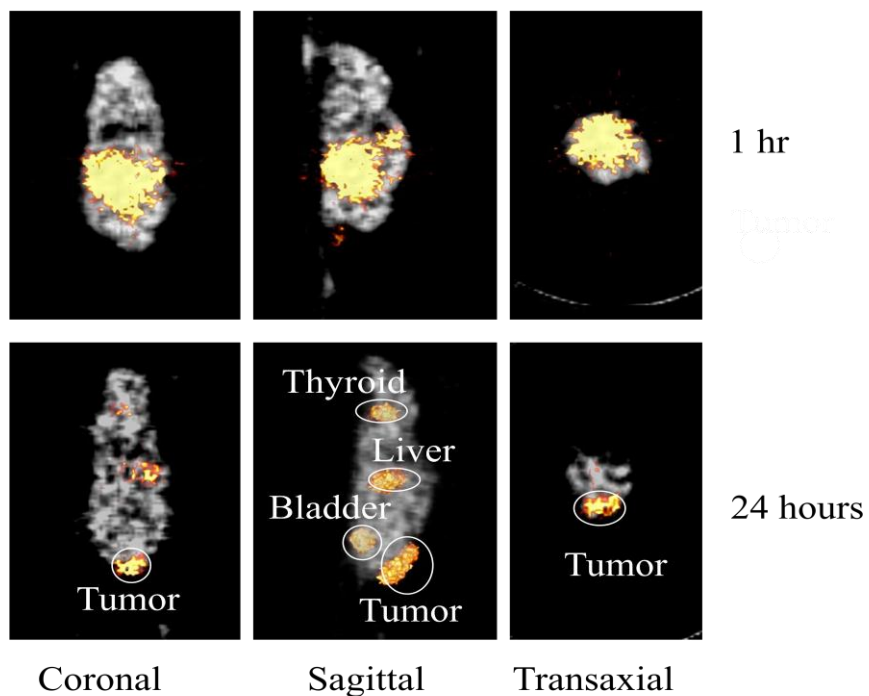
Figure 3.3 Intravenous (i.v.) administration of ^{18}F-FDG for microPET imaging of LS174T xenograft mouse model. ^{18}F-FDG at a dose of 7.4 MBq was injected i.v. through the tail vein. MicroPET imaging is shown at approximately 50 minutes after injection in coronal, sagittal, and transaxial views.

^{18}FDG-PET (i.v. 7.4 MBq)

Coronal   Sagittal   Transaxial
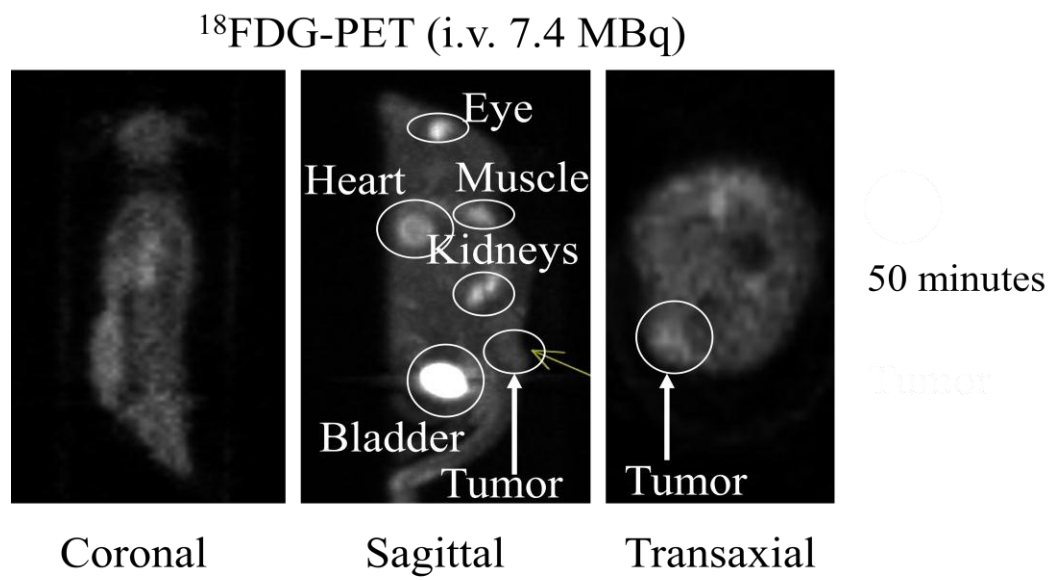
Figure 3.4 Fused microPET/CT image of a xenograft mouse at 26 hours after receiving an intravenous (i.v.) injection of 0.6 MBq of ^{124}I-HuCC49ΔC$_H$2.

CHAPTER IV

Superparamagnetic Iron Oxide "Nanotheranostics" for Targeted Colon Cancer Imaging and pH-Dependent Intracellular Drug Release

4.1 Abstract

Superparamagnetic iron oxide nanoparticles (SPIOs) have emerged as a feasible "nanotheranostics" for tumor imaging and targeted anti-cancer drug delivery. The purpose of this study is to develop antibody- and fluorescence-labeled SPIO "nanotheranostics" for magnetic resonance imaging (MRI) and fluorescence imaging of cancer cells and pH-dependent intracellular drug release. HuCC49ΔC$_H$2 and fluorescent dye 5-FAM were conjugated to SPIOs. Anticancer drugs doxorubicin (Dox), and azido-doxorubicin (Adox), MI-219, 17-DMAG containing primary amine, azide, secondary amine, and tertiary amine, respectively, were entrapped into SPIOs. Fluorescent imaging, magnetic resonance imaging (MRI) and Prussian blue staining demonstrated that HuCC49ΔC$_H$2-SPIO increased cancer cell targeting. HuCC49ΔC$_H$2-SPIO "nanotheranostics" decreased the T_2 values in MRI of LS174T cells from 117.3±1.8 ms to 55.5±2.6 ms. The loading capacities of Dox, Adox, MI-219, and 17-DMAG were 3.16 ± 0.77%, 6.04± 0.61%, 2.22± 0.42%, and 0.09±0.07%, respectively. Dox, MI-219 and 17-DMAG showed pH-dependent release while Adox did not. Fluorescent imaging demonstrated the accumulation of HuCC49ΔC$_H$2-SPIO "nanotheranostics" in endosomes/lysosomes. The entrapped Dox was released in acidic lysosomes and diffused

into cytosol and nuclei. In contrary, the entrapped Adox only showed limited release in endosomes/lysosomes. HuCC49ΔC$_H$2-SPIO "nanotheranostics" targetedly delivered more Dox to LS174T cells than nonspecific IgG-SPIO and resulted in a lower IC$_{50}$ (1.44 µM v.s. 0.44 µM). The developed HuCC49ΔC$_H$2-SPIO "nanotheranostics" provides an integrated platform for cancer cell imaging, targeted anticancer drug delivery and pH-dependently drug release.

4.2 Introduction

One of the major challenges in cancer chemotherapy is the serious side effects caused by cytotoxicity of anticancer drugs. Novel strategies are needed to site-specifically deliver anticancer drugs to tumor cells. Superparamagnetic iron oxide nanoparticles (SPIOs) have emerged as a feasible "nanotheranostics" for tumor imaging and targeted anti-cancer drug delivery[1-20]. SPIOs are a contrast agent for Magnetic Resonance Imaging (MRI) since it induces a shorter T_2 relaxation (transverse or spin-spin relaxation), producing a decreased signal intensity on a T_2-weighted image[21]. Various SPIO products have been clinically used as contrast agents due to their high contrast effects and biocompatibility[22]. The standard water-soluble SPIOs are composed of an iron-oxide magnetic core coated with hydrophobic oleic acid (OA) and a surface of amphiphilic polymers [8]. The surface polymers not only stabilize the nanoparticles, but also provide active functional groups for controllable bioconjugation of targeting ligands. Furthermore, surface coating with biocompatible polymers such as PEG can reduce reticuloendothelial system (RES) uptake of SPIOs as well as non-specific interaction with plasma membranes. It has been demonstrated that the cancer-targeting ligand labeled

SPIOs could specifically bind to cancer cells and accumulate in tumor tissues [1-3, 10, 18].

SPIOs have been utilized as a carrier for targeted drug delivery [1, 2, 6, 8, 20, 23]. Drug molecules were either entrapped in the SPIO surface polymer layer using physical interactions (electrostatic interaction or hydrophobic interaction) or covalently conjugated to the functional groups on SPIO surface for pH dependent release or enzymatic cleavage release in targeted tissues[12, 24]. Doxorubicin (Dox) has been used as a model drug for targeted drug delivery since the hydrophobic compound can partition into the oleic acid shell of SPIOs [8] and its intracellular distribution can be visualized under a fluorescent microscope. Dox has been reported to exhibit pH dependent release from SPIOs[2, 4, 7, 12]. Approximately 60% of the Dox was released within 50 min at pH 5.1 in acetate buffer[1].

The reasons for the rapid release of Dox at low pH are still not clear. One explanation was the protonation of the primary amine of Dox which dramatically increased the solubility of Dox in aqueous solution[2]. Another explanation is the weakened interaction between Dox and the partially neutralized carboxyl groups of polymers or oleic acid [1, 4]. The pH dependent release of Dox suggests that Dox may be rapidly released from SPIOs in acidic environment of tumor tissues or endosomes/lysosomes after internalized into cancer cells.

Ideally, "nanotheranostics" can be used for non-invasive cancer imaging, visualizing drug delivery, assessing the efficiency of targeted drug delivery, and monitoring the therapeutic responses. In this study, we developed a tumor-associated glycoprotein-72 (TAG-72) targeted SPIO "nanotheranostics" for simultaneous MRI and fluorescent

95

imaging of cancer cells and targeted anticancer drug delivery. Our previous studies demonstrated that anti-TAG-72 antibody HuCC49ΔC$_H$2 could specifically bind to TAG-72 expressing LS174T colon cancer cells *in vitro* and *in vivo* [25]. HuCC49ΔC$_H$2 and fluorescent dye 5-FAM were conjugated to the carboxyl groups of pegylated SPIOs. The targeting of the "nanotheranostics" to LS174T cells was assessed using MRI, fluorescent imaging and Prussian blue staining.

To further study the mechanism of intracellular release of Dox, we prepared azido-doxorubicin (Adox) by replacing the primary amine of Dox with a non-ionizable azido group. The intracellular release of Dox and Adox was compared to confirm their release mechanism. An HDM2 inhibitor (MI-219)[26] and an Hsp90 inhibitor (17-DMAG), which have a secondary amine and a tertiary amine, respectively, were used for comparison. The drug-loading capacity and drug release at various pHs among the four compounds were compared. The intracellular localization of SPIOs and pH-dependent drug release in endosomes/lysosomes were visualized by tracking the fluorescence of 5-FAM, Dox and Adox. To our knowledge, our studies first visualized the pH dependent drug release from SPIOs in endosomes/lysosomes of cancer cells.

4.3 Materials and Methods

4.3.1 Materials

SPIOs with a 10 nm iron-oxide core (Catalog No. SHP-10-50) and SuperMag Separator™ were supplied by Ocean NanoTech (Springdale, AR). SPIOs coated with oleic acid and amphiphilic polymer were dissolved in deionized water (5mg/ml). The oleic acid layer and polymer layer are approximately 2 nm in thickness, respectively.

Heterobifunctional PEG polymer (NH2-PEG-COOH) was purchased from JenKem Technology USA Inc. (Allen, TX). 5-FAM cadaverine was purchased from AnaSpec (Fremont, CA). HuCC49ΔC$_H$2 antibody was supplied by National Cancer Institute (Bethesda, MD). Cell culture media and phosphate buffered saline (PBS) were purchased from Invitrogen (Carlsbad, CA). PD-10 desalting columns were purchased from GE Healthcare (Piscataway, NJ). 17-DMAG was purchased from LC Laboratories (Woburn, MA). The non-specific IgG antibodies from human serum, N-(3-Dimethyl aminopropyl)-N'-ethylcarbodiimide (EDC), and N-Hydroxysulfosuccinimide sodium salt (Sulfo-NHS), as well as all other chemical reagents, were purchased from Sigma-Aldrich Chemical Co. (St. Louis, MO).

4.3.2 SPIO pegylation and conjugation

A total of 10 mg (9 nanomoles) of SPIOs were dissovled in 5 ml borate buffer (pH 5.5). EDC (0.3 mg) and sulfo-NHS (0.4 mg) were added to the mixture and kept stirring to activate the carboxyl on the surface of SPIOs. After 20 min, excessive EDC and sulfo-NHS were removed using a desalting column balanced with pH 5.5 borate buffer. HOOC-PEG-NH$_2$ (MW 2,000, 0.3 g) was added to the eluted SPIO solution under stirring and immediately adjusted pH to >8.0 by adding 0.5 ml of 30 mM borax solution. Desalting columns were used to remove excessive PEG polymers. The pegylated SPIOs were concentrated using a superMag separator™ and dissolved in pH 5.5 borate buffer for antibody and 5-FAM conjugation.

Pegylated SPIOs (2 mg/ml, 1 ml) was added with 30 µg EDC and 40 µg of sulfo-NHS and stirred for 20 min. Excessive EDC and sulfo-NHS were removed using a desalting column. Antibody (1 mg, HuCC49ΔC$_H$2 or non-specific IgG in PBS) was

added to the eluted solution under stirring. Five minutes later, 0.1 ml of 5-FAM cadaverine (2 mg/ml in 30 mM borax solution) was added to the mixture. The mixture was stirred at 4 °C and in dark for overnight. A PD-10 column was used to remove the excessive 5-FAM cadaverine and SuperMag Separator™ was used to remove the unlabeled antibody. SPIOs labeled with HuCC49ΔC$_H$2 and 5-FAM were named MAb-SPIOs and the SPIOs labeled with non-specific Human IgG and 5-FAM were named IgG-SPIOs. Similarly, 1 ml of pegylated SPIOs (2 mg/ml) was labeled with 5-FAM using the amide formation reaction.

4.3.3 Characterization

Hydrodynamic size and zeta-potential of nanoparticles in each preparation step were measured by Dynamic Laser light Scattering (DLS) and M3-PALS technology on a Zetasizer Nano ZS particle sizer (Malvern Instruments Ltd, Westborough, MA), respectively. Each sample was dispersed in deionized water (0.01 mg/mL) using a water-bath sonicator for 2 min and measured in a disposable capillary cell cuvette (Malvern Instruments Ltd, Westborough, MA). Agarose gel electrophoresis was performed to test the migration of the SPIO and its conjugates. Agarose gel (1%) was prepared in 1×TAE buffer. The nanoparticles were mixed with bromophenol blue loading buffer (Sigma, St. Louis, MO) and 20 µl of sample was loaded into each well. The gel was run in 1×TAE buffer at a voltage of 100 V for 1 hr.

4.3.4 Cell culture

Human colon cancer cell line LS174T (TAG-72 positive) and human skin cancer cell line A375 (TAG-72 negative) obtained from American Type Culture Collection (ATCC, Rockville, MD) were cultured in Dulbecco's modified Eagle high glucose medium

(DMEM) supplemented with 10% fetal bovine serum (FBS) and 1% penicillin-streptomycin (Invitrogen Life Technologies, Carlsbad, CA). The cells were maintained in a humidified atmosphere of 5% CO_2 at 37 ºC, with the medium changed every other day.

4.3.5 *In vitro* MRI scan of cancer cells

MRI scan of cancer cells was carried out as described previously [11, 27, 28]. Briefly, 5×10^5 LS174T cells per well were seeded in a 6-well plate and allowed to grow for 24 hr. Cells were incubated with MAb-SPIOs at a concentration equivalent to 0.03 mg/ml SPIOs at 37 °C for 1 or 4 hr. The unlabeled SPIOs and IgG-SPIOs were used as controls. Then cells were washed twice with PBS and digested by 0.25% trypsin. One million of cells were suspended in 1 ml of 1% agarose in 1.5 mL eppendorf tubes and vertexed for 30 s. After 1% agarose was solidified, samples were then sealed with additional 1% agarose to avoid air susceptibility artifacts. The samples were scanned on a Varian 7T MRI scanner (Varian, Palo Alto, CA). A spin-echo pulse sequence with multi-echo acquisitions was selected from the Varian VnmrJ software package to acquire MR phantom images at multiple echo times. Sequence parameters used were: repetition time (TR) of 3000 ms, echo times (TE) of 15–150 ms, echo train length of 6 and echo spacing of 15 ms, respectively. The spatial resolution parameters were set as follows: an acquisition matrix of 128 x 64, field of view of 30 x 30 mm^2, section thickness of 1 mm, and 1 average. The MRI signal intensity (SI) was measured using the Matlab software (MathWorks, Inc., Natick, MA). T_2 values were obtained by plotting the SI of each sample over a range of TE values. T_2 relaxation times were then calculated by fitting a first-order exponential decay curve to the plot. A copper pseudocolor was added to the MR phantom images using Matlab.

4.3.6 Prussian blue staining

A total of 1×10^5 LS174T cells were seeded in a 24-well plate and allowed to grow for 24 hr. Cells were incubated with MAb-SPIOs, SPIOs and IgG-SPIOs (equivalent to 20 ug/ml of SPIO) at 37°C for 4 hr, washed with PBS twice, and fixed with formaldehyde (2%). Then, the cells were treated with a staining solution containing 1:1 mixture of 5% potassium ferrocyanide and 5% HCl acid at 37 °C for 1hr. The cells were then examined under an Olympus BX-51 upright light microscope equipped with an Olympus DP-70 high resolution digital camera (Olympus Imaging America Inc., Center Valley, PA).

4.3.7 Fluorescent microscopy

A total of 2×10^4 LS174T or A375 cells were seeded in a 96-well plate and allowed to grow for 24 hr. After incubated with 5-FAM labeled SPIOs, MAb-SPIOs and IgG-SPIOs for 4 hr, LS174T or A375 cells were washed and stained with Hoechst (10 μM) at 37 ºC for 1 hr and imaged using Nikon TE2000S epifluorescence microscope coupled with a standard mercury bulb illumination, a CCD camera (Roper Scientific, Tucson, AZ), a 20 X objective, and a triple-pass DAPI/FITC/TRITC filter set (Chroma Technology Corp. 86013v2). The acquired 12-bit grayscale images were background subtracted. The images obtained with DAPI and FITC channels were overlaid using MetaMorph® software (Molecular Devices Corporation, Sunnyvale, CA). To visualize the intracellular drug release, LS174T cells were incubated with Dox or Adox loaded MAb-SPIO for 1, 6 and 24 hr and their nuclei were stained with Hoechst. The images obtained with DAPI, FITC and TRITC filters were overlaid.

4.3.8 Drug loading and release

Dox and Adox were synthesized in water-insoluble base form. The hydrochloride salt of 17-DMAG and MI-219 was converted into water-insoluble free base. 5 mg of hydrochloride salt of 17-DMAG or MI-219 was dissolved in 2 ml of 0.1M sodium carbonate solution and vortexed for 1 min. 17-DMAG or MI-219 in free base was extracted by acetyl acetate (4 ml × 3). Acetyl acetate was evaporated using a Speedvac concentrator (Thermo Scientific, Waltham, MA) to obtain 17-DMAG or MI-219 in free base. Methanol solution (0.13 ml) of the drug in free base (5 mg/mL) was added dropwise with stirring to 2 ml of SPIOs or conjugates (equivalent to 1 mg/ml of SPIOs in pH 8.0 buffer). An air flow was used to evaporate methanol and the remaining aqueous solution was stirred overnight to allow the drug partition into the oleic acid shell. Drug-loaded SPIOs or conjugates passed through a PD-10 desalting column to remove unencapsulated drug molecules. The eluted SPIO or conjugates were concentrated to 1mg/ml using a SuperMag Separator™. To determine the loading capacity, a 50 µl aliquot of SPIOs or conjugate suspension was diluted with methanol (1 ml), sonicated for 1 min and centrifuged at 21,000 g for 30 min to spin down nanoparticles. The supernatant was diluted with methanol and injected on a LC-MS/MS to quantify the amount of released drug. To test pH dependent drug release, a 50 µl aliquot of SPIOs or conjugate solution was suspended in 0.95 ml of a series of HOAc/ NH_4OAc/ NH_4OH buffers at pH 3.21, 4.19, 4.95, 5.66, 6.65 and 7.21. After incubated for 1 or 24 hr, the buffer solutions were centrifuged at 21,000 g for 30 min and the supernatant was further diluted with methanol before LC-MS/MS analysis. The percentages of drug release at various pH were calculated as the ratios of the amount of released drug in buffers and methanol.

LogP of MI-219 was predicted by using MarvinSketch from ChemAxon (Budapest, Hungary).

4.3.9 LC-MS/MS analysis

LC-MS/MS analysis was performed on an Agilent 1200 HPLC system and a Qtrap 3200 mass spectrometer (Applied Biosystems, MDS Sciex Toronto, Canada) equipped with an electrospray ionization (ESI) source. Aliquots (10 μL) were injected onto a reversed-phase Zorbax Bonus-RP column (5 cm x 2.1 mm I.D., 3.5 μm) (Agilent, Santa Clara, CA). The mobile phase consisted of 0.1% formic acid in water (A) and 0.1% formic acid in methanol (B). The mobile phase A was held at 10% for 1.0min, linearly increased from 10% to 90% over 0.1 min, held at 90% for an additional 2 min, and then immediately stepped back down to 10 for re-equilibration. The mobile phase flow rate was 0.4 mL/min. Quantification of Dox and 17-DMAG was performed by using positive multiple reaction monitoring (MRM) scan of the $[M+H]^+$ ions and the product ions of each compound. The MRM transition channels were 544/361 and 617/58 respectively. The collision energy was set as 39 and 67, respectively. Adox and MI-219 were quantified using negative MRM scan and transition channels were 568/395 and 550/306, respectively. The collision energy was -18 for Adox and -38 for MI-219. HPLC and mass spectrometric parameters are optimized by using sample infusion and flow injection analysis (FIA).

4.3.10 MTS assay

LS174T cells were seeded at 4000 per well in 96-well plates 24 hr prior to the experiment. A series of solutions of Dox or Dox-loaded nanoparticles (MAb-SPIOs and SPIOs) were prepared in DMEM media and added to the wells. The final concentrations

of Dox ranged from 0.01 μM to 5 μM. Adox and Adox loaded nanoparticles were dissolved in DMEM media and incubated with LS174T cells. The final concentrations of Adox ranged from 0.01 μM to 20 μM. SPIOs without drug and blank medium were used as controls. Cell viability was determined after incubated for 4 days. The absorption of the cells in each well at 490 nm was measured using a plate reader before and after incubated with MTS and PMS (Promega, Madison, WI) for 2 hr. The first measured absorption was subtracted from the second measure absorption to minimize the errors caused by the absorption of SPIOs at 490 nm. The effect of drug on cell proliferation was calculated as the percentage of inhibition in cell growth with respect to the controls. IC_{50} values were calculated using WinNonlin Version 5.2.1 (Pharsight, Mountain View, CA).

4.4 Results

4.4.1 Conjugation and characterization of antibody labeled SPIOs

Figure 4.1 shows the schematic production of $HuCC49\Delta C_H 2$ labeled SPIOs (MAb-SPIOs) or non-specific IgG labeled SPIOs (IgG-SPIOs). The SPIOs contain an iron oxide core of 10 nm in diameter. Oleic acid shell, amphiphilic polymer coating and hydrated layer increased hydrodynamic size of SPIOs to 18.7 ± 5.1 nm (Figure 4.1). To reduce non-specific binding with cell membranes and stabilize SPIOs, SPIOs were pegylated using excessive heterobifunctional PEG polymer (NH_2-PEG-COOH). The carboxyl groups on the surface of SPIOs were activated by EDC and sulfo-NHS and then covalently coupled to the primary amine of PEG by forming an amide bond. Pegylation of SPIOs resulted in a hydrodynamic size of 27.9 ± 7.7 nm but didn't significantly change zeta-potentials (-35.3 mV v.s. -37.4 mV) (Table 4.1). The carboxyl group of PEG

on SIPO surface was covalently linked to the amines of antibody and 5-FAM cadaverine through amide formation. SPIOs labeled with antibodies and 5-FAM showed increased hydrodynamic sizes (44.6 ± 20.3 nm for MAb-SPIOs and 43.5 ± 22.4 nm for IgG-SPIOs) and zeta-potentials (-26.1 mV for MAb-SPIOs and -25.5 mV for IgG-SPIOs). Agarose gel electrophoresis was utilized to characterize pegylated SPIOs and nanoconjugates. It was found that MAb-SPIOs and IgG-SPIOs migrated slower than SPIOs and pegylated SPIOs (Figure 4.2), indicating that MAb-SPIOs and IgG-SPIOs have larger sizes and less surface charges. Consistent with DLS measurement, pegylated SPIOs migrated slower than SPIOs due to the increased particle size. The results from particle size and zeta-potential measurement as well as electrophoresis suggested that SPIOs were successfully pegylated and labeled with antibodies.

4.4.2 *In vitro* imaging of MAb-SPIOs bound to cancer cells

In current study, fluorescence microscopy imaging, Prussian blue staining and MRI scan were used to test cancer cell targeting efficiency of SPIO conjugates. Figure 4.3 shows the fluorescent microscope images of LS174 cells (TAG-72 positive) after incubated with 5-FAM labeled SPIOs (A, B), IgG-SPIOs (C, D) and MAb-SPIOs (E, F). Figure 4.3G and 4.3H show the fluorescent images of A375 cells (TAG-72 negative) after incubated with MAb-SPIOs. The green fluorescence in Figure 4.3A, 4.3C, and 4.3E was from 5-FAM. Nuclei were stained in blue using Hoechst. The merged image (Figure 4.3F) shows that the incubation with MAb-SPIOs for 4hr resulted in binding and uptake of MAb-SPIOs to LS174T cells. However, the binding and uptake of non-targeted IgG-SPIOs (Figure 4.3D) and SPIOs (Figure 4.3B) were limited. Furthermore, MAb-SPIOs didn't exhibit specific binding to A375 cells with low TAG-72 expression.

Figure 4.4 shows Prussian blue staining of LS174T cells incubated with SPIOs (A), nonspecific IgG labeled SPIOs (B), and HuCC49ΔC$_H$2 labeled SPIOs (C). The blue color indicated the presence of SPIOs. The blue color in Figure 4.3C revealed that HuCC49ΔC$_H$2 greatly improved the cancer cell targeting and uptake of SPIOs.

LS174T cells from the *in vitro* cellular uptake experiments were examined by MRI to evaluate the potential of MAb-SPIOs as a targeted MR contrast agent. The T_2-weighted MR phantom images of the cells incubated with SPIOs, IgG-SPIOs, and MAb-SPIOs, respectively, for 1 and 4 hr are shown in Figure 4.5. The images of the cells incubated with MAb-SPIOs show a negative contrast enhancement (signal darkening) over other cells at both 1 and 4 hr. Slight darkening were also observed for cells incubated with SPIOs and IgG-SPIOs when compared with control cells. T_2 transverse relaxation times of the samples were also measured, as shown in Table 4.2. All the nanoparticles exhibited a time-dependent uptake. More nanoparticle uptake was observed after 4hr incubation compared with 1 hr incubation. LS174T cells incubated with MAb-SPIOs have much lower T_2 values (87.1-55.5 ms) than those incubated with SPIOs (113.9-91.9 ms) and IgG-SPIOs (106.2-100.9 ms), which is consistent with the increased MAb-SPIO uptake observed by fluorescence microscopy and Prussian blue staining.

4.4.3 Drug loading and pH–dependent release from SPIOs

Four anti-cancer drugs, doxorubicin (Dox), azido-doxorubicin (Adox), HDM2 inhibitor (MI-219), and Hsp90 inhibitor (17-DMAG) were selected as the model drugs and their structures were shown in Figure 4.6A. The four compounds have diverse lipophilicity. Dox is a liphophilic compound with a logP of 1.85[10]. The lipophilicity of Adox is further increased by attaching a lipophilic azide group. MI-219 is also a

lipophilic compound. The predicted clogP of MI-219 by MarvinSketch was 3.12. In contrast, 17-DMAG is a hydrophilic compound with aqueous solubility of 1.4 mg/ml[29].

Figure 4.6B shows the loading capacities (i.e. wt% of drug/SPIOs) of the four compounds. The data showed that 6.91±0.47% of Adox, 3.85±0.62% of Dox, 2.50±0.31% of MI-219 and 0.1±0.08% of 17-DMAG were encapsulated into SPIOs, suggesting that the loading capacity was correlated with lipophilicity of compounds. Compared with Dox, Adox has 1.8-fold loading capacity due to the replacement of NH_2 with azide group. The loading capacity of MI-219 was lower than that of Adox and Dox. When SPIOs were pegylated and labeled with antibody, the loading capacities of Adox, Dox, MI-219 and 17-DMAG were 6.04±0.61%, 3.16± 0.77%, 2.22 ± 0.42% and 0.09± 0.07%, which are similar to SPIOs. The hydrophilic PEG polymer and protein probably slightly affected the partitioning of drugs into the oleic acid shell, which is also observed in a previous study[2].

Dox, MI-219 and 17-DMAG contain a primary amine, secondary amine, and tertiary amine, respectively, suggesting the compounds can be protonated under various neutral or acidic pH values. In contrast, the azide of Adox cannot be protonated. Since protonation increases aqueous solubility of lipophilic drugs, the four compounds loaded in SPIOs are expected to exhibit different drug release profiles.

Figure 4.6C shows the percentages of released drugs in buffers of various pH in 1hr. Only 22.4% of Dox was released at pH 7.21. However, 55.5% of Dox was released at pH 5.66 and Dox was almost completely released at pH 3.20. In contrast, the release of Adox didn't change significantly in either neutral or acidic buffers (only 17.6-33.4% of Adox was released at these conditions). In spite of the similar structure, Dox and Adox

106

exhibited totally different release profiles, suggesting that the protonation of the primary amine resulted in the rapid release of Dox. MI-219 and 17-DMAG also showed pH dependent release from SPIOs. More MI-219 and 17-DMAG were released when buffer pH decreased. Compared with Dox, comparable percentages of MI-219 (30.7%) and 17-DMAG (31.7) were released at pH 7.21, but less percentages were released at low pH buffers (77.0% of MI-219 and 52.1% of 17-DMAG were released at pH 3.20).

Figure 4.6D shows the percentages of drug release in buffers of various pH after incubated for 24 hr. Compared with the incubation for 1 hr, all the four compounds exhibited increased release after 24 hr, suggesting the drug release from SPIOs was a dynamic process. The long-term incubation under low pH probably triggered the conformation changes and/or dissociation of polymers and oleic acid. Different from the other three compounds, the release of Adox was only slightly increased to 33.4-42.0% at various pH for 24 hr, indicating the release of Adox is not pH-dependent.

4.4.4 Intracellular release of Dox and Adox from SPIOs

Since Dox and Adox in SPIO "nanotheranostics" show different release profiles in buffers, Dox is expected to be released more rapidly than Adox after the "nanotheranostics" are internalized into the endosomes and lysosomes of cancer cells (LS174T). To visualize the intracellular release of Dox and Adox, LS174T cells were incubated with Dox-loaded SPIO "nanotheranostics" (Figure 4.7A) and Adox-loaded SPIO "nanotheranostics" (Figure 4.7C). These SPIO "nanotheranostics" were labeled with tumor targeting antibody (HuCC49ΔC$_H$2) and fluorescent dye (5-FAM) in addition to loaded Dox or Adox.

The cells were imaged after incubated for 1 hr (first row), 6 hr (second row) and 24 hr (third row). The images obtained with DAPI (first column), FITC (second column) and TRITC (third column) filters were overlaid to generate the merged images (fourth column). Green color showed the localization of 5-FAM labeled SPIO "nanotheranostics." Nuclei were stained in blue color. Red color showed the distribution of Dox or Adox. The yellow color in the merged images indicated co-localization of 5-FAM-SPIOs and Dox or Adox. As a control, LS174T cells were also incubated with Dox alone (Figure 4.7B) and Adox alone (Figure 4.7D) for 1, 6 and 24 hr.

As shown in Figure 4.7A, after incubated for 1 hr, the cell membrane was stained with weak green fluorescence, indicating the binding of "nanotheranostics" to TAG-72 on the membrane. The red fluorescence from Dox also distributed on the membrane and a small fraction of the Dox was released into the cells. After 6 hr, the green fluorescence concentrated into bright dots, suggesting the accumulation of "nanotheranostics" in endosomes/lysosomes. The red fluorescence showed that Dox molecules were released from "nanotheranostics" and partitioned into cytosol but the limited co-localization (weak yellow color in merged image) of SPIOs and Dox was still observed. After 24 hr, almost all the green fluorescence localized in endosomes/lysosomes while most Dox accumulated in nucleus. As a comparison, the free Dox partitioned into cell cytosol in 1hr (Figure 4.7B), which was much faster than the Dox in SPIO "nanotheranostics." Most free Dox localized in nuclei after incubated for 6 hr and 24 hr.

In a sharp contrast, when Adox-loaded SPIO "nanotheranostics" were incubated with LS174T cells, the staining pattern was different from that of Dox-loaded SPIO "nanotheranostics." More co-localization of SPIOs and Adox was observed at 1 hr

(Figure 4.7C). After incubated for 6 hr and 24 hr, most Adox-loaded SPIO "nanotheranostics" localized in endosomes/lysosomes. However, different from Dox, a bright yellow color in the merged images was observed, indicating the co-localization of SPIOs and Adox in endosomes/lysosomes. This suggest that most Adox was not released from lysosome even at the low pHs, and only a fraction of Adox partitioned into cytosol even after 24 hr. Figure 4.7D showed the images of cells incubated with free Adox. Compared with Dox, the amount of Adox in nuclei was much lower even after 24 hr, which was also observed in cells incubated with Adox-loaded SPIO "nanotheranostics" (Figure 4.7C).

4.4.5 Targeted SPIO "nanotheranostics" increase cytotoxicity

Dox-loaded SPIO "nanotheranostics" (HuCC49ΔC_H2 targeted) demonstrated a dose-dependent cytotoxicity with IC$_{50}$ of 0.44 µM in LS174T cells (Figure 4.8A), which is lower than that of Dox-loaded SPIO "nanotheranostics" (non-targeted) with IC$_{50}$ of 1.42 µM. These data suggest that targeted "nanotheranostics" delivered Dox into cancer cells and Dox is released from SPIO "nanotheranostics" for anticancer activity.

In contrast, Adox with an azide group was less potent than Dox. When Adox was encapsulated into SPIO "nanotheranostics," the IC$_{50}$ was 19.46 µM (non-targeted) and 13.25 µM (targeted). No significant different was observed. These data suggested that Adox was not efficient released from "nanotheranostics" even if they were targeted delivered to cancer cells. As a control, 0.1 mg/ml of SPIOs without drugs were incubated LS174T cells and no inhibition on cell growth was observed (data not shown).

4.5 Discussion

The stability of amphiphilic polymer coated SPIOs in aqueous solution was maintained by the electrostatic repulsion between the negatively charged SPIOs. To avoid agglomeration, it is critical to maintain the electrostatic repulsion during conjugation of antibody and 5-FAM. SPIO agglomeration was observed when 5-FAM cadaverine was added to SPIOs (pH 5.5) activated by EDC and sulfo-NHS. The agglomeration was probably caused by the positive charges of 5-FAM cadaverine since the amines of cadaverine were protonated at pH 5.5. To reduce the positive charges, 5-FAM cadaverine was dissolved in 30 mM borax solution (pH 9.1) and then added to the activated SPIOs. The pH of the mixed solution was adjusted to >8.0, an optimal pH for EDC-mediated coupling reactions[30]. Positive charges of 5-FAM cadaverine were minimized at pH>8 and no agglomeration was observed. Meanwhile, the mass ratio of 5-FAM cadaverine and SPIOs was reduced to 1:10 to avoid agglomeration. Additionally, the surface conjugation with proteins such as antibody[31, 32] and scFv fragment[33] have been reported to be able to stabilize nanoparticles due to the steric stabilization. Hence, antibody was first added to the activated SPIOs to stabilize the SPIOs and 5-FAM cadaverine was added 5 min later. By using this method, stable MAb-SPIOs, IgG-SPIOs and SPIO-5FAM conjugates were prepared. Although 5-FAM and antibody labeling increased zeta-potentials of the conjugates, the nanoconjugates still exhibited low zeta-potentials (-25 to -26 mV) under which there was enough electrostatic repulsion to prevent flocculation.

Although SPIOs can be accumulated in tumors through EPR effect[1] or by applying an external magnetic field[6, 34], coupling SPIOs with antibodies or targeting molecules

could be an approach to deliver the SPIOs and drugs more effectively[2-4]. Tumor associated glycoprotein 72 (TAG-72) is a human mucin like glycoprotein complex, which is over-expressed in many epithelial-derived cancers[35]. HuCC49ΔC_H2 is a humanized C_H2 domain-deleted anti-TAG-72 monoclonal antibody. Compared with murine CC49 antibody, the humanized antibody will overcome immunogenicity problem in clinical investigation and the deletion of C_H2 domain will decrease the size of nanoconjugates. Our previous studies [25, 36] showed that HuCC49ΔC_H2 could specifically bind to LS174T colon cancer cells which had overexpression of TAG-72. The *in vitro* binding studies by fluorescence microscopy, Prussian blue staining and MRI scan showed the specific targeting of the HuCC49ΔC_H2 labeled SPIOs (MAb-SPIOs) in LS174T colon cancer cells in comparison with SPIOs and IgG-SPIOs.

SPIOs have been widely used as a negative contrast agent for MRI. Different sizes of SPIOs can lead to different magnetic properties. For instance, size dependent MR signal is in the range of 4-12 nm, where a continual decrease in the T_2-weighted MR signal intensity correlated with the increase of the size of SPIOs [21, 37]. Hence, we chose SPIOs with an iron oxide core of 10 nm in diameter for cancer cell imaging and drug delivery. The T_2-weighted phantom images of LS174T cells showed that the SPIOs could effectively decrease T_2 relaxation time of cancer cells incubated with MAb-SPIOs, suggesting that it is feasible to use the nanoconjugate as a MRI contrast agent to image the tumors and monitor drug delivery.

The iron oxide core of SPIOs is coated with a lipophilic oleic acid shell and an outer surface of amphiphilic polymer. Lipophilic molecules are expected to penetrate the polymer surface and distribute into the oleic acid shell. Hence, the drug loading

111

capacities are found to be correlated with the lipophilicity of the drugs. In this study, the loading capacity of Dox was determined as 3.85 wt%. Various Dox loading capacities into SPIOs have been reported such as 2%[1], 2.3%[2],and 3.7-8.2%[8, 10]. The variation of Dox loading capacities may be caused by the weight percentage of oleic acid in the SPIOs, particle size, the amount of added Dox and the separation process. For example, 5 nm SPIOs were found to have a slightly higher Dox loading capacity than 10 nm SPIOs [2] due to the higher surface area/weight ratio or higher percentage of oleic acid. The weight ratio of added Dox and SPIOs may affect the drug loading. Since the electrostatic interaction between amine of Dox and carboxyl of SPIOs may change zeta-potential of SPIOs and probably result in flocculation, a low weight ratio of added Dox and SPIOs of 1:3 was used as previously reported[2]. LC-MS/MS assays were used to quantify the four anti-cancer drugs in this study, which led to accurate and reliable estimations of drug loading capacity and release profile. LC-MS friendly acetic acid/ammonium acetate/ammonium hydroxide buffer was used for drug loading and release.

pH-dependent release of Dox from nanoparticles have been previously reported[2, 4, 7, 12], which has been explained by the protonation of NH_2 group of Dox under low pH[2], weakened interaction between Dox and the partially neutralized carboxyl groups[4], and conformation change of amiphiphilic polymers or oleic acid[21]. In this study, Dox and Adox exhibited dramatically different release profiles in terms of both rate and extent. Furthermore, MI-219 and 17-DMAG which can be protonated at low pH also exhibited pH triggered release. The results suggested protonation play a major role in drug release at low pH. It was observed that more drugs were release from SPIOs after

incubated for 24 hr, indicating the conformation change or dissociation of amiphiphilic polymers and oleic acid may also contribute to the drug release. Although 17-DMAG has an aqueous solubility of 1.4 mg/ml and a very low loading capacity, it was not totally released even at pH 3.20, implying the existence of other interactions between 17-DMAG and SPIOs (i.e. electrostatic interaction).

It has been reported that SPIOs are normally taken up by cells via endocytosis into phagosomes, which then eventually fuse with lysosomes for degradation[38]. Due to the acidic environment in endosomes and lysosomes, Dox and Adox were expected to show different release profiles. A fluorescent microscope was used to visualize the intracellular release of Dox and Adox from SPIOs. The very limited co-localization of Dox and 5-FAM-SPIOs in endosomes/lysosomes at 6 hr suggested that most Dox were released from SPIOs and escaped into cytosol, which was consistent with the drug release observed in various pH buffers. For Adox release, the co-localization of 5-FAM-SPIO and Adox indicates that the release rate of Adox in endosomes/lysosomes was much slower than that of Dox. It is not surprising to observe the low accumulation of Adox in nuclei even after incubated with either Adox-loaded MAb-SPIOs or free Adox for 24 hr. The amino sugar residue especially the amine group was reported[39, 40] to be necessary to maintain the maximum van der Waals contact between Dox and DNA base pairs.

MTS assays showed that HuCC49ΔC$_H$2 labeled SPIO "nanotheranostics" could increase the cytoxicity of Dox by more than 3-fold (IC$_{50}$ 1.42 μM v.s. 0.44 μM) compared to non-targeted SPIO "nanotheranostics." This suggests that HuCC49ΔC$_H$2 labeled SPIO "nanotheranostics" was targeted to cancer cells, internalized, and drug was released to achieve anticancer effect. In contrast, the non-targeted SPIO

113

"nanotheranostics" which did not bind to cancer cells, were not efficiently internalized, and the drug was not efficiently released in the cell culture medium at pH 7.4. However, when SPIO "nanotheranostics" were loaded with Adox, the targeted SPIO "nanotheranostics" did not improve its efficacy compared to non-targeted ones, which suggested that Adox were not efficiently released intracellularly even the "nanotheranostics" were internalized into cancer cells.

In summary, we prepared targeted SPIO "nanotheranostics", which was labeled with fluorescence dye and TAG-72 targeting antibody, and loaded with anticancer drugs for both cancer cell imaging and anti-cancer drug delivery. The SPIO "nanotheranostics" could specifically target to LS174T colon cancer cells for fluorescent cancer imaging and effectively decrease the T_2 relaxation times in MR imaging. Four anticancer drugs (Doxorubicin, azido-doxorubicin, MI-219 and 17-DMAG) were encapsulated into SPIO "nanotheranostics" and exhibited pH-dependent release in cancer cells, resulting in an improved anticancer efficacy. This targeted "nanotheranostics" provide an integrated platform for targeted drug delivery, cancer imaging and visualization of drug release.

4.6 References

1.	Yu, M.K., et al., *Drug-loaded superparamagnetic iron oxide nanoparticles for combined cancer imaging and therapy in vivo.* Angew Chem Int Ed Engl, 2008. **47**(29): p. 5362-5.
2.	Yang, L.L., et al., *Development of Receptor Targeted Magnetic Iron Oxide Nanoparticles for Efficient Drug Delivery and Tumor Imaging.* Journal of Biomedical Nanotechnology, 2008. **4**(4): p. 439-449.
3.	Yang, L.L., et al., *Single Chain Epidermal Growth Factor Receptor Antibody Conjugated Nanoparticles for in vivo Tumor Targeting and Imaging.* Small, 2009. **5**(2): p. 235-243.
4.	Maeng, J.H., et al., *Multifunctional doxorubicin loaded superparamagnetic iron oxide nanoparticles for chemotherapy and magnetic resonance imaging in liver cancer.* Biomaterials. **31**(18): p. 4995-5006.

5. Kumar, A., et al., *Multifunctional magnetic nanoparticles for targeted delivery.* Nanomedicine. **6**(1): p. 64-9.

6. Chertok, B., et al., *Iron oxide nanoparticles as a drug delivery vehicle for MRI monitored magnetic targeting of brain tumors.* Biomaterials, 2008. **29**(4): p. 487-496.

7. Munnier, E., et al., *Novel method of doxorubicin-SPION reversible association for magnetic drug targeting.* Int J Pharm, 2008. **363**(1-2): p. 170-6.

8. Jain, T.K., et al., *Iron oxide nanoparticles for sustained delivery of anticancer agents.* Mol Pharm, 2005. **2**(3): p. 194-205.

9. Jain, T.K., et al., *Biodistribution, clearance, and biocompatibility of iron oxide magnetic nanoparticles in rats.* Mol Pharm, 2008. **5**(2): p. 316-27.

10. Jain, T.K., et al., *Magnetic nanoparticles with dual functional properties: drug delivery and magnetic resonance imaging.* Biomaterials, 2008. **29**(29): p. 4012-21.

11. Das, M., et al., *Biofunctionalized, phosphonate-grafted, ultrasmall iron oxide nanoparticles for combined targeted cancer therapy and multimodal imaging.* Small, 2009. **5**(24): p. 2883-93.

12. Yang, Y., et al., *Preparation and properties of a novel drug delivery system with both magnetic and biomolecular targeting.* Journal of Materials Science-Materials in Medicine, 2009. **20**(1): p. 301-307.

13. Nasongkla, N., et al., *Multifunctional polymeric micelles as cancer-targeted, MRI-ultrasensitive drug delivery systems.* Nano Letters, 2006. **6**(11): p. 2427-2430.

14. Jain, T.K., et al., *Magnetic resonance imaging of multifunctional pluronic stabilized iron-oxide nanoparticles in tumor-bearing mice.* Biomaterials, 2009. **30**(35): p. 6748-6756.

15. Liu, S.J., et al., *A Novel Type of Dual-Modality Molecular Probe for MR and Nuclear Imaging of Tumor: Preparation, Characterization and in Vivo Application.* Molecular Pharmaceutics, 2009. **6**(4): p. 1074-1082.

16. Hafelli, U.O., et al., *Cell Uptake and in Vitro Toxicity of Magnetic Nanoparticles Suitable for Drug Delivery.* Molecular Pharmaceutics, 2009. **6**(5): p. 1417-1428.

17. Talelli, M., et al., *Superparamagnetic Iron Oxide Nanoparticles Encapsulated in Biodegradable Thermosensitive Polymeric Micelles: Toward a Targeted Nanomedicine Suitable for Image-Guided Drug Delivery.* Langmuir, 2009. **25**(4): p. 2060-2067.

18. Guthi, J.S., et al., *MRI-Visible Micellar Nanomedicine for Targeted Drug Delivery to Lung Cancer Cells.* Molecular Pharmaceutics, 2010. **7**(1): p. 32-40.

19. Wang, B.D., et al., *pH Controlled Release of Chromone from Chromone-Fe3O4 Nanoparticles.* Journal of the American Chemical Society, 2008. **130**(44): p. 14436-+.

20. Rao, K.S., et al., *TAT-conjugated nanoparticles for the CNS delivery of anti-HIV drugs.* Biomaterials, 2008. **29**(33): p. 4429-38.

21. Yanke Yu, D.S., *Superparamagnetic iron oxide nanoparticle `theranostics' for multimodality tumor imaging, gene delivery, targeted drug and prodrug delivery* Expert Review of Clinical Pharmacology, 2010. **3**(1): p. 117-130.

22. Wang, Y.X., S.M. Hussain, and G.P. Krestin, *Superparamagnetic iron oxide contrast agents: physicochemical characteristics and applications in MR imaging.* Eur Radiol, 2001. **11**(11): p. 2319-31.

23. Park, J.H., et al., *Micellar hybrid nanoparticles for simultaneous magnetofluorescent imaging and drug delivery.* Angewandte Chemie-International Edition, 2008. **47**(38): p. 7284-7288.

24. Wang, A.Z., et al., *Superparamagnetic iron oxide nanoparticle-aptamer bioconjugates for combined prostate cancer imaging and therapy.* ChemMedChem, 2008. **3**(9): p. 1311-5.

25. Zou, P., et al., *Near-infrared fluorescence labeled anti-TAG-72 monoclonal antibodies for tumor imaging in colorectal cancer xenograft mice.* Mol Pharm, 2009. **6**(2): p. 428-40.

26. Shangary, S., et al., *Temporal activation of p53 by a specific MDM2 inhibitor is selectively toxic to tumors and leads to complete tumor growth inhibition.* Proc Natl Acad Sci U S A, 2008. **105**(10): p. 3933-8.

27. Yang, L., et al., *Single chain epidermal growth factor receptor antibody conjugated nanoparticles for in vivo tumor targeting and imaging.* Small, 2009. **5**(2): p. 235-43.

28. Yang, L., et al., *Molecular Imaging of Pancreatic Cancer in a Preclinical Animal Tumor Model Using Targeted Multifunctional Nanoparticles.* Gastroenterology, 2009.

29. Tian, Z.Q., et al., *Synthesis and biological activities of novel 17-aminogeldanamycin derivatives.* Bioorg Med Chem, 2004. **12**(20): p. 5317-29.

30. Grabarek, Z. and J. Gergely, *Zero-Length Crosslinking Procedure with the Use of Active Esters.* Analytical Biochemistry, 1990. **185**(1): p. 131-135.

31. Watanabe, H., et al., *Human Anti-gold Antibodies BIOFUNCTIONALIZATION OF GOLD NANOPARTICLES AND SURFACES WITH ANTI-GOLD ANTIBODIES.* Journal of Biological Chemistry, 2008. **283**(51): p. 36031-36038.

32. Pissuwan, D., et al., *Gold nanosphere-antibody conjugates for hyperthermal therapeutic applications.* Gold Bulletin, 2007. **40**(2): p. 121-129.

33. Liu, Y., et al., *Single chain fragment variable recombinant antibody functionalized gold nanoparticles for a highly sensitive colorimetric immunoassay.* Biosensors & Bioelectronics, 2009. **24**(9): p. 2853-2857.

34. Kumar, A., et al., *Multifunctional magnetic nanoparticles for targeted delivery.* Nanomedicine-Nanotechnology Biology and Medicine, 2010. **6**(1): p. 64-69.

35. Johnson, V.G., et al., *Analysis of a Human Tumor-Associated Glycoprotein (Tag-72) Identified by Monoclonal-Antibody B72.3.* Cancer Research, 1986. **46**(2): p. 850-857.

36. Xiao, J., et al., *Pharmacokinetics and clinical evaluation of 125I-radiolabeled humanized CC49 monoclonal antibody (HuCC49deltaC(H)2) in recurrent and metastatic colorectal cancer patients.* Cancer Biother Radiopharm, 2005. **20**(1): p. 16-26.

37. Jun, Y.W., et al., *Nanoscale size effect of magnetic nanocrystals and their utilization for cancer diagnosis via magnetic resonance imaging.* Journal of the American Chemical Society, 2005. **127**(16): p. 5732-5733.

38.   Schwalbe, M., et al., *Selective reduction of the interaction of magnetic nanoparticles with leukocytes and tumor cells by human plasma.* Journal of Magnetism and Magnetic Materials, 2005. **293**(1): p. 433-437.

39.   Yan, Q., et al., *Interaction of doxorubicin and its derivatives with DNA: Elucidation by resonance Raman and surface-enhanced resonance Raman spectroscopy.* Biospectroscopy, 1997. **3**(4): p. 307-316.

40.   Bailly, C., et al., *Enhanced binding to DNA and topoisomerase I inhibition by an analog of the antitumor antibiotic rebeccamycin containing an amino sugar residue.* Molecular Pharmacology, 1999. **55**(2): p. 377-385.

Table 4.1 Zeta-potential of SPIOs, Pegylated SPIOs, and antibody-labeled SPIOs

	$Zeta$-potential (mv)
SPIOs	-37.4 ± 1.1
Pegylate SPIOs	-35.3 ± 0.8
IgG-SPIOs	-25.5 ± 2.9
MAb-SPIOs	-26.1± 3.4

Table 4.2 T_2 relaxation time of LS174T cells incubated with SPIOs and antibody-labeled SPIOs

	T_2 values (ms)	
	1 hr incubation	4 hr incubation
Blank control	117.3 ± 1.8	118.9 ± 2.9
SPIOs	113.9 ± 4.6	91.9 ± 6.3
IgG-SPIOs	106.2 ± 4.5	100.9 ± 5.1
MAb-SPIOs	87.1± 3.7	55.5 ± 2.6

Figure 4.1 SPIO pegylation and conjugation with antibody and 5-FAM
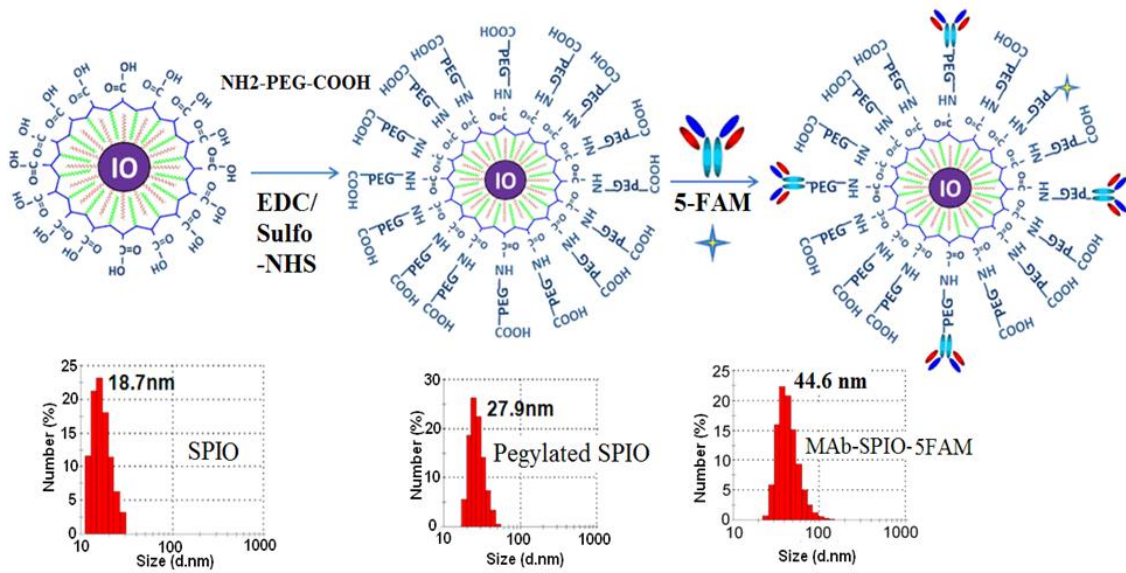
Figure 4.2 Migration of SPIOs, Pegylated SPIOs, and antibody-labeled SPIOs in agarose gel electrophoresis

Figure 4.3 Fluorescent microscope images of LS174 cells after incubated with 5-FAM labeled SPIOs (A, B), nonspecific IgG-SPIO (C, D) and HuCC49ΔC_H2-SPIOs (E, F) and A375 cells after incubated with HuCC49ΔC_H2-SPIOs (G, H). Nuclei were stained with Hoechst.
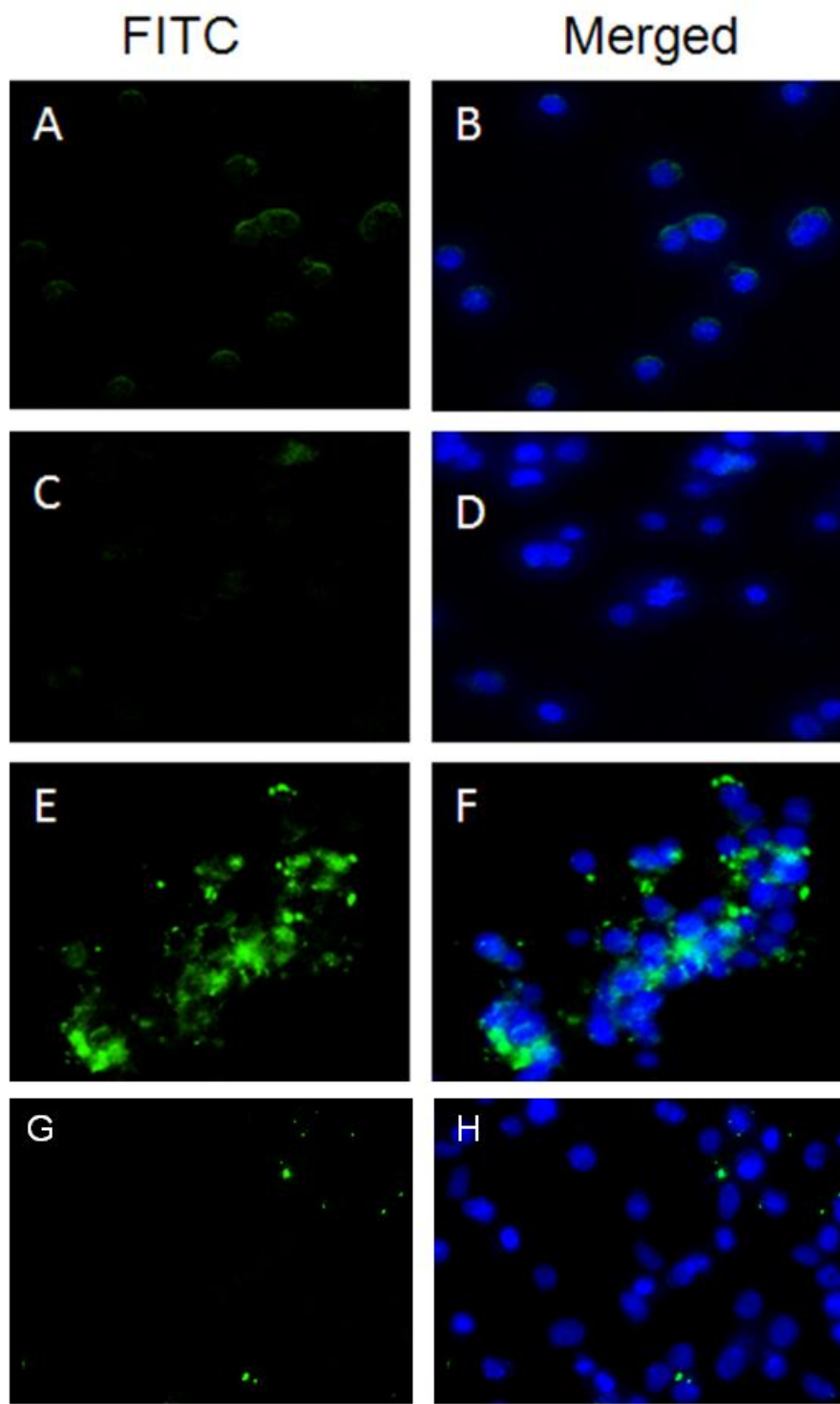
Figure 4.4 Prussian blue staining of LS174T cells incubated with SPIOs (A), nonspecific IgG labeled SPIOs (B); and HuCC49ΔC_H2 labeled SPIOs (C)
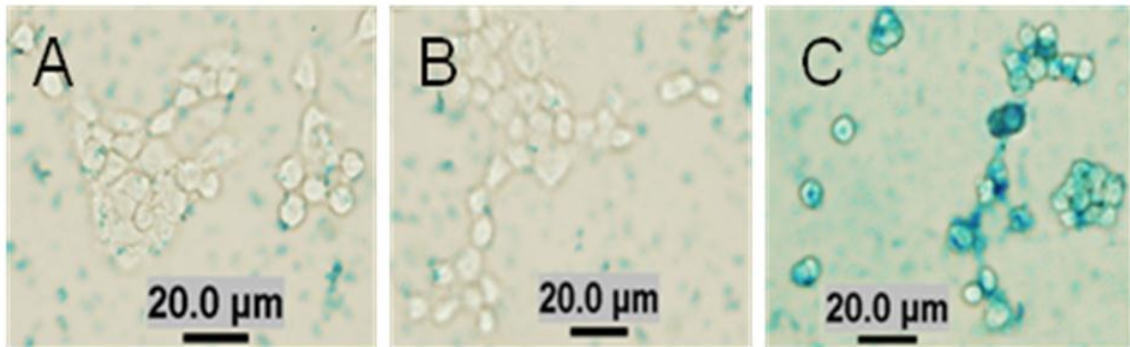
Figure 4.5 T_2-weighted spin-echo MR phantom images of LS174T cells incubated with SPIOs, nonspecific IgG labeled SPIOs; and HuCC49ΔC$_H$2 labeled SPIOs
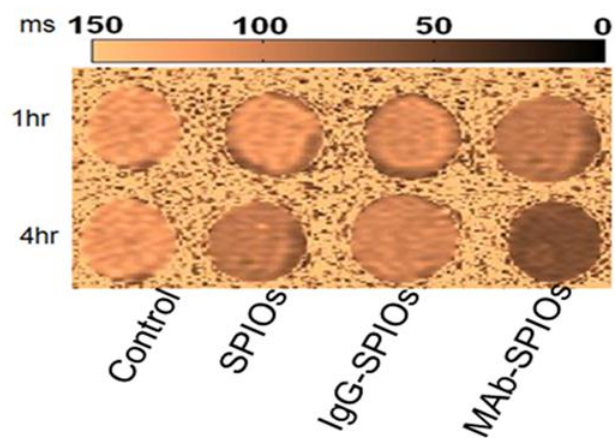
Figure 4.6 Anti-cancer drug loading capacities and pH-dependent release from SPIOs and HuCC49ΔC$_H$2 labeled SPIOs. Structures of anti-cancer drugs (A); Anti-cancer drug loading capacities of SPIOs and HuCC49ΔC$_H$2 labeled SPIOs (B); Percentages of released drug at various pH in 1 hr (C) and 24 hr (D).
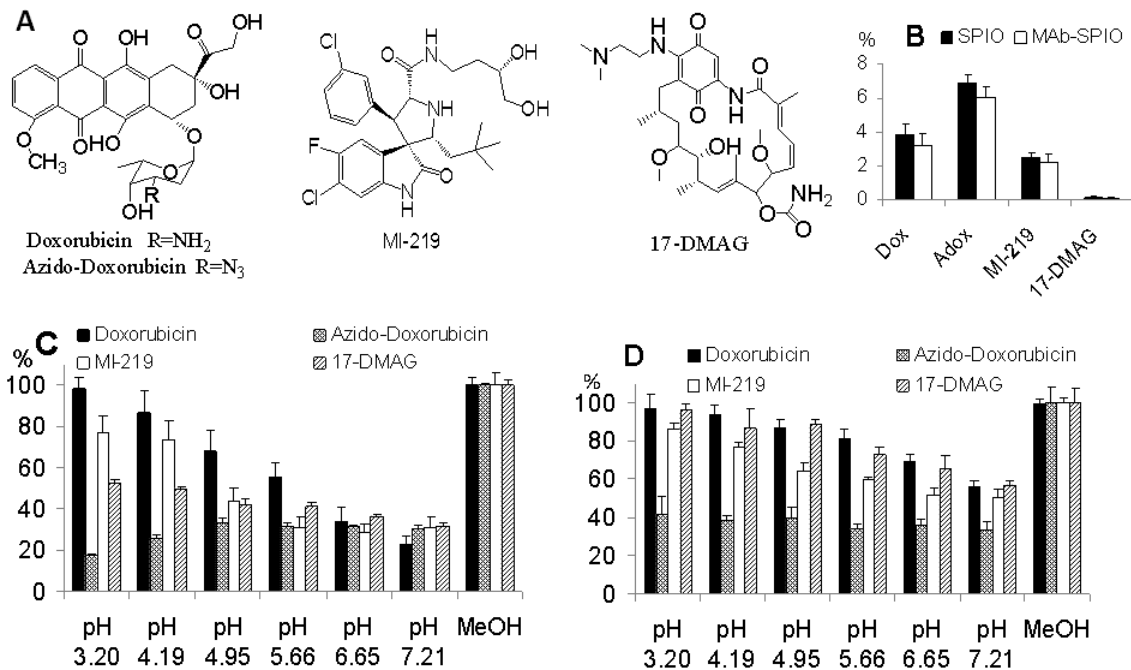
Figure 4.7 Intracellular distribution of doxorubicin (Dox), azido-doxorubicin (Adox), and HuCC49ΔC$_H$2-SPIOs in LS174T cells. Fluorescent images of cells incubated with HuCC49ΔC$_H$2-SPIOs loaded with Dox (A); free Dox (B); HuCC49ΔC$_H$2-SPIOs loaded with Adox (C) and free Adox (D). Green color shows the localization of SPIOs (5-FAM). Nuclei are stained in blue color. Red color shows the distribution of Dox or Adox. The yellow color in the merged images indicates co-localization of SPIOs and Dox or Adox.
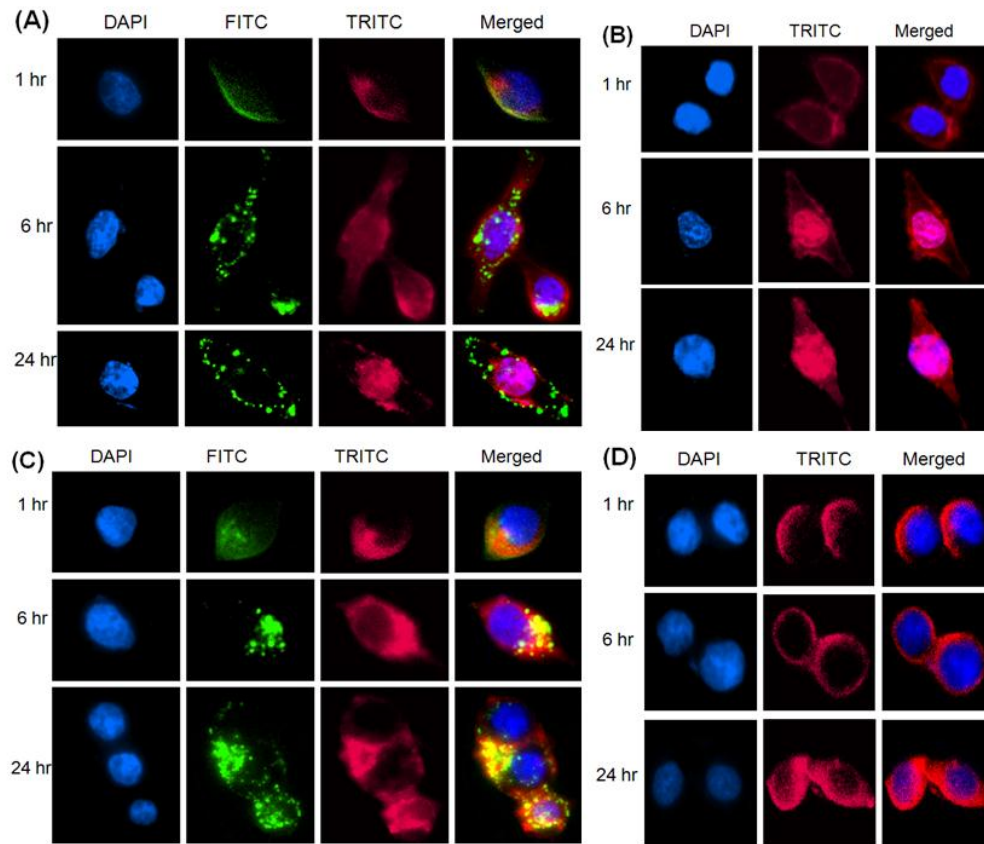
Figure 4.8 Anti-proliferation activities of Dox-loaded HuCC49ΔC$_H$2-SPIOs (A) and Adox -loaded HuCC49ΔC$_H$2-SPIOs (B) on LS174T cells.

A

%

Dox in SPIOs IC50=1.42μM
Dox in HuCC49ΔCH2-SPIOs IC50=0.44μM

B

%

Adox in SPIOs IC50=19.46 μM
ADox in HuCC49ΔCH2-SPIOs IC50=13.25 μM
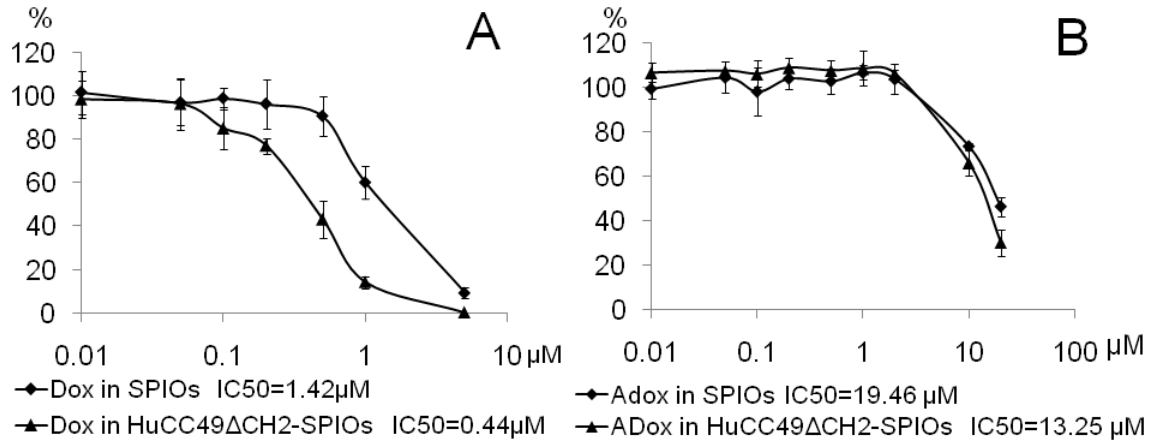
CHAPTER V

Visualization of cell membrane-triggered premature cargo release
from polymeric micelles

5.1 Abstract

The clinical application of polymeric micelles for anticancer drug delivery has been limited by the rapid premature release. Understanding the mechanisms of premature drug release is critical for design and optimization of nanoscale drug delivery systems. In this work, fluorescence resonance energy transfer (FRET) imaging was utilized to visualize the *in vitro* and *in vivo* release of hydrophobic cargos entrapped in polymeric micelles. For in vitro study, a pair of FRET dye, $DiOC_{18}(3)/DiIC_{18}(3)$ (DiO/DiI) was encapsulated into poly(ethylene oxide)-*b*-polystyrene (PEO-PS) micelles separately and both physically entrapped DiO and DiI loaded micelles were mixed together and incubated with cancer cells. Our results indicated that the payload hydrophobic dyes could be rapidly released to cellular membrane as confirmed by increased FRET ratio from *** to *** on cellular membrane. For in vivo study, another near-infra FRET dye, $DiIC_{18}(5)/DiIC_{18}(7)$ (DiD/DiR) was applied. The near-infrared emission of DiD and DiR allowed their detection by *in vivo* FRET imaging in real time. In vivo data showed that DiD and DiR could be released within 10 minutes as FRET ratio was increased from 0.23 to 0.32 after tail vein injection and further increased to 0.49 at 2 h post injection. Our results also indicated that when co-loaded with hydrophobic nanocrystals like iron oxide nanoparticles, this uncontrolled release could be slow down. FRET ratio increase from

donor and acceptor individually loaded micelles was an effective way to monitor cargo release. By comparing the average FRET ratios of mice treated with mixed donor micelles and acceptor micelles and donor/acceptor co-loaded micelles, the extent of *in vivo* release was estimated.

5.2 Introduction

Nanoscale drug delivery systems have emerged as a promising tool for cancer therapy [1]. For drug molecules physically entrapped and chemically conjugated in the core of polymeric nanoparticles, lipid micelles and liposomes, their delivery efficacy depends on the integrity of nanoparticles in blood circulation and specific release in target tissues[2]. An intractable concern for these delivery systems is the premature release of drugs before the nanoparticles reach their targets [3-6]. To develop and optimize the drug nanocarriers, it is necessary to detect the possible *in vitro* and *in vivo* premature drug release. Dual radiolabeling of cargo and liposome with two different radio tracers was utilized to detect the *in vivo* premature drug release [4]. However, this approach was tedious and failed to visualize the drug release in real-time.

Quantitative fluorescence resonance energy transfer (FRET) has been proposed to investigate the cargo release from polymeric nanoparticles and nanoparticle-cell membrane interaction [3, 7-12]. To monitor the cargo release, FRET micelles were prepared by encapsulating the hydrophobic donor dye $DiOC_{18}(3)$ and acceptor dye $DiIC_{18}(3)$ (referred to as DiO and DiI, respectively) into poly(ethylene glycol)-block-poly(D,L-lactic acid) (PEG-*b*-PDLLA) micelles [10, 12]. During the incubation of FRET micelles with cancer cells, FRET efficiencies were observed to rapidly decrease on the

cell membrane, inside of cells and in the blood vessels, indicating a premature cargo release before cell internalization. However, the accumulation of released dyes in membrane of nanoscale subcellular organelles (3-4 nm) [13] caused the recovery of FRET and even increased FRET efficiency, which compromised the specificity and sensitivity of the approach for cargo release detection. Furthermore, the high background fluorescence from animal tissues at the emission of $DiIC_{18}$ (570-580nm) made it difficult to visualize the cargo release in individual tissues.

Superparamagnetic iron oxide nanoparticles (SPIOs) are increasingly used as contrast agents and nanocarriers for MRI and drug delivery [14]. Oleic acid-coated lipophilic SPIOs and therapeutic drugs were encapsulated into various block copolymer micelles for simultaneous MRI and drug delivery [15-18]. Since hydrophobic drugs partitioned into the oleic acid coating of SPIOs, sustained drug release from oleic acid layer of SPIOs to aqueous buffer was observed over 2 weeks [19]. Since rapid cargo release can be attenuated by increasing the hydrophobicity of the micelle core[9], it is reasonable to expect that the encapsulation of hydrophobic SPIOs will decrease the premature drug release rate.

In this study, we investigated the *in vitro* and *in vivo* cargo release from poly(ethylene oxide)-*b*-poly(ε-caprolactone) (PEO-PCL) and poly(ethylene oxide)-*b*-polystyrene (PEO-PS) nanoparticles and SPIO-loaded polymeric nanoparticles. By encapsulating donor dye and acceptor dye into the core of individual nanoparticles, the FRET efficiency increase on cell membrane and various tissues was found to be an effective way to visualize the *in vitro* and *in vivo* cargo release. A FRET pair of hydrophobic near-infrared dyes $DiIC_{18}(5)$ and $DiIC_{18}(7)$ (referred to as DiD and DiR,

respectively) were encapsulated into the core of polymeric nanoparticles to visualize the cargo release in xenograft mice. Meanwhile, hydrophobic SPIOs were encapsulated into the polymeric nanoparticles to examine if SPIOs can slow down the rapid premature drug release.

5.3 Materials and Methods

5.3.1 Materials

Lipophilic SPIOs with a 10 nm iron-oxide core and SuperMag Separator™ were supplied by Ocean NanoTech (Springdale, AR). PEO-PCL (5.8 kD-b-22.5 kD) and PEO-PS (9.5 kD-b-18kD) were purchased from Polymer Source Inc. (Dorval, Quebec, Canada). DiO, DiI, DiD, and DiR were purchased from Invitrogen (Carlsbad, CA). Sephadex LH-20 was purchased from GE Healthcare (Piscataway, NJ). Centrifugal filter units (MWCO 10 kD) were purchased from Millipore (Billerica, MA). Human plasma and CD-1 mouse plasma in sodium citrate, THF as well as all other chemicals, were purchased from Sigma-Aldrich Chemical Co. (St. Louis, MO).

5.3.2 Polymeric nanoparticle preparation

SPIO-loaded PEO-PS micelles were prepared by a precipitation method. 10 mg of PEG-PS was dissolved in 0.5 ml of THF with 0.075 mg of DiI and 1mg of SPIOs in 50μL of THF. 2 mL of deionized water was dropped at a speed of 6 ml/min using a syringe pump (Fisher Scientific, Pittsburgh, PA) under vigorous stirring. The solution was then dialyzed against 2 liters of deionized water using Spectra/Por (MWCO 6-8 kD) (Spectrum OR, Irving, TX) for 2 days. Water was changed after 1 day. SPIO-loaded nanoparticles were isolated and concentrated using a magnetic separator (Ocean

NanoTech, Springdale, AR). Finally, the SPIO-loaded nanoparticles were resuspended in PBS and filtered through a 0.45 µm filter, and stored at 4°C. Following this procedure, 0.75% of DiI and 0.75% of DiO were individually loaded or co-loaded into PEO-PS micelles. The micelles were concentrated using a 10 kD MWCO centrifugal filter unit and suspended in PBS. 10% of SPIOs and 0.75% or 2.5% of DiO or DiI or both were encapsulated into PEO-PS micelles. Similarly, PEO-PCL micelles were prepared by individually loading or co-loading 0.75% of DiO and 0.75% of DiI. For *in vivo* imaging, 6% of DiD and DiR were individually loaded or co-loaded into PEO-PS micelles in the absence or presence of 10% of SPIOs. The concentrations were calculated according to the amount of polymers, dyes and deionized water used.

5.3.3 Characterization of polymeric nanoparticles

The average hydrodynamic sizes and zeta-potential of nanoparticles were measured by dynamic light scattering (DLS) and M3-PALS techniques on a Zetasizer Nano ZS particle sizer (Malvern Instruments Ltd, Westborough, MA).

The morphology of SPIO-loaded polymeric nanoparticles was obtained on a Philips CM-100 transmission electron microscope (TEM). Nanoparticle dispersion was dropped onto a carbon-coated copper grid, dried in air at room temperature and imaged within the next 24 h.

Fluorescence spectra of various nanoparticles were measured on an LS55 PerkinElmer luminescence spectrometer (Waltham,MA) with an excitation at 480 nm (DiO) or 610 nm (DiD) and an emission scan from 490 to 600 nm (DiO and DiI) or 650 nm to 850 nm (DiD and DiR). To monitor the possible cargo release or exchange, time-resolved fluorescence study of nanoparticles individually loaded or co-loaded with donor

and acceptor dyes was performed in human plasma, mouse plasma and rat blood. Fluorescent spectra were recorded every 5 min over a 2 hr period. Fresh rat blood was collected from an anesthetized Sprague Dawley rat (Charles River, Wilmington, MA) by cardiac puncture.

5.3.4 Cell culture and xenograft mice

A breast cancer cell line MDA-MB-231 obtained from American Type Culture Collection (ATCC, Rockville, MD) was cultured in RPMI medium 1640 supplemented with 10% fetal bovine serum (FBS) and 1% penicillin-streptomycin (Invitrogen Life Technologies, Carlsbad, CA). The cells were maintained in a humidified atmosphere of 5% CO_2 at 37 ºC, with the medium changed every other day. Cells were cultured on 8-well Lab-Tek glass chamber slides (Thermo Fisher Scientific, Rochester, NY) for FRET confocal imaging. 1×10^4 cells per well were incubated for 2 days to allow cell adherence. The cells in 0.2 ml of culture medium were added with 20μL of nanoparticles and incubated at 37°C for the desired lengths of time before imaging.

The animal procedures were performed according to a protocol approved by the University Committee for the Use and Care of Animals (UCUCA) at University of Michigan. Female athymic nude mice (nu/nu), obtained from National Cancer Institute (Bethesda, MD) at 8 weeks of age, were subcutaneously inoculated in the back with 5×10^6 MDA-MB-231 cells suspended in a mixture of 50 μL of PBS and 50 μL of matrixgel basement membrane (BD Biosciences, San Jose, CA). When the tumor implants reached 0.4 cm in diameter, the tumor-bearing mice were subjected to the *in vivo* studies.

5.3.5 FRET confocal microscopy

The confocal images were acquired by using a digital camera (C9100, Hamamatsu Photonics, Japan) mounted on a Visitech VT Infinity 3 array-scanning confocal system (VisiTech International Ltd., United Kingdom) attached to a Nikon TE-2000U microscope with a 60X Nikon Plan Apo water-immersion objective at room temperature. Images were recorded in DiO channel (488 nm excitation, 535 ± 20 nm emission), FRET channel (488 nm excitation, 620 ± 20 nm emission) and DiI channel (543 nm excitation, 620 ± 20 nm emission). The exposure time was 200 ms for DiO and FRET channels and 100 ms for DiI channel. Cells were incubated with 0.2 mg/mL of PEO-PS or PEO-PCL nanoparticles co-loaded with 0.75% of DiO and 0.75% of DiI. Additionally, cells were incubated with mixed 0.2 mg/mL of PEO-PS (or PEO-PCL) nanoparticles with 0.75% of DiO and 0.2 mg/mL of PEO-PS (or PEO-PCL) nanoparticles with 0.75% of DiI. Similarly, PEO-PS nanoparticles loaded with 10% of SPIO and FRET dyes were incubated with cells. After 2 hr incubation, images were obtained before and after PBS washing by using MetaMorph v6.5.3 (Universal Imaging, Malvern, PA).

The images obtained after PBS washing were background-subtracted using the "Background Correction" tool in MetaMorph. Crosstalk correction and FRET ratios calculation were carried out using an in-house FRETCalculator program and Matlab. To correct crosstalk, correction coefficients α and β were determined from cells incubated with DiI micelles only ($\alpha = I_{FRET}/I_{DiI}$) and DiO micelles only ($\beta = I_{FRET}/I_{DiO}$) [20-22]. I_{FRET}, I_{DiI} and I_{DiO} were intensities in each region of interest (ROI) under FRET, DiI, and DiO filter sets, respectively. Net FRET was calculated as follows $I_{FRET}' = I_{FRET} - \alpha \times I_{DiI} -$

$\beta \times I_{DiO}$ and FRET ratio = $I_{FRET}'/(I_{FRET}' + I_{DiO}')$. Where I_{FRET}' and I_{DiO}' are the crosstalk subtracted I_{FRET} and I_{DiO}.

5.3.6 *In vivo* **FRET imaging**

In vivo fluorescence imaging was performed with an IVIS Spectrum imaging system (Xenogen, Alameda, CA). Images were recorded in DiD channel (640 nm excitation, 680 nm emission), FRET channel (640 nm excitation, 780 nm emission) and DiR channel (710 nm excitation, 780 nm emission). The exposure time was 1s for all the channels. Identical illumination settings were used for acquiring all images. Images were acquired and analyzed using Living Image 2.5 software (Xenogen, Alameda, CA).

To determine FRET ratios of various micelles under the IVIS Spectrum imaging system, 1 mL of micelles (0.05 mg/mL in PBS) in an eppendorf tube were imaged using DiD (Ex/Em 640/680 nm) and FRET (Ex/Em 640/780 nm) filter sets. The average fluorescent intensities were calcuated using automatic ROI (Region of Interest) tool of Living Image 2.5 software. The FRET ratio was calculated as follows: FRET ratio = $I_{FRET}/(I_{FRET} + I_{DiD})$, where I_{FRET} and I_{DiD} are the average intensities of micelles under FRET and DiD filter sets, respectively,

Four mice bearing MDA-MB-231 tumors were injected via the tail vein with 1 mg of PEO-PS nanoparticles with 6% DiD, 1mg of PEO-PS nanoparticles with 6% DiR, mixed DiD nanoparticles (1mg) and DiR nanoparticles (1mg), and 1mg of PEO-PS nanoparticles with 6% DiD and 6% DiR. One untreated mouse was used as a blank control. The five mice were imaged at 10 min and 2 hr after injection. Similarly, four xenograft mice were i.v. injected with 1mg of SPIO-loaded PEO-PS nanoparticles with 6% of DiD, 6% of DiR or both DiD (6%) and DiR (6%). The mice were imaged at 10 min, 2

hr and 6 hr after injection. To monitor the FRET ratio on mice, the average I_{FRET} and I_{DiD} from the whole mouse body were calculated using ROI tool.

At the end of experiment, the mice were sacrificed using CO_2. Blood and tissues (tumor, lung, heart, spleen, liver and kidneys) were collected and tissues were rinsed with PBS. Blood and tissue samples as well as various nanoparticles in eppendorf tubes were imaged using the identical settings as *in vivo* imaging. The average I_{FRET} and I_{DiD} of each sample were calculated using automatic ROI tool and the average FRET ratio of each tissue or blood sample was obtained.

5.4 Results

5.4.1 Preparation and characterization of polymeric nanoparticles

To visualize the cargo release from polymeric nanoparticles in real-time and investigate the release mechanism, a pair of FRET dyes, DiO and DiI, were encapsulated into PEO-PS or PEO-PCL micelles individually or together [12, 23]. Figure 5.1and Table 5.1 show the hydrodynamic sizes of polymeric micelles loaded with donor and acceptor dyes in the presence and absence of SPIOs. The incorporation of 10% of SPIOs increased the average size of PEO-PS micelles from 46 nm to 142 nm and the incorporation of 6% of DiD and 6% of DiR further increased the average size to 160 nm. PEO-PCL micelles loaded with 0.75% of DiO and 0.75% of DiI showed an average size of 106 nm. TEM of SPIO-loaded PEO-PS micelles showed clusters of 10 nm SPIOs in the cores of micelles (Figure 5.1F).

To examine the *in vitro* stability, polymeric micelles loaded with 0.75% of DiO (donor) and 0.75% of DiI (acceptor) were incubated in rat blood and human plasma at a

concentration of 0.2 mg/mL and the spectra were recorded every 5 min until 2 hrs. The FRET ratios were calculated as: FRET ratio = $I_{FRET}/(I_{FRET} + I_{DiO})$ [12]. The release of DiO and DiI will increase the distance between the two dyes, resulting in a decrease of FRET ratio. As shown in Figure 5.2A and 5.2D, the FRET ratio (0.96) of PEO-PS micelles kept constant in rat blood and human plasma over 2 hr. Similarly, the FRET ratios of PEO-PCL micelles (0.93) and SPIO-loaded PEO-PS micelles (0.84) did not change over 2 hr (Figure 5.2B, C, E and F). The results revealed that no significant of cargos were released from PEO-PS and PEO-PCL micelles when they were incubated with blood and plasma.

5.4.2 FRET imaging of cells incubated with DiO/DiI co-loaed micelles

To visualize cargo release during micelle-cell interaction, PEO-PS micelles co-loaded with 0.75% of DiO and DiI were incubated with MDA-MB-231cancer cells at a concentration of 0.2 mg/mL for 2 hrs. Images were obtained in the presence of micelles in the media (Figure 5.3, A1-4) and after washing with PBS (Figure 5.3, B1-4). As shown in A1 and A2, both DiI and DiO were detected on the cell membrane and intracellular organelles. It's not surprising since DiO and DiI are designed to stain cell membrane by inserting their long alkyl tails into the cell membranes. Once applied to cells, the dyes diffused laterally within the plasma membrane and were then internalized in to cells [24]. The accumulation of DiI and DiO resulted in strong FRET signals in plasma membrane and endosomes/lysosomes (Figure 5.3A3). Meanwhile, FRET effect diminished fluorescence of DiO on cell membrane (Figure 5.3A2). The pseudo colors in Figure 5.3A4 showed higher FRET ratios on plasma membrane and endosomes/lysosomes than that of micelles in the media, suggesting that DiO and DiO were released from micelles

137

to plasma membrane and accumulated in endosomes/lysosomes. Considering the thickness of cell membrane (3-4 nm) [13] and diameter of PEO-PS micelles (46 nm), it is understandable that the accumulation of DiO and DiI in cell membrane results in a higher FRET ratio in cell membrane than that of micelles in the media, which was decreased by the release of DiO and DiI. Furthermore, the accumulation of DiO and DiI in plasma membrane indicated that DiO/DiI release from micelles was faster than their cell internalization. Due to the existence of micelles in the media, background subtraction could not be performed and accurate FRET ratios were not obtained. Figure 5.3B1-4 showed the images obtained after washing with PBS. After background subtraction and crosstalk correction, the average FRET ratio on plasma membrane was determined as 0.99. Rapid cargo release was also observed when MDA-MB-231 cells were incubated with PEO-PCL micelles loaded with 0.75% of DiO and 0.75% of DiI (Figure 5.4).

10% of SPIOs, 0.75% of DiO and 0.75% of DiO loaded PEO-PS micelles were incubated with MDA-MB-231 cells for 2hr. In the presence of micelles in the media, the FRET signals (Figure 5.3C3) and FRET ratios (Figure 5.3C4) on plasma membrane were observed to be lower than that on endosomes/lysosomes and micelles in the media, indicating lower concentrations of DiO and DiI in plasma membrane than that in endosomes/lysosomes. This suggested that DiO/DiI release from SPIO-loaded micelles was slower than DiO/DiI cell internalization. The incorporation of 10% of SPIOs decreased DiO/DiI release rate. After washing with PBS (Figure 5.3D1-4), the images showed low FRET signals on plasma membrane and an average FRET ratio of 0.86, which was due to the reduced DiO/DiI release and nonspecific binding between SPIO-loaded micelles and cell membrane.

5.4.3 Cargo release from micelles individually loaded with DiO and DiI

To monitor the cargo release, 0.75% of DiO or DiI were encapsulated into polymeric micelles individually. 0.1 mg/mL of DiO-loaded micelles was mixed with 0.1 mg/mL of DiI-loaded micelles. FRET spectra of the mixed micelles were recorded every 5 min over 2 hr. The results (Figure 5.5) showed that the FRET ratios did not increase in cell culture media with 10% FBS over 2 hr, suggesting that DiO/DiI exchange between DiO micelles and DiI micelles was very slow. The fluorescence at 570 nm was caused by spectra crosstalk (DiI was slightly excited at 480 nm).

Since the DiO/DiI exchange in media was very limited, the mixed PEO-PS DiO micelles (0.2 mg/mL) and PEO-PS DiI micelles (0.2 mg/mL) were incubated with MDA-MB-231 cells for 2 hr. As shown in Figure 5.6A4, the increased FRET ratios on both plasma membrane and intracellular organelles indicated the release of DiO and DiI from PEO-PS micelles. Similarly, incubation with DiO loaded PEO-PCL micelles and DiI-loaded PEO-PCL micelles resulted in higher FRET ratios on plasma membrane and organelles (Figure 5.6B4), suggesting that DiO and DiI were released from PEO-PCL micelles to cell membrane. Figure 5.6C3 and C4 showed that the incorporation of 10% of SPIOs almost totally eliminate FRET signal in the cells, indicating only a small fraction of DiO and DiI was released into cells. The fluorescence of DiO and DiI detected on the cells (Figure 5.6C1 and C2) were mainly from the internalized micelles and micelles nonspecifically bound to plasma membrane. To test if the effect of SPIOs on cargo release was dose-dependent, 2.5% of DiO and 2.5% of DiI were individually encapsulated into 10% SPIO-loaded PEO-PS micelles. Figure 5.6D1-4 showed the FRET effect on plasma membrane and endosomes/lysosomes when the cells were incubated

with 0.2 mg/mL of SPIO-loaded DiO (2.5%) micelles and 0.2 mg/mL of SPIO-loaded DiI

(2.5%) micelles for 2 hr. The results suggested that SPIOs decreased the release of

DiO/DiI at low concentration (0.75%) but did not prevent the release when DiO/DiI

saturated the oleic acid coating of SPIOs.

5.4.4 *In vivo* cargo release from DiD/DiR loaded micelles

To visualize the *in vivo* cargo release, two near-infrared dyes, DiD and DiR

(analogues of DiI), were used as FRET donor and acceptor, respectively. Considering the

large volume of cell membrane in mice, 6% of DiD and 6% of DiR were co-loaded or

individually loaded into PEO-PS micelles in the absence and presence of 10% of SPIOs.

Time-resolved spectra of mixed DiD micelles and DiR micelles at 0.1 mg/mL in mouse

plasma revealed that the DiD and DiR exchange between PEO-PS micelles was very

limited during 2 hr incubation (Figure 5.7).

Under the IVIS imaging system, DiD (6%) and DiR (6%) co-loaded PEO-PS

micelles exhibited an average FRET ratio of 0.89 in the absence of SPIOs and 0.86 in the

presence of 10% SPIOs. Due to the spectral crosstalk, the mixed DiD micelle (0.05

mg/mL) and DiR micelles (0.05 mg/ml) showed an average FRET ratio of 0.23 in the

absence of SPIOs and 0.19 in the presence of 10% of SPIOs.

Figure 5.8 A and B showed the images of mice 10 min (A) and 2 hr (B) after i.v.

injection of DiD micelles, DiR micelles, mixed DiD micelles and DiR micelles, and

DiD/DiR co-loaded micelles. As shown in Figure 5.8A and B, FRET was detected on the

mouse treated with mixed micelles in at 10 min and FERT signal dramatically increased

at 2 hr, suggesting the rapid cargo release to cell membrane. Figure 5.8D showed the

changes of FRET ratios from the mice treated with mixed micelles and co-loaded

micelles. At 10 min after injection, FRET ratio of mixed micelles increased from 0.23 to 0.29 while the FRET ratio of co-loaded micelles decreased from 0.89 to 0.60. At 2 hr post injection, the FRET ratio of mixed micelles further increased to 0.48 while the FRET ratio of co-loaded micelles also decreased to 0.48. The comparable FRET ratios between the mice treated with mixed micelles and co-loaded micelles suggested that most DiD and DiR were released from PEO-PS micelles in 2 hr. Figure 5.8C showed the images of blood and tissue samples of the mice scarificed 2 hr post injection of mixed micelles and co-loaded micelles. Figure 5.8E showed the FRET ratios of the blood and tissue samples. The similar FRET ratios in tissues of the two mice indicated the complete DiD/DiR release. Both high FRET intensities and high FRET ratios (0.61-0.69) were observed from liver and spleen of the mice treated with mixed micelles and co-loaded micelles, indicating a large amount of DiD/DiR in the tissues and high concentrations of DiD/DiR in the cell membrane, which was due to reticuloendothelial system (RES) uptake of nanoparticles by phagocytes in spleen and Kupffer cells in liver [25]. A high FRET intensity but a low FRET ratio (0.41) in the lungs of the mouse treated with co-loaded micelles sugested the accumulation of micelles in the lungs but low DiD/DiR concentrations in lung cell membrane, which might be explained by the large surface area of capillaries in the lungs. Both low FRET inentsities and low FRET ratios (0.27- 0.29) in blood of the two mice indicated limited DiD/DiR release to red blood cells, which was reported previously[10].

The effect of hydrophobic SPIOs on the cargo release was investigated *in vivo*. Figure 5.9A, B and C showed the images of mice 10 min (A), 2 hr (B) and 6 hr (C) after *i.v*. injection of SPIO/DiD micelles, SPIO/DiR micelles, mixed SPIO/DiD micelles and

SPIO/DiR micelles, and SPIO/DiD/DiR co-loaded micelles. Figure 5.9E showed the change of FRET ratios from the mice treated with mixed micelles and SPIO/DiD/DiR micelles. FRET signal was detected in 10 min from the mouse treated with mixed micelles (Figure 5.9A), indicating a rapid release of DiD/DiR from SPIO-loaded micelles. The FRET ratios of mixed micelles in the mouse increased from 0.22 (10 min) to 0.44 (2 hr) and 0.47 (6 hr) while the FRET ratios of SPIO/DiD/DiR micelles decreased from 0.65 (10 min) to 0.58 (2hr) and 0.56 (6 hr). Even at 6 hr, FRET ratio from the mouse treated with mixed micelles (0.47) was still lower than that from the mouse treated with SPIO/DiD/DiR micelles, indicating that the incorparation of 10% of SPIOs slowed down the release of DiD/DiR. Images of blood and tissues of the two mice (Figure 5.9D) showed the accumulation of DiD/DiR in liver and spleen. The low blood FRET ratio (0.22) of the mouse treated with mixed micelles (Figure 5.9F), which was similar to that of mixed micelles in PBS (0.19), suggested that the DiD/DiR exchange between SPIO-loaded micelles and the cargo release to red blood cells were very limited. The tissue FRET ratios of the mouse treated with SPIO/DiD/DiR micelles were higher than that of the mouse treated with mixed micelles, suggesting that DiD and DiR were not completely released from the oleic acid layer of SPIOs.

5.5 Discussion

Clinical trails have revealed dramatically different pharmacokinetic profiles of doxorubicin (DOX) in liposomes and polyemric micelles[26, 27]. Liposomal formation of DOX resulted in a 556-fold increase in AUC and 300-fold decrease in volume of distribution [26]. In contrast, DOX encapsulated into Pluronic® block copolymer

micelles showed similar AUC to free doxorubicin in humans [27]. To successfully deliver drug to its target, it is critical to understand the mechanisms of premature drug release.

In current study, PEO-PS and PEO-PCL block copolymers were selected to prepare FRET micelles. Due the high glass transition temperature of polystyrene (107ºC) [28] and polycaprolactone (60ºC) [29], PEO-PS and PEO-PCL micelles were kinetically frozen with low liquidity at 37ºC. Thus, when DiO micelles and DiI micelles were mixed in cell culture media, the inter-micelles cargo exchange was very slow (Figure 5.5). Both PEO-PS micelles and PEO-PCL micelles showed limited cargo release in rat blood, human plasma (Figure 5.2) and mouse plasma (Figure 5.7). Although serum protein α- and β-globulins were reported to trigger the rapid disassembly of PEG-PDLLA micelles and release of DiO/DiI[10], it was also observed that DiO/DiI release in serum could be reduced by increasing the hydrophobicity of the core-forming block of copolymer [9]. The high hydrophobicity of PS and PCL blocks prevented the release of DiO/DiI to serum proteins. Furthermore, the accumulation of DiD/DiR in lungs, spleen and liver (Figure 5.8C), a typical biodistribution pattern of nanoparticles, suggested that DiD and DiR were not totally released in blood circulation and micelles were not disrupted by serum proteins.

Consistent with previous reports [6, 8, 12], the rapid release of hydrophobic dyes to plasma membrane was visualized in current study by FRET imaging. The FRET ratios on plasma membrane depended on the cargo release rate and membrane internalization rate. For leaky micelles, the rapid cargo release caused the accumulation of DiO and DiI in plasma membrane. It was not surprising to observe high FRET ratio on plasma membrane

saturated with DiO and DiI since the thickness of the lipid bilayer is only 3-4 nm. When cells were incubated with DiO/DiI co-loaded micelles, the decrease in FRET ratio caused by the cargo release was attenuated by the FRET ratio increase on cell membrane. Hence, to monitor drug release, especially *in vivo* release, it is more sensitive and specific to detect FRET increase on cell membrane by using micelles individually loaded with FRET dyes.

Since the incubation concentration of micelles (0.2 mg/mL) was much higher than critical micelle concentrations (CMC) of PEO-PS and PEO-PCL micelles, the rapid release was not likely caused by micelle disassembly or polymer exchange [8, 12]. Recently, the mechanisms of rapid cargo release from nanocarrier to nanoacceptors were investigated [30]. The rapid cargo release from nanocarriers which were stable in bulk solution, was found to be induced by abundant empty nanoacceptors. The cargo was translocated between carrier and acceptor through a short-distance ($< 1\mu$m) diffusion by following a Fickian spherical diffusion model. Hence, the rapid release of DiO/DiI was probably driven by the large volume of cell membrane. The Brownian motion of micelles in the media increased their short-distance ineraction with plasma membrane and facilitated cargo release. For nanoscale drug delivery systems, it is recommended that the cargo release assay should be conducted in the presence of abundant cell membrane or artificial lipid bilayer.

As expected, oleic acid layer in SPIOs slowed down the release of DiO/DiI, especially for micelles with 0.75% of DiO/DiI. It is not surprising since oleic acid is as hydrophobic as oleate and palmitate, the hydrophobic tails of membrane phospholipids, which are more hydrophobic than PS and PCL blocks. Hence, the relative high

hydrophobicity of lipid bilayer also triggers the rapid cargo release from micelles. This can partially explain the less premature release of DOX from liposomes than that from polymeric micelles. For drugs with a low loading capacity, the encapsulation of hydrophobic nanoparticles into the micelles is an effective way to reduce premature drug release. However, for drugs with high loading capacity, increasing the core hydrophobicity to be comparable to that of cell membrane is another option.

In current study, near-infrared FRET imaging was utilized to noninvasively visualize *in vivo* caro release. The FRET ratio increase from DiD/DiR individually loaded micelles was employed to monitor the DiD/DiR release and the FRET ratio decrease from DiD/DiR co-loaded micelles was used as a control. In theory, if two mice are given the same amount of FRET pair dyes and the volumes of phospholipid bilayer bteween the two mice are assumed to be equal, the avearge FRET ratios of the mice should be same when the dyes are totally released to cell membrane. Hence, the difference between the FRET ratios of mice treated with individually loaded micelles and co-loaded micelles can be used to monitor the extent of cargo release in real-time. For *in vitro* FRET imaging, FRET ratio on cell membrane was observed to increase since the membrane was rapidly saturated with DiO/DiI in the presence of abundant of micelles in the media. In contrast, due to the large volume of cell membrane in mouse tissues, the FRET ratios of all the collected tissues were lower than that of intact DiD/DiR co-loaded micelles.

5.6 Conclusion

In summary, *in vitro* and *in vivo* FRET iamging was used to visualize the rapid cargo release from polymeric nanoparticles and SPIO-loaded polymeric nanoparticles.

SPIOs were found to be able to slow down *in vitro* and *in vivo* cargo release in a dose-dependent mode. The large volume and high hydrophobicity of cell membrane were found to trigger premature cargo release of nanoparticles. The FRET ratio increase from donor and acceptor individually loaded micelles was an effective way to monitor cargo release. Although the FRET imaging method was designed to monitor the release of hydrophobic dyes physically entrapped into nanocarriers, it may be modified to detect the release of dyes covalently conjugated to nanoparticles.

5.7 References

1. Peer, D., et al., *Nanocarriers as an emerging platform for cancer therapy.* Nat Nanotechnol, 2007. **2**(12): p. 751-60.
2. Bae, Y.H. and H. Yin, *Stability issues of polymeric micelles.* J Control Release, 2008. **131**(1): p. 2-4.
3. Savic, R., A. Eisenberg, and D. Maysinger, *Block copolymer micelles as delivery vehicles of hydrophobic drugs: micelle-cell interactions.* J Drug Target, 2006. **14**(6): p. 343-55.
4. Zolnik, B.S., et al., *Rapid distribution of liposomal short-chain ceramide in vitro and in vivo.* Drug Metab Dispos, 2008. **36**(8): p. 1709-15.
5. Lanza, G.M., et al., *Targeted antiproliferative drug delivery to vascular smooth muscle cells with a magnetic resonance imaging nanoparticle contrast agent: implications for rational therapy of restenosis.* Circulation, 2002. **106**(22): p. 2842-7.
6. Partlow, K.C., G.M. Lanza, and S.A. Wickline, *Exploiting lipid raft transport with membrane targeted nanoparticles: a strategy for cytosolic drug delivery.* Biomaterials, 2008. **29**(23): p. 3367-75.
7. Barauskas, J., et al., *Interactions of lipid-based liquid crystalline nanoparticles with model and cell membranes.* Int J Pharm. **391**(1-2): p. 284-91.
8. Xiao, L., et al., *Role of cellular uptake in the reversal of multidrug resistance by PEG-b-PLA polymeric micelles.* Biomaterials. **32**(22): p. 5148-57.
9. Diezi, T.A., Y. Bae, and G.S. Kwon, *Enhanced stability of PEG-block-poly(N-hexyl stearate l-aspartamide) micelles in the presence of serum proteins.* Mol Pharm. **7**(4): p. 1355-60.
10. Chen, H., et al., *Fast release of lipophilic agents from circulating PEG-PDLLA micelles revealed by in vivo forster resonance energy transfer imaging.* Langmuir, 2008. **24**(10): p. 5213-7.
11. Jiwpanich, S., et al., *Noncovalent encapsulation stabilities in supramolecular nanoassemblies.* J Am Chem Soc. **132**(31): p. 10683-5.

12. Chen, H., et al., *Release of hydrophobic molecules from polymer micelles into cell membranes revealed by Forster resonance energy transfer imaging.* Proc Natl Acad Sci U S A, 2008. **105**(18): p. 6596-601.

13. Lewis, B.A. and D.M. Engelman, *Lipid bilayer thickness varies linearly with acyl chain length in fluid phosphatidylcholine vesicles.* J Mol Biol, 1983. **166**(2): p. 211-7.

14. Zou, P., et al., *Superparamagnetic iron oxide nanotheranostics for targeted cancer cell imaging and pH-dependent intracellular drug release.* Mol Pharm. **7**(6): p. 1974-84.

15. Kumagai, M., et al., *Enhanced magnetic resonance imaging of experimental pancreatic tumor in vivo by block copolymer-coated magnetite nanoparticles with TGF-beta inhibitor.* J Control Release, 2009. **140**(3): p. 306-11.

16. Kamps, A.C., et al., *Nanoparticle-directed self-assembly of amphiphilic block copolymers.* Langmuir. **26**(17): p. 14345-50.

17. Hickey, R.J., et al., *Controlling the self-assembly structure of magnetic nanoparticles and amphiphilic block-copolymers: from micelles to vesicles.* J Am Chem Soc. **133**(5): p. 1517-25.

18. Lee, P.W., et al., *The characteristics, biodistribution, magnetic resonance imaging and biodegradability of superparamagnetic core-shell nanoparticles.* Biomaterials. **31**(6): p. 1316-24.

19. Jain, T.K., et al., *Iron oxide nanoparticles for sustained delivery of anticancer agents.* Mol Pharm, 2005. **2**(3): p. 194-205.

20. Xia, Z. and Y. Liu, *Reliable and global measurement of fluorescence resonance energy transfer using fluorescence microscopes.* Biophys J, 2001. **81**(4): p. 2395-402.

21. Hoppe, A.D. and J.A. Swanson, *Cdc42, Rac1, and Rac2 display distinct patterns of activation during phagocytosis.* Mol Biol Cell, 2004. **15**(8): p. 3509-19.

22. Hoppe, A., K. Christensen, and J.A. Swanson, *Fluorescence resonance energy transfer-based stoichiometry in living cells.* Biophys J, 2002. **83**(6): p. 3652-64.

23. Jiwpanich, S., et al., *Noncovalent encapsulation stabilities in supramolecular nanoassemblies.* Journal of the American Chemical Society. **132**(31): p. 10683-5.

24. Sparks, D.L., et al., *Neural tract tracing using Di-I: a review and a new method to make fast Di-I faster in human brain.* J Neurosci Methods, 2000. **103**(1): p. 3-10.

25. Iga, K., Y. Ogawa, and H. Toguchi, *Rates of systemic degradation and reticuloendothelial system (RES) uptake of thermosensitive liposome encapsulating cisplatin in rats.* Pharm Res, 1993. **10**(9): p. 1332-7.

26. Gabizon, A., et al., *Prolonged circulation time and enhanced accumulation in malignant exudates of doxorubicin encapsulated in polyethylene-glycol coated liposomes.* Cancer Res, 1994. **54**(4): p. 987-92.

27. Danson, S., et al., *Phase I dose escalation and pharmacokinetic study of pluronic polymer-bound doxorubicin (SP1049C) in patients with advanced cancer.* Br J Cancer, 2004. **90**(11): p. 2085-91.

28. Rharbi, Y., *Reduction of the glass transition temperature of confined polystyrene nanoparticles in nanoblends.* Phys Rev E Stat Nonlin Soft Matter Phys, 2008. **77**(3 Pt 1): p. 031806.

29.   Sinha, V.R., et al., *Poly-epsilon-caprolactone microspheres and nanospheres: an overview.* Int J Pharm, 2004. **278**(1): p. 1-23.

30.   Wang, H., et al., *Probing the kinetics of short-distance drug release from nanocarriers to nanoacceptors.* Angew Chem Int Ed Engl. **49**(45): p. 8426-30.

Table 5.1 Hydrodynamic size of polymeric nanoparticles

	Average hydrodynamic sizes (nm)
PEO-PS with DiO/DiI	46 ± 9
PEO-PCL with DiO/DiI	106 ± 30
PEO-PS with SPIO, DiO/DiI	142 ± 50
PEO-PS with DiD and DiR	54 ± 13
PEO-PS with SPIO, DiD/DiR	160 ± 61

Figure 5.1 Hydrodynamic size of PEO-PS with DiO/DiI (A), PEO-PCL with DiO/DiI (B), PEO-PS with SPIOs and DiO/DiI (C), PEO-PS with DiD/DiR (D), PEO-PS with SPIOs and DiD/DiR (E), and TEM of SPIO-loaded PEO-PS micelles (F)
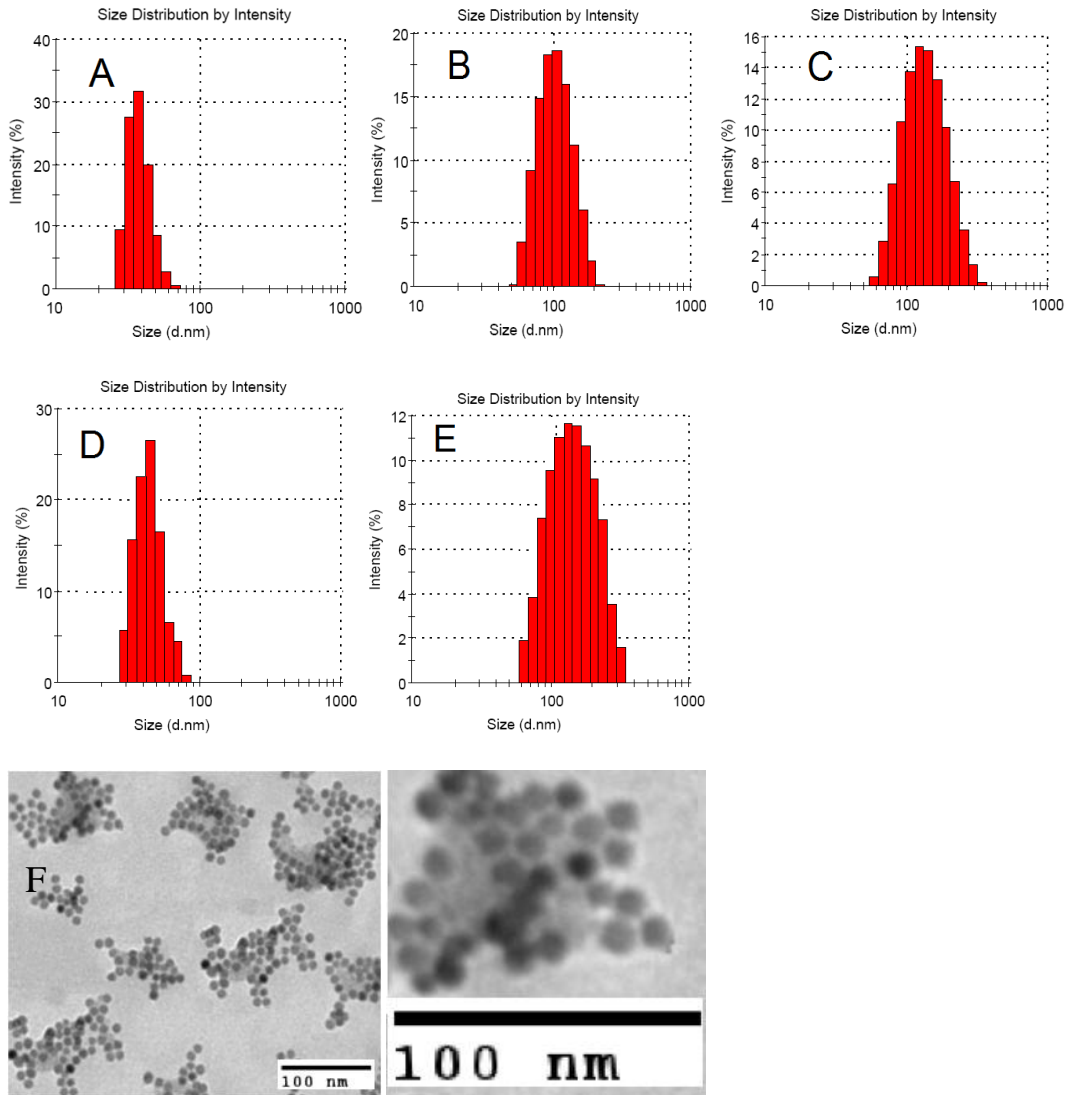
Figure 5.2 Time-resolved spectra of DiO and DiI co-loaded micelles in rat blood (A, B, C) and human plasma (D, E, F). Spectra were recorded every 5 min over a 2 hr period. (A) and (D): PEO-PS micelles with DiO/DiI; (B) and (E): PEO-PCL micelles with DiO/DiI; (C) and (F): PEO-PS micelles with SPIO, DiO and DiI.
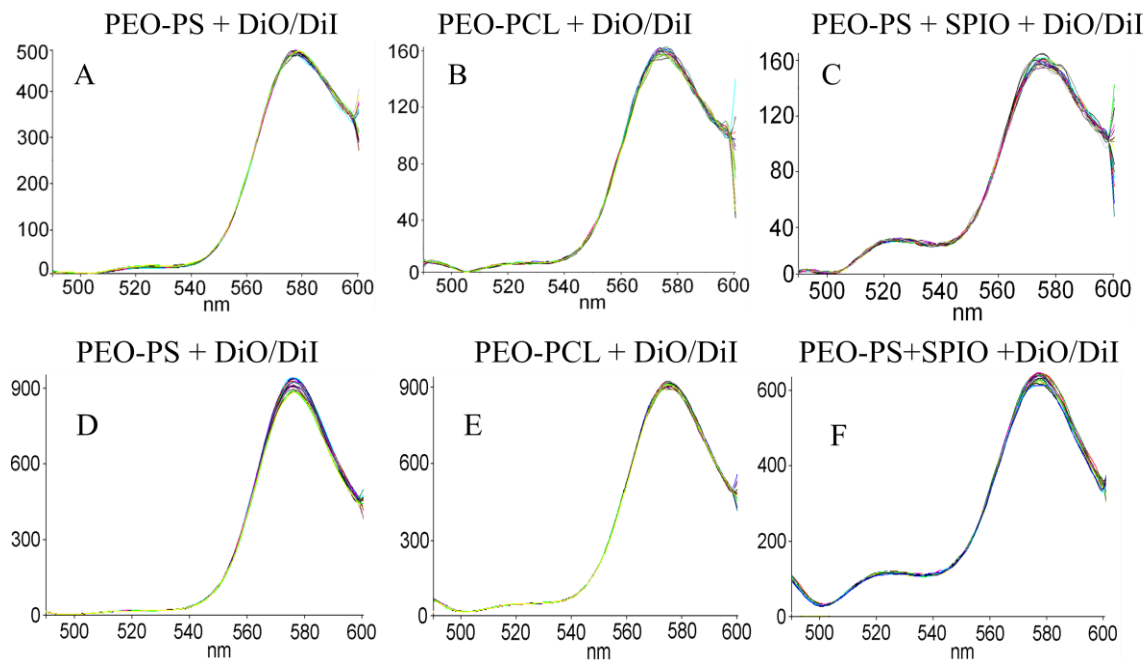
Figure 5.3 FRET images of MDA-MB-231 cells incubated with DiO/DiI co-loaded PEO-PS micelles for 2 hr (Row A, with micelles in the media; Row B, micelles were washed with PBS), or SPIOs/DiO/DiI co-loaded PEO-PS micelles for 2hr (Row C, with micelles in the media; Row D, micelles were washed with PBS)

DiI channel   DiO channel   FRET channel   FRET ratio
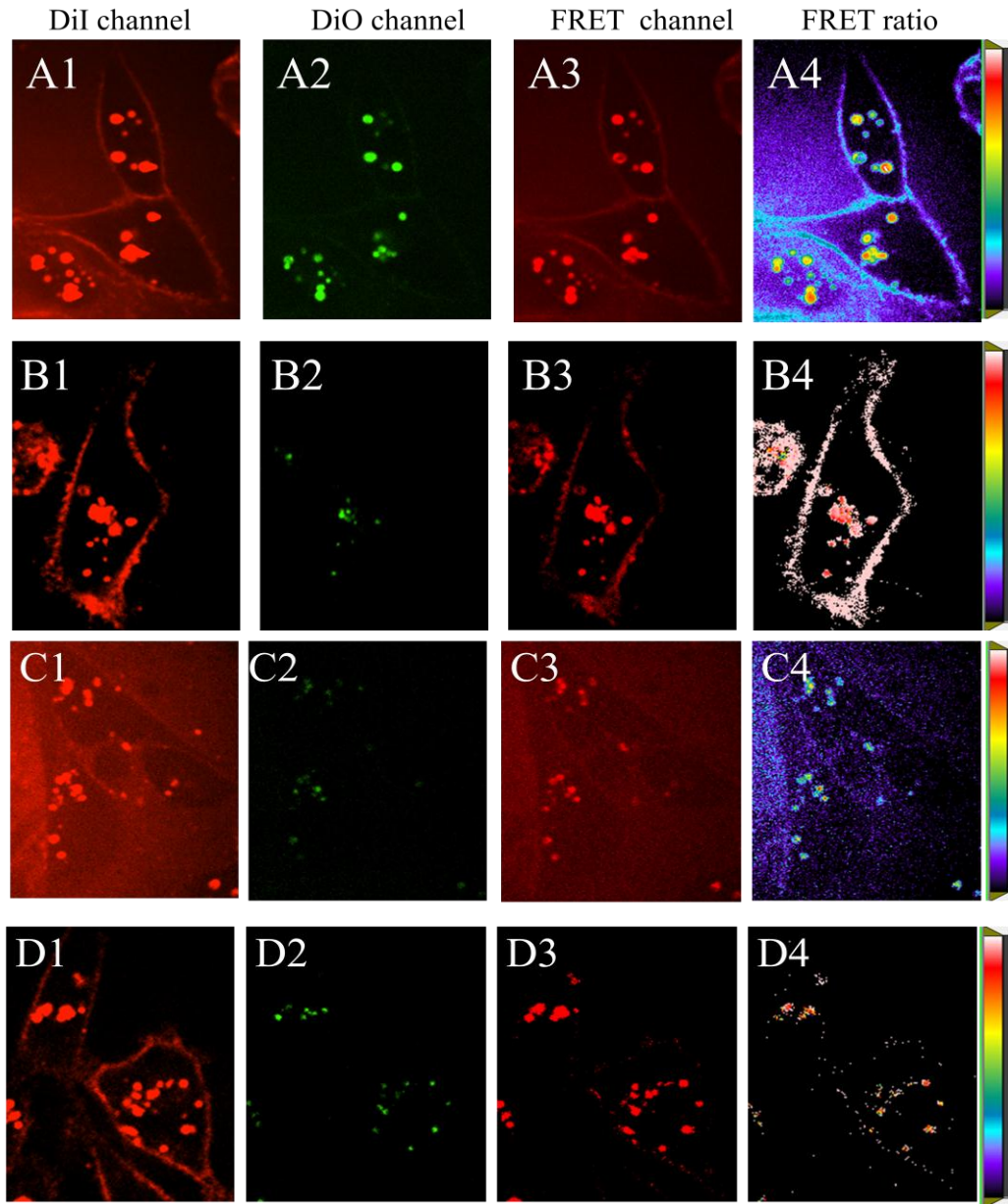
Figure 5.4 FRET images of MDA-MB-231 cells incubated with DiO/DiI co-loaded PEO-
PCL micelles for 2 hrs (Row A, with micelles in the media; Row B, micelles
were washed with PBS).

DiI channel	DiO channel	FRET channel	FRET ratio
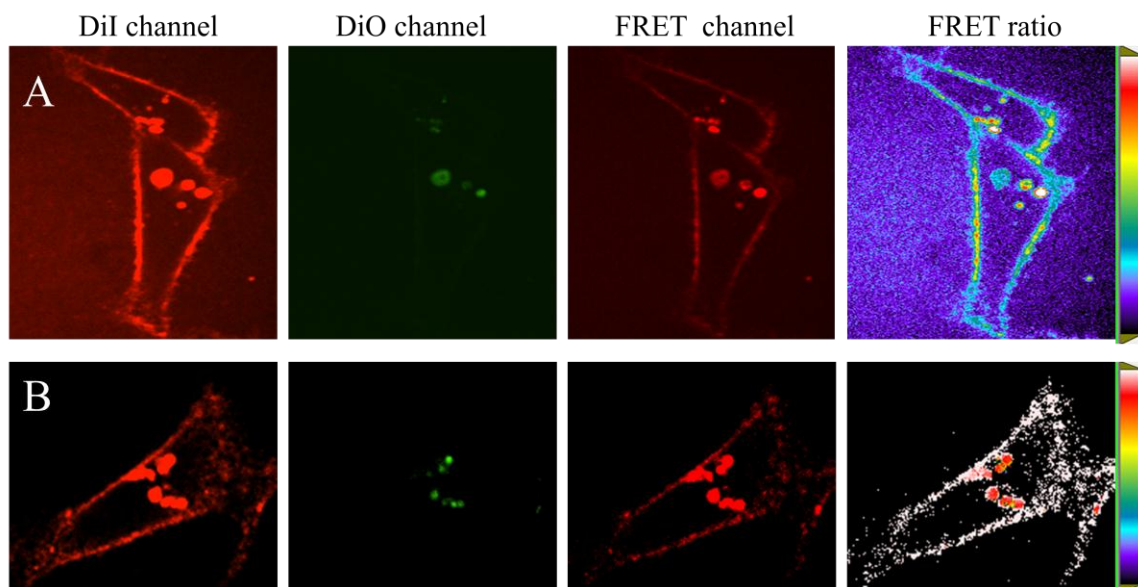
Figure 5.5 Time-resolved spectra of mixed micelles individually loaded with DiO and DiI in cell culture media with 10% FBS. Spectra were recorded every 5 min over a 2 hr period. (A) PEO-PS micelles; (B) PEO-PCL micelles; and (C) SPIO-loaded PEO-PS micelles.
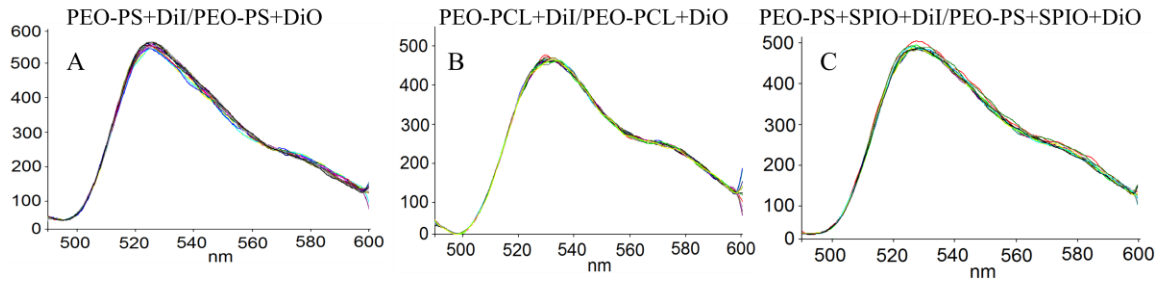
Figure 5.6 FRET images of MDA-MB-231 cells incubated with mixed DiO micelles and DiI micelles for 2 hrs. A1-A4, mixed PEO-PS micelles with 0.75% of DiO or DiI; B1-B4, mixed PEO-PCL micelles with 0.75% of DiO or DiI; C1-C4, mixed SPIO-loaded PEO-PS micelles with 0.75% of DiO or DiI; and D1-D4, mixed SPIO-loaded PEO-PS micelles with 2.5% of DiO or DiI.
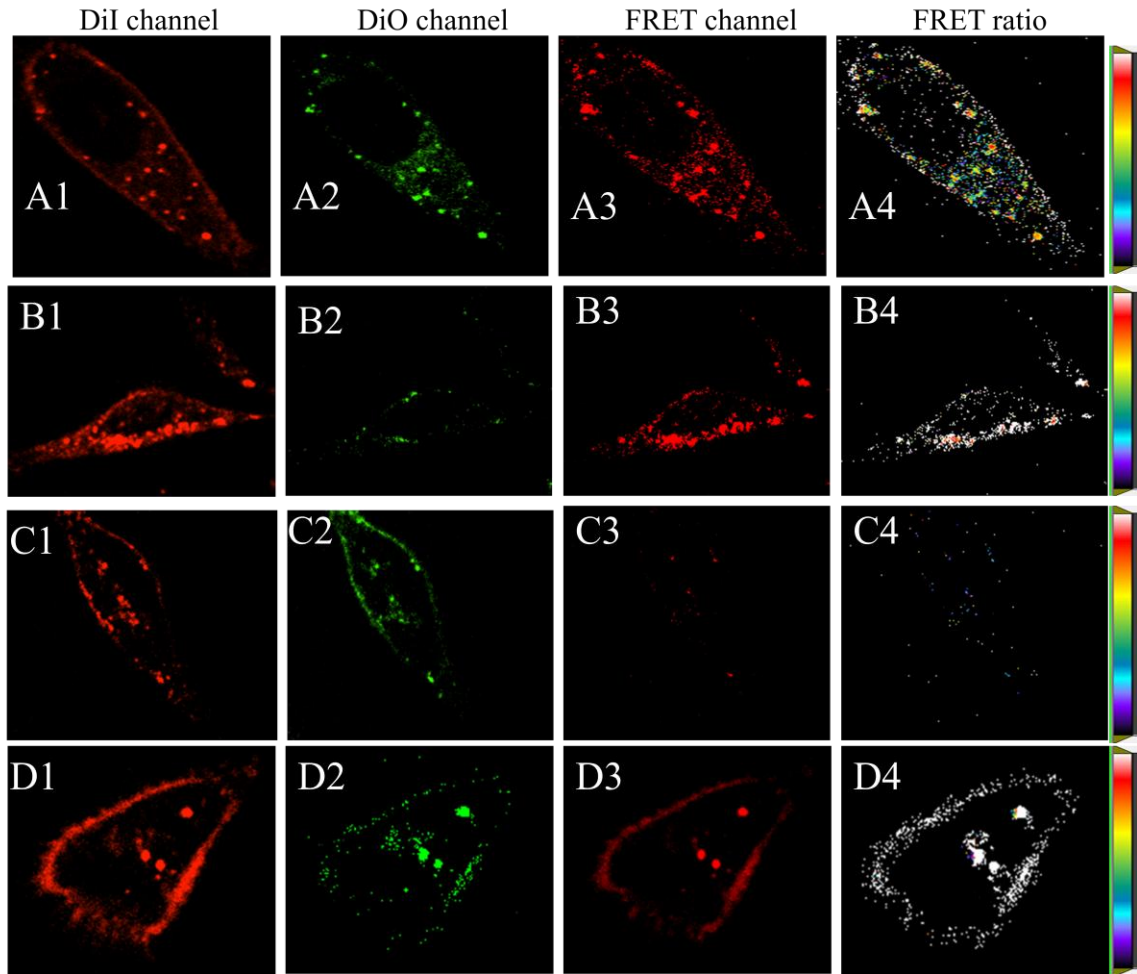
Figure 5.7 Time-resolved spectra of mixed DiD micelles and DiR micelles in mouse plasma. Spectra were recorded every 5 min over a 2 hr period. (A) PEO-PS micelles with 6% DiD or 6% DiR; (B) SPIO-loaded PEO-PS micelles with 6% DiD or 6% DiR.

PEO-PS+DiD/PEO-PS+DiR

PEO-PS+SPIO+DiD/PEO-PS+SPIO+DiR
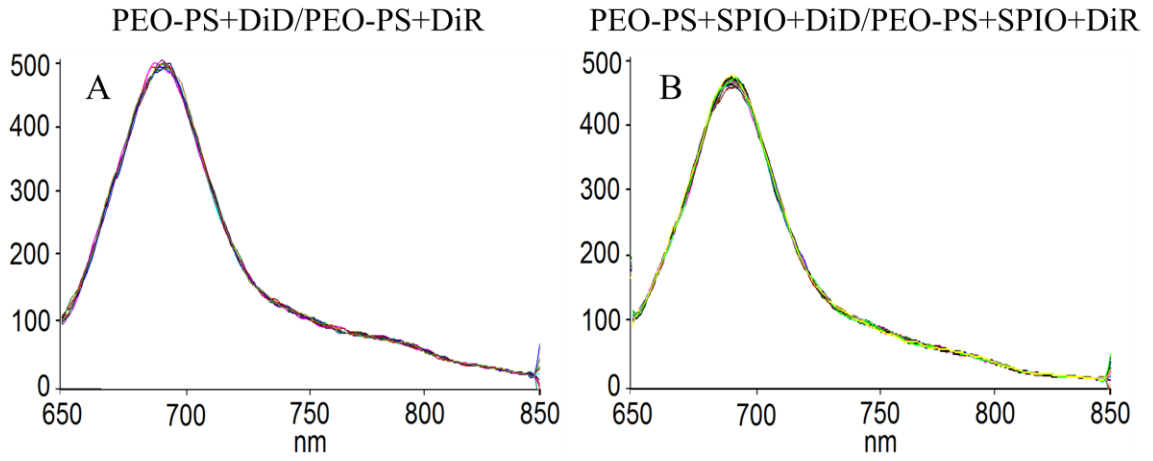
Figure 5.8 *In vivo* and *ex vivo* FRET images of xenograft mice administered with DiD/DiR loaded micelles. Images were acquired at (A) 10 min and (B) 2 hr post i.v. injection. (C) Images of tissues collected 2 hr post i.v. injection; (D) Average FRET ratios measured on the whole mouse body. (E) Average FRET ratios measured on the dissected tissues.
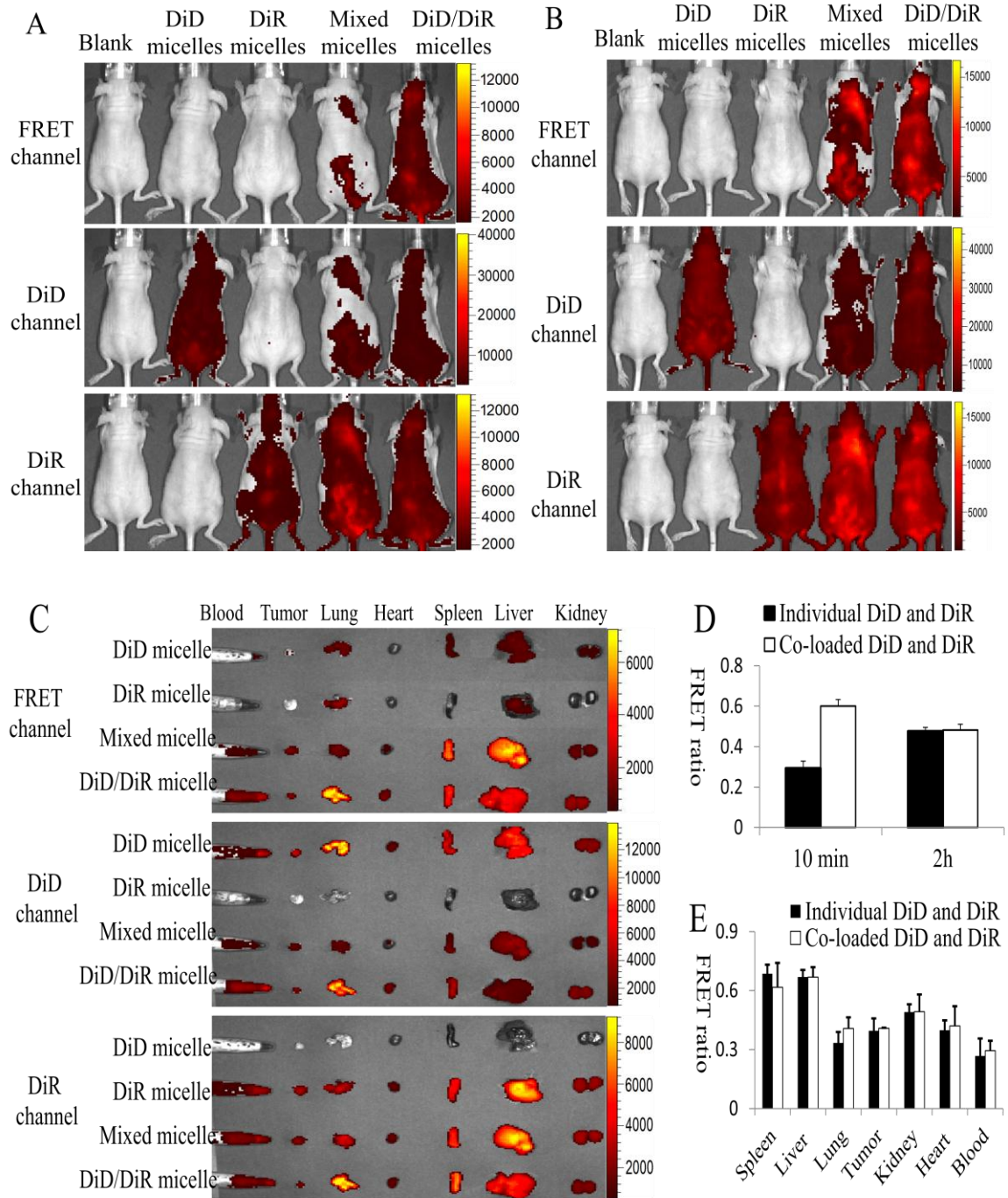
Figure 5.9 *In vivo* and *ex vivo* FRET images of xenograft mice administered with SPIO/DiD/DiR loaded micelles. Images were acquired at (A) 10 min, (B) 2 hr and (C) 6 hr post i.v. injection. (D) Images of tissues collected 6 hr post i.v. injection; (E) Average FRET ratios measured on the whole mouse body. (F) Average FRET ratios measured on the dissected tissues.
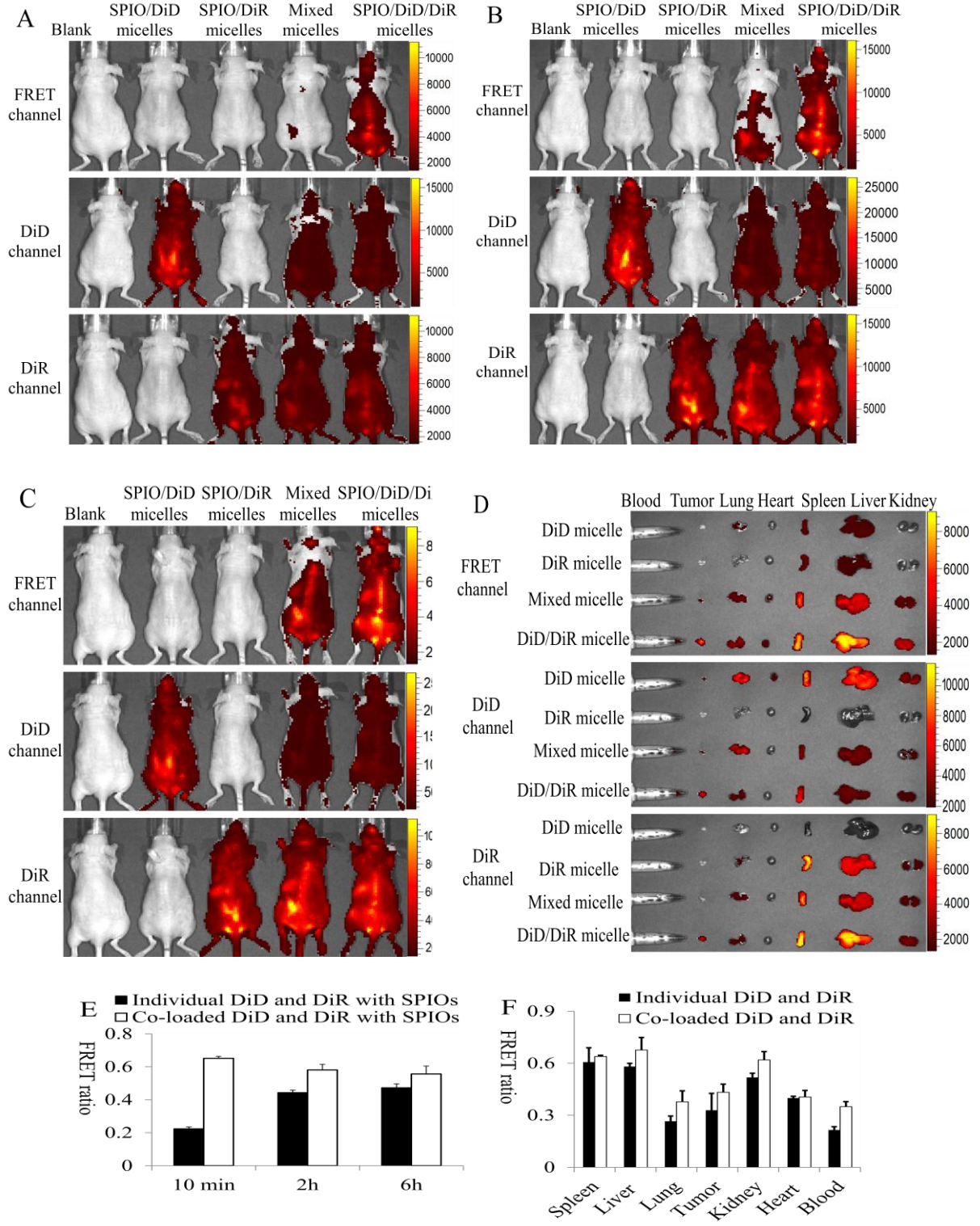
CHAPTER VI

Assessment of the Integrity of SPIO-Loaded Poly(ethylene oxide)-*b*-Polystyrene Nanoparticles in Cancer Cells and Xenograft Mice

6.1 Abstract

Premature drug release is one of the challenges which limit the clinical application of polymeric micelles for drug delivery. Investigating the micelle integrity is therefore essential to understanding the mechanisms of premature drug release. In this study, fluorescence-quecnhing by SPIOs and FRET analysis were used to assess *in vitro* and *in vivo* integrity of PEO-PS micelles and SPIO-loaded PEO-PS micelles. The micelle disassembly in cell culture media and FBS was limited over 24 h. PEO-PS micelles kept integrity during cell internalization and the micelles gradually lost integrity in endosomes/lysosomes of cancer cells. Rapid *in vivo* disassembly upon blood dilution was not observed and the gradual micelle disassembly mainly occurred in livers, spleens and tumors over 24h. In summary, the premature drug release from PEO-PS micelles was not caused by micelle disassembly.

6.2 Introduction

In polymeric nanoassemblies, polymer unimers always exist in a dynamic equilibrium with the nanoparticles at concentrations above (Critical Micelle Concentration) CMC. It's generally believed that the premature drug release in blood circulation is mainly caused by blood dilution and subsequent nanoparticle disassembly after i.v. administration [1, 2]. However, rapid cargo release was detected even when the blood concentrations of polymers were much higher than their aqueous CMC [3], suggesting the rapid release was not caused simply by blood dilution. To decrease premature drug release, it's important to determine if the rapid release is caused by premature disassembly or leakage. It is generally believed that the contacts with biological fluids, macromolecules, proteins, lipids and cells might cause the disassembly of polymeric nanoparticles [4]. Serum proteins alpha- and beta- globulins were found to accelerate the cargo release from poly(ethylene glycol)-poly(D,L-lactic acid) (PEG-PDLLA) micelles [3]. However, no direct evidence was provided to support the rapid *in vivo* disassembly of micelles.

Although the disassembly of polymeric nanoparticles in simple aqueous solutions has been studied using classical microscopy-, spectroscopy-, and chromatography-based methods, the intracellular and *in vivo* disassembly is still hard to be monitored and the direct evidence for rapid *in vivo* disassembly of micelles is very limited [4, 5]. The only reported effort to monitor the intracellular and *in vivo* disassembly of polymeric micelles was the development of a fluorogenic-based approach [4]. In this design, a fluorogenic dye fluorescein-5-carbonyl azide diacetate (F-5-CADA) was covalently conjugated to the hydrophobic block end of PEO-*b*-PCL. The fluorescence was not detectable until the

PEO-*b*-PCL micelle was disrupted and the ester group of the dye was cleaved. The *in vitro* and *in vivo* micelle disruption was monitored by detecting fluorescence. However, the limitation of this fluorogenic-based approach is obvious since it requires an additional F-5-CADA activation step (ester cleavage). The estimation of disassembly was based on two assumptions: F-5-CADA in the core of intact micelles cannot be activated and F-5-CADA is rapidly and totally activated upon the micelle disassembly, which might not be always true.

Due to their strong absorbance, gold nanoparticles and SPIOs are able to quench the fluorescence of dyes [6, 7] and quantum dots[8, 9] in close proximity by attenuating both the excitation beam and the fluorescence signal (inner filter effect). In previous reports, cationic tetramethylrhodamine (TAMRA)[10] and sulforhodamine 101[11] were conjugated to the hydrophobic end of block copolymers and the fluorescent dye-labeled polymers were used to encapsulate SPIOs. However, fluorescent dyes could not be self-quenched or quenched by SPIOs since the positive charges prevented their intramolecular interaction and close interaction with oleic acid-coated SPIOs. Furthermore, it was argued that the conjugation with cationic or anionic dyes changed cell internalization and intracellular distribution of nonionic block copolymers [12, 13]. To acquire a potent fluorescence quenching by the core-loaded SPIOs and monitor the integrity of nonionic micelles, neutral and nonpolar dyes are required.

BODIPY dyes are relatively nonpolar and the chromophore is electrically neutral [14-16]. These properties tend to minimize dye-induced perturbation of conjugate functional properties. In current study, SPIOs were encapsulated into the core of poly(ethylene oxide)-*b*-polystyrene micelles to quench the BODIPY dyes conjugated to

161

polystyrene end. The quenched fluorescence recovered upon the *in vitro* and *in vivo* disassembly of polymeric micelles. Furthermore, a pair of FRET dyes BODIPY-FL (donor) and BODIPY-TMR (acceptor) was conjugated to polystyrene end of PEO-PS. The conjugation with neutral and nonpolar BODIPY dyes allowed the formation of a compact micelle core and a strong FRET effect between the two dyes. The FRET effect was utilized to monitor the *in vitro* disassembly of PEO-PS micelles.

6.3 Materials and Methods

6.3.1 Materials

Lipophilic SPIOs with a 10 nm iron-oxide core and SuperMag Separator™ were supplied by Ocean NanoTech (Springdale, AR). PEO-b-PS-NH$_2$ (5 kD-b-5kD) were purchased from Polymer Source Inc. (Dorval, Quebec, Canada). BODIPY-FL (ex/em 504/513 nm), BODIPY-TMR (ex/em 535/574 nm), BODIPY-665 (ex/em 650/665 nm) succinimidyl ester and DiO were purchased from Invitrogen (Carlsbad, CA). Sephadex LH-20 was purchased from GE Healthcare (Piscataway, NJ). Centrifugal filter units (MWCO 10 kD) were purchased from Millipore (Billerica, MA). Dialysis tubing (MWCO 3.5-5 kD) was supplied by Spectrum Laboratories, Inc (Rancho Dominguez, CA). Tetrahydrofuran (THF) and other chemical reagents were purchased from Sigma-Aldrich Chemical Co. (St. Louis, MO).

6.3.2 Synthesis of BODIPY dye-labeled PEO-PS

A total of 128.5 mg of PEO-PS-NH$_2$ (12.8μmol) was dissolved in 2 ml anhydrous THF. 10 mg of BODIPY-FL succinimidyl ester (25.7 μmol) was added under stirring. To the mixture, 10 μL of triethylamine was added and the reaction continued overnight

under stirring. BODIPY-FL labeled PEO-PS (PEO-PS-FL) was purified using Sephadex LH-20 columns in triplicate. The purified PEO-PS-FL in THF was filtered through a 0.45μM filter and dried under vaccum. The powder was stored at -20ºC. The extent of BODIPY-FL conjugation was determined by ^{1}H-NMR. PEO-PS polymer was labeled with BODIPY-TMR (PEO-PS-TMR) and BODIPY-650/665 (PEO-PS-665) following similar procedures.

6.3.3 Polymeric nanoparticle preparation

SPIO-loaded PEO-PS-BODIPY micelles were prepared by a precipitation method. 10 mg of PEG-PS-FL, PEG-PS-TMR, or PEG-PS-665 was dissolved in 0.5 ml of THF and 1mg of SPIOs was added to the solution. 2 mL of deionized water was dropped at a speed of 6 ml/min using a syringe pump (Fisher Scientific, Pittsburgh, PA) under vigorous stirring and followed by 20 min of stirring. The solution was then dialyzed against 2 liters of deionized water for 2 days. Water was changed every day. SPIO-loaded nanoparticles were isolated and concentrated using a magnetic separator (Ocean NanoTech, Springdale, AR). Finally, the SPIO-loaded nanoparticles were resuspended in PBS (0.2 mM polymer) and filtered through a 0.45 µm filter, and stored at 4°C. By following this procedure, SPIO-free PEG-PS-FL, PEG-PS-TMR, and PEG-PS-665 micelles were prepared. The micelles were concentrated using a 10 kD MWCO centrifugal filter unit and suspended in PBS (equivalent to 0.5 mM of polymer). To prepare FRET micelles, 10 mg of PEG-PS-FL and 10 mg of PEG-PS-TMR were dissolved in 0.5 mL of THF in the presence or absence of 2 mg of SPIOs. The FRET micelles were suspended in PBS at a concentration equivalent to 1 mM of polymer.

6.3.4 Characterization of polymeric nanoparticles

The average hydrodynamic sizes were measured using a Zetasizer Nano ZS particle sizer (Malvern Instruments Ltd, Westborough, MA). The morphology of SPIO-loaded polymeric micelles was obtained on a Philips CM-100 transmission electron microscope (TEM). Nanoparticle dispersion was dropped onto a carbon-coated copper grid, dried in air at room temperature and imaged within the next 24 h. Fluorescence spectra of various micelles were measured on an LS55 PerkinElmer luminescence spectrometer (Waltham, MA) with an excitation at 480 nm for BODIPY-FL and FRET signal, 520 nm for BODIPY-TMR and 610 nm for BODIPY-665. To evaluate the quenching effect of SPIOs on fluorescence of BODIPY-TMR and BODIPY-665, SPIO-loaded micelles were suspended in PBS or THF (5μM) and the fluorescent spectra of micelles were recorded.

6.3.5 Integrity of micelles in PBS, cell culture media and fetal bovine serum

Aliquots of FL-TMR FRET micelles and SPIO-loaded FRET micelles were incubated in the medium (phosphate-buffered saline, RPMI 1640 with 10% fetal bovine serum (FBS), or 100% FBS) in triplicate in a 96-well plate for 0-24 h. The final polymer concentrations were 50 μM and 5 μM for FRET micelles and 20 μM and 2 μM for SPIO-loaded FRET micelles. Fluorescence of BODIPY-FL (ex/em 488/520 nm) and FRET signals (ex/em 488/590 nm) were measured using a Synergy plate reader (BioTek, Winooski, VT) at the end of each time point. The FRET ratios were calculated as FRET ratio = $I_{FRET}/ (I_{FRET} + I_{FL})$. Meanwhile, the FRET ratios of FRET micelles (50 μM) and SPIO-loaded FRET micelles (20 μM) in THF/water (50%/50%) were measured as a positive control. The FRET ratio of mixed PEO-PS-FL micelles and PEO-PS-TMR micelles (molar ratio 1:1) in PBS was also measured as a negative control.

6.3.6 Fluorescence and FRET confocal microscopy

A prostate cancer cell line PC-3 obtained from American Type Culture Collection (ATCC, Rockville, MD) was cultured on an 8-well Lab-Tek glass chamber slides (Thermo Fisher Scientific, Rochester, NY) for FRET and fluorescent confocal imaging. 10^4 cells per well were incubated for 2 days to allow cell adherence. To detect the possible disassembly of micelles on plasma membrane, cells were incubated with 10 μM of PEO-PS micelles containing 1% of DiO for 1 h to stain cell membrane. After washed with PBS, cells were incubated with 50 μM of PEO-PS-TMR micelles or 50 μM of SPIO-loaded PEO-PS-TMR micelles for 0.5 h or 8 h, and then washed with PBS for imaging. Additionally, to monitor the possible intracellular disassembly of micelles, cells were incubated with 50 μM of PEO-PS-FL/TMR FRET micelles or SPIO-loaded FRET micelles for 8 h. In parallel, cells were incubated with mixed PEO-PS-FL micelles (25 μM) and PEO-PS-TMR micelles (25 μM) or mixed SPIO-loaded PEO-PS-FL micelles (25 μM) and PEO-PS-TMR micelles (25 μM) for 8 h as a control. Finally, the cells were washed with PBS for imaging.

The FRET confocal images were acquired by using a digital camera (C9100, Hamamatsu Photonics, Japan) mounted on a Visitech VT Infinity 3 array-scanning confocal system (VisiTech International Ltd., United Kingdom) attached to a Nikon TE-2000U microscope with a 60X Nikon Plan Apo water-immersion objective at room temperature. Images were recorded under DiO or BODIPY-FL channel (488 nm excitation, 535 ± 20 nm emission), FRET channel (488 nm excitation, 580 ± 20 nm emission) and BODIPY-TMR channel (543 nm excitation, 580 ± 20 nm emission). The exposure time was 200 ms. Images were obtained using MetaMorph v6.5.3 (Universal

Imaging, Malvern, PA). The images were background-subtracted using the "Background Correction" tool in MetaMorph. Crosstalk correction and FRET ratios calculation were carried out using an in-house FRETCalculator program and Matlab. To correct crosstalk, correction coefficients α and β were determined from cells incubated with DiI micelles only ($\alpha = I_{FRET}/I_{TMR}$) and DiO micelles only ($\beta = I_{FRET}/I_{DiO}$ or $\beta = I_{FRET}/I_{FL}$) [17-19]. I_{FRET}, I_{TMR}, I_{DiO} and I_{FL} were intensities in each region of interest (ROI) under FRET, TMR, and DiO filter sets, respectively. FRET ratios were calculated as: $I_{FRET} / (I_{FRET} + I_{DiO})$ or $I_{FRET} / (I_{FRET} + I_{FL})$.

To monitor the disassembly of micelles, PC-3 cells were incubated with 50 µM of PEO-PS- TMR micelles or 50 µM of SPIO-loaded PEO-PS- TMR micelles. Images were obtained in the presence of micelles in the media at 10 min, 2 h and 8 h. After 8 h incubation, cells were washed with PBS and imaged under a BODIPY-TMR channel (543 nm excitation, 580 ± 20 nm emission)

6.3.7 Xenograft mice and *in vivo* fluorescent imaging

The animal procedures were performed according to a protocol approved by the University Committee for the Use and Care of Animals (UCUCA) at University of Michigan. Female athymic nude mice (nu/nu), obtained from National Cancer Institute (Bethesda, MD) at 8 weeks of age, were subcutaneously inoculated in the back with 5×10^6 PC-3 cells suspended in a mixture of 50 µL of PBS and 50 µL of matrixgel basement membrane (BD Biosciences, San Jose, CA). When the tumor implants reached 0.8 cm in diameter, the tumor-bearing mice were subjected to the imaging studies.

In vivo fluorescence imaging was performed with an IVIS Spectrum imaging system (Xenogen, Alameda, CA). The exposure time was 1s. Images were acquired and analyzed

using Living Image 2.5 software (Xenogen, Alameda, CA). Images were recorded under an excitation of 610 nm and an emission of 680 nm at 2 h and 24 h after i.v. administration of PEO-PS-665 micelles (equivalent to 0.1 μmole of polymer) or SPIO-loaded PEO-PS-665 micelles (equivalent to 0.1 μmole of polymer). Simultaneously, 0.2 ml of PEO-PS-665 micelles or SPIO-loaded PEO-PS-665 micelles in an eppendorf tube (10 μM in THF, PBS or mouse plasma) were imaged with mice.

At the end of experiment, the mice were sacrificed using CO_2. Blood and tissues (tumor, heart, lung, liver, spleen, and kidneys) were collected and tissues were rinsed with PBS. Blood and tissue samples were imaged using the identical settings as *in vivo* imaging.

6.4 Results

6.4.1 Preparation and characterization of polymeric nanoparticles

To test the *in vitro* and *in vivo* integrity of PEO-PS micelles and SPIO loaded PEO-PS micelles, lipophilic and neutral BODIPY dyes (FL, TMR and 665) were conjugated to amine at the end of polystyrene block. Oleic acid coated SPIOs were entrapped in the core of the micelles (Scheme 6.1). Figure 6.1 and Table 6.1 show the hydrodynamic sizes of various micelles. The average particle sizes of BODIPY labeled micelles ranged from 35 nm to 46 nm. The incorporation of 10% of SPIOs increased the average size of PEO-PS micelles to 115-178 nm. TEM of SPIO-loaded PEO-PS micelles showed clusters of 10 nm SPIOs in the cores of PEO-PS-TMR micelles (Figure 6.1I).

The formation of core-shell micelles caused autoquenching of BODIPY dyes in the core. For example, the PEO-PS-TMR polymers (5 μM) in THF exhibited a fluorescent

intensity 5-fold higher than that of micelles in PBS (5 µM) while SPIO-loaded PEO-PS-TMR micelles (5 µM) showed a 21-fold higher fluorescence in THF than in PBS (Figure 6.2A). Similar fluorescence quenching was also observed for PEO-PS-665 micelles and SPIO-loaded PEO-PS-665 micelles (Figure 6.2B). Figure 6.2C showed the FRET spectra of various BODIPY-FL and BODIPY-TMR labeled micelles in PBS (10 µM). PEO-PS-FL/TMR micelles showed a FRET ratio of 0.78 while the mixed PEO-PS-FL micelles and PEO-PS-TMR micelles (molar ratio 1:1) resulted in a FRET ratio of 0.23.

6.4.2 Integrity of PEO-PS micelles in PBS, cell culture media and FBS

To assess the *in vitro* integrity of micelles, FL/TMR FRET micelles were incubated in PBS, RPMI 1640 with 10% of FBS and 100% FBS at concentrations of 50 µM and 5 µM while SPIO-loaded FL/TMR FRET micelles were incubated at concentrations of 20 µM and 2 µM. Fluorescence of BODIPY-FL and FRET intensity of BODIPY-FL/TMR were measured at 0.5 h, 6 h and 24 h. FRET ratios of micelles were calculated as: FRET ratio = $I_{FRET}/(I_{FRET} + I_{FL})$[20]. The disassembly of FRET micelles was expected to result in a decrease of FRET ratio. As shown in Figure 6.3A, the FRET ratios of micelles in PBS were constant over 24 h. FRET ratios of FRET micelles were 0.75 at 5 µM and 0.77 at 50 µM. The FRET ratios of SPIO-loaded FRET micelles were 0.70 at 2 µM and 0.73 at 20 µM. The results revealed that micelles were not disrupted in PBS within 24 h. In RPMI 1640 media with 10% of FBS (Figure 6.3B), FRET ratio of FRET micelles (50 µM) decreased from 0.76 at 1h to 0.74 at 24h and the FRET ratio of SPIO-loaded micelles (20 µM) decreased from 0.73 to 0.69, suggesting the disassembly of limited amount of micelles or a slight increase of the particle size of micelles. In 100% of FBS, the FRET ratios of FRET micelles keep constant over 24 h while the FRET ratio of SPIO-loaded

micelles (20 µM) slightly decreased from 0.69 to 0.67. In contrast, FRET micelles and SPIO-loaded FRET micelles in 50% of THF showed FRET ratios of 0.48 and 0.44, respectively. By using the plate reader, the FRET ratios of mixed PEO-PS-FL and PEO-PS-TMR micelles in PBS were measured as 0.32 and 0.33 in the absence of SPIOs and presence of SPIOs, respectively. The results suggested that most micelles kept their integrity in PBS, RPMI 1640 and FBS within 24 h.

6.4.3 FRET confocal imaging

To visualize the possible disassembly of micelles on plasma membrane, PC-3 cells were incubated with PEO-PS-TMR micelles or SPIO-loaded PEO-PS-TMR micelles. After washed with PBS, cell membrane was stained with DiO, a green donor fluorescent dye. If micelle disassembly occurs on plasma membrane, the distance between DiO (donor) and TMR (acceptor) is short enough for FRET effect (the thickness of cell membrane is 3-4 nm) [21, 22]. As shown in Figure 6.4A1-4, cell uptake of PEO-PS-TMR was very low in 0.5h and no FRET signal was detected on cell membrane. After incubation with micelles for 8h and DiO for 1h, both the polymers and DiO accumulated in endosomes/lysosomes (Figure 6.4B1-4). FRET signals were not detectable from from plasma membrane, suggesting micelles kept integrity during cell internalization. However, FRET signals were detected from endosomes/lysosomes, indicating that micelles were disrupted in endosomes/lysosomes or DiO gradually partitioned into micelles in 8h. Similar results were observed when cells were incubated with SPIO-loaded PEO-PS-TMR micelles (Figure 6.4 C and D).

To monitor the possible intracellular disassembly of micelles, PC-3 cells were incubated with PEO-PS-FL/TMR FRET micelles (Figure 6.5A) and mixed FL and TMR

micelles (Figure 6.5B) in parallel. FRET signals were detected on both plasma membrane and organelle membrane after incubation with FRET micelles for 8h (Figure 6.5A3), indicating the integrity of micelles during cell internalization. The FRET ratios from endosomes/lysosomes were slightly lower than that from plasma membrane (Figure 6.5A4), suggesting partial disassembly of micelles in endosomes/lysosomes. However, no FRET was observed from plasma membrane when the cells were incubated with mixed FL and TMR micelles (Figure 6.5B3). The weak FRET signal and low FRET ratio (Figure 6.5B4) in endosomes/lysosomes revealed the disassembly of micelles. Similar results were observed when the cells were incubated with SPIO-loaded FRET micelles (Figure 6.5C). For cells incubated with mixed SPIO-loaded FL and TMR micelles (Figure 6.5D), the FRET signals from endosomes/lysosomes reveled the intracellular disassembly of SPIO-loaded micelles.

6.4.4 Fluorescent imaging of PC-3 cells

PC-3 cells were incubated with PEO-PS-TMR micelles (Figure 6.6A-D) and SPIO-loaded PEO-PS-TMR micelles (Figure 6.6E-H). Images were obtained at 10 min, 2h and 8h in the presence micelles in the media. During the first 2h, the intracellular fluorescent intensities were found to be lower than that of micelles in the media (Figure 6.6 A, B, E, F). However, at 8h, the disassembly of micelles relieved the autoquenching of TMR and quenching by SPIOs. Both intracellular micelle disassembly and accumulation of micelles in endosomes/lysosomes resulted in the higher intracellular fluorescence than that of micelles in media (Figure 6.6C and G).

6.4.5 *In vivo* **micelle disassembly in xenograft mice**

To assess the *in vivo* integrity of micelles and SPIO-loaded micelles, PEO-PS polymer was labeled with BODIPY-665, a neutral dye with an emission at 665 nm. Similar to PEO-PS-TMR micelles, compared with the PEO-PS-665 unimers in THF, the formation of micelles in PBS and mouse plasma decreased the fluorescence of BODIPY-665 (Figure 6.7A). When SPIO-loaded PEO-PS-665 micelles were excited at 610 nm, SPIOs were found to be able to quench BODIPY-665 (Figure 6.7A). PEO-PS-665 micelles and SPIO-loaded PEO-PS-665 micelles were i.v. injected to nude mice with xenograft tumors. At 2h following the injection of PEO-PS-665 micelles, due to the very limited disassembly of micelles and poor tissue penetration of BODIPY-665, only very low fluorescence was detected from the mouse. Fluorescence was not detectable from mouse treated with SPIO-loaded PEO-PS-665 micelles. However, after 24 h, both the mouse treated with PEO-PS-665 micelles and the mouse treated with SPIO-loaded PEO-PS-665 micelles showed dramatically increased fluorescence. The large particle size of SPIO-loaded PEO-PS-665 micelles (167±43 nm) caused the rapid elimination from the mouse, which might explain the lower fluorescence than that of the mouse treated with PEO-PS-665 micelles.

The mice were sacrificed at 2h and 24 h following the injection of micelles to collect the blood and tissues. Figure 6.7B showed the image of blood and tissue samples from blank control mouse and mice treated with SPIO-loaded PEO-PS-665 micelles. At 2h after the injection of SPIO-loaded micelles, the fluorescent intensities of the blood and tissues were similar to that of blank mouse, suggesting that most micelles kept integrity in 2h. At 24h post the injection of micelles, high fluorescence was detected in livers,

spleens, lungs and tumors, indicating the accumulation and disassembly of micelles in these tissues.

6.5 Discussion

Premature drug release is one of the challenges which limit the clinical application of polymeric micelles for drug delivery [23, 24]. It's generally believed that polymeric micelles, upon administration into the blood stream, were diluted to a concentration lower than CMC by the large volume of blood, resulting in the disassembly of micelles and premature drug release [1, 2]. However, in our previous study, premature cargo release from PEO-PS micelles was observed although the polymer concentration was much higher than CMC. Investigating the micelle integrity is therefore essential to understating the mechanisms of premature drug release.

One of the reasons for the limited understanding of *in vivo* integrity of micelles is currently there are no practical experimental methods available to trace the micelles and to detect the disassembly of micelles without micelle modification [1]. Various fluorescent dyes such as tetramethylrhodamine (TAMRA)[10, 12] and sulforhodamine 101[11] have been used to label the hydropobic end of block copolymers. Although the formation of micelles was observed, the cationic dyes could not form a compact core and efficient fluorescence quenching was not achieved. In our experiment, PEO-PS was labeled with 5-FAM or TAMRA, SPIOs entrapped in the core of micelles were not able to quench 5-FAM or TAMRA (data not shown). In contrast, neutral and lipophilic BODIPY dye PEO-PS formed micelles with a compact core. The encapsulation of SPIOs could dramatically quench the fluorescence of BODIPY dyes. BODIPY-FL and

172

BODIPY-TMR in core of micelles showed effective FRET effect, which was utilized to monitor the disassembly of micelles in real time.

The incubation of FL/TMR FRET micelles and SPIO-loaded FRET micelles with PBS showed that the micelles kept integrity in PBS within 24 h, which was consistent with previous report [4]. In RPMI 1640 media containing 10% of FBS and 100% of FBS, the FRET ratios of micelles only slightly decreased, suggesting that most micelles kept integrity and the decrease of FRET ratio was likely due to the particle size changes in different media. In a previous report [4], incubation with RPMI 1640 media and 100% of FBS for 24h caused 36% and 74% integrity loss of poly(caprolactone)-b-poly(ethylene oxide) (PEO-PCL) micelles. However, the micelles disassembly was probably overestimated since this method was based on the activation of a dye F-5-CADA (to cleave an ester of the fluorescent dye to generate fluorescence). Considering the dynamic equilibrium between PEO-PCL unimers and micelles in the incubations, the endogenous esterases in FBS could rapidly activitate F-5-CADA even without the disassembly of micelles. Additionally, compared with PEO-PCL, PEO-PS polymer has a much lower CMC and higher glass transition temperature of polystyrene (107ºC)[25], which also explained the less disassembly of PEO-PS micelles in FBS.

FRET has been utilized to investigated the lipid exchange of micelles and liposomes [26, 27]. In current study, the FRET between BODIPY-FL and BODIPY-TMR was used to monitor the micelles disassembly. The FRET confocal imaging showed that PEO-PS micelles kept integrity during cell internalization and the micelles gradually lost integrity in endosomes/lysosomes of cancer cells. This was consistent with a previous study, in which 20% of internalized micelles were disrupted after incubation with HTB-4 cancer

173

cells for 20 h [4]. Ideally, FRET effect between BODIPY dyes can be used to visualize the *in vivo* disassembly of micelles. Unfortunately, a pair of near-infrared BODIPY dyes (emission > 750 nm) is still not commercially available. The available BODIPY dye with the longest emission is BODIPY-665. Although SPIO-loaded PEO-PS-655 micelles were assessed in mice, the poor tissue penetration limited its application to noninvasive imaging.

6.6 Conclusion

In this study, fluorescence-quecnhing by SPIOs and FRET analysis were used to assess *in vitro* and *in vivo* integrity of PEO-PS micelles and SPIO-loaded PEO-PS micelles. The micelle disassembly in cell culture media and FBS was limited over 24 h. PEO-PS micelles kept integrity during cell internalization and the micelles gradually lost integrity in endosomes/lysosomes of cancer cells. Rapid i*n vivo* disassembly upon blood dilution was not observed and the gradual micelle disassembly mainly occurred in livers, spleens and tumors over 24h. In summary, the premature drug release from PEO-PS micelles was not caused by micelle disassembly.

6.7 References

1.   Bae, Y.H. and H. Yin, *Stability issues of polymeric micelles.* J Control Release, 2008. **131**(1): p. 2-4.
2.   Moghimi, S.M., A.C. Hunter, and J.C. Murray, *Long-circulating and target-specific nanoparticles: theory to practice.* Pharmacol Rev, 2001. **53**(2): p. 283-318.
3.   Chen, H., et al., *Fast release of lipophilic agents from circulating PEG-PDLLA micelles revealed by in vivo forster resonance energy transfer imaging.* Langmuir, 2008. **24**(10): p. 5213-7.

4.   Savic, R., et al., *Assessment of the integrity of poly(caprolactone)-b-poly(ethylene oxide) micelles under biological conditions: a fluorogenic-based approach.* Langmuir, 2006. **22**(8): p. 3570-8.

5.   Savic, R., A. Eisenberg, and D. Maysinger, *Block copolymer micelles as delivery vehicles of hydrophobic drugs: micelle-cell interactions.* J Drug Target, 2006. **14**(6): p. 343-55.

6.   Wang, H., et al., *Probing the kinetics of short-distance drug release from nanocarriers to nanoacceptors.* Angew Chem Int Ed Engl. **49**(45): p. 8426-30.

7.   Manciulea, A., A. Baker, and J.R. Lead, *A fluorescence quenching study of the interaction of Suwannee River fulvic acid with iron oxide nanoparticles.* Chemosphere, 2009. **76**(8): p. 1023-7.

8.   Mandal, S.K., et al., *Encapsulation of magnetic and fluorescent nanoparticles in emulsion droplets.* Langmuir, 2005. **21**(9): p. 4175-9.

9.   Quarta, A., et al., *Fluorescent-magnetic hybrid nanostructures: preparation, properties, and applications in biology.* IEEE Trans Nanobioscience, 2007. **6**(4): p. 298-308.

10.   Kessinger, C.W., et al., *In vivo angiogenesis imaging of solid tumors by alpha(v)beta(3)-targeted, dual-modality micellar nanoprobes.* Exp Biol Med (Maywood). **235**(8): p. 957-65.

11.   GuangHui Gao, H.H., JungHee Lee and DooSung Lee, *An acidic pH-triggered polymeric micelle for dual-modality MR and optical imaging.* Journal of Materials Chemistry, 2010. **20**: p. 5454-5461.

12.   Savic, R., et al., *Micellar nanocontainers distribute to defined cytoplasmic organelles.* Science, 2003. **300**(5619): p. 615-8.

13.   Moghimi, S.M., et al., *Cellular distribution of nonionic micelles.* Science, 2004. **303**(5658): p. 626-8; author reply 626-8.

14.   Arroyo, I.J., et al., *The smallest and one of the brightest. Efficient preparation and optical description of the parent borondipyrromethene system.* J Org Chem, 2009. **74**(15): p. 5719-22.

15.   Schmitt, A., et al., *Synthesis of the core compound of the BODIPY dye class: 4,4'-difluoro-4-bora-(3a,4a)-diaza-s-indacene.* J Fluoresc, 2009. **19**(4): p. 755-8.

16.   Aurore Loudet, K.B., *BODIPY Dyes and Their Derivatives: Syntheses and Spectroscopic Properties.* Chemical Reviews, 2007. **107**(11): p. 4891-4932.

17.   Xia, Z. and Y. Liu, *Reliable and global measurement of fluorescence resonance energy transfer using fluorescence microscopes.* Biophys J, 2001. **81**(4): p. 2395-402.

18.   Hoppe, A.D. and J.A. Swanson, *Cdc42, Rac1, and Rac2 display distinct patterns of activation during phagocytosis.* Mol Biol Cell, 2004. **15**(8): p. 3509-19.

19.   Hoppe, A., K. Christensen, and J.A. Swanson, *Fluorescence resonance energy transfer-based stoichiometry in living cells.* Biophys J, 2002. **83**(6): p. 3652-64.

20.   Chen, H., et al., *Release of hydrophobic molecules from polymer micelles into cell membranes revealed by Forster resonance energy transfer imaging.* Proc Natl Acad Sci U S A, 2008. **105**(18): p. 6596-601.

21.   Lewis, B.A. and D.M. Engelman, *Lipid bilayer thickness varies linearly with acyl chain length in fluid phosphatidylcholine vesicles.* J Mol Biol, 1983. **166**(2): p. 211-7.

22. Xiao, L., et al., *Role of cellular uptake in the reversal of multidrug resistance by PEG-b-PLA polymeric micelles.* Biomaterials. **32**(22): p. 5148-57.

23. Gabizon, A., et al., *Prolonged circulation time and enhanced accumulation in malignant exudates of doxorubicin encapsulated in polyethylene-glycol coated liposomes.* Cancer Res, 1994. **54**(4): p. 987-92.

24. Danson, S., et al., *Phase I dose escalation and pharmacokinetic study of pluronic polymer-bound doxorubicin (SP1049C) in patients with advanced cancer.* Br J Cancer, 2004. **90**(11): p. 2085-91.

25. Rharbi, Y., *Reduction of the glass transition temperature of confined polystyrene nanoparticles in nanoblends.* Phys Rev E Stat Nonlin Soft Matter Phys, 2008. **77**(3 Pt 1): p. 031806.

26. Reulen, S.W. and M. Merkx, *Exchange kinetics of protein-functionalized micelles and liposomes studied by Forster resonance energy transfer.* Bioconjug Chem. **21**(5): p. 860-6.

27. Skajaa, T., et al., *Quantum Dot and Cy5.5 Labeled Nanoparticles to Investigate Lipoprotein Biointeractions via Forster Resonance Energy Transfer.* Nano Lett.

Table 6.1 Hydrodynamic size of polymeric nanoparticles

	Average hydrodynamic sizes (nm)
PEO-PS-FL	35 ± 8
PEO-PS-TMR	46 ± 15
PEO-PS –FL/TMR	39 ± 11
PEO-PS-665	40 ± 9
PEO-PS-FL+SPIOs	115 ± 41
PEO-PS-TMR+SPIOs	178 ± 66
PEO-PS-FL/TMR+SPIOs	149 ± 45
PEO-PS-665+SPIOs	167 ± 43

Scheme 6.1 Structures of BODIPY dye labeled micelles, SPIO-loaded micelles and FL/TMR FRET micelles

PEO-PS-TMR micelle or
PEO-PS-665 micelle
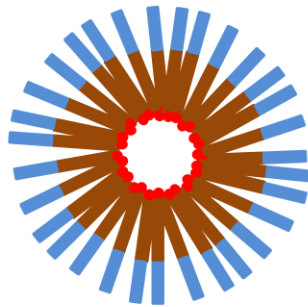
SPIO-loaded PEO-PS-TMR micelles or
SPIO-loaded PEO-PS-665 micelle
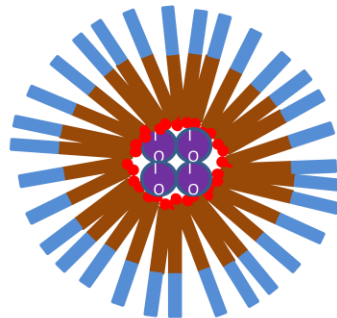
PEO-PS-FL/TMR micelle
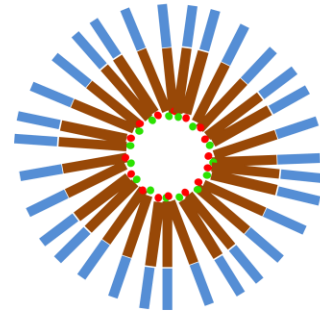
| | | PEO-PS | | SPIO | | BODIPY-FL | | BODIPY-TMR or BODIPY-665 |

Figure 6.1 Hydrodynamic sizes of various micelles: PEO-PS-FL(A), PEO-PS-TMR (B), PEO-PS-FL/TMR (C), SPIO-loaded PEO-PS-FL (D), SPIO-loaded PEO-PS-TMR (E), SPIO-loaded PEO-PS-FL/TMR (F), PEO-PS-665 (G), and SPIO-loaded PEO-PS-665 micelles (H); TEM image of SPIO-loaded PEO-PS-TMR micelles (I)
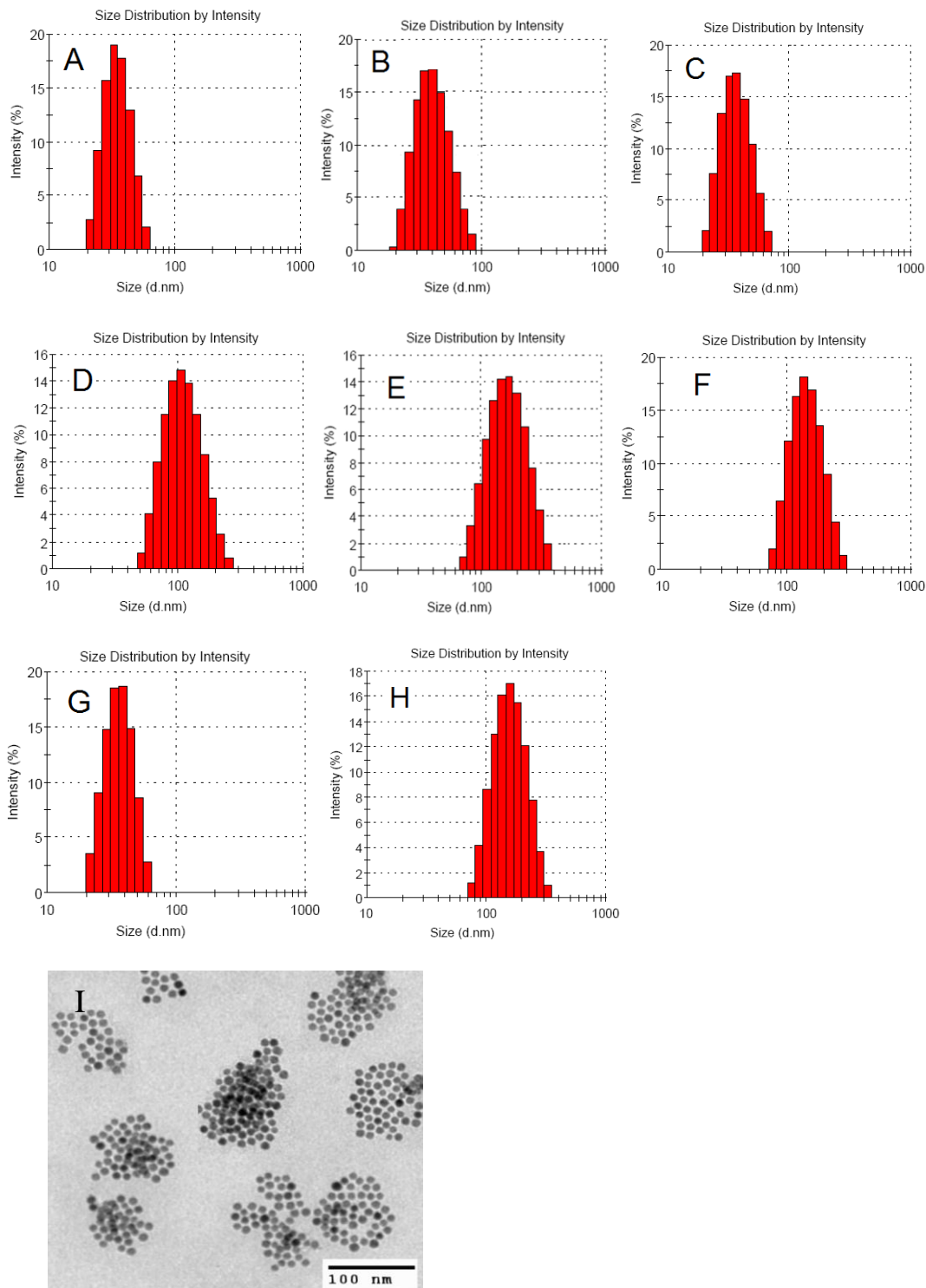
Figure 6.2 Fluorescent spectra of PEO-PS-TMR micelles (A), PEO-PS-665 micelles (B), and PEO-PS-FL/TMR FRET micelles (C).

— PEO-PS-TMR micelles in THF
— SPIO-loaded PEO-PS-TMR micelles in THF
— PEO-PS-TMR micelles in PBS
— SPIO-loaded PEO-PS-TMR micelles in PBS

— PEO-PS-665 micelles in THF
— SPIO-loaded PEO-PS-665 micelles in THF
— PEO-PS-665 micelles in PBS
— SPIO-loaded PEO-PS-665 micelles in PBS

— Mixed PEO-PS-FL and PEO-PS-TMR micelles

— PEO-PS-FL/TME micelles

180
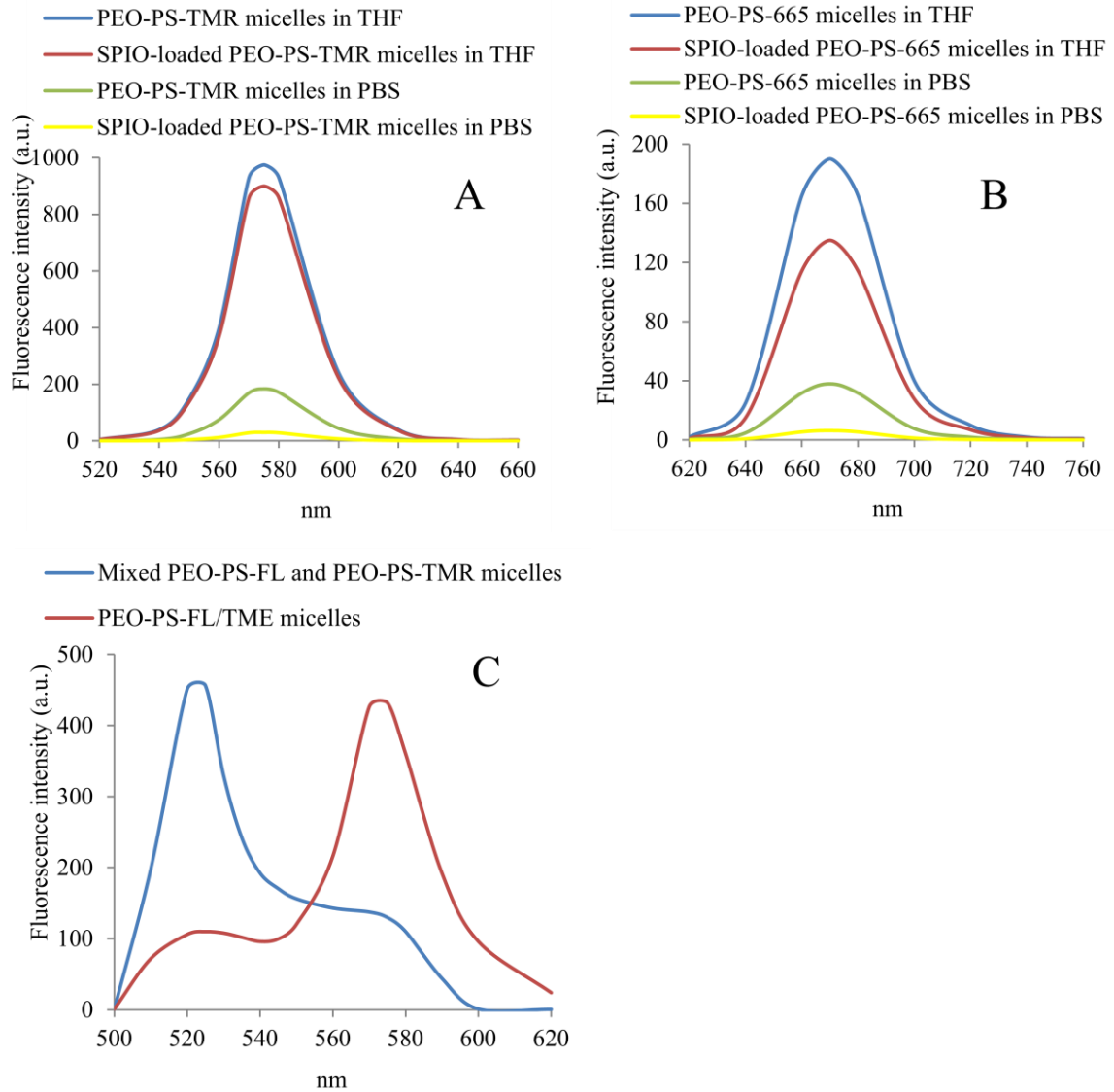
Figure 6.3 Integrity of micelles and SPIO-loaded micelles in PBS (A), RPMI 1640 medium (B), FBS (C) and 50% THF (D)
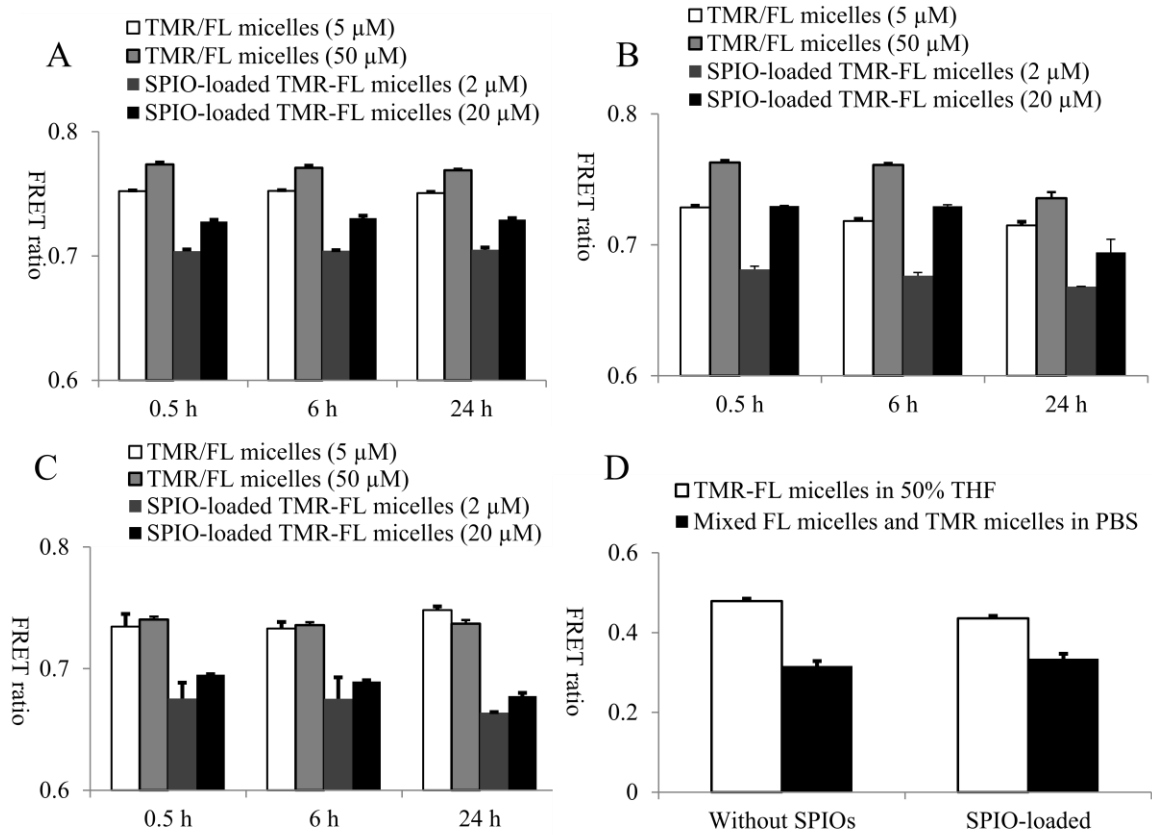
Figure 6.4 FRET images of PC-3 cells incubated with PEO-PS-TMR micelles (A1-A4 and B1-B4) and SPIO-loaded PEO-PS-TMR micelles (C1-C4 and D1-D4). Cell and organelle membrane was stained with DiO.
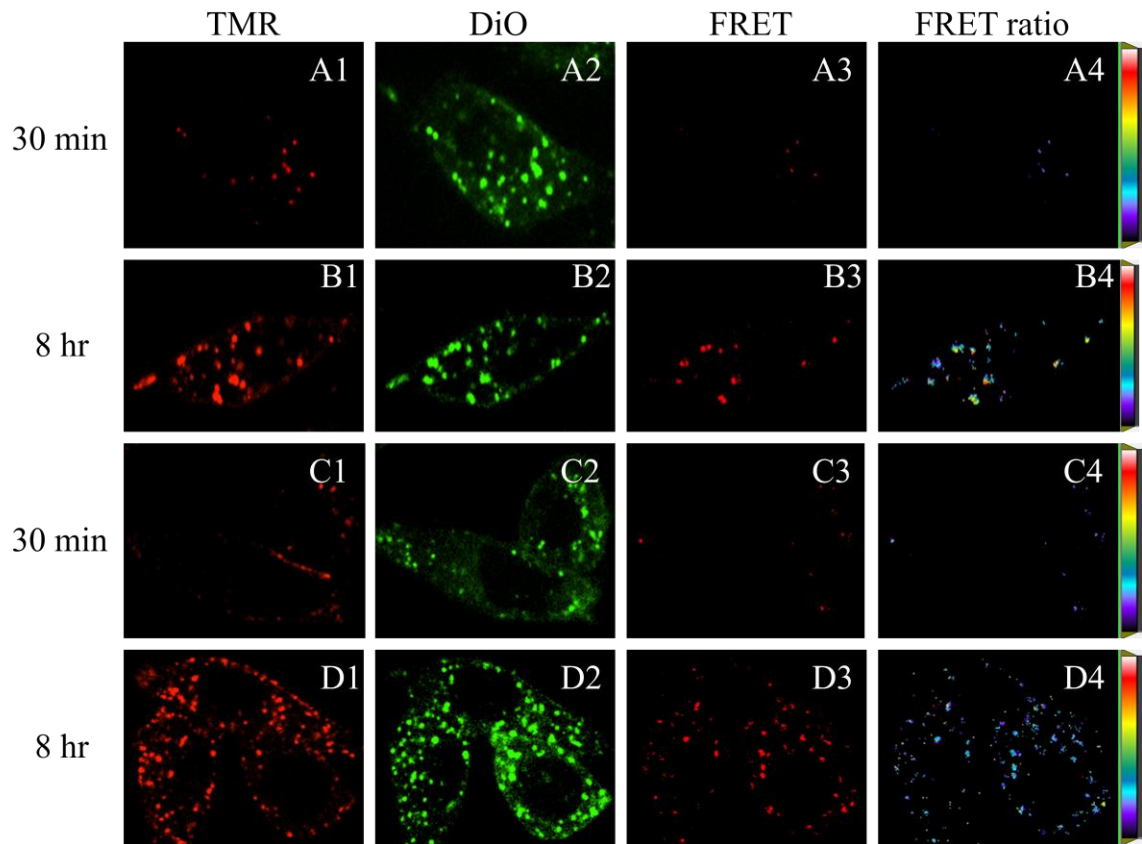
Figure 6.5 FRET images of PC-3 cells incubated with PEO-PS-FL/TMR micelles (A1-A4), mixed PEO-PS-PL and PEO-PS-TMR micelles (B1-B4), SPIO-loaded PEO-PS-FL/TMR micelles (C1-C4), and mixed PEO-PS-PL and PEO-PS-TMR micelles with SPIOs (D1-D4).

Figure 6.6 Fluorescent images of PC-3 cells incubated with PEO-PS-TMR micelles (A-D) and SPIO-loaded PEO-PS-TMR micelles (E-H).
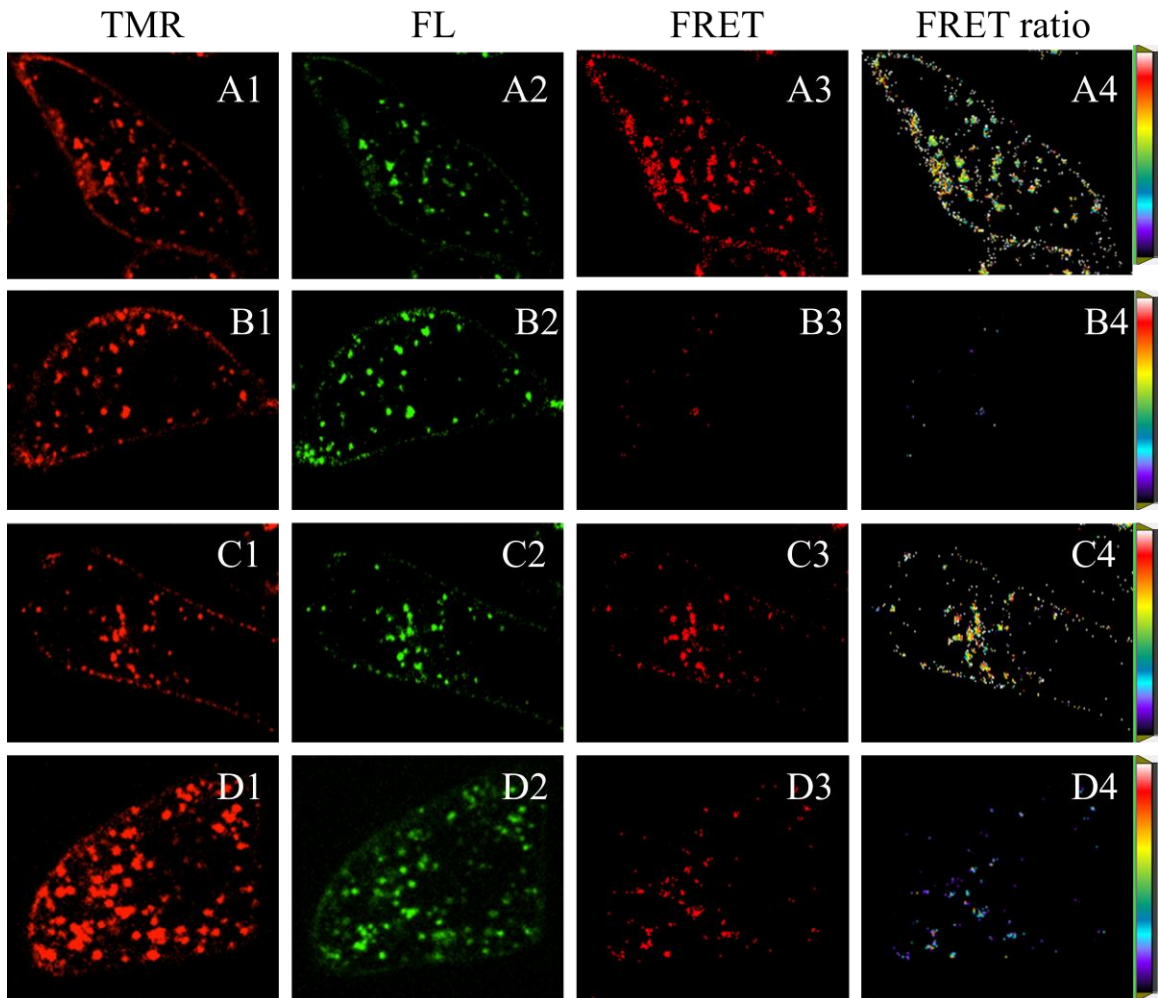
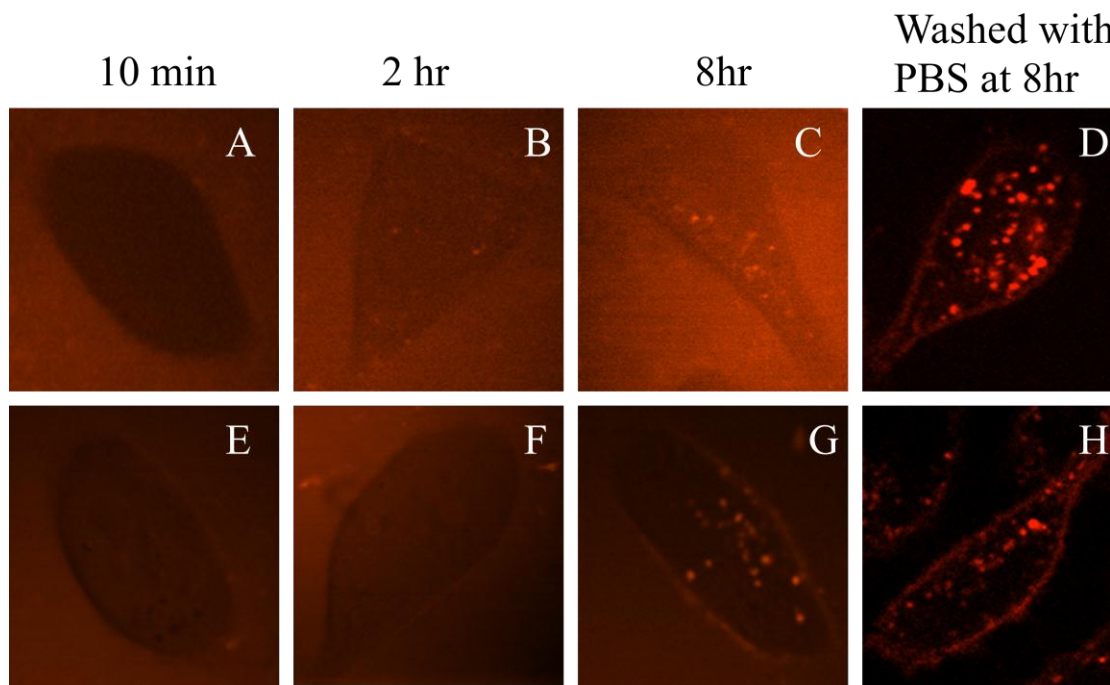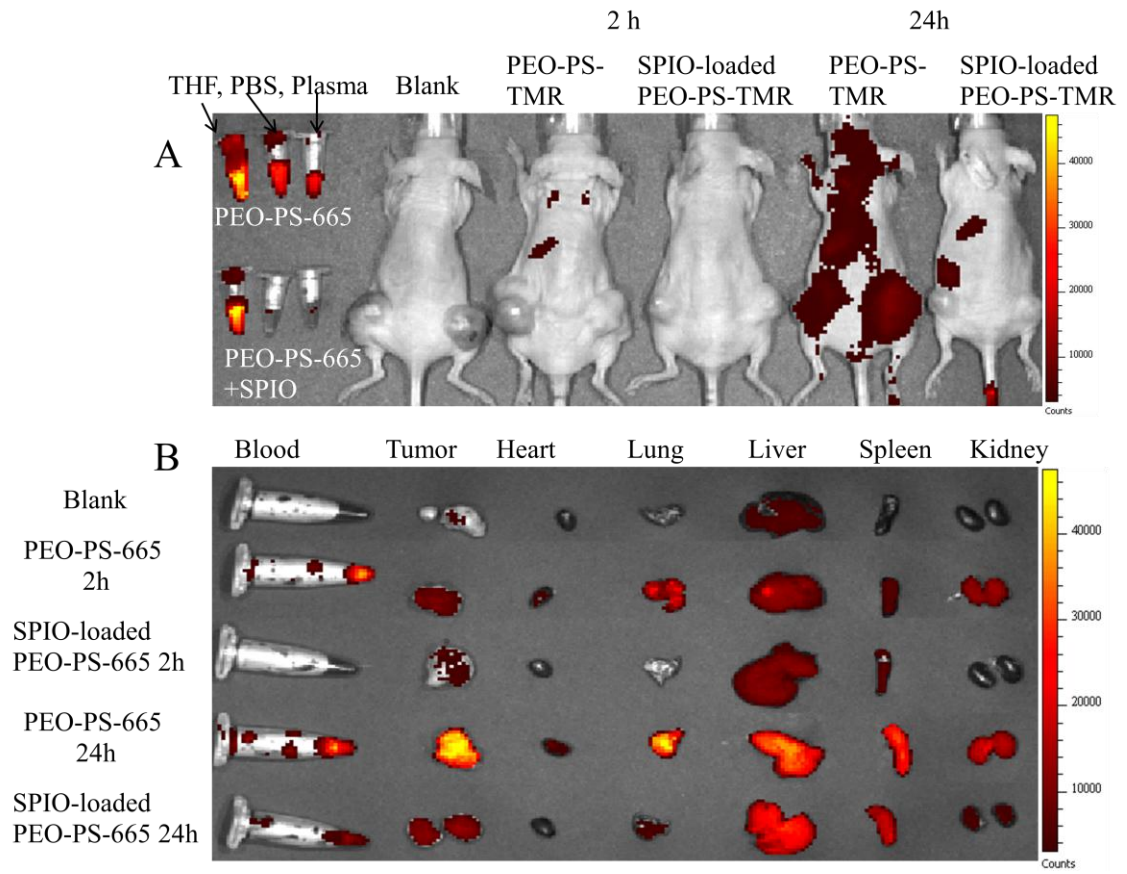| 10 min	2 hr	8hr	Washed with PBS at 8hr
A	B	C	D
E	F	G	H

Figure 6.7 *In vivo* and *ex vivo* fluorescent images of xenograft mice administered with PEO-PS-665 micelles and SPIO-loaded PEO-PS-665 micelles.

CHAPTER VII

Summary

The overall goal of this project is to develop cancer-specific multifunctional SPIOs for tumor magnetic resonance imaging and targeted drug delivery. To realize our goal, we focused on two critical issues: cancer-specific targeting and integrity of nanocarriers.

Tumor associated glycoprotein 72 (TAG-72) is a human mucin-like glycoprotein complex, which is over-expressed in many epithelial-derived cancers. To identify a colorectal cancer targeting ligand, tumor specific binding and pharmacokinetics of anti-TAG-72 antibodies, murine CC49, and humanized, C_H2 domain deleted $HuCC49\Delta C_H2$ were examined on cultured LS174T colon cancer cells and xenograft mice. The results showed that near-infrared fluorophore Cy7 labeled antibodies were indeed localized in tumor tissues. Murine CC49 antibody achieved a tumor/blood ratio of 15 at 96 hours postinjection. In comparison, $HuCC49\Delta C_H2$ showed a short half-life in xenograft mice and achieved a tumor/blood ratio of 12 at 18 hours postinjection. The high tumor accumulation and fast plasma clearance make $HuCC49\Delta C_H2$ a good targeting ligand for tumor imaging and anticancer drug delivery.

Although near-infrared fluorescent imaging detected the accumulation of $HuCC49\Delta C_H2$ antibody in xenograft tumor, the weak tissue penetration of fluorescence resulted in the difficulties in imaging and accurate quantitation of antibody in deep tissues $HuCC49deltaC_H2$ was radiolabeled with [124]I and its biodistribution in xenograft

mice was visualized by using PET imaging. ^{124}I-HuCC49deltaC$_H$2 demonstrated an increased level of specific localization to xenograft colon tumors after both i.v. and i.p. adminstration.

To realize simultaneous MRI, fluorescent imaging and targeted drug delivery, SPIOs were conjugated with HuCC49ΔC$_H$2 and fluorescent dye 5-FAM. Anticancer drugs doxorubicin (Dox), and azido-doxorubicin (Adox), MI-219 and 17-DMAG with various pKa were entrapped into the oleic acid layer of SPIOs. The SPIO "nanotheranostics" could specifically target to LS174T colon cancer cells for fluorescent cancer imaging and effectively decrease the T_2 relaxation times in MRI. The drugs entrapped in SPIOs exhibited a pH-dependent release in cancer cells, which was visualized under a fluorescent microscope. The cancer-specific targeting and pH-dependent release resulted in an improved anticancer efficacy of SPIO-delivered Dox.

Although Dox entrapped in SPIOs showed potent anticancer effect, its *in vivo* efficacy might be compromised by the premature release in blood circulation. Understanding the mechanisms of *in vitro* and *in vivo* drug release from nanocarriers is critical for design and optimization of nanoscale drug delivery systems. FRET imaging was used to investigate mechanisms of cargo release from polymeric nanoparticles and SPIO-loaded polymeric nanoparticles. Rapid release (10 min) of hydrophobic dyes from nanoparticles to cell membrane was observed in both cultured cancer cells and xenograft mice. FRET ratio increase from donor and acceptor individually loaded micelles was found to be an effective way to monitor cargo release. By comparing the average FRET ratios of mice treated with mixed donor micelles and acceptor micelles and the mice treated with donor/acceptor co-loaded micelles, the extent of *in vivo* release was

estimated. The large volume of phospholipid bilayer and high hydrophobicity of cell membrane were found to trgger the premature drug release. The encapsulation of hydrophobic SPIOs could slow down *in vitro* and *in vivo* cargo release in a dose-dependent mode.

Investigating the micelle integrity was essential to understanding the mechanisms of premature drug release. In this work, fluorescence-quecnhing by SPIOs and FRET analysis were used to detect *in vitro* and *in vivo* disassembly of PEO-PS micelles and SPIO-loaded PEO-PS micelles. The micelle disassembly in cell culture media and FBS was limited over 24 h. PEO-PS micelles kept integrity during cell internalization and the micelles gradually lost integrity in endosomes/lysosomes of cancer cells. Rapid *in vivo* disassembly upon blood dilution was not observed and the gradual micelle disassembly mainly occurred in livers, spleens and tumors over 24h. The rapid premature drug release from PEO-PS micelles was not caused by micelle disassembly.

In this work, cancer-specific antibody could facilitae the delivery of SPIOs to cancer cells. However, due to the rapid drug release from nanocarriers, targeted drug delivery was not realized by improving cacner-targeting. Since the rapid cargo release is trggered by the large volume of phospholipid bilayer, no drug leakage from nanocarriers in bulk solution does not guaranttee their integrity *in vivo*. It is recommended that the cargo release from nanocarriers should be examined in the presence of abundant cell membrane or artificial lipid bilayer. Considering the high hydrophobicity of cell membrane, the encapsulation of hydrophobic nanoparticles and increasing the core hydrophobicity of nanoparticles might be effective options to reduce premature drug release.

APPENDIX I

Prediction of Human Pharmacokinetic Parameters of MI-219, a Novel Human Double Minute 2 (HDM2) Inhibitor, Using *In Vitro* Liver Microsome Metabolisms, Protein Binding, and *In Vivo* Animal Pharmacokinetics

I.1 Abstract

The purpose of this study is to predict clearance (CL) and volume of distribution at steady-state (Vd_{ss}) of MI-219 in humans using liver microsomal metabolisms, protein binding, and in vivo animal pharmacokinetics. Metabolic stability of MI-219 was assessed in liver microsomes of mouse, rat, dog, monkey and human. Pharmacokinetic studies were conducted on mice, rats, dogs, and monkeys. Human CL values were predicted using allometric scaling (SA), multi-exponential allometric scaling (ME), role of exponents (RoE), single species scaling, two-term power equation (TTPE), physiologically based *in vitro-in vivo* extrapolation (IVIVE), and f_u corrected intercept method (FCIM). The predicted human clearance values ranged from 0.064 to 0.346 $L*h^{-1}*kg^{-1}$. Comparable CL values were obtained from TTPE (0.184 $L*h^{-1}*kg^{-1}$), FCIM (0.168 $L*h^{-1}*kg^{-1}$) and IVIVE (0.237 $L*h^{-1}*kg^{-1}$ for well-stirred model and 0.282 $L*h^{-1}*kg^{-1}$ for parallel-tube model). The Vd_{ss} values predicted using SA, allometric scaling of unbound volume of distribution of tissues (V_T/fu_T) and Oie-Tozer method were 0.418, 1.05 and 0.93 $L*kg^{-1}$, respectively. The plasma concentration–time profile in humans was predicted using a two-compartmental model equation to fit transformed animal data following kallynochron, apolysichron and dienetichron time transformation (Dedrick

189

plots) and normalization with MRT and Vd$_{ss}$ (Wajima's method). Superimposition of rat, monkey and dog data and good curve fitting were observed after apolysichron time transformation and normalization with MRT and Vd$_{ss}$. Nonlinear mixed effects modeling (NONMEM) was applied to describe rat, monkey and dog data by a two-compartment model. Then, the plasma concentration–time profile in human was extrapolated from animals using the NONMEM model based on allometric scaling. The similarity of the estimated values of pharmacokinetic parameters from various prediction methods provides confidence for the prediction of human pharmacokinetics of MI-219.

I.2 Introduction

MI-219 is a potent, highly selective and orally active small-molecule inhibitor of the HDM2 (Human Double Minute 2)–p53 interaction [1-3]. MI-219 stimulates rapid but transient p53 activation in tumor tissues, resulting in inhibition of cell proliferation, selective induction of cancer cell apoptosis, and complete tumor growth inhibition in xenograft models. Preclinical studies have shown that MI-219 is a promising lead candidate for p53 wild-type cancer therapy.

Prediction of human pharmacokinetics is an essential element in clinical development of a potential drug molecule. Over the past few decades, numerous empirical or physiological approaches have been developed for quantitative predictions of human clearance (CL) [4, 5], volume of distribution at steady-state (Vd$_{ss}$) [6, 7] and human plasma concentration-time profile from preclinical animal data [8, 9]. These predictive approaches typically use either *in vivo* preclinical animal data or *in vitro* metabolism and disposition data obtained from human tissue such as microsomes or

190

hepatocytes. However, there is not a standard method superior to other methods for each individual compound. Each approach has its unique advantages and disadvantages in its application to predicting human pharmacokinetics [5].

The preclinical studies showed that the elimination of MI-219 was mainly due to drug metabolism. In the present study, various methods were utilized to predict a range of CL and Vd_{ss} values of MI-219 in human. The plasma concentration–time profile in humans was also predicted using Dedrick plots, Wajima's method and nonlinear mixed effects modeling (NONMEM) [9-13]. A narrow distribution of the estimated values gave us greater confidence for the prediction of human pharmacokinetics of MI-219.

I.3 Materials and methods

I.3.1 Reagents

MI-219 and MI-343 (internal standard) were synthesized using a previously published method [2, 14]. Mouse, rat, dog, monkey and human liver microsomes were supplied by Sigma (St. Louis, MO, USA) or Xenotech (Lenexa, KS, USA). All other chemicals and reagents were purchased from commercial suppliers and were of HPLC grade.

I.3.2 Metabolic stability assay

The metabolic stability of MI-219 was assessed in human (a pool of fifty subjects), CD-1 mouse (a pool of ten male mice), Sprague–Dawley rat (a pool of fifteen male rats), beagle dog (a pool of eight male dogs), and cynomolgous monkey (a pool of six male monkeys) liver microsomes. The enzymes were activated by beta-NADPH (reduced form). The incubation solution was diluted with 0.1 M phosphate buffer (containing

MgCl$_2$) to 0.4 mL. The final concentrations of MI-219, liver microsomes, beta-NADPH, and MgCl$_2$ were 1 μM, 0.5 mg/mL, 1 mM, and 3.3 mM respectively. An aliquot of 40 μl of mixture was collected at 0, 5, 10, 15, 30, 45 and 60 min, and then proteins were precipitated with 120 μl of ice-cold acetonitrile containing an internal standard (100 ng/mL). The samples were centrifuged at 14000 rpm × 5 min and 10 μl of supernatant was injected into LC-MS/MS. All incubations were performed in triplicate.

An Agilent 1200 HPLC system coupled with a Qtrap 3200 mass spectrometer (Applied Biosystems, MDS Sciex Toronto, Canada) was used to quantify the remaining MI-219 in the liver microsome samples. The processed samples were injected on a Zorbax Bonus-RP column (2.1 mm × 50 mm, 5 μm). The system was run in isocratic mode with mobile phase consisting of methanol and water in the ratio of 85:15 (v/v) at a flow rate of 0.3 mL/min. Mass spectrometric parameters were similar to those for plasma sample analysis. The peak area ratios (MI-219 peak area/ internal standard peak area) were plotted against time and the gradient of the line is determined as the elimination rate constant (k).

I.3.3. Animals

Male CD-1 (ICR) mice (n=33, body weight 18 ± 1.7 g), male Sprague Dawley rats (n=3, body weight 195 ± 15 g), male cynomolgus monkeys (n=6, body weight 2.5 ± 0.26 kg), and male beagle dogs (n=3, bodyweight 8.0 ± 1.1 kg) were used for pharmacokinetic studies. Animals were maintained under a 12-h light/ dark cycle in cages with free access to commercial food pellets. Water was supplied *ad libitum*.

I.3.4 Mouse pharmacokinetic study

Thirty three male CD-1 mice were given an intravenous dose of 10 mg/kg of MI-219 dissolved in saline containing 20% polyethylene glycol (PEG 400) and 3% cremophor via the tail vein. Approximately 0.2 mL of blood was collected from each mouse by terminal cardiac puncture under isoflurane. Blood samples (n = 3 mice per time point) were taken from intravenously dosed mice at the following time points: before dosing and subsequently at 5, 15, 30, 45 min, 1, 2, 3, 5, 9, and 24 h after i.v administration. All blood samples were collected into heparinized polypropylene microcentrifuge tubes. Blood samples were centrifuged at 3,500 rpm for 10 min within 30 min of collection and plasma was harvested. Plasma samples were stored at -70°C until analysis.

I.3.5 Rat pharmacokinetic study

Two days before the initiation of the study, Sprague–Dawley rats were carotid cannulated using anaesthesia consisting of intraperitoneal administration of ketamine (100 mg/kg) and xylazine (10 mg/kg). Three male Sprague–Dawley rats were given an intravenous dose of 5 mg/kg of MI-219 in 30% PEG 400. Blood samples (approximately 0.2 mL per sample) were collected from each animal via vein cannulae at pre-dose and 5, 15, 30 min, 1, 2, 4, 6, 8, and 24 hours post-dose. Blood samples were centrifuged within 30 min of collection and plasma was harvested. Plasma samples were stored at approximately -70°C until analysis.

I.3.6 Monkey pharmacokinetic study

Six male cynomolgus monkeys were given 10mg/kg of MI-219 in 80% PEG 400 via a saphenous vein. Blood samples (approximately 1 mL per sample) were collected from the femoral vein of each animal at pre-dose, 5, 15, 30, 60 min, and 1.5, 2, 3, 4, 6, 8, and

24 h post-dose. All blood samples were collected into heparinized polypropylene microcentrifuge tubes. Blood samples were centrifuged within 1 hr of collection and plasma was harvested and stored at approximately -70°C until analysis.

I.3.7 Dog pharmacokinetic study

Three male beagle dogs were given a single intravenous dose of 2 mg/kg of MI-219 in 80% PEG 400 via a cephalic vein. Blood samples (approximately 2 mL per sample) were collected from the jugular vein of animals at pre-dose, 7, 12 and 30 min post-dose; and 1, 3, 4, 6, 8, 12 and 24 h postdose. All blood samples were collected in tubes containing heparin. Blood samples were centrifuged and plasma was harvested within 1 h of collection. Plasma samples were stored at approximately -70°C until analysis.

I.3.8 Plasma sample preparation and LC-MS/MS analysis

To prepare the plasma sample for LC-MS/MS analysis, ice-cold acetonitrile containing 100ng/mL internal standard (MI-343) was added to 50 µl mouse plasma samples or 100 µl of plasma samples of rats, monkeys or dogs to precipitate proteins. After centrifugation at 13,000 rpm for 5 min, 10 µL of the supernatant was introduced into the LC/MS/MS system. Chromatographic separation of MI-219 was achieved using a Luna C18 column (2 × 100 mm, 5 µM particle size) (Phenomenex, Torrance, CA, USA) and water: methanol (10:90 v/v) as the mobile phase. A Sciex API 3000 equipped with an electrospray source in the negative-ion multiple reaction monitoring (MRM) mode was used for detection. The MRM transition channel was m/z 550 to m/z 306 for MI-219 and m/z 596 to m/z 352 for IS. The ion spray voltage was set at -2700 V. Ionization temperature was set as 700 °C. Data acquisition and quantitation were performed using analyst software version 1.4.1 (Applied Biosystems, MDS Sciex Toronto, Canada). The

lower limit of quantitation (LOQ) ranged from 1.00 to 2.1 ng/mL in mouse, rat, monkey and dog plasma.

I.3.9 Pharmacokinetic analysis

All pharmacokinetic parameters were calculated by noncompartmental methods using WinNonlin® version 3.2 (Pharsight Corporation, Mountain View, CA, USA). Parameters are presented as a mean ± standard deviation (SD).

I.3.10 Plasma and liver microsome protein binding

Plasma protein binding was measured using a previously published method [15]. Plasma was spiked with MI-219 to yield a final concentration of 5 µM. After incubation at 37°C for 1 h, an aliquot was transferred to a 10 kD cut-off ultrafiltration device (Millipore Corporation, Billerica, MA, USA), which was centrifuged at 2000g for 3 h at 37°C. Samples were analyzed by LC-MS/MS as described above. The concentrations of MI-219 in the filtrate were determined by comparing with those of a standard curve containing known amounts of MI-219 dissolved in protein-free plasma (Macromolecules had been removed from the plasma by 10 kD cut-off ultrafiltration). The unbound fraction was estimated from the ratio of MI-219 concentration in the filtrate to that in the original plasma samples. Parallel studies using protein-free plasma instead of plasma indicated that MI-219 was bound minimally to the ultrafiltration device.

To determine the protein binding of MI-219 in liver microsomes, liver microsomes were diluted with 0.1 M phosphate buffer to 1 mg/mL and spiked with MI-219 to yield a final concentration of 1 µM. After incubation at 37°C for 1 h, an aliquot was transferred to a 10 kD cut-off ultrafiltration device, which was centrifuged at 2000g for 3 h at 37°C. The concentrations of MI-219 in the filtrate were determined by comparing with those of

a standard curve containing known amounts of MI-219 dissolved in ultrafiltrated 1mg/mL liver microsome solution. The unbound fraction was estimated from the ratio of MI-219 concentration in the filtrate to 1μM.

I.3.11 Blood-plasma partitioning (BP ratio)

MI-219 was added to whole blood to obtain a final concentration of 5 μM and incubated at 37°C for 30 min. Plasma was separated from blood samples and concentration of MI-219 was determined by comparing with a standard curve prepared in blank plasma. The blood/plasma concentration ratio (BP) was determined by dividing 5 μM by that found in plasma separated from blood samples.

The concentration of MI-219 in blood cells is assumed to be equal to its unbound concentration in plasma. The theoretical BP ratio was calculated according to the equation[15].

$$BP = 1 + H \times (f_u - 1)$$

where fu is the fraction of unbound in plasma, and H is the hematocrit (mouse, 0.45; rat, 0.46; dog, 0.42; monkey, 0.41; rabbit, 0.36; human, 0.44)[16].

I.3.12 Prediction of pharmacokinetics of MI-219 in human

Simple Allometric scaling (SA)

The CL (L/h) and Vd_{ss} (L) values of MI-219 in animals and body weight W (kg) of animals after logarithmic conversion were fitted to log-transformed form of the following allometric equations [17] by linear regression:

$$CL = a \times W^b$$
$$Vd_{ss} = a' \times W^c$$

Where a and a' are the coefficients; b and c are the exponents of simple allometry. Human clearance was extrapolated using the fitted line and an assumed body weight of 70 kg.

Allometric scaling after normalized by in-vitro metabolic data

Human and animal in vitro intrinsic clearance ($CL_{int,in\ vitro}$) was used to correct in vivo CL prior to allometric scaling. $CL_{int,in\ vitro}$ of MI-219 was derived from the *in vitro* $T_{1/2}$ of the drug in various liver microsomes.

$$CL_{int,invitro} = \frac{0.693}{T_{1/2} \times C_{protein}} = \frac{K_e}{C_{protein}}$$

$$CL'_{animal} = CL_{animal} \times \frac{HumanCL_{int,invitro}}{AnimalCL_{int,invitro}} = \frac{K_{e,human}}{K_{e,animal}}$$

where K_e and $C_{protein}$ (1mg/mL) were the rate constant of drug elimination in liver microsomes and the concentration of liver microsomes respectively.

Rule of Exponents (RoE)

The RoE method [18] was also utilized to predict CL of MI-219 in human. The following guidelines were proposed for the selection of correction factors:

If $0.55 < b < 0.70$, $CL = a \times (W)^b$

If $0.71 < b < 0.99$, $CL_{human} = a \times (MLP_{animal} \times CL_{animal})^b / MLP_{human}$

If $b \geq 1$, $CL_{human} = a \times (BrW_{animal} \times CL_{animal})^b / 1.53$ kg

If $b > 1.3$, CL will be overpredicted

If $b < 0.55$, CL will be underpredicted by allometric scaling

where BrW is the brain wight (kg) and MLP (Year) is the maximum life-span potential. The values of brain weight (kg) were as follows: mouse 0.0004; rat, 0.0018;

monkey 0.052, dog 0.072 and human 1.53[19, 20]. MLP was calculated using the following equation:

$$MLP(years) = 185.4 \times BrW^{0.636} \times W^{-0.225}$$

Two-term power equation (TTPE)

CL was scaled allometrically by using an empirical equation which contains two power terms.

$$CL = a \times W^{\alpha} \times BrW^{\beta}$$

where BrW is the brain weight.

Multi-exponential Allometric scaling (ME)

To eliminate the uncertainty around the selection of correction factor used with SA, multi-exponential allometric scaling equation [21] was used to predict CL of MI-219 in human.

$$CL = a \times W^{b} + \frac{1 - \frac{3}{2}b}{1 - \frac{1}{2}b} \times a \times W^{0.9}$$

where a and b are the coefficient and exponent of SA; W is human body weight (70 kg).

Single species scaling

The following single species scaling equations [22] were employed to predict CL of MI-219 in human:

$$CL_{human}/kg = 0.41 \times CL_{dog}/kg$$

$$CL_{human}/kg = 0.152 \times CL_{rat}/kg$$

$$CL_{human}/kg = 0.407 \times CL_{monkey}/kg$$

f_u corrected intercept method (FCIM)

$$CL = 33.35 ml/\min \times \left(\frac{a}{Rf_u}\right)^{0.77}$$

where Rf_u is the ratio of unbound fraction in plasma between rats and humans and a is the coefficient of SA.

Physiologically based in vitro-in vivo extrapolation (IVIVE)

CL of MI-219 in humans was also predicted using the physiologically based *in vitro-in vivo extrapolation (IVIVE)*. To assess the prediction performance of this method, CL of MI-219 in mice and rats were also predicted using IVIVE. The in vitro intrinsic clearance of MI-219 in mouse, rat and human liver microsomes were scaled up to whole-organ *in vivo* intrinsic clearance by using the following scaling factors: microsomal protein yield per gram of liver (mg/g): rat and mouse, 45; and human, 32; and liver weight (g/kg body weight): mouse, 87.5; rat, 40; and human, 26 [15, 16]. The in vivo intrinsic clearance was corrected with the fractions unbound in plasma and liver microsomes. Then, the corrected in vivo intrinsic clearance was used to calculate hepatic clearance in mice, rats and humans by using well-stirred model and parallel-tube model [23]. The values of liver blood flow (L/h/kg) were as follows: mouse 5.4; rat, 4.2; and human 1.24[15, 16]. The calculated hepatic clearance was then converted to plasma clearance by multiplying BP ratio of MI-219 (MI-219 was assumed to be cleared exclusively by hepatic metabolism).

$$CL_{int,invivo} = \frac{K_e}{C_{protein}} \times \frac{32mg \quad protein}{1g \quad liver \quad weight} \times \frac{26g \quad liver \quad weight}{kg \quad body \quad weight}$$

$$CL'_{int} = \frac{fu_p}{fu_m} \times CL_{int,in \quad vivo}$$

199

Well-stirred model
$$CL_H = \frac{Q_H \times CL'_{int,in\ vivo}}{Q_H + CL'_{int,in\ vivo}}$$

Parallel-tube model
$$CL_H = Q_H \times (1 - e^{-\frac{CL'_{int,in\ vivo}}{Q_H}})$$

$$CL_p = CL_H \times BP$$

Allometric scaling of unbound volume of distribution of tissues (V_T/fu_T)

The correlation between human and rat unbound volume of distribution of tissues (V_T/fu_T) was utilized to estimate human Vd_{ss}.[24]

$$\left(\frac{V_T}{fu_T}\right)_{rat} = \frac{Vd_{ss,rat} - V_{b,rat} \times BP_{rat}}{fu_{p,rat}} \qquad \left(\frac{V_T}{fu_T}\right)_{human} = \left(\frac{V_T}{fu_T}\right)_{rat}^{0.951}$$

$$Vd_{SS,human} = fu_{p,human} \times \left(\frac{V_T}{fu_T}\right)_{human} + V_{b,human} \times BP_{human}$$

where V_T was volume of tissue and fu_T was the drug unbound fraction in tissue; V_b was the blood volume (human, 0.0743 L/kg; rat, 0.054 L/kg).

Oie-Tozer equation

Oie-Tozer equation as used to calculate human Vd_{ss} from unbound fraction in plasma (fu_p) and tissue (fu_T), the plasma volume (V_p: 0.0313, 00448, 0.0515 and 0.0436 L/kg for rat, monkey, dog and human), the extracellular fluid volume (V_e: 0.265, 0.208, 0.216 and 0.151 L/kg for rat, monkey, dog and human), the ratio of extravascular to intravascular proteins ($R_{e/i}$: 1.4 for all the species), the tissue volume minus extracellular space (V_r: 0.364, 0.485, 0.450 and 0.38 L/kg)[25]. The unbound fractions in tissue fu_T of rats, monkey and dogs were calculated from corresponding Vd_{ss} and the average value of fu_T was used to calculate human Vd_{ss}.

$$fu_T, animal = \frac{V_r \times fu_p}{Vd_{SS} - V_p - fu \times V_e - (1 - fu_p) \times R_{e/i} \times V_p}$$

$$Vd_{SS,human} = V_p + fu_{p,human} \times V_e + (1 - fu_{p,human}) \times R_{e/i} \times V_p + V_r \times \left(\frac{fu_{p,human}}{fu_{T,average}} \right)$$

Dedrick plots

The plasma concentration–time profile of MI-219 in humans (assume an i.v administration of 5mg/kg of MI-219) was simulated by using four Dedrick plot methods (based on Kallynochrons, Apolysichrons, Dienetichrons and equivalent times)[8, 11, 26]. The equations of the four Dedrick plot methods were listed as below.

$$CL \times MLP = a'' \times W^d$$

Kallynochrons (elementary Dedrick plot):

$$Time_H = Time_A \times \left(\frac{W_H}{W_A} \right)^{1-b}$$

$$Conc._H = Conc._A \times \frac{Dose_H}{Dose_A} \times \frac{W_A}{W_H}$$

Apolysichrons:

$$Time_H = Time_A \times \left(\frac{W_H}{W_A} \right)^{c-b}$$

$$Conc._H = Conc._A \times \frac{Dose_H}{Dose_A} \times \left(\frac{W_A}{W_H} \right)^c$$

Dienetichrons (complex Dedrick plot):

$$Time_H = Time_A \times \frac{MLP_H}{MLP_A} \times \left(\frac{W_H}{W_A} \right)^{c-d}$$

$$Conc._H = Conc._A \times \frac{Dose_H}{Dose_A} \times \left(\frac{W_A}{W_H} \right)^c$$

Where W (kg) was the average body weight of animal or humans; Dose was in milligram. b and c were the exponents of simple allometry of CL and Vd_{ss}. The clearances in different animal species were multiplied by their respective MLP and plotted as a function of the body weight on a log-log scale to generate exponent d. The

superimposition of the transformed animal concentration-time curves was expected. A two-compartment model (WinNonlin, version 5.2.1) was used to fit the superimposed curves. The goodness of fit was evaluated by correlation of observed and predicted values (r^2) and Akaike Information Criteria (AIC)[10].

Wajima's method

The plasma concentration–time profile of MI-219 in humans was also predicted by normalizing concentration–time profiles in animals with MRT (MRT = Vd_{ss}/CL) and C_{ss} (C_{ss} = Dose/Vd_{ss}) [9]. The superimposition of the normalized animal concentration-time curves was expected. The normalized animal concentrations and times were transformed into human concentrations and times by multiplying the predicted human C_{ss} and MRT. Similar to Dedrick plot analysis, a two-compartment model (WinNonlin, version 5.2.1) was used to fit the predicted human plasma concentration–time profile of MI-219.

NONMEM

NONMEM (version VI; ICON Development Solutions, Ellicott City, MD, USA) was applied to describe the pooled rat, monkey and dog concentration-time data by a two-compartment pharmacokinetic model (ADVAN3, TRAN4). The NONMEM parameters (THETAs, ETAs and ERRORs) were acquired based on the allometric relationship of pharmacokinetic parameters among rats, monkeys and dogs [27]. The concentration-time profile in human was simulated using the established NONMEM model. Then, a two-compartment model (WinNonlin, version 5.2.1) was used to fit the simulated human curve and calculate the pharmacokinetic parameters.

To validate the allometric scaling-based NONMEM approach, 100 simulations of the concentration-time profile for each animal species were performed, resulting in 90%

202

confidence intervals. The simulations were then compared with the observations in animals. Furthermore, three NONMEM models were individually developed from rat, monkey and dog concentration-time data. The animal pharmacokinetic parameters (CL, V1, V2 and Q) estimated from individual models were compared with those obtained from combined model.

I.4 Results

I.4.1. Metabolic stability assay

The percentages of MI-219 remaining in mouse, rat, dog, monkey and human liver microsomes (1mg/mL) after 5, 10, 15, 30, 45 and 60 min incubation are presented in Figure I.1. In all species tested, more than 50% of MI-219 was metabolized after incubation for 1 hr, suggesting MI-219 was extensively metabolized by CYP450 enzymes. During 0-15 min incubation, the clearance of MI-219 followed the first-order kinetics. The elimination rate constants and half-lives of MI-219 in mouse, rat, monkey, dog and human liver microsomes were shown in Table I.1.

I.4.2 Plasma and liver microsome protein binding and blood-plasma partitioning

As shown in Table I.2, the unbound fraction of MI-219 in mouse, rat, monkey, dog and human plasma at a concentration of 5 µM ranged from 1.39% to 4.45%. The unbound fractions of MI-219 (1µM) in 1 mg/mL of mouse, rat and human liver microsomes are 2.03%, 2.44% and 6.16% respectively. The BP ratios of MI-219 in mice, rats and humans are experimentally measured and range from 0.572 to 0.597, which agree with the BP ratio values calculated from corresponding $fu_{,p}$.

203

I.4.3 Pharmacokinetics of MI-219 in rat, mouse, dog and monkey

Figure I.2 is a semi-log plot of MI-219 plasma concentration versus time for mouse, rat, dog, and monkey following intravenous administration. The concentrations of MI-219 in mouse plasma are lower than the limit of quantification of the LC-MS assay. The pharmacokinetic parameters of MI-219 in the four species are summarized in Table I.3. MI-219 has a high plasma clearance in mice and rats at 7.15 and 2.13 $L*h^{-1}*kg^{-1}$, respectively. The corresponding blood clearances in mice and rats are 12.31 and 3.57 $L*h^{-1}*kg^{-1}$, respectively (more than 80% of hepatic blood flow). Especially, the blood clearance exceeds hepatic blood flow in mice. In monkeys, MI-219 had a moderate plasma clearance of 0.85 $L*h^{-1}*kg^{-1}$ and blood clearance of 1.42 $L*h^{-1}*kg^{-1}$ (approximately 53% of hepatic blood flow) [16]. In dogs, MI-219 had a moderate plasma clearance of 0.36 $L*h^{-1}*kg^{-1}$ and blood clearance of 0.61 $L*h^{-1}*kg^{-1}$ (approximately 34% of hepatic blood flow). The terminal half-life ($t_{1/2}$) ranged from 1.89 h in mice to 3.90 h in dogs. The volume of distribution at steady-state (Vd_{ss}) ranged from 0.60 $L*kg^{-1}$ in dogs to 6.37 $L*kg^{-1}$ in mice.

I.4.4 Prediction of clearance of MI-219 in humans

Simple allometric scaling (SA) was performed to provide a predicted clearance of MI-219 in humans. The predicted CL by SA was 0.146 $L*h^{-1}*kg^{-1}$. The coefficient and exponent for SA of CL were 0.0317 and 0.5301, respectively (Figure I.3A). According to Role of Exponents (RoE), the CL value 0.146 $L*h^{-1}*kg^{-1}$ is likely to be underpredicted since the exponent is less than 0.55 [4]. Animal CL was corrected by multiplying the ratio of elimination rate constants in human and animal liver microsomes ($K_{e,human}/K_{e,animal}$). Allometric scaling of the corrected animal CL resulted in an equation

with a higher coefficient of determination (0.9997 vs 0.9901) and a lower predicted CL

(0.08 $L*h^{-1}*kg^{-1}$) (Figure I.3B). Similarly, maximum life-span potential (MLP) and brain

weight (BrW) were used as the correction factors for allometric scaling of CL and also

resulted in lower human CL values and r^2 values compared with SA. The predicted CL

values in humans were 0.086 and 0.064 $L*h^{-1}*kg^{-1}$ when incorporating MLP and BrW

into the allometric scaling, respectively (Figure I.3C, I.3D).

Figure I.4 shows the plot of CL against body weight (W) and brain weight (BrW) by

using two-term power equation (TTPE). TTPE showed a good correlation among CL, W

and BrW and the coefficient of determination (r^2) was 0.9988. The predicted human CL

was 0.184 $L*h^{-1}*kg^{-1}$.

The coefficient (0.0317) and exponent (0.5301) obtained from SA of CL were

applied to the multi-exponential allometric scaling (ME) equation to estimate CL in

human. The predicted human CL was 0.342 $L*h^{-1}*kg^{-1}$.

To simplify SA, single-species scaling methods proposed by Tang et. al. [22] were

also applied to the prediction of CL of MI-219 in humans. A big variation was observed

when the CL in humans was derived from rats (0.342 $L*h^{-1}*kg^{-1}$), dogs (0.148

$L*h^{-1}*kg^{-1}$), and monkeys (0.346 $L*h^{-1}*kg^{-1}$).

Considering the extremely high plasma protein binding of MI-219, the f_u corrected

intercept method (FCIM) was utilized to estimate CL of MI-219 in humans. The ratio of

$fu_{,p}$ in rats and human (0.0387/0.0165 = 2.345) and coefficient of simple allometry

(0.0317) were applied to FCIM equation. The resulted CL in humans was 0.168

$L*h^{-1}*kg^{-1}$.

CL of MI-219 was also scaled from *in vitro* intrinsic clearance determined in human liver microsome incubation using physiologically based *in vitro-in vivo* extrapolation method. The elimination rate constant of MI-219 in 1 mg/mL human liver microsome was 0.04747 min^{-1}. fu$_{,m}$ in human liver microsome and BP ratio in human blood were determined as 6.16% and 0.572. The predicted CL value in human was 0.237 or 0.282 L*h^{-1}*kg^{-1} when well-stirred model or parallel-tube model was employed. To assess the prediction performance of IVIVE, the CL of MI-219 in mice and rats were also scaled from *in vitro* intrinsic clearance in mouse and rat liver microsomes. The CL in rats was estimated to be 1.675 L*h^{-1}*kg^{-1} (well-stirred model) and 2.172 L*h^{-1}*kg^{-1} (parallel-tube model). The later one agreed well with the observed value (2.13 L*h^{-1}*kg^{-1}), suggesting that parallel-tube model provided more accurate prediction than well-stirred model. The predicted CL values in mice by both well-stirred model (2.66 L*h^{-1}*kg^{-1}) and parallel-tube model (3.23 L*h^{-1}*kg^{-1}) were lower than the observed value (7.15 L*h^{-1}*kg^{-1}), indicating other elimination mechanisms such as extrahepatic metabolism contributed to the total clearance in mice. CL values of MI-219 in humans predicted by various approaches were summarized in Table I.4.

I.4.5 Prediction of Vd$_{ss}$ of MI-219 in humans

Estimates of Vd$_{ss}$ from mouse, rat, dog and monkey pharmacokinetic studies were plotted against body weight (kg) to predict human Vd$_{ss}$. Human Vd$_{ss}$ predicted by simple allometry was 0.418 L*kg^{-1} and the exponent of the equation was 0.9638 (Figure I.3E). As a comparison, unbound Vd$_{ss}$ (Vd$_{ss}$/fu$_p$) determined in the four species exhibited a better allometric correlation ($r^2 = 0.98$) with body weight than Vd$_{ss}$ and the extrapolated Vd$_{ss}$ in human was 0.694 L/kg (Figure I.3F).

Besides simple allometric scaling, interspecies scaling of the unbound volume of distribution of tissues (V_T/fu_T) was also used to estimate Vd_{ss} of MI-219 in human. V_T/fu_T in rats was derived from rat Vd_{ss} as 75.4 $L*kg^{-1}$. V_T/fu_T in human was 61.0 $L*kg^{-1}$, resulting in a Vd_{ss} in human of 1.05 $L*kg^{-1}$.

Physiologically based Oie-Tozer equation was used to predict Vd_{ss} in human. fu_T in rats (0.00491), dogs (0.0131) and monkeys (0.00475) were derived from corresponding Vd_{ss}. The average fu_T of the three species was used to calculate Vd_{ss} of MI-219 in human, which was determined as 0.93 $L*kg^{-1}$.

I.4.6 Dedrick plot analysis

Three Dedrick plot methods were applied for the prediction of the plasma concentration–time profile for MI-219 in humans. The plasma concentration–time curves obtained from mice, rats, monkeys and dogs were normalized according to the pharmacokinetic times of kallynochrons (elementary Dedrick plot), apolysichrons (complex Dedrick plot) and dienetichrons. As shown in Figure I.5, reasonable superimposition was observed among the curves transformed from rat, monkey and dog plasma concentration–time profiles. However, the curve transformed from mouse plasma concentration–time profile was not superimposable to other curves. Hence, only the three curves derived from rats, monkeys and dogs were used to predict human pharmacokinetics. A two-compartment model was employed to fit the superimposed curves by using WinNonlin. The predicted human pharmacokinetic parameters (alpha, beta, A, B, CL, Vd_{ss}, MRT, and $t_{1/2}$), coefficients of correlation and AIC were shown in Table I.5. According to r^2 and AIC values, it is obvious that kallynochron and apolysichron time transformations resulted in a better superimposition and curve-fitting

than dienetichron transformations. The kallynochron transformation resulted in CL (0.148 L*h^{-1}*kg^{-1}) and Vd$_{ss}$ (0.406 L*kg^{-1}) comparable with that derived from SA. The CL in humans predicted by apolysichron time transformation (0.164 L*h^{-1}*kg^{-1}) was more comparable with those obtained by TTPE, FCIM and IVIVE methods. Compared with SA, apolysichron time transformation resulted in a lower Vd$_{ss}$ (0.370 L*kg^{-1}). The dienetichron time transformation resulted in a CL (0.091 L*h^{-1}*kg^{-1}) comparable with that predicted from the allometric scaling of CL×MLP (0.086 L*h^{-1}*kg^{-1}), and a Vd$_{ss}$ (0.471 L*kg^{-1}) comparable with that obtained from SA.

I.4.7 Wajima's method

The concentration–time profiles in mice, rats, dogs and monkeys were normalized by MRT and C$_{ss}$. Reasonable superimposition was observed among the normalized curves from rats, monkeys and dogs (Figure I.6A). The normalized mouse curve was not superimposable to other curves. The normalized concentrations and times from rats, monkeys and dogs were transformed into human concentrations and times by multiplying the predicted human C$_{ss}$ and MRT. Since allometric scaling tends to underpredict CL and Vd$_{ss}$, the average CL predicted from TTPE (0.184 L*h^{-1}*kg^{-1}), ME (0.342 L*h^{-1}*kg^{-1}) FCIM (0.168 L*h^{-1}*kg^{-1}), and IVIVE methods (0.237 and 0.282 L*h^{-1}*kg^{-1}) and the Vd$_{ss}$ predicted from Oie-Tozer equation (0.93 L*kg^{-1}) were utilized to generate MRT (3.85 h) and C$_{ss}$ (5.38 mg*L^{-1}) in humans. The transformed human concentrations and times were plotted (Figure I.6B) and fitted with a two-compartment model using WinNoNlin. The predicted human pharmacokinetic parameters (alpha, beta, A, B, CL, Vd$_{ss}$ and MRT) were listed in Table I.5. The r^2 (0.979) and AIC (543) values suggested a good curve-fitting.

I.4.8 NONMEM

The allometric scaling-based NONMEM model (Supplementary Materials) was developed from rat, monkey and dog data. The model was then utilized to simulate human concentration–time profile (Figure I.7) and estimate human PK parameters. The predicted human CL and Vd_{ss} were 0.186 L* kg^{-1} and 0.843 L*h^{-1}*kg^{-1} respectively (Table I.5), which are consistent with the predictions obtained from IVIVC, TTPE, FCIM and Oie-Tozer equation.

As shown in Figure I.8, the observed dog concentration-time profile falls in the 5th and 95th quantile of model simulations. Similarly, observations in rats and monkeys also fall in the 90% confidence intervals of simulations (data not shown). Meanwhile, animal pharmacokinetic parameters (CL, V1, V2 and Q) estimated from individual models were similar to those obtained from the combined model (Table I.6).

I.5 Discussion

The effective inhibition of p53 wild-type tumors in preclinical models makes MI-219 an attractive candidate for anti-cancer drug development [1]. The accurate prediction of human pharmacokinetics of MI-219 is critical for the assessment of its potential to succeed as a drug. Numerous approaches based on in vitro and in vivo preclinical data for human pharmacokinetics are available but there is no universal approach that will work for every compound. Although the allometric scaling techniques are simple and most widely used in industry, the use of allometric scaling should be cautious due to its empirical nature. In current study, we intend to utilize and evaluate various approaches

including both empirical and physiologically based approaches for predicting pharmacokinetic parameters of MI-219 in humans.

The results from animal pharmacokinetic studies showed that MI-219 has moderate to high plasma clearance in all species (E_H >0.3). Especially, the plasma clearance in mice exceeds the mouse hepatic blood flow, implying the existence of non-hepatic clearance of MI-219 in mice. Since renal clearance did not contribute significantly to the systemic clearance of MI-219, the high clearance of MI-219 was likely due to both hepatic and extrahepatic metabolism. The rapid metabolic turnover of MI-219 in mouse, rat, monkey, dog and human liver microsome incubation suggested the extensive hepatic metabolism. The high protein binding in combination with the low-to-moderate volume of distribution did not suggest that MI-219 underwent extensive distribution to peripheral tissues.

Considering the moderate to high hepatic extraction ratios of MI-219 in animals, it is not surprising that simple allometric scaling (SA) of CL showed good correlation ($r^2 =$ 0.9901) between the CL of MI-219 and body weights since clearance of compounds with high hepatic extraction ratios is limited by liver blood flow, which is well correlated with body weight across species [28]. As expected, the incorporation of elimination rate constants determined in live microsome incubations further improved the r^2 of allometric scaling to 0.9997. However, it has been suggested that a high r^2 value does not warrant the accuracy of CL prediction[29]. As declared in the Rule of Exponent (RoE), the CL of MI-219 in humans will be underpredicted by using SA since the exponent is less than 0.55 and the application of correction factors will not improve the prediction [4]. As expected, the application of the correction factors such as BrW, MLP or *in vitro*

microsomal data definitely resulted in lower predicted CL values of MI-219 in humans (Table I.4). The CL (0.342 $L*h^{-1}*kg^{-1}$) of MI-219 in humans obtained from multi-exponential allometric scaling (ME) is very likely to deviate since ME is inferior to SA when the exponent of SA is less than 0.7[30]. The CL values of MI-219 estimated using single-species scaling exhibited great variation when scaled from different species. The interspecies difference limits the application of single-species scaling in prediction of CL.

CL of MI-219 in human predicted by two other empirical approaches, TTPE and FCIM, are higher than that obtained from SA. In TTPE, CL is allometrically correlated with both body weight and brain weight, which probably performs better than SA when CL is not correlated well with body weight. Compared with SA, FCIM is improved by incorporating interspecies difference in protein binding between rats and humans.

Clearance predictions using empirical allometric scaling are challenging due to interspecies differences in protein binding and metabolism [31]. The physiologically based IVIVE method minimizes the errors caused by interspecies differences by incorporating in vitro intrinsic CL, fu_p and fu_m into the equations. The CL values of MI-219 in humans predicted by IVIVE are comparable to those obtained from empirical approaches. To verify the predictability of IVIVE, CL of MI-219 in mice and rats were estimated using this approach. Although the predicted CL in rats agreed well with the observed value, the CL in mice was underpredicted due to the extrahepatic clearance of MI-219 in mice. Hence, to accurately predict CL of MI-219 in humans, more *in vitro* investigation is required to detect the possible extrahepatic clearance of MI-219 in humans.

Although the simple allometric scaling of Vd_{ss} shows a reasonable correlation between Vd_{ss} of MI-219 and body weight (r^2=0.96), the interspecies differences in plasma and tissue protein binding probably cause prediction errors. The correction with plasma protein binding improved the correlation (r^2=0.98) and resulted in a larger Vd_{ss} in human (0.694 L*kg^{-1}). Mahmood suggested that allometric scaling is more likely to produce an accurate prediction of Vd_{ss} when the exponent is between 0.8 to 1.1 [4]. Hence, allometric scaling of unbond Vd_{ss} perhaps performed better than SA for the case of MI-219. Oie-Tozer method and allometric scaling of V_T/fu_T method minimize the effects of protein binding by incorporating unbound fractions in plasma and tissue into the equations and resulted in Vd_{ss} higher than that from SA.

The Detrick plot methods were used to predict the plasma concentration-time profile of MI-219 in humans. After kallynochron, apolysichron and dienetichron transformation, the data from rats, monkeys and dogs were superimposable. Kallynochron and apolysichron transformations exhibited better superimpositions than dienetichron transformation. Essentially, Detrick plot method originated from the allometric scaling approach and its prediction performance depends on the allometric relationships of the pharmacokinetic parameters cross species. Therefore, it is not surprising that the CL and Vd_{ss} estimated by kallynochron and apolysichron methods are comparable to those obtained from SA.

To avoid possible underpredictions of both CL and Vd_{ss} from allometric scaling and Detrick plots, Wajima's normalization method was also employed to predict the concentration-time profile of MI-219 in humans. CL and Vd_{ss} derived from IVIVE, FCIM and Oie-Tozer equation instead of simple allometric scaling were used to estimate

human concentration-time profile, which fitted the two-compartment model better than the data transformed from Detrick plots.

Allometric scaling-based NONMEM is a good alternative approach for human PK profile prediction. CL and Vd_{ss} predicted by NONMEM were comparable to those from IVIVC, TTPE, FCIM, Oie-Tozer equation and Wajima's method. The prediction performance of NONMEM was successfully validated using animal observations.

I.6 Conclusion

In summary, the pharmacokinetics of MI-219 was studied in mice, rats, monkeys and dogs after i.v. injection. The pharmacokinetic parameters of MI-219 in humans were predicted using various empirical and physiologically based methods. The plasma concentration-time profile in humans was predicted using Detrick plot methods. These methods provide an approximate range of the systemic CL of 0.064 to 0.472 $L*h^{-1}*kg^{-1.}$ Comparable CL values were obtained from TTPE (0.184 $L*h^{-1}*kg^{-1}$), FCIM (0.168 $L*h^{-1}*kg^{-1}$), and IVIVE (0.237 $L*h^{-1}*kg^{-1}$ for well-stirred model and 0.282 $L*h^{-1}*kg^{-1}$ for parallel-tube model), while CL from SA and ME methods were deviated from above methods due to low exponent values. Superimposition of rat, monkey and dog data and good curve fitting were observed after apolysichron time transformation and normalization with MRT and Vd_{ss}. Human CL and Vd_{ss} values predicted by Wajima's method and NONMEM were comparable to those from TTPE, FCIM, IVIVE and Oie-Tozer equation. The similarity of the estimated values of pharmacokinetic parameters from various prediction methods may provide confidence for the prediction of human pharmacokinetics of MI-219.

I.7 References

1. Shangary, S., et al., *Temporal activation of p53 by a specific MDM2 inhibitor is selectively toxic to tumors and leads to complete tumor growth inhibition.* Proc Natl Acad Sci U S A, 2008. **105**(10): p. 3933-8.
2. Ding, K., et al., *Structure-based design of spiro-oxindoles as potent, specific small-molecule inhibitors of the MDM2-p53 interaction.* J Med Chem, 2006. **49**(12): p. 3432-5.
3. Shangary, S. and S. Wang, *Targeting the MDM2-p53 interaction for cancer therapy.* Clin Cancer Res, 2008. **14**(17): p. 5318-24.
4. Mahmood, I., *Application of allometric principles for the prediction of pharmacokinetics in human and veterinary drug development.* Adv Drug Deliv Rev, 2007. **59**(11): p. 1177-92.
5. Hosea, N.A., et al., *Prediction of human pharmacokinetics from preclinical information: comparative accuracy of quantitative prediction approaches.* J Clin Pharmacol, 2009. **49**(5): p. 513-33.
6. Fagerholm, U., *Prediction of human pharmacokinetics--evaluation of methods for prediction of volume of distribution.* J Pharm Pharmacol, 2007. **59**(9): p. 1181-90.
7. Oie, S. and T.N. Tozer, *Effect of altered plasma protein binding on apparent volume of distribution.* J Pharm Sci, 1979. **68**(9): p. 1203-5.
8. Shin, B.S., et al., *Pharmacokinetic scaling of SJ-8029, a novel anticancer agent possessing microtubule and topoisomerase inhibiting activities, by species-invariant time methods.* Biopharm Drug Dispos, 2003. **24**(5): p. 191-7.
9. Wajima, T., et al., *Prediction of human pharmacokinetic profile in animal scale up based on normalizing time course profiles.* J Pharm Sci, 2004. **93**(7): p. 1890-900.
10. Cho, C.Y., et al., *Pharmacokinetic scaling of bisphenol A by species-invariant time methods.* Xenobiotica, 2002. **32**(10): p. 925-34.
11. Mahmood, I. and R. Yuan, *A comparative study of allometric scaling with plasma concentrations predicted by species-invariant time methods.* Biopharm Drug Dispos, 1999. **20**(3): p. 137-44.
12. Shim, H.J., et al., *Interspecies pharmacokinetic scaling of DA-8159, a new erectogenic, in mice, rats, rabbits and dogs, and prediction of human pharmacokinetics.* Biopharm Drug Dispos, 2005. **26**(7): p. 269-77.
13. Dong JQ, et al., *Quantitative Prediction of Human Pharmacokinetics for Monoclonal Antibodies.* Clinical Pharmacokinetics, 2011. **50**(2): p. 131-142.
14. Ding, K., et al., *Structure-based design of potent non-peptide MDM2 inhibitors.* J Am Chem Soc, 2005. **127**(29): p. 10130-1.
15. Laufer, R., et al., *Quantitative prediction of human clearance guiding the development of Raltegravir (MK-0518, isentress) and related HIV integrase inhibitors.* Drug Metab Dispos, 2009. **37**(4): p. 873-83.
16. Davies, B. and T. Morris, *Physiological parameters in laboratory animals and humans.* Pharm Res, 1993. **10**(7): p. 1093-5.
17. Boxenbaum, H., *Interspecies pharmacokinetic scaling and the evolutionary-comparative paradigm.* Drug Metab Rev, 1984. **15**(5-6): p. 1071-121.

18. Mahmood, I., *Prediction of human drug clearance from animal data: application of the rule of exponents and 'fu Corrected Intercept Method' (FCIM).* J Pharm Sci, 2006. **95**(8): p. 1810-21.

19. Boxenbaum, H. and J.B. Fertig, *Scaling of antipyrine intrinsic clearance of unbound drug in 15 mammalian species.* Eur J Drug Metab Pharmacokinet, 1984. **9**(2): p. 177-83.

20. Bailey, S.A., R.H. Zidell, and R.W. Perry, *Relationships between organ weight and body/brain weight in the rat: what is the best analytical endpoint?* Toxicol Pathol, 2004. **32**(4): p. 448-66.

21. Goteti, K., et al., *Estimation of human drug clearance using multiexponential techniques.* J Clin Pharmacol, 2008. **48**(10): p. 1226-36.

22. Tang, H., et al., *Interspecies prediction of human drug clearance based on scaling data from one or two animal species.* Drug Metab Dispos, 2007. **35**(10): p. 1886-93.

23. Chiba, M., Y. Ishii, and Y. Sugiyama, *Prediction of hepatic clearance in human from in vitro data for successful drug development.* AAPS J, 2009. **11**(2): p. 262-76.

24. Sawada, Y., et al., *Prediction of the disposition of nine weakly acidic and six weakly basic drugs in humans from pharmacokinetic parameters in rats.* J Pharmacokinet Biopharm, 1985. **13**(5): p. 477-92.

25. Obach, R.S., et al., *The prediction of human pharmacokinetic parameters from preclinical and in vitro metabolism data.* J Pharmacol Exp Ther, 1997. **283**(1): p. 46-58.

26. Shibayama, T., et al., *Prediction of pharmacokinetics of CS-023 (RO4908463), a novel parenteral carbapenem antibiotic, in humans using animal data.* Xenobiotica, 2007. **37**(1): p. 91-102.

27. Zheng N, et al., *Interspecies Pharmacokinetic Scaling of Mycophenolic Acid.*, in *FIP Pharmaceutical Sciences 2010 World Congress in Association with the AAPS Annual Meeting* 2010: New Orleans, LA.

28. Lave, T., P. Coassolo, and B. Reigner, *Prediction of hepatic metabolic clearance based on interspecies allometric scaling techniques and in vitro-in vivo correlations.* Clin Pharmacokinet, 1999. **36**(3): p. 211-31.

29. Tang, H. and M. Mayersohn, *Utility of the coefficient of determination (r2) in assessing the accuracy of interspecies allometric predictions: illumination or illusion?* Drug Metab Dispos, 2007. **35**(12): p. 2139-42.

30. Goteti, K., C.E. Garner, and I. Mahmood, *Prediction of human drug clearance from two species: a comparison of several allometric methods.* J Pharm Sci, 2009. **99**(3): p. 1601-13.

31. Lin, J.H., *Applications and limitations of interspecies scaling and in vitro extrapolation in pharmacokinetics.* Drug Metab Dispos, 1998. **26**(12): p. 1202-12.

Table I.1 Elimination rate constants and half-lives of MI-219 in liver microsomes

Species	Mouse	Rat	Monkey	Dog	Human
Elimination rate constant (min^{-1})	0.04449	0.04935	0.07842	0.06535	0.04747
Half-life (min)	15.6	14.0	8.8	10.6	14.6

Table I.2 Unbound fraction of MI-219 in plasma and liver microsomes and blood-plasma partition

Species	Unbound fraction in plasma(fu_p)	Unbound fraction in liver microsome(fu_m)	Blood-Plasma partition (calculated)	Blood-Plasma partition (measured)
Mouse	4.45%±0.04%	2.03%±0.29%	0.570	0.581±0.010
Rat	3.87%±0.79%	2.44%±0.73%	0.558	0.597±0.008
Monkey	1.96%±0.65%	N.A.	0.598	N.A.
Dog	1.39%±0.48%	N.A.	0.586	N.A.
Human	1.65%±0.27%	6.16%±0.58%	0.567	0.572± 0.006

Table I.3 Pharmacokinetics (mean ± standard deviation) of MI-219 in animals

Species	Body weight (kg)	Dose (mg/kg)	$AUC_{(0-\infty)}$ (h*ng/L)	$MRT_{(0-\infty)}$ (h)	$T_{\frac{1}{2}}$ (h)	Vd_{ss} (L/kg)	CL (L/h/kg)
Mouse	0.018	10	7046±760	0.9±0.04	1.89±0.04	6.37±0.40	7.15±0.76
Rat	0.2	5	2349±30	1.38±0.12	2.20±0.34	2.95±0.31	2.13±0.03
Monkey	2.5	10	11884±1714	2.41±0.28	3.35±0.09	2.07±0.35	0.85±0.12
Dog	8	2	6236±2312	1.63±0.36	3.90±0.78	0.60±0.32	0.36±0.14

Table I.4 Predicted clearance of MI-219 in humans

Methods	Predicted human clearance (L/h/kg)
Simple allometry	0.146
Allometric scaling normalized by in vitro microsomal data	0.080
Allometric scaling with CL×MPL	0.086
Allometric scaling with CL×BW	0.064
Two term power equation	0.184
Multi-exponential allometric scaling	0.342
Single species scaling	0.324 (rat), 0.148 (dog), 0.346 (monkey)
Physiologically based *in vitro-in vivo* scaling	0.237 (well-stirred model)
	0.282 (parallel-tube model)
f_u corrected intercept method	0.168

Table I.5 Predicted pharmacokinetic parameters of MI-219 in humans by Dedrick plots, Wajima's method and NONMEM modeling

Parameters	Kallynochrons	Apolysichrons	Dienetichrons	Wajima's method	NONMEM
alpha	5.671	4.521	1.587	4.644	2.839
beta	0.225	0.274	0.109	0.253	0.161
A	76308	56043	40934	32457	21714
B	4554	4957	3165	3017	3109
CL (L/h/kg)	0.148	0.164	0.091	0.265	0.186
Vd_{ss} (L/kg)	0.406	0.370	0.471	0.679	0.843
MRT (h)	2.74	2.25	5.16	2.57	4.53
R^2	0.958	0.952	0.894	0.979	N.A.
AIC	556	619	643	543	N.A.

Table I.6 Pharmacokinetic parameters of rats, dogs and monkeys estimated from
individual and combined NONMEM models

Species		CL (L/h/kg)	V1 (L/kg)	V2 (L/kg)	Q (L/h/kg)
Rats	Combined	2.486	1.150	3.321	0.897
	Individual	2.374	0.989	3.437	0.958
Dogs	Combined	0.504	0.364	1.052	0.490
	Individual	0.515	0.353	1.024	0.409
Monkeys	Combined	0.834	0.523	1.511	0.593
	Individual	0.884	0.452	2.140	1.516

Figure I.1 Metabolic stability of MI-219 in animal and human liver microsomes
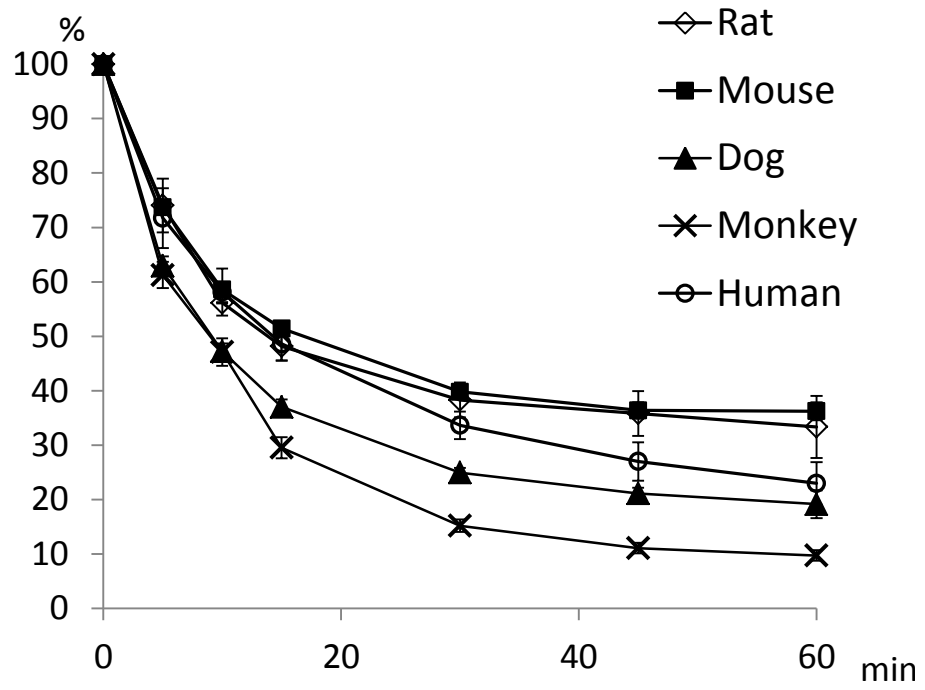
Figure I.2 Mean plasma concentration–time following single intravenous administration
of MI-219. Mouse (n = 33; three animals per time point), rat (n = 3), dog (n = 3), and monkey (n = 6).
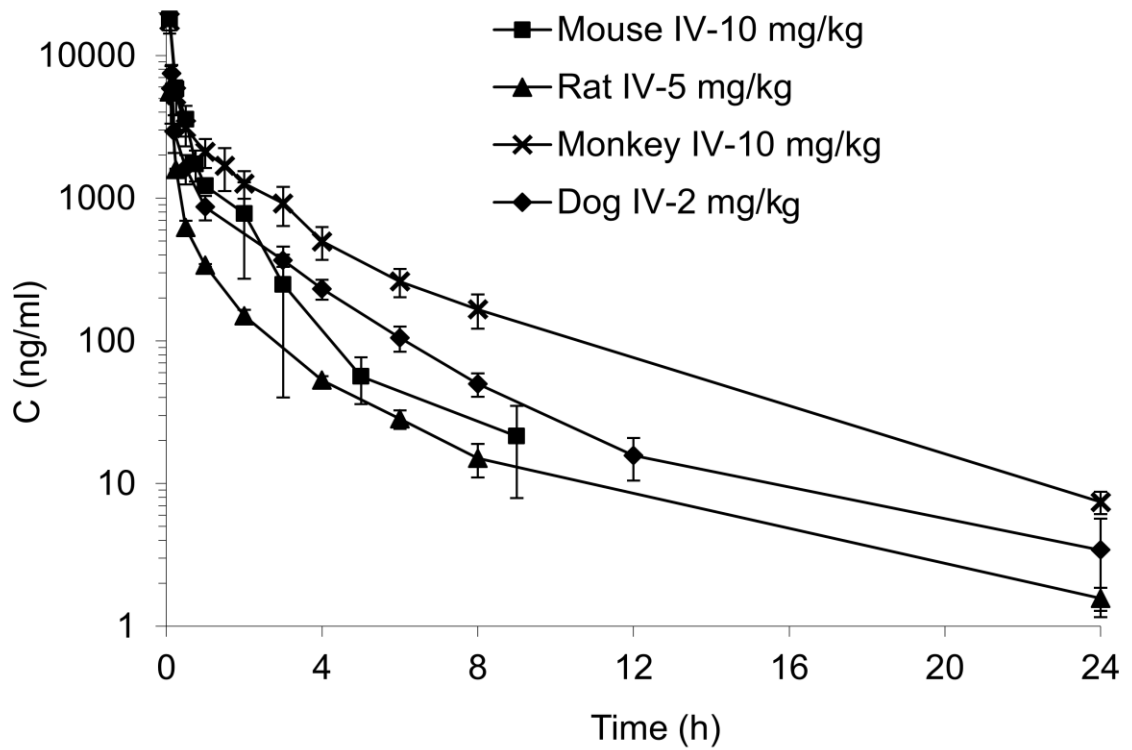
* The concentrations of MI-219 in mouse plasma at 24 hr postinjection were lower than LOQ.

Figure I.3 Allometric scaling of CL (A); CL corrected by microsomal data (B); CL corrected by MLP (C); and CL corrected by brain weight (D); Vd_{ss} (E); unbound Vd_{ss} (F).

A
y = 0.5301x + 0.0317
R^2 = 0.9901

B
y = 0.4468x - 0.0784
R^2 = 0.9997

C
y = 0.8918x + 1.1049
R^2 = 0.9706

D

$\log(CL*BrW)$ (L/h)

Human

Monkey   Dog

Rat

$y = 1.4526x - 1.8471$
$R^2 = 0.9784$

Mouse

LogW (kg)

E

$\log Vd_{ss}$ (L/kg)

Human

Monkey   Dog

Rat

$y = 0.6618x + 0.2458$
$R^2 = 0.9638$

Mouse

LogW (kg)

F

$\log(Vd_{ss}/fu_p)$ (L/kg)

Human

Monkey

Dog

Rat

$y = 0.8594x + 1.8832$
$R^2 = 0.98$

Mouse

Log W (kg)
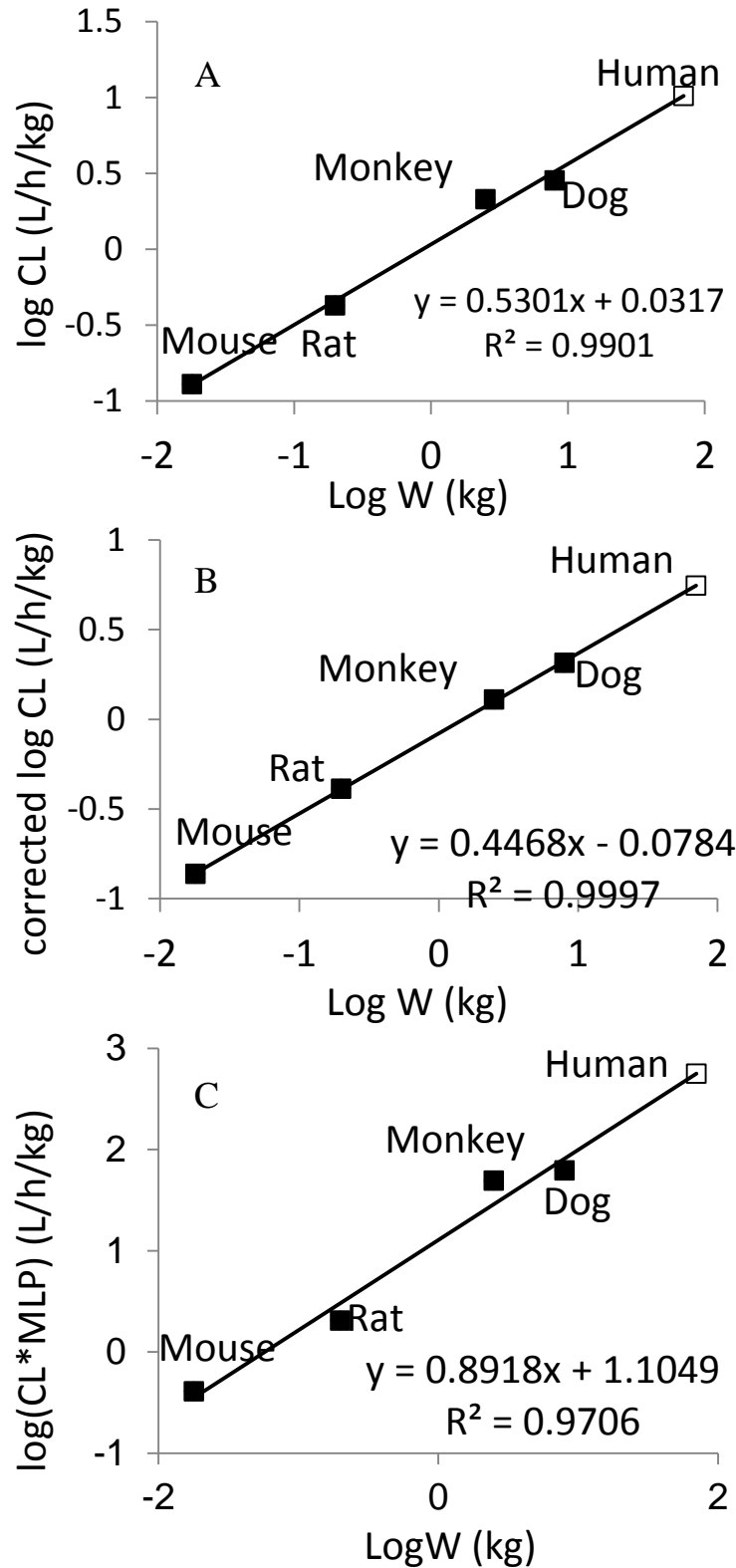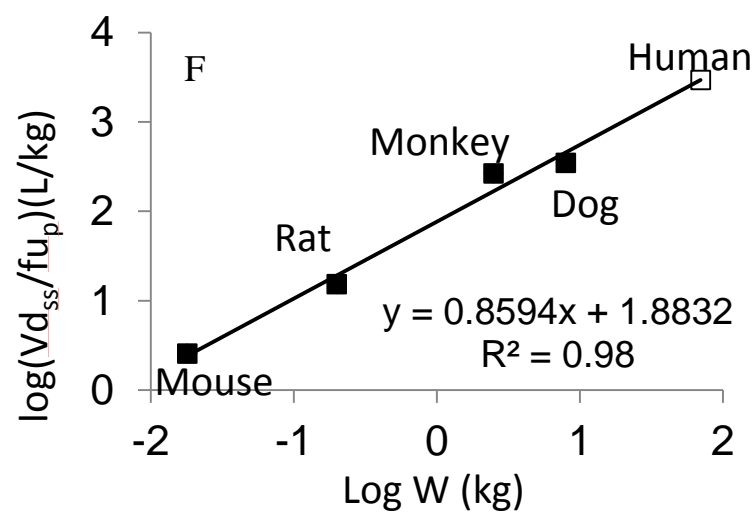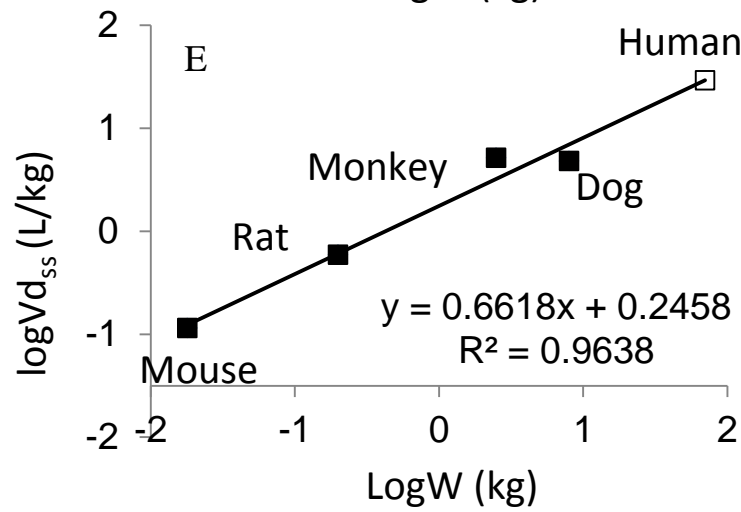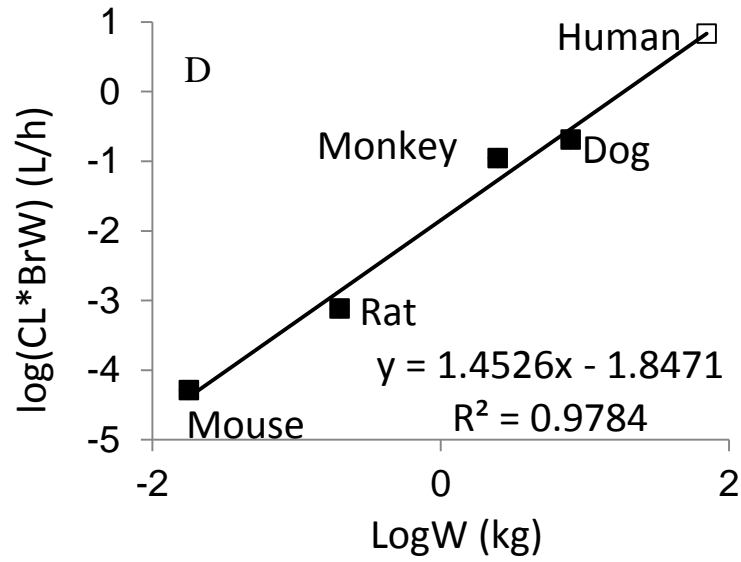
Figure I.4 Predicted human clearance using two-term power equation

$$CL = 3.52 * W^{0.277} * (BrW)^{0.274}$$
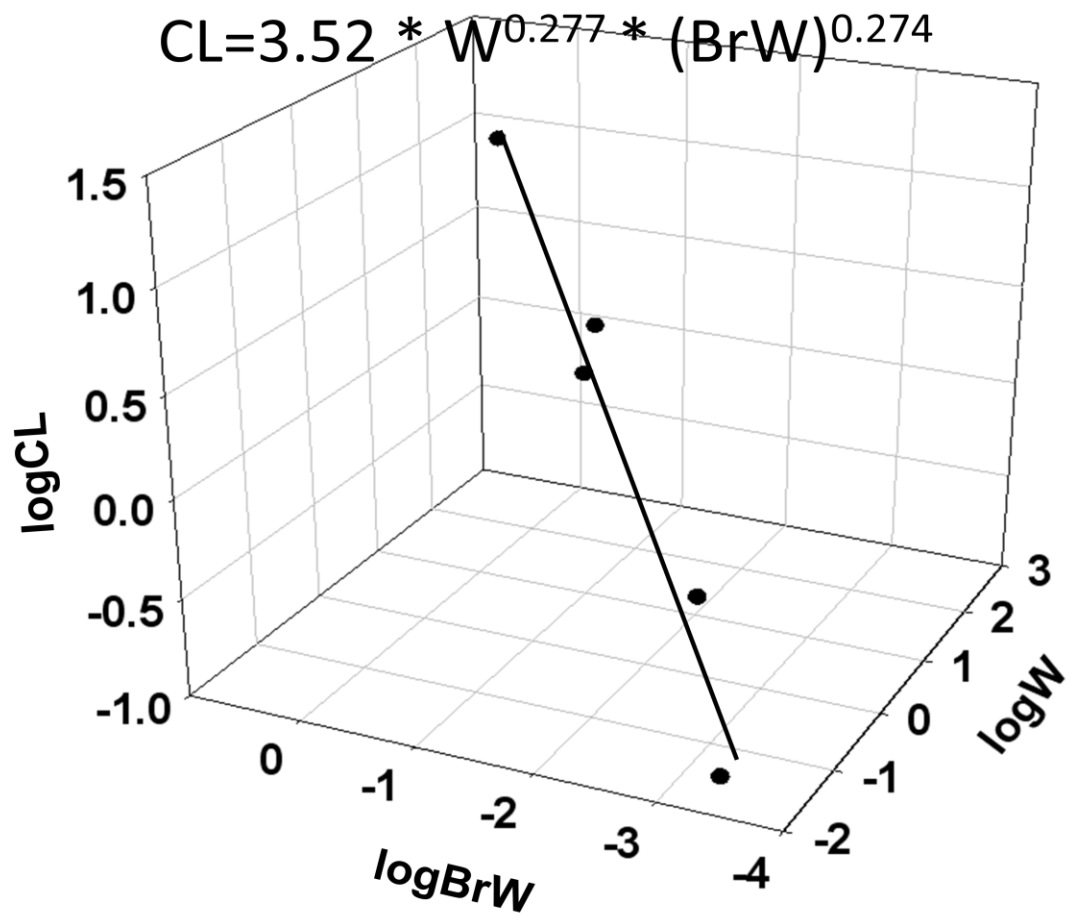
Figure I.5 The predicted plasma concentration-time profiles in humans following a single i.v. injection of MI-219 (5 mg*kg^{-1}) based on Kallynochrons, Apolysichrons and Dienetichrons time transformation.
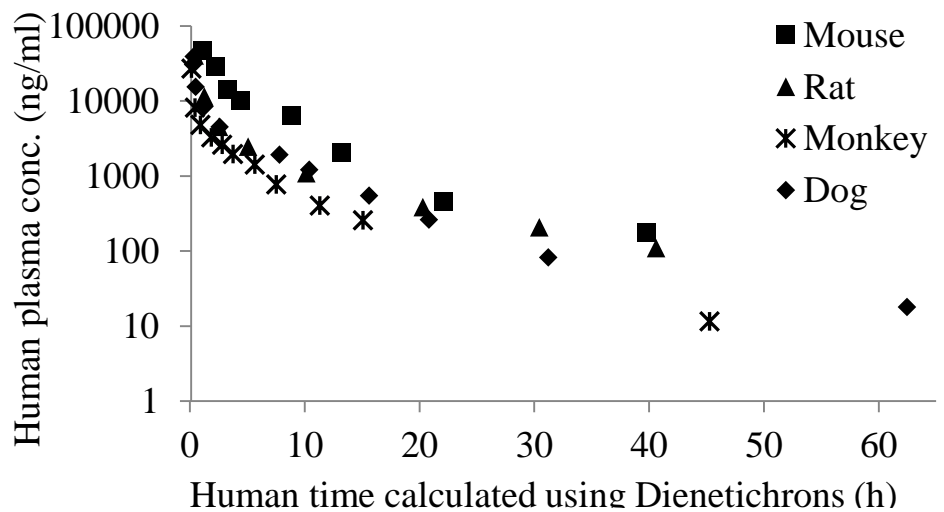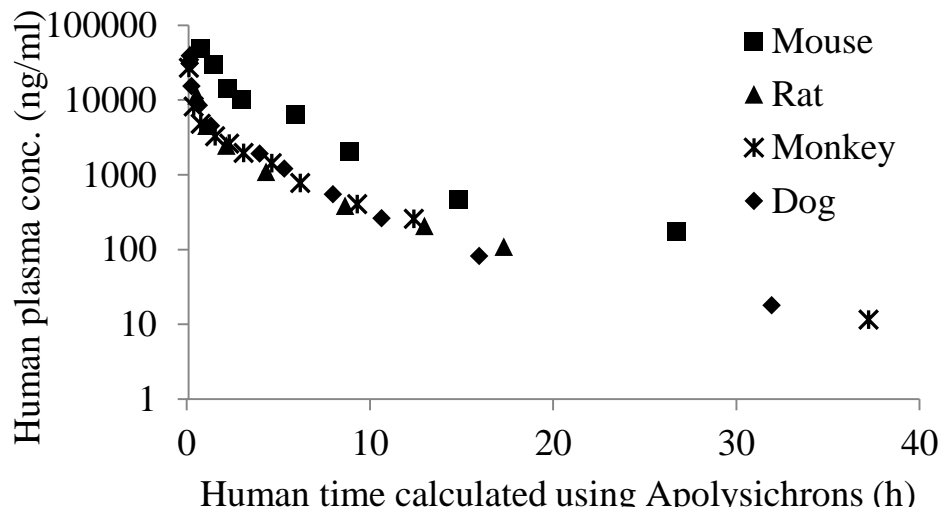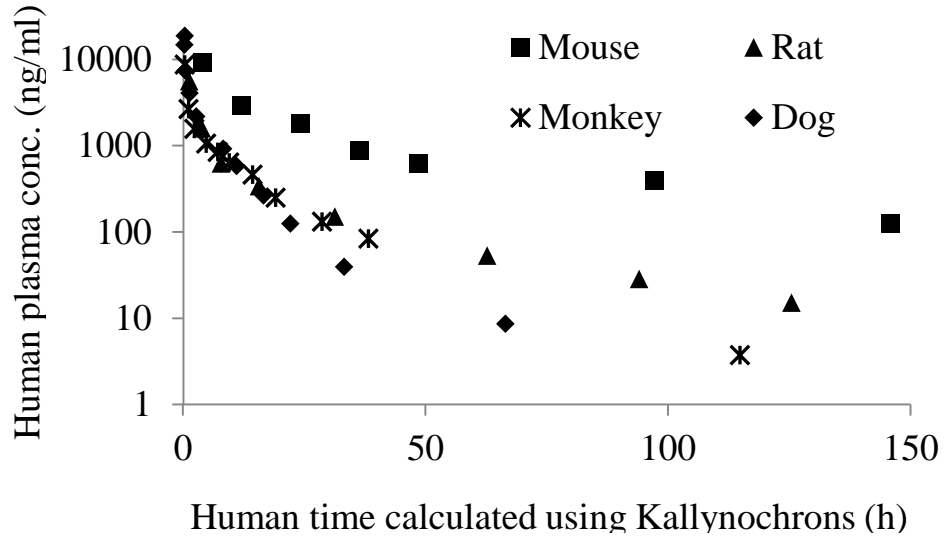
Figure I.6 Superimposition of normalized concentration-time profiles of MI-219 in animals using Css and MRT (Wajima's method) (A) and predicted human concentration-time profile following a single i.v. injection of MI-219 (5 mg*kg^{-1}) (B)
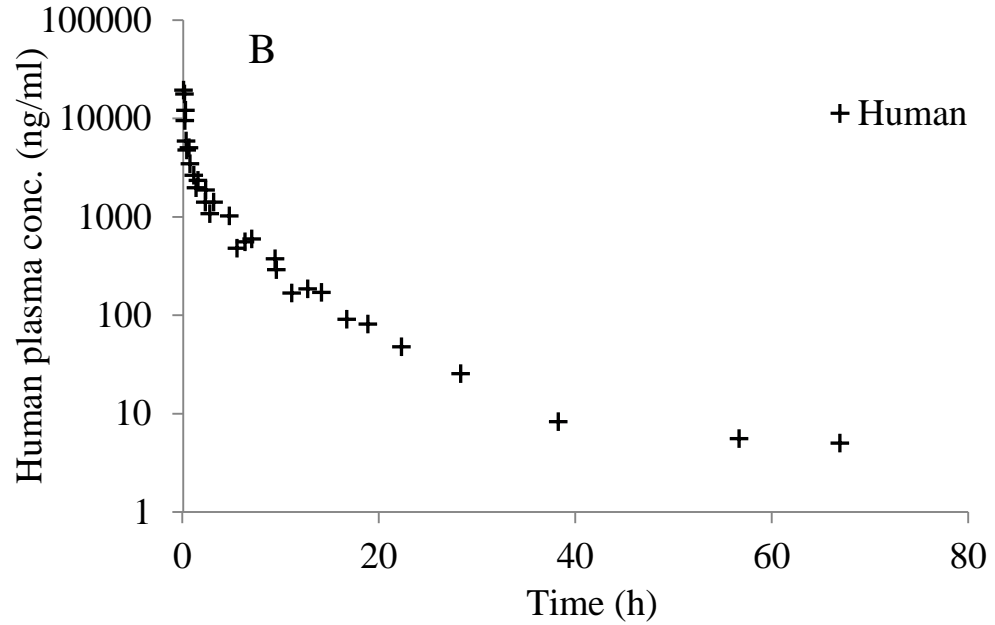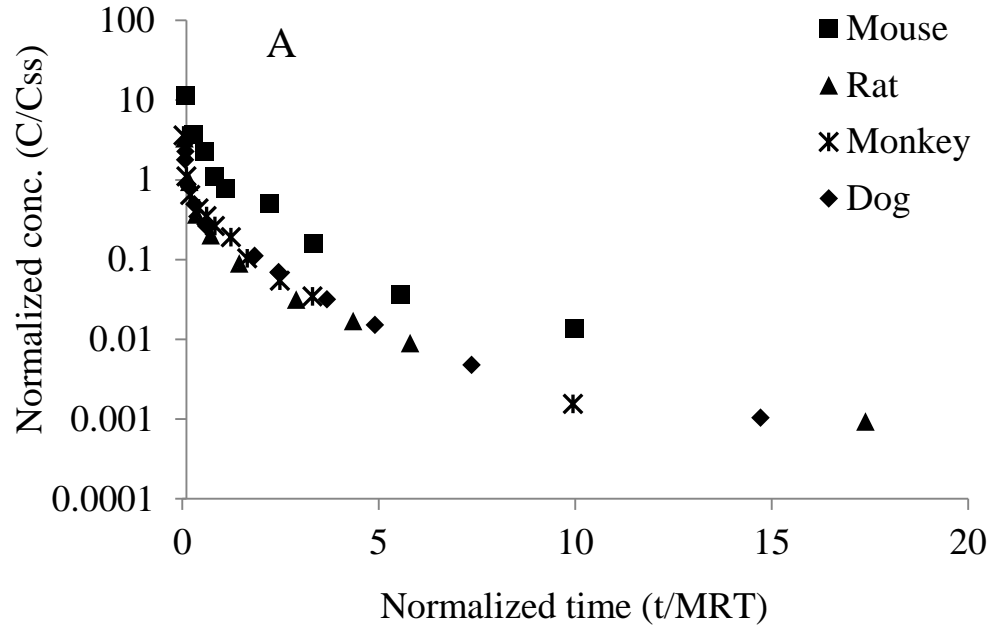
Figure I.7 Human concentration-time profile following a single i.v. injection of MI-219 (5 mg*kg^{-1}) predicted by allometric scaling-based NONMEM modeling.
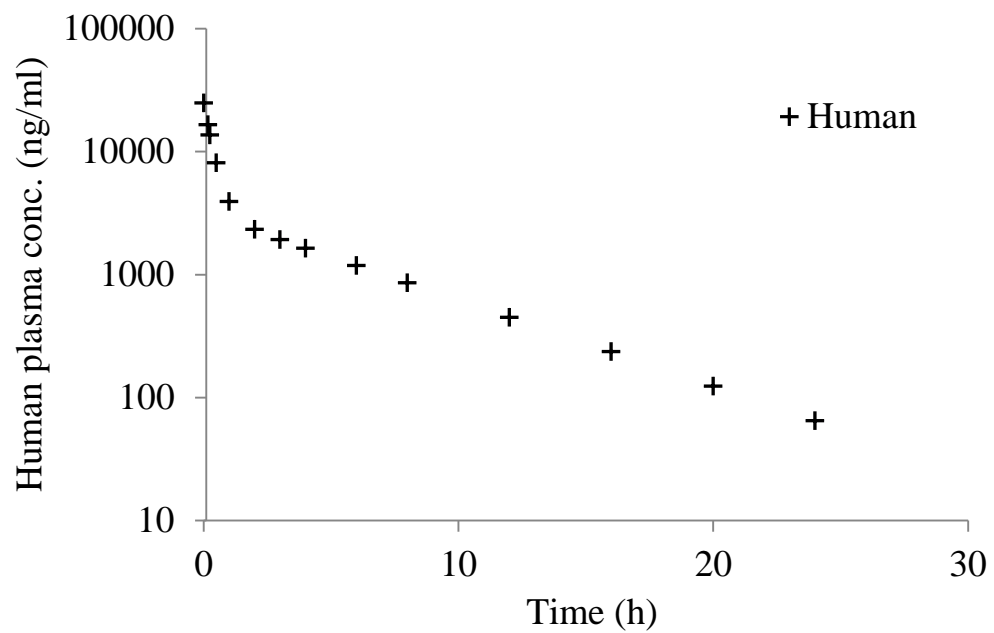
Figure I.8 Model validation - Observations in dogs (n =3) fell in 90% confidence intervals of simulations